Optimization of
A Micromechanical Single Element Oscillator
Using Nonlinear Electrostatic Control

by

Jonathan Andrew Kossuth

B.S., Massachusetts Institute of Technology (1993)
M.S., Massachusetts Institute of Technology (1993)

SUBMITTED TO THE DEPARTMENT OF
AERONAUTICS AND ASTRONAUTICS
IN PARTIAL FULFILLMENT OF THE REQUIREMENTS
FOR THE DEGREE OF

Doctor of Philosophy

at the

Massachusetts Institute Of Technology

February 1998

Signature of Author: _____
Department of Aeronautics and Astronautics
September 30, 1997

Certified by: _____
Wallace E. Vander Velde
Thesis Supervisor, Professor of Aeronautics and Astronautics

Certified by: _____
Anthony Kourepenis
Technical Supervisor, C.S. Draper Laboratory

Certified by: _____
John J. Deyst
Professor of Aeronautics and Astronautics

Certified by: _____
Dr. Marc S. Weinberg
C.S. Draper Laboratory

Accepted by _____
Jaime Peraire
Professor of Aeronautics and Astronautics
Chairman, Department Graduate Committee

OPTIMIZATION OF
A MICROMECHANICAL SINGLE ELEMENT OSCILLATOR
USING NONLINEAR ELECTROSTATIC CONTROL

by

Jonathan Andrew Kossuth

ABSTRACT

This thesis presents a detailed examination of the closed-loop behavior of a micromechanical single element oscillator. First, describing function analysis techniques are used to demonstrate the existence and stability of a limit cycle for a micromechanical resonator self-excitation loop. It is shown that this limit cycle exists at the amplitude-dependent resonant frequency of the drive axis, and it is stable if the restoring force is a linear or hard spring. The amplitude regulator is adequately modeled with the slowly varying parameter method of Krylov and Bogoliubov. Transfer functions relating parameter variations to the frequency and amplitude of the limit cycle are derived.

A rotational degree of freedom is added to the traditional, two degree of freedom (horizontal and vertical), coupled, nonlinear, second-order dynamic model of a micromechanical resonator. It is shown through finite element analysis that rotations less than 0.01 degrees do not affect the interdigitated comb finger capacitance. The impact of angular displacement is limited to the parallel plate capacitor between the rotor and the substrate electrodes. A new method for simultaneously observing the vertical and angular displacements of the rotor is used to measure the open-loop responses of both motions due to on-axis applied forces and coupling from horizontal oscillations.

Force-rebalance loops are designed to eliminate both vertical and rotational motions and to provide information on the magnitude of the in-phase and quadrature (with respect to the rotor horizontal velocity) components for both degrees of freedom. Extensive numerical simulations demonstrated the stability and robustness of these force-rebalance loops. The vertical rebalance loop was successfully implemented on a laterally oscillating micromechanical resonator. Vertical motion was reduced by a factor of 175. Information on both the in-phase and quadrature components of vertical motion was provided through the control voltages. An applied rate sinusoidal disturbance was introduced to generate in-phase Coriolis force errors. The vertical motion was held at zero by the force rebalance loop, and the in-phase control signal provided information on the magnitude of the disturbance.

Thesis Committee:
        Wallace E. Vander Velde, Sc.D., Professor of Aeronautics and Astronautics
        Anthony Kourepenis, C.S. Draper Laboratory
        John J. Deyst, Sc.D., Professor of Aeronautics and Astronautics
        Marc S. Weinberg, Ph.D., C.S. Draper Laboratory

This thesis was researched and written at the Charles Stark Draper Laboratory under Contract 15901.

Publication of this thesis does not constitute approval by the Laboratory of the findings or conclusions contained herein. It is published for the exchange and stimulation of ideas.

Permission is hereby granted by the author to the Massachusetts Institute of Technology to reproduce any or all of this thesis.

Jonathan Andrew Kossuth

Acknowledgments

Having spent the last nine years at MIT, there are more than enough people that need to be thanked. To those people whom I mention below, I thank you for your support and encouragement throughout the years. For those whom I have forgotten, consider my hat silently tipped to you in appreciation.

First, I must thank Professor Wallace Vander Velde, who has been my advisor in one form or another for the past eight years. From my undergraduate years, through my Master's thesis, and to my doctoral dissertation, his genius, support, and advice have made the MIT experience very special. His breadth and depth of knowledge are truly amazing, and he never failed to help me overcome the obstacles of my research.

Thanks also to Anthony Kourepenis, who welcomed me into the micromechanical program at Draper Laboratory many years ago. He has been a friend, a role model, and an inspiration for getting the job right. Tony has, by example, shown me the balance of a successful engineer. Without his mentoring, I would not be where I am today.

Dr. Marc Weinberg has also been a knowledge source on matters micromechanical. He has provided me with significant insight on the dynamics of micromechanical resonators and on the design of control systems. Without Marc's assistance and time, this thesis would not have materialized.

Professor John Deyst has been an invaluable member of my doctoral committee. As both my minor advisor and a committee member, he has given me an appreciation of the field of systems engineering, as well as numerous suggestions to improve the flow and organization of this thesis.

Of course, none of this would have been possible if, 8 years ago, Charles Kochakian did not take a chance and hire an MIT sophomore to intern at Draper Laboratory. I thank him very much for providing me with an opportunity to excel that I may not otherwise have had.

Much thanks and gratitude goes to the gang down in the test lab. Richard Elliott helped with so much electronic design that I cannot begin to express my gratitude to him. I also appreciate the efforts of Philip Rose in constructing the test electronics, and for reminding me to work with pride and perfection. The test lab would not have been as

enjoyable without the presence of Jamie Bolotin and David Hom. Paul Magnussen never failed to amuse with one of his fishing stories, and Larry Weldon has been a great officemate for the better part of three years.

Thanks also are extended to James Campbell, who assisted with the fabrication and packaging of the SEO, and who also seemed to know how to get things done in a minimum amount of time. I'd also like to thank Lance Niles and the fabrication team for laying out and etching my device.

Special thanks go to Liz Zotos, the Aero/Astro graduate secretary, who has listened to more excuses and complaints from graduate students than any human should have to, but has never failed to help us solve and overcome our difficulties. The entire Aero/Astro graduate community thanks her for her efforts.

Well, I would have been committed long ago if not for Rick Grinnell. He made sure that I always got out just enough to keep from going crazy. The advice and counsel of Rob Kassel over the years are greatly appreciated. ...And, even though he didn't have much to do with my Ph.D., and he lives in Texas, the friendship of Jim Goldinger is appreciated.

As I near the end of my thanks, I'd like to thank my family for their support over the years. Now that I'm married, I'd like to thank my in-laws, the Santagates, for their encouragement. My sister, Mary Beth, has inspired me through the tough times. James, my brother, has been an inspiration to me, and I look forward to catching a few more ball games with him, now that I have some free time. My parents have been a source of strength throughout my life. I'd like to thank my mother, Beth, for always supporting and encouraging me to do my best and to strive for excellence...and for perhaps caring a bit too much. I'd also like to thank my father, George, for helping to land men on the moon and providing me with a great role model, someone in whose footsteps I hope to follow.

Finally, I owe an enormous debt of gratitude and a multitude of thanks to my wife, Kimberly Ann. Over the past nine years, her quiet strength has inspired and supported me through the easy and rough times. She may never realize how great a role she played in this thesis, but without her, none of this would have been possible. She believed in me the entire time, and, for that faith, I am eternally grateful. I look forward to spending a lot more time with her, and I love her very, very much.

Table of Contents

List of Figures

13

List of Tables

Chapter 1

Introduction

1.0 History of Resonant-Structure Micromotors

Resonant-structure micromotors are "a class of mechanisms that operate on the principle of mechanical resonance so that the armature is driven for maximum displacement and power [25, 26]." The desire to keep time accurately has yielded several significant developments in resonant structure motors over the last 700 years. In the thirteenth century, the first resonant-structure motor was constructed: a clock based on the verge escapement and resonant pendulum. To avoid bearing friction and wear, these mechanisms used flexural components; thus, they may be considered the oldest resonant-structure motors. These devices kept time poorly and were abandoned in 1675, when the recoil escapement was invented [25, 26].

This concept of the resonant-structure motor was refined over the next three centuries. The first miniaturization of these motors occurred between 1510 and 1765, when portable clocks, i.e., watches, such as pocket watches, were developed; these were the first resonant-structure mini-motors. The invention of the "remontoire escapement" by Thomas Mudge in 1765 greatly aided this reduction in size. These chronometers were capable of 21,600 beats per hour by the late eighteenth century: a very high frequency for that time [25, 26].

The main drawback of the pendulum clocks is that they depended on gravity to generate resonance. The development of the balance wheel freed clock designers from gravity's limitations and focused research on improved clock design and material performance for resonant-structure motors. The transition from timepieces to micromotors begin with the introduction of the first resonant-structure millimotor: the Bulova Accutron watch. In this device, a miniature tuning fork was mechanically resonated at 100 Hz with electric forcing. This fork drove a gear wheel at 380,000 teeth per hour, making it one of the first commercially available resonant-structure millimechanical motors [25, 26].

The next step, which led to resonant-structure micromotors, came in the 1980s, when, at the University of California at Berkeley, Roger T. Howe and William C. Tang developed resonant structures on silicon, using traditional integrated circuit etching techniques [31-33]. Tang's invention of the comb drive permitted electrostatic forces to resonate suspended micromechanical rotors. In this design, a flat, planar proof mass, guided by a flexure suspension, moves translationally, parallel to the substrate, as shown in Figure 1.1. Applying a voltage to the comb drive generates a position-independent force on the rotor. By using a comb drive to sense the motion of the rotor, closed-loop oscillations may be sustained at frequencies on the order of tens of kiloHertz. By exploiting a double-ended tuning fork design for the rotor, many applications for the resonant-structure micromotor, including gyroscopes, accelerometers, and time references, have emerged.
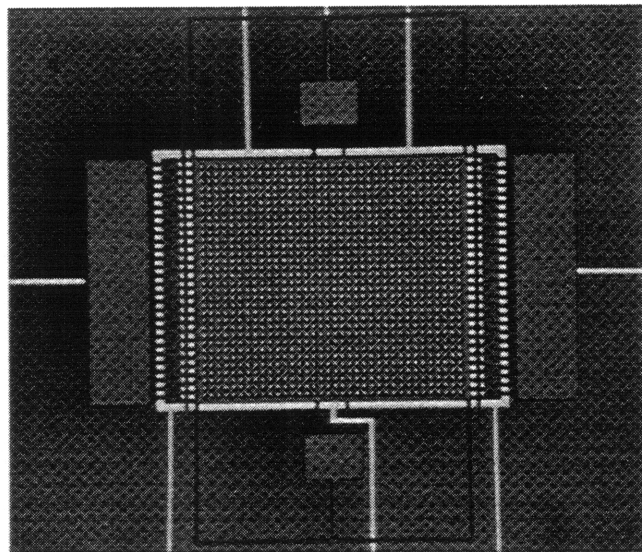
Figure 1.1. Optical Micrograph of a Typical Single Element Oscillator

It is interesting to note that the current issues of resonant-structure micromotors are very similar to those encountered 700 years ago. In the early development of the clock, friction on the macro level was a significant concern and forced designers to use flexural components. As the timepieces became smaller, it was clear that friction and wear limited performance, regardless of the size of the device. Presently, micro-friction is a major dissipative force, and suspended rotors are used in micromotors to minimize the effects of friction by eliminating moving mechanical contact. In addition, the micromechanical resonators are operated in a vacuum, either sealed to hold the vacuum or connected to a pump to remove the air. However, as clocks continued to shrink in size, the material choice and design became major issues. In micromotors, silicon is used

because of its attractive properties, and careful design will maximize the performance of the silicon while minimizing the effects of drag [25, 26].

1.1 Fabrication of Micromechanical Resonators

At Draper Laboratory, micromechanical structures, including oscillators, gyroscopes, and accelerometers, are built using a dissolved-wafer process, which results in crystal silicon structures anodically bonded to glass substrates [37]. The silicon and glass are both defined and etched separately, and then joined together to yield a micromechanical structure.

In the silicon process, a recess is etched into a p-type (100) silicon wafer using KOH to define the gap spacing of the conducting plates. Next, the thickness of the device is determined by using a high temperature boron diffusion. Reactive ion etching (RIE) cuts out the structure features, which are then released by etching past the p++ etch stop.

In the first glass step, a #7740 Corning glass wafer is recessed by 1600 Å, and a multi-metal system is deposited and lifted off of the wafer. With this method, the metalprotrudess only about 500 Å above the surface of the glass, and it defines both sense and drive plates for the proof mass, as well as provide output leads from the silicon transducers to the controlling electronics.

Finally, the glass and silicon are electrostatically bonded together at 375° C with a potential of 1000 V. During this process, the silicon and glass are drawn tightly together, insuring a low resistance silicon to gold contact. The last step is a selective etch in ethylene diamine pyrocatechol, which dissolves the silicon up to the heavily doped (p+) diffused layers. This fabrication sequence requires only single-sided processing, with three masking steps on the silicon and one on the glass. Yield from this approach is high, and it is compatible with batch processing.

1.2 Motivation for Advanced Modeling and Control

The traditional dynamic model for a laterally driven micromechanical resonator has two degrees of freedom: horizontal and vertical. As these devices mature and fabrication becomes more precise, the effects of a rotating proof mass on performance need to be quantified. By adding a rotational degree of freedom to the dynamic model, the impact of angular displacements on the dynamics of the system and on the capacitor sensing and forcing models can be investigated.

As a first step in advanced dynamic modeling, the existence of a limit cycle at the lateral resonant frequency for the oscillator closed-loop system with a relay feedback element is demonstrated. This limit cycle is shown to be stable for linear and hard

19

springs, and the effects of system parameter perturbations on the amplitude and frequency are determined. The amplitude regulator loop is simplified using the slowly varying parameter method, and the resulting model is shown to be an accurate representation of the loop.

In addition to modeling the rotational behavior of the system, the next step in the development of micromechanical devices is to force rebalance both the vertical and rotational motions of a laterally oscillating proof mass. Previous efforts at vertical closed-loop control have included static vertical positioning of a stationary proof mass [9, 10]. To be truly effective, the vertical and rotational control loops should be capable of eliminating all out-of-plane motion that couples from the proof mass lateral dynamics. In this scenario, the controllers can compensate for dynamic and transient errors, such as spring cross-coupling or rate-induced Coriolis forces. When implemented, this micromechanical resonator is operating with three closed loops: the drive axis loop to sustain lateral oscillations, and the vertical and rotational force-rebalance loops to eliminate out-of-plane motions.

1.3 A 3 DOF Dynamic Model with Force-Rebalance Loops

In the following chapters, the fundamental theories of micromechanical resonators are presented for a single element oscillator (SEO). The stability of the self-exciting motor loop is then demonstrated. Next, the third degree of freedom is added, and its impact on the entire electromechanical model of the oscillator is examined. Force-rebalance loops for both the vertical and rotational degrees of freedom are then designed. Finally, the three DOF dynamic parameters are characterized, and the vertical axis is controlled with a force-rebalance loop.

1.3.1 Organization of Thesis

This thesis was organized so that someone with a basic grasp of mechanics and control theory could follow the development of the dynamic model and force-rebalance loops. Each chapter begins with a brief description of the problem examined in that chapter. Therefore, in places, the text may seem fundamental. This was done intentionally to permit the reader an opportunity to understand the direction of the investigation.

1.3.2 Fundamental Micromechanical Resonator Theory

The two most important concepts for microelectromechanical resonators are mass-damper-spring second-order mechanics and capacitor electrostatics. In Chapter 2, an

overview of the mechanical models is given, and cubic spring behavior is examined in detail, because of the significant role that it plays in the closed-loop performance of the horizontal axis.

Electrostatic fundamentals are also presented in Chapter 2. Forcing and sensing models for both the interdigitated comb finger and parallel plate capacitors are developed. For the comb fingers, finite element analysis leads to conclusions that are not readily apparent from the analytic models of the comb drive, such as comb sensitivity to vertical motion. The spring softening effect of the parallel plate capacitor is also explored, and its constraints on control system implementation are highlighted.

1.3.3 Sustained Limit Cycles in Micromechanical Resonators

For mass production of these devices, self-excitation loops have been developed to sustain lateral oscillations of the proof mass. In Chapter 3, describing function analysis is used to linearize the sinusoidal responses of the cubic spring and hysteretic relay and to develop a state-space representation of the system dynamics. This analysis is then expanded to demonstrate closed-loop stability of a limit cycle at the nonlinear, amplitude-dependent, horizontal resonant frequency of the self-oscillation loop. The stability criterion is based solely on the nature of the nonlinear spring, and the system is stable for linear and hard springs. Stable lateral oscillations do not depend on the pressure at the device. Finally, the effects of transient perturbations of the system parameters on the limit cycle amplitude and frequency are investigated with describing function analysis.

In addition, a first-order model of the amplitude regulator is developed by assuming that, compared to a resonant frequency of 20 kHz, the oscillation amplitude and frequency are slowly varying functions of time. With this model, the behavior of the oscillator amplitude during startup can be studied. From the analysis, it is clear that the amplitude regulator is a very nonlinear controller. This simplified model is compared to simulation results in order to show that it is an adequate representation of the amplitude regulator.

Finally, a numerical simulation is developed for the closed self-excitation loop. By using the basic horizontal and vertical dynamic model, the startup and steady-state behaviors of the simulation correspond well with observed performance in micromechanical resonators. This simulation contributes understanding and a simpler mathematical model of the resonator behavior.

1.3.4 Three Degree of Freedom Micromechanical Resonator Model

In Chapter 4, a rotational degree of freedom, θ, is added to the dynamic model. First, the impact of dynamic coupling between this mode and the other two modes is discussed, and this model is then linearized to a state-space representation using describing function analysis. The simulation introduced in Chapter 3 is modified to include the proof mass rotational dynamics, and the stability of the θ-dynamics is demonstrated.

Investigating the impact of rotation on the electrostatic analysis of Chapter 2 requires re-evaluating both the comb and parallel plate capacitor models. First, the comb drive model is rederived for a rotating proof mass, and finite element analysis is used to verify that small rotations, on the order of $0.01°$, do not affect the comb drive model developed in Chapter 2. Next, the parallel plate capacitor model is rederived, with significant rotational effects. From this new parallel plate model, sensing methods for both vertical and rotational motion are presented. Since vertical motion is the common mode and rotational motion is the differential mode, it is proposed that the sense plate be split, and the integrated charge outputs from these plates summed and differenced to yield indications of both vertical and rotational motions.

1.3.5 Force-Rebalance Loops for Vertical and Rotational Motion

In Chapter 5, force-rebalance loops for both vertical and rotational motion are developed. First, the required modulations and demodulations are linearized to derive a baseband model for the disturbances and the control signals. With this model, a PI compensator is designed to guarantee stability for both the vertical and rotational force-balance loops. Here, the compensator gain depends on the pressure in the system; as the pressure in the system decreases, the required gain increases.

For rotational control, the control plate design requires nonlinear torquing coefficients. To linearize these terms, complex control signals are required; solutions are presented for both the actual and an alternative oscillator design. The nonlinearity is introduced by the proof mass oscillations; a torquing model is also developed for a stationary proof mass.

Finally, the simulation from Chapter 4 is modified to include both force-rebalance loops. After verifying the performance and robustness of the vertical and rotational control loops independently, the micromechanical oscillator is successfully simulated with all three loops closed. The horizontal oscillation is sustained by the oscillator loop and amplitude regulator, and the vertical and rotational motions are driven to zero by their respective force-rebalance loops.

1.3.6 Parameter Measurement and Closed-Loop Oscillator Experiments

In Chapter 6, the single element oscillator is constructed and experiments are performed to determine the parameters of the device. First, the dimensions of the oscillator are determined with a WYCO® profilometer [5]. Next, the mass and moment of inertia are calculated from analytic models. All of the capacitors are then measured. From these values, forcing and sensing constants for all degrees of freedom are estimated.

The on-axis and cross-coupling parameters of the device are determined with open-loop frequency responses. Here, a reduced model is used to determine the significant couplings, which include the drive axis motion and force coupling into both the vertical and rotational degrees of freedom.

Finally, the vertical force-rebalance loop is implemented about an advanced resonator design. Here, the vertical motion is reduced substantially, and the in-phase and quadrature rebalance channels provide independent information on the magnitudes of each component of the vertical motion. The effectiveness and robustness of the control system is demonstrated by introducing a sinusoidal disturbance to the system and verifying that the control voltages compensate for this additional error.

1.3.7 Conclusions and Future Work

Finally, in Chapter 7, conclusions from this thesis and recommendations for future work are presented. The next significant step would be to independently force rebalance two proof masses, such as in a tuning fork gyroscope. With this accomplishment, the dynamic range and sensitivity of such devices would be greatly increased.

Chapter 2

Micromechanical Resonator
Lumped Parameter Modeling

2.0 Theory of Micromechanical Oscillators

The development of silicon micromechanical single element oscillators (SEO) combines many disciplines: classical mechanics, electrostatics, electronic design, finite element analysis, fluid dynamics, and many other diverse fields. The dynamics of a resonator are typically a second-order, damped-spring system, often with nonlinear characteristics. The damping of the device depends greatly on the pressure within the enclosed device; Q's on the order of 250,000 have been observed in very low pressure resonators. Electrostatic actuation is used to generate motion; the invention of the comb drive permits position-independent forcing. Capacitive sensors are used for resonator motion detection. The goal of this chapter is to present a basic mechanical model of the oscillator and to describe how electrostatics are used both to generate and to sense proof mass motion.

2.1 Two Degree of Freedom Dynamic Resonator Model

The basic dynamic model for a micromechanical resonator or SEO consists of two degrees of freedom, both vertical and horizontal, and it may be derived from Lagrange's energy formulation. Although this result is useful, non-dimensionalizing the equations of motion results in more powerful conclusions and improves numerical simulations of the system. Because the proof mass is supported by beams, the springs for both degrees of freedom may exhibit nonlinear behavior at large oscillation amplitudes. In this section, the dynamic model for a typical micromechanical oscillator is derived, and cubic spring behavior is explored in detail.

25

2.1.1 Lagrangian Derivation of 2-D Lumped Parameter Model

The basic dynamic model for a micromechanical resonator is a coupled pair of second-order, nonlinear, differential equations [2]. The two generalized coordinates for the SEO are the horizontal, or drive, motion along the x-axis; and the vertical, or out-of-plane, motion along the y-axis, as shown in Figure 2.1. In this schematic, a top and side view are shown with the drive and sense combs included so that positive x-axis motion is towards the motor sense comb, and that positive y-motion is away from the substrate, i.e., out of the page. A third coordinate, z, is used only as a reference axis. These coordinates are defined with respect to the substrate, not the inertial reference frame. The proof mass is assumed to be constrained by design to be rigid, i.e., immovable, along the z-axis, and unable to rotate about any axis.
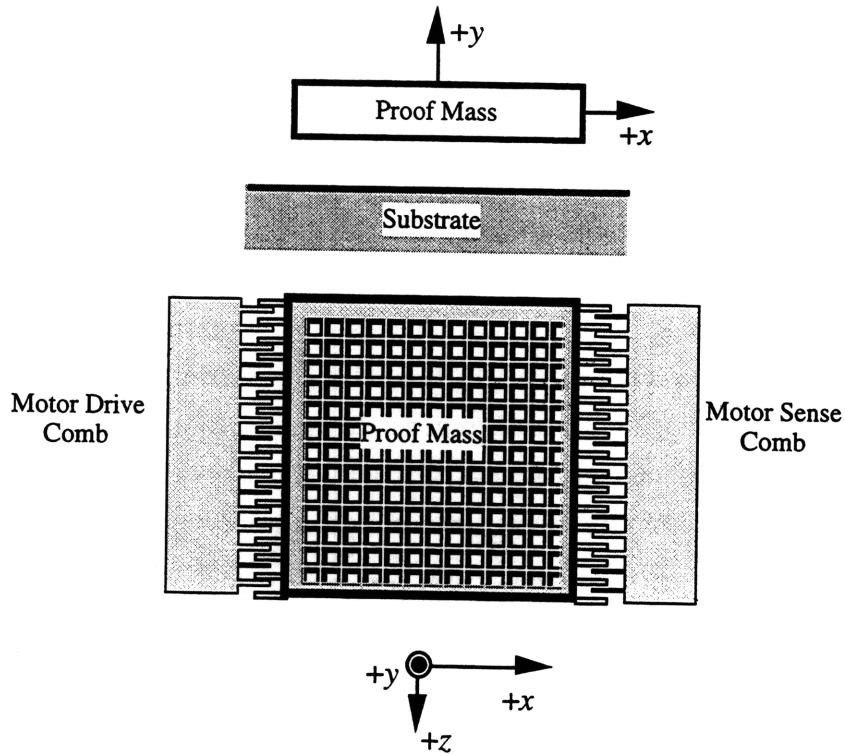
Figure 2.1. Top and Side Views of Two-Dimensional SEO Coordinate System

The equations of motion for this system may be derived using Lagrange's equation for a system of n generalized coordinates, ξ_i, and time, t:

$$\frac{d}{dt}\left(\frac{\partial L}{\partial \dot{\xi}_i}\right) - \frac{\partial L}{\partial \xi_i} = \Xi_i \quad \text{for } i = 1, \ldots, n \tag{2.1}$$

26

where,

L = Lagrangian operator = $T^* - V$

T^* = total kinetic co-energy of system

V = total potential energy of system from conservative forces, and

Ξ_i = total non-conservative and external forces for ξ_i.

The only non-conservative force in a micromechanical resonator is assumed to be viscous damping, which is proportional to velocity. Lagrange's equation may now be rewritten as

$$\frac{d}{dt}\left(\frac{\partial L}{\partial \dot{\xi}_i}\right) - \frac{\partial L}{\partial \xi_i} + \frac{\partial D_v}{\partial \dot{\xi}_i} = \Xi_{ext,i} \quad \text{for } i = 1,\ldots,n \tag{2.2}$$

where D_v is the viscous damping energy term and $\Xi_{ext,i}$ are the applied external forces.

Since the velocities must be expressed with respect to inertial space, if the device is rotating about its z-axis at a rate Ω, then the horizontal and vertical velocities will have angular velocity components. The total kinetic energy of the basic resonator may be expressed in terms of the two generalized coordinates

$$T = \frac{1}{2}m(\dot{x} - \Omega y)^2 + \frac{1}{2}m(\dot{y} + \Omega x)^2 \tag{2.3}$$

where m is the mass of the oscillator element. It is assumed that a cross-inertia term does not exist in this system. However, both stiffness and damping cross-coupling do exist. The total potential energy may be expressed as

$$V = \frac{1}{2}k_x x^2 + \frac{1}{3}k_{x_2} x^3 + \frac{1}{4}k_{x_3} x^4 + \frac{1}{2}k_y y^2 + \frac{1}{3}k_{y_2} y^3 + \frac{1}{4}k_{y_3} y^4 + k_{xy}xy + \frac{1}{2}CV^2 \tag{2.4}$$

where k_x, k_{x2}, and k_{x3} are the linear, quadratic and cubic spring terms along the x-axis, respectively; k_y, k_{y2}, and k_{y3} are the linear, quadratic and cubic spring terms along the y-axis; and k_{xy} is the cross-coupling term between the x- and y-axes. The CV^2 term is the energy stored in the capacitor; this term is used to generate motion in the micromechanical resonator. Here, C represents all of the capacitors, and the effects of the individual capacitors will be addressed in significant detail in Section 2.2

The non-conservative viscous damping function, D_v, may then be written as

$$D_v = \frac{1}{2}b_x \dot{x}^2 + \frac{1}{2}b_y \dot{y}^2 + b_{xy}\dot{x}\dot{y} \tag{2.5}$$

where b_x, b_y, and b_{xy} are the x-axis, y-axis and cross-coupling damping coefficients for the micromechanical resonator. There are no external forces in this system.

If, for now, all of the electrostatic terms (from CV^2) acting along the x-axis are defined as F_x, and those along the y-axis as F_y; and the centripetal force terms are

neglected as higher order; then, by inserting Equations 2.3, 2.4, and 2.5 into Equation 2.2, the Lagrangian formulation of the equations of motion are

$$m\ddot{x} + b_x\dot{x} + k_x x + k_{x_2} x^2 + k_{x_3} x^3 + k_{xy} y + b_{xy}\dot{y} - 2m\Omega\dot{y} = F_x \qquad (2.6)$$

$$m\ddot{y} + b_y\dot{y} + k_y y + k_{y_2} y^2 + k_{y_3} y^3 + k_{xy} x + b_{xy}\dot{x} + 2m\Omega\dot{x} = F_y \qquad (2.7)$$

which is a nonlinear, coupled, second-order system consisting of four states: a position and velocity for motion along both x and y.

2.1.2 Non-dimensionalization of the Equations of Motion

Before proceeding, it is useful to non-dimensionalize the dynamic model. By normalizing both the time and the displacement, further analysis and simulation will be greatly simplified. The resonant frequency of a typical system is about 20 kHz, and the displacements are on the order of microns, requiring very, very small time steps in order to simulate this system adequately. By non-dimensionalizing the system, the required time steps and resulting displacements are much closer to one, permitting a more accurate simulation, since problems with roundoff errors, numerical quantization effects, and poorly conditioned matrices are greatly reduced. An additional motivation for non-dimensional analysis is that conclusions and observations, when stated in normalized parameters, are applicable to a range of resonator sizes with similar non-dimensional values.

The first step in the normalization of these equations is to define a non-dimensional time and two non-dimensional displacements,

$$\tau = \omega_n t = \sqrt{\frac{k_x}{m}}\, t$$

$$\tilde{x} = \frac{x}{x_0} \qquad (2.8)$$

$$\tilde{y} = \frac{y}{x_0}$$

where,

ω_n = nominal natural frequency of the x-axis, and

x_0 = nominal steady-state oscillation amplitude along x-axis, normally about 10 μm. By first substituting these three values into Equations 2.6 and 2.7; then by separating the electrostatic forces into on-axis and coupled terms, retaining the Coriolis forces, and neglecting the centripetal forces; and finally by dividing each equation by $m\omega_n^2 x_0$, the following non-dimensional equations are derived:

$$\ddot{\tilde{x}} + \frac{1}{Q}\dot{\tilde{x}} + \tilde{x} + \tilde{k}_{x_2}\tilde{x}^2 + \tilde{k}_{x_3}\tilde{x}^3 + \tilde{\omega}_{xy}^2\tilde{y} + \frac{1}{Q_{xy}}\dot{\tilde{y}} = \tilde{F}_x + \alpha\tilde{F}_y + 2\tilde{\Omega}\dot{\tilde{y}} \qquad (2.9)$$

$$\ddot{\tilde{y}} + \frac{\tilde{\omega}_y}{Q_y}\dot{\tilde{y}} + \tilde{\omega}_y^2\tilde{y} + \tilde{k}_{y_2}\tilde{y}^2 + \tilde{k}_{y_3}\tilde{y}^3 + \tilde{\omega}_{xy}^2\tilde{x} + \frac{1}{Q_{xy}}\dot{\tilde{x}} = \tilde{F}_y + \beta\tilde{F}_x - 2\tilde{\Omega}\dot{\tilde{x}} \qquad (2.10)$$

where,

$$Q = \frac{m\omega_n}{b_x} \qquad \tilde{\omega}_y = \sqrt{\frac{k_y}{k_x}} = \frac{1}{\omega_n}\sqrt{\frac{k_y}{m}} \qquad \tilde{\omega}_{xy}^2 = \frac{k_{xy}}{k_x} = \frac{k_{xy}}{m\omega_n^2}$$

$$\tilde{k}_{x_3} = \frac{k_{x_3}x_0^2}{k_x} \qquad Q_y = \frac{m\omega_y}{b_y} \qquad Q_{xy} = \frac{m\omega_n}{b_{xy}} \qquad (2.11)$$

$$\tilde{k}_{x_2} = \frac{k_{x_2}x_0}{k_x} \qquad \tilde{k}_{y_2} = \frac{k_{y_2}x_0}{k_x} \qquad \tilde{\Omega} = \frac{\Omega}{\omega_n}$$

$$\tilde{F}_x = \frac{F_x}{k_x x_0} \qquad \tilde{k}_{y_3} = \frac{k_{y_3}x_0^2}{k_x}$$

$$\tilde{F}_y = \frac{F_y}{k_x x_0}$$

and Ω is an applied input rate that generates a Coriolis force. In these definitions, both $\tilde{\omega}_{xy}^2$, the cross-frequency, and Q_{xy}, the cross-damping, may be negative. These terms have been defined only to assist in the understanding of the system, i.e., as a cross-resonant frequency and cross-damping. For now, α and β are simply scaling coefficients to describe the cross-coupling of the vertical and horizontal forces. In Section 2.2.3, more accurate models of these terms will be presented.

2.1.3 Duffing's Equation and Non-linear Springs

A significant nonlinear element in the dynamics of both degrees of freedom is the cubic spring. In 1918, G. Duffing first proposed a harmonic solution to this problem by using the iteration method, and, therefore, this equation is known as Duffing's Equation. In general terms, a non-dimensionalized, damped, forced, Duffing equation may be expressed as [22]

$$\ddot{x} + \delta\dot{x} + x + \lambda x^3 = \gamma\cos\omega t$$
$$x(0) = \alpha \qquad (2.12)$$
$$\dot{x}(0) = \beta$$

where,

ω = frequency of the applied force

t = dimensional time

δ = the damping parameter

λ = the cubic spring parameter

γ = the force amplitude

and α and β are the initial conditions of the system. The character of the nonlinear spring is determined by λ. For $\lambda > 0$, the spring is hard; for $\lambda < 0$, the spring is soft; and for $\lambda = 0$, the spring is linear. This equation is identical in form to Equations 2.9 and 2.10 if the cross-coupling terms are neglected.

Duffing's equation may be analyzed by a variety of methods. Here, Lindstedt's perturbation method is used to develop the classic solution to the damped Duffing equation and to provide analysis of the behavior of the cubic spring. In Chapter 3, a describing function approach yields identical results that are then used in the state-space model of the system. Perturbation methods, such as Lindstedt's, are very effective at analyzing nonstationary systems when the amplitudes and frequencies are slowly varying functions of time.[1]

First, the parameters are defined as functions of ε (a small parameter), so that, as ε goes to zero, the system reduces to an unforced, undamped, linear oscillator:

$$x(\varepsilon) = x_0 + \varepsilon x_1 + \ldots$$

$$\alpha(\varepsilon) = \alpha_0 + \varepsilon \alpha_1 + \ldots$$

$$\beta(\varepsilon) = \beta_0 + \varepsilon \beta_1 + \ldots$$

$$\gamma(\varepsilon) = \varepsilon \gamma_1 + \ldots \qquad (2.13)$$

$$\delta(\varepsilon) = \varepsilon \delta_1 + \ldots$$

$$\lambda(\varepsilon) = \varepsilon \lambda_1 + \ldots$$

$$\omega(\varepsilon) = \omega_0 + \varepsilon \omega_1 + \ldots$$

By defining the coefficients in this manner, small input forces near the resonant frequency will generate large amplitude responses because of the very light damping provided by small δ. In this perturbation analysis, only terms to the first order in ε are kept. In order to examine the harmonic response of the system, let $\omega_0 = 1$, so that the

---

[1] This is not the only time that this condition is required. Krylov and Bogoliubov required this for their describing function-like analysis shown in Chapter 3. The describing function analysis and most of the stability analyses also assume systems of slowly varying amplitude and frequency (or phase).

30

forcing is at a frequency that varies slightly from the ideal resonator[2]. Substituting the values above into Equation 2.12 yields[3]

$$\ddot{x} + \varepsilon\delta_1\dot{x} + x + \varepsilon\lambda_1 x^3 = \varepsilon\gamma_1 \cos(1 + \varepsilon\omega_1)t \qquad (2.14)$$

Differential equations for x_0 and x_1 may be found by first defining $\tau = \omega(\varepsilon)t$ in the derivatives and trigonometric terms of Equation 2.14, then by expanding the result with respect to ε, and finally by equating the ε^0 and ε^1 coefficients:

$$x_0'' + x_0 = 0 \qquad (2.15)$$

$$x_1'' + x_1 = -2\omega_1 x_0'' - \delta_1 x_0' - \lambda_1 x_0^3 + \gamma_1 \cos\tau \qquad (2.16)$$

where $'$ denotes $d/d\tau$. The solution to Equation 2.15 is straightforward; it is simply the combination of sines and cosines that yields the correct magnitude and phase of the zeroth order term of x for a given set of initial conditions:

$$x_0 = \alpha_0 \cos\tau + \beta_0 \sin\tau = A_0 \cos(\tau - \varphi) \qquad (2.17)$$

where,

A_0 = magnitude of x_0, and

φ = the phase angle between x_0 and the forcing function.

Inserting this solution into Equation 2.16 leads to a differential equation for x_1:

$$x_1'' + x_1 = 2\omega_1 A_0 \cos(\tau - \varphi) - \delta_1\left(A_0 \sin(\tau - \varphi)\right)$$
$$-\lambda_1\left(A_0 \cos(\tau - \varphi)\right)^3 + \gamma_1 \cos\tau \qquad (2.18)$$

Before proceeding, it is useful to define $\cos\tau$ in terms of τ and φ,

$$\cos\tau = \cos(\tau - \varphi + \varphi) = \cos(\tau - \varphi)\cos\varphi - \sin(\tau - \varphi)\sin\varphi \qquad (2.19)$$

Substituting Equation 2.19 into Equation 2.18 and using the trigonometric identity

$$\cos^3\theta = \frac{3}{4}\cos\theta + \frac{1}{4}\cos3\theta \qquad (2.20)$$

leads to a differential equation for x_1:

$$x_1'' + x_1 = \left\{2\omega_1 A_0 - \frac{3}{4}\lambda_1 A_0^3 + \gamma_1 \cos\varphi\right\}\cos(\tau - \varphi)$$
$$+\left\{\delta_1 A_0 - \gamma_1 \sin\varphi\right\}\sin(\tau - \varphi) - \frac{1}{4}\lambda_1 A_0^3 \cos3(\tau - \varphi) \qquad (2.21)$$

---

[2]This is the linear, non-dimensional, natural frequency of the x-axis motion, as shown in Equation 2.12.
[3]In this analysis, sub- and super-harmonics are acknowledged, but neglected from the analysis. Neither has been observed in closed loop operation of a resonator.

The terms in the braces are linearly resonant, and they lead to secular terms in x_1. Setting them equal to zero defines the resonance in terms of the space spanned by $\cos(\tau-\varphi)$ and $\sin(\tau-\varphi)$

$$2\omega_1 A_0 - \frac{3}{4}\lambda_1 A_0^3 + \gamma_1 \cos\varphi = 0 \tag{2.22}$$

$$\delta_1 A_0 - \gamma_1 \sin\varphi = 0 \tag{2.23}$$

Equation 2.23 gives a solution for φ,

$$\sin\varphi = \frac{\delta_1 A_0}{\gamma_1} \tag{2.24}$$

which implies that

$$\cos\varphi = \sqrt{1 - \left(\frac{\delta_1 A_0}{\gamma_1}\right)^2} \tag{2.25}$$

Substituting this into Equation 2.22 gives an equation relating ω_1 to A_0

$$\left(\omega_1 - \frac{3}{8}\lambda_1 A_0^2\right)^2 = \frac{\gamma_1^2}{4A_0^2} - \frac{\delta_1^2}{4} \tag{2.26}$$

This solution, however, is not expressed in terms of the original Duffing equation parameters. By using the definitions of Equation 2.13 and eliminating ε, substitutions may be made to obtain a function of the original terms,

$$\left(\omega - 1 - \frac{3}{8}\lambda A_0^2\right)^2 = \frac{\gamma^2}{4A_0^2} - \frac{\delta^2}{4} \tag{2.27}$$

which is known as the frequency response equation for Duffing's equation.

Equation 2.27 may then be solved for ω in terms of A_0, and the phase angle may be defined from Equations 2.22 and 2.23:

$$\omega = 1 + \frac{3}{8}\lambda A_0^2 \pm \sqrt{\frac{\gamma^2}{4A_0^2} - \frac{\delta^2}{4}} \tag{2.28}$$

$$\varphi = \pm\tan^{-1}\frac{\delta}{\sqrt{\frac{\gamma^2}{A_0^2} - \delta^2}} \tag{2.29}$$

where, by comparing Equations 2.28 and 2.29 with Equation 2.9,

$$\lambda = \tilde{k}_{x_3}$$

$$\delta = 1/Q, \text{ and}$$

$$\gamma = \tilde{F}_x.$$

The cubic spring nonlinearity shifts the phase of the response by $-\varphi$ with respect to the excitation. The frequency varies nonlinearly with both the amplitude of the oscillation and the forcing of the system. The peak amplitude, defined by the square root term in Equation 2.28, is $A_p = \gamma/\delta$. This amplitude corresponds to a phase of 90°. It will be shown that, in steady-state closed-loop operation, the forcing, γ, will be equal to the damping, δ, resulting in only one possible resonant frequency.

Equations 2.28 and 2.29 may be plotted for various forcing and physical parameters. In Figures 2.2a and 2.2b, the frequency response magnitudes and phases are plotted for a soft ($\lambda < 0$), a linear ($\lambda = 0$), and a hard ($\lambda > 0$) spring versus a normalized frequency. For the soft spring, the frequency is reduced as the amplitude A_0 is increased. Electrostatic forces along the vertical axis cause spring softening. The linear spring behaves as expected, with a symmetric amplitude response and a phase shift of 90° at the resonant frequency of the system. The hard spring shows increasing frequency for larger amplitudes, as is the case on the motor axis. Each of these responses are similar in appearance. For the linear spring, the system exhibits a peak at the resonant frequency of 1, and is at a much lower magnitude away from this point. For the hard spring, this peak amplitude has been "pushed" to the right, such that both the amplitude and phase are multi-valued at frequencies slightly greater than the linear resonant frequency. Similarly, the soft spring has "pushed" the peak to the left, such that the amplitude and phase are multi-valued at frequencies lower than the linear resonant frequency. Far from the normalized frequency of 1, the amplitudes and phases of these systems are identical. However, the nonlinear behavior of these systems near resonance deserves more detailed study.
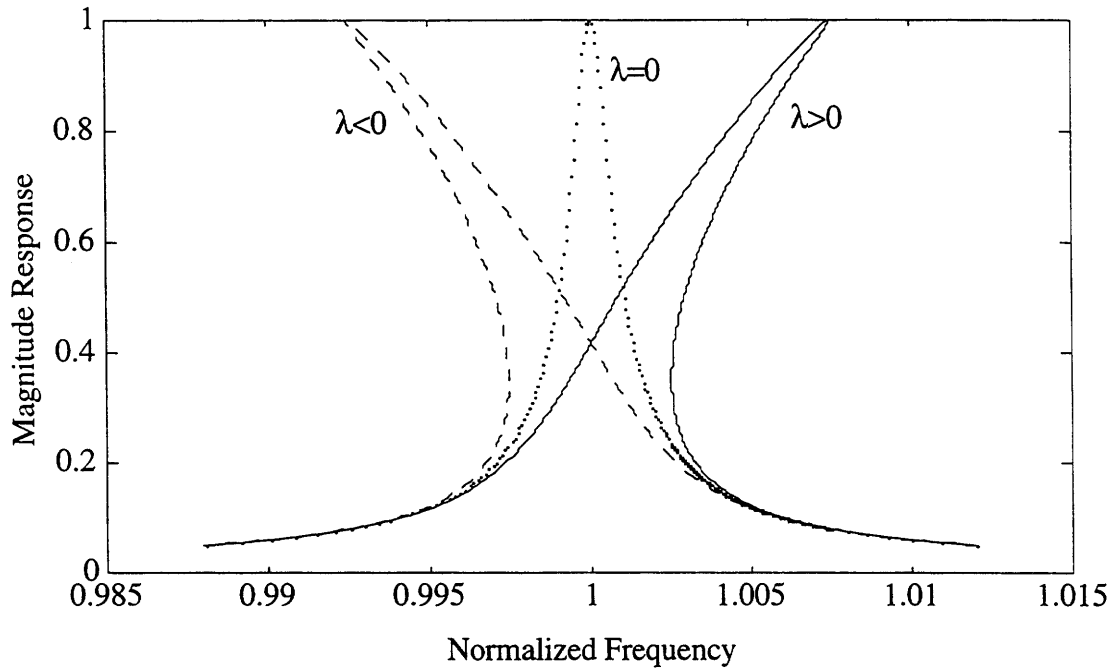
Figure 2.2a. Magnitude Response of Soft, Linear and Hard Springs
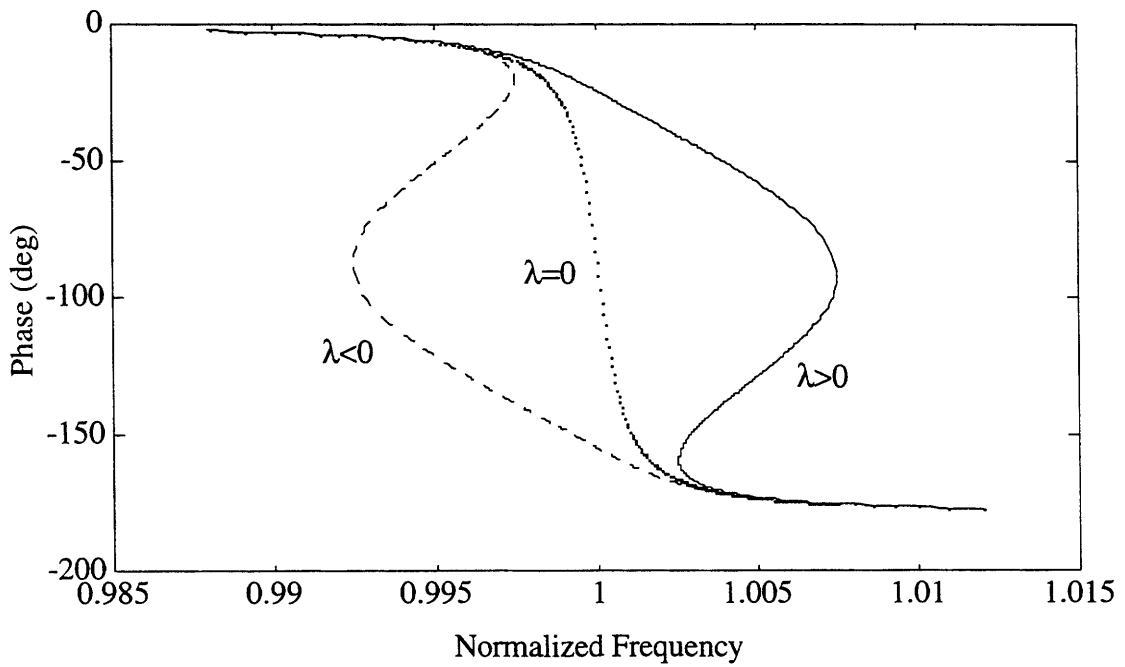
Figure 2.2b. Phase Response of Soft, Linear and Hard Springs

2.1.3.1 Jump Phenomenon

Both the hard and soft spring are multi-valued in both magnitude and phase in critical regions. If a constant amplitude force is applied at increasing frequencies, then the cubic spring may exhibit jump phenomena. This event is a discontinuity in the open-loop response of the system. Both linear and hard spring responses are shown in Figures 2.3a and 2.3b. The upward frequency sweep is started at point 1 in Figure 2.3a, a hard spring response. The amplitude slowly climbs the "shark fin" as the forcing frequency is increased. When the amplitude reaches point 2, it is at its peak value. As ω is increased further, the amplitude jumps suddenly and drastically from point 2 to point 3. Additionally, the phase angle $-\varphi$ drops from $-90°$ to $-180°$, as shown in Figure 2.3b. The response is then at a much lower amplitude for further increases in ω past point 4. If the frequency is instead decreased, starting at point 4, the amplitude will increase from point 4 to point 5. At point 5, a further decrease in ω will cause the amplitude to jump to point 6. The amplitude will continue to decrease as the frequency is lowered past point 1.

If instead the spring is a soft spring, a decreasing frequency sweep starting at point 4 in Figure 2.4a will generate the larger amplitude response with the jump occurring from point 5 to point 6. Sweeping up in frequency beginning at point 1 results in a jump from point 2 to point 3. The phase in Figure 2.4b also undergoes significant jumps at these critical points.

For both the soft and hard springs, the dashed region on the curve between points 2 and 5 is unstable for an open-loop constant drive amplitude excitation, and it cannot be reproduced experimentally because of the jump phenomenon, but this region can be reached in closed-loop operation. The location of the vertical tangent points, i.e., the jump transition points, may be calculated by finding $d\omega/dA_0=0$ from Equation 2.28:

$$\frac{d\omega}{dA_0} = \frac{3}{4}\lambda A_0 \pm \frac{\gamma^2}{2A_0^3}\left(\frac{\gamma^2}{A_0^2} - \delta^2\right)^{-\frac{1}{2}} = 0 \tag{2.30}$$

This equation is difficult to solve algebraically; but, for a given system, it can be used to determine the amplitude and frequency for which jump phenomena might occur. For the hard spring system modeled in Figures 2.3a and 2.3b, the increasing frequency sweep jump occurs at an amplitude of 0.9992, which corresponds to a non-dimensional frequency of 1.0075 (point 2). The decreasing frequency sweep jumps happens at an amplitude of 0.3495 and a frequency of 1.0025 (point 5). Similar values may be calculated for the soft spring response.
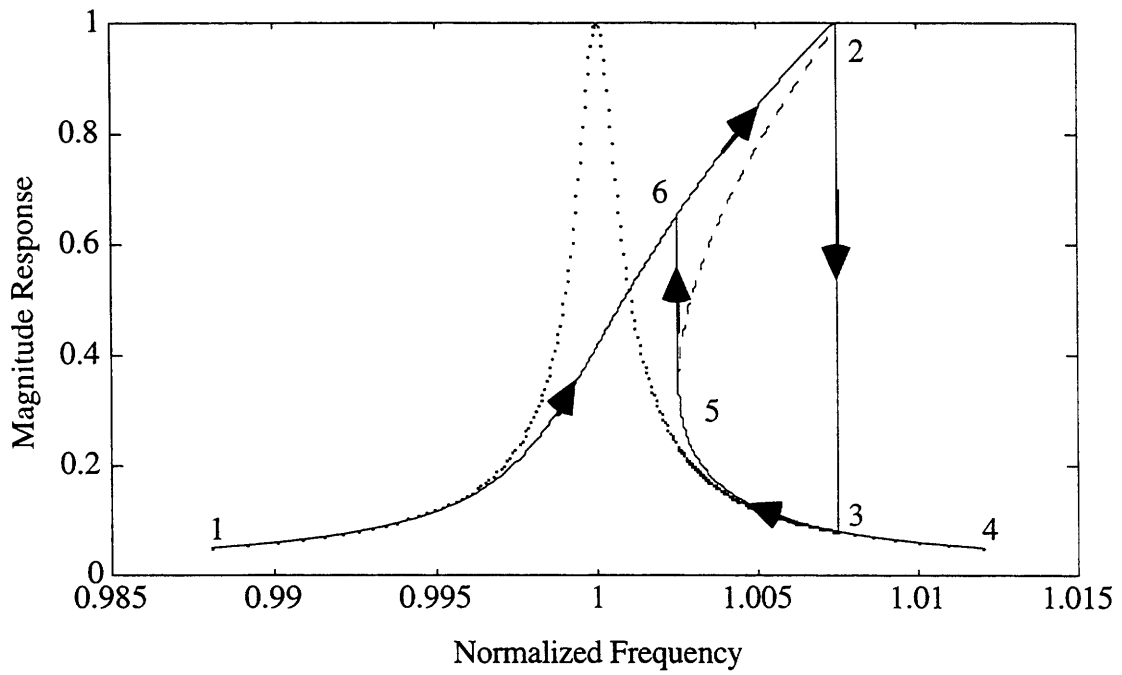
Figure 2.3a. Magnitude of Frequency Response for Hard Spring
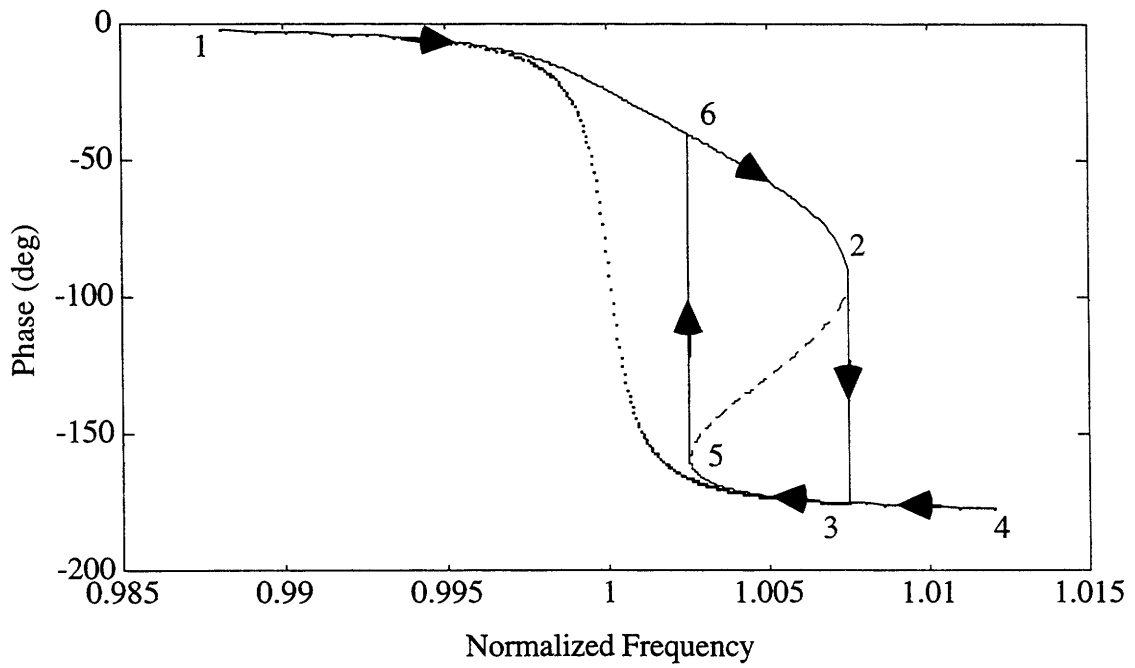
Figure 2.3b. Phase of Frequency Response for Hard Spring
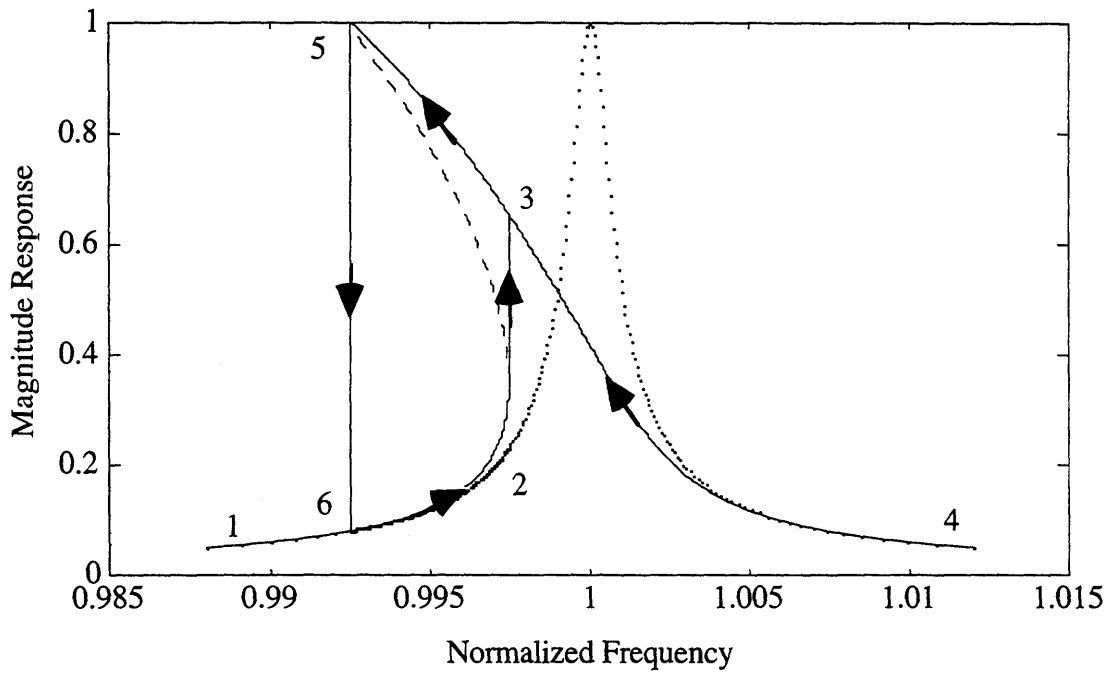
Figure 2.4a. Magnitude of Frequency Response for Soft Spring
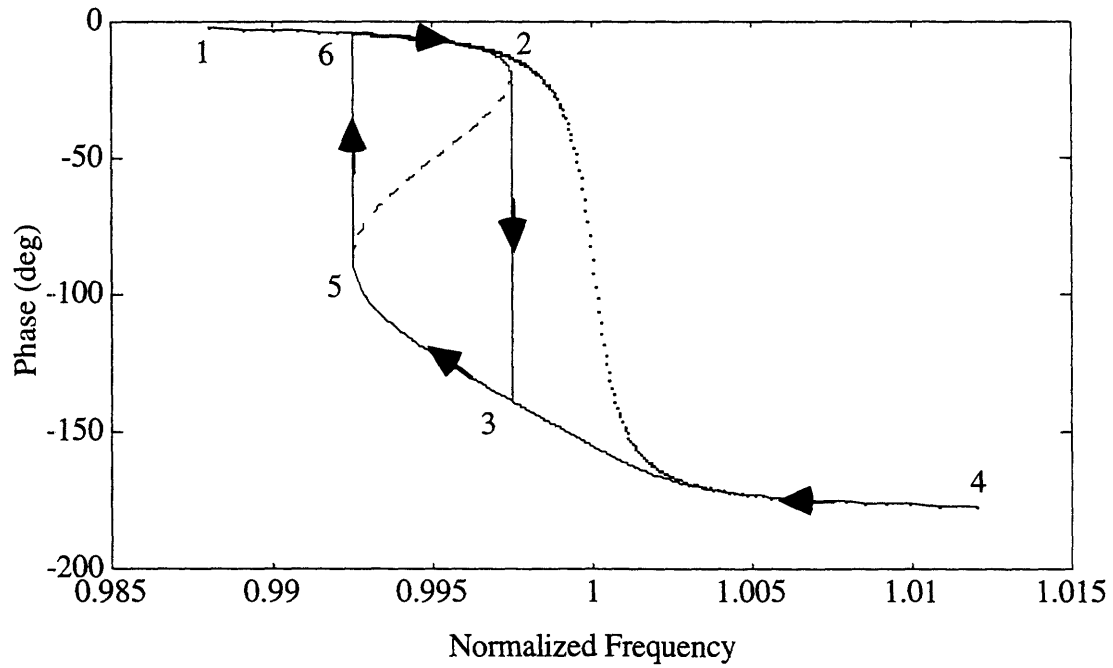
Figure 2.4b. Phase of Frequency Response for Soft Spring

2.1.3.2 Quadratic and Cubic Spring

It will be shown in Section 2.2.4 that the sense axis dynamic equation includes a forcing term that is proportional to $1/y^2$. Through a Taylor series expansion, the force can be represented as a nonlinear spring with linear, quadratic and cubic terms. Once again, the Lindstedt perturbation method can be used to determine the relationship between the resonant frequency and the amplitude of the oscillation [22]. The general equation for this nonlinear spring is

$$\ddot{x} + \delta\dot{x} + x + \mu x^2 + \lambda x^3 = \gamma\cos\omega t$$
$$x(0) = \alpha \tag{2.31}$$
$$\dot{x}(0) = \beta$$

where μ is the quadratic spring parameter. As before, the parameters are expressed as a function of ε. In this case, some first-order dependencies have been neglected, and all terms are expanded to second order:

$$x(\varepsilon) = x_0 + \varepsilon x_1 + \varepsilon^2 x_2 + ...$$
$$\alpha(\varepsilon) = \alpha_0 + \varepsilon\alpha_1 + \varepsilon^2\alpha_2 + ...$$
$$\beta(\varepsilon) = \beta_0 + \varepsilon\beta_1 + \varepsilon^2\beta_2 + ...$$
$$\gamma(\varepsilon) = \varepsilon^2\gamma_2 + ...$$
$$\delta(\varepsilon) = \varepsilon^2\delta_2 + ... \tag{2.32}$$
$$\lambda(\varepsilon) = \varepsilon^2\lambda_2 + ...$$
$$\mu(\varepsilon) = \varepsilon\mu_1 + \varepsilon^2\mu_2 + ...$$
$$\omega(\varepsilon) = \omega_0 + \varepsilon\omega_1 + \varepsilon^2\omega_2 + ...$$

Substituting these approximations into Equation 2.31, letting $\tau = \omega(\varepsilon)t$ (and, consequently, $\omega(\varepsilon)dt = d\tau$), and grouping the ε^0, ε^1, and ε^2 terms yields

$$x_0'' + x_0 = 0 \tag{2.33}$$

$$x_1'' + x_1 = -2\omega_1 x_0'' - \mu_1 x_0^2 \tag{2.34}$$

$$x_2'' + x_2 = -\left(\omega_1^2 + 2\omega_2\right)x_0'' - 2\omega_1 x_1'' - \delta_2 x_0' \tag{2.35}$$
$$-2\mu_1 x_1 x_0 - \lambda_2 x_0^3 + \gamma_2\cos\tau$$

The solution for x_0 from Equation 2.33 is again a sinusoidal term with constant amplitude and phase. This solution is then inserted into Equation 2.34 and solved for x_1 by eliminating the secular terms. Finally, x_0 and x_1 are used in Equation 2.35 to find x_2 by again setting the secular terms equal to zero. These solutions are [22]

$$x_0 = A_0 \cos(\tau - \varphi) \tag{2.36}$$

$$x_1 = -\frac{\mu_1}{2} A_0^2 \left[1 - \frac{1}{3} \cos(2(\tau - \varphi)) \right] \tag{2.37}$$

$$x_2 = \frac{A_0^3}{16} \left(\frac{\mu_1^2}{3} + \frac{\lambda_2}{2} \right) \cos(3(\tau - \varphi)) \tag{2.38}$$

The amplitude, phase, forcing frequency, and forcing amplitude are related by solving the secular terms of Equations 2.34 and 2.35

$$0 = \omega_1 \tag{2.39}$$

$$0 = 2A_0 \left[\omega_2 - A_0^2 \left(\frac{3}{8} \lambda_2 - \frac{5}{12} \mu_1^2 \right) \right] + \gamma_2 \cos \varphi \tag{2.40}$$

$$0 = \delta_2 A_0 - \gamma_2 \sin \varphi \tag{2.41}$$

By replacing the expansions of Equation 2.32 into the previous three equations, the phase and frequency are classic functions of the input and response amplitudes [22]:

$$\omega = 1 + A_0^2 \left(\frac{3}{8} \lambda - \frac{5}{12} \mu^2 \right) \pm \sqrt{\frac{\gamma^2}{4A_0^2} - \frac{\delta^2}{4}} \tag{2.42}$$

$$\varphi = \pm \tan^{-1} \frac{\delta}{\sqrt{\frac{\gamma^2}{A_0^2} - \delta^2}} \tag{2.43}$$

which are very similar to Equations 2.28 and 2.29, and in fact reduce to those equations as μ, the quadratic spring term, goes to zero. A system with both a quadratic and cubic spring may be expressed as an equivalent cubic spring system by letting the coefficient to the cubic term be

$$\lambda_e = \lambda - \frac{10}{9} \mu^2 \tag{2.44}$$

In this system, the quadratic term acts as a spring softener. The equivalent nonlinear spring will then be hard, linear, or soft, depending on the values of both λ and μ. The only difference between the two systems, to second order in ε, is that the quadratic spring introduces a DC component that is second order in ε

$$\begin{aligned} x(t) &= x_0(t) + \varepsilon x_1(t) + \varepsilon^2 x_2(t) \\ &= A_0 \cos(\tau - \varphi) - \varepsilon^2 \frac{\mu}{2} A_0^2 \left[1 - \frac{1}{3} \cos(2(\tau - \varphi)) \right] \end{aligned} \tag{2.45}$$

No further discussion is necessary, since the analysis mirrors the previous investigation of the cubic spring.

2.1.4 Theory of Damping in Micromechanical Resonators

Air is the most significant source of damping in a micromechanical oscillator [6, 7]. The next greatest contributor to energy loss is the intrinsic damping of the beams supporting the proof mass. The damping of the resonator may be modeled by determining its behavior over four distinct pressure regimes: intrinsic, molecular, viscous laminar and viscous turbulent, as shown in Figure 2.5 [4, 23]. In each region, the dominant factor may be used to provide an estimate of Q.
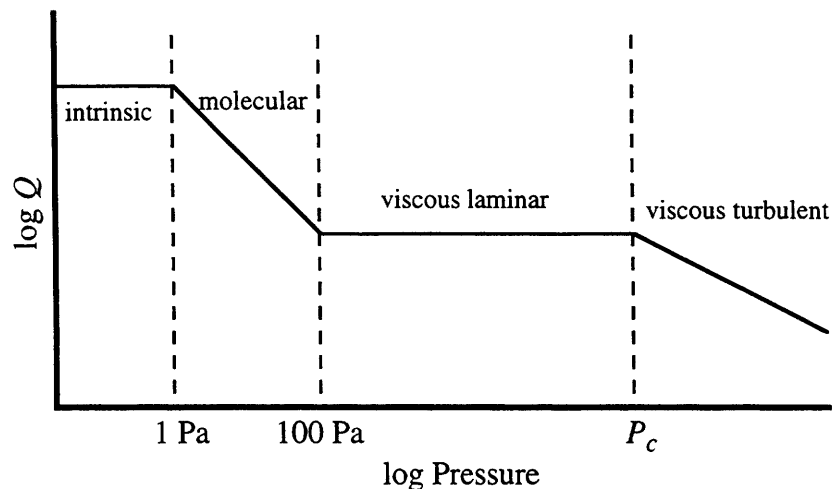
Figure 2.5. Q vs. Pressure for Micromechanical Resonators

In the intrinsic region, the air pressure is so low that the damping of the beam itself is much greater than that due to the air. Here, Q will reach its greatest value, and the best resonator performance is achieved in or near this region. At pressures between 1 and 100 Pa, known as the molecular or Knudsen regime, the dynamics of the gas molecules become the dominant damping force. This increase in damping is caused by "independent collisions of non-interacting air molecules with the moving surface" [4] of the proof mass. The quality factor in this regime varies inversely with the pressure. When the pressure reaches about 100 Pa, there is "sufficient" air for the damping to be modeled as a viscous laminar fluid flow, and the mean free path is about equal to the gaps in the resonator combs. In this region, the quality factor is again independent of the pressure. However, at a critical pressure, Q will become inversely proportional to the square root of the pressure when viscous turbulent damping is created. This occurs at about 5000 Pa, and is never seen in micromechanical resonators.

2.2 Electrostatic Theory of Micromechanical Resonators

Micromechanical resonators rely heavily on the electrostatic forces generated by a capacitor. Most systems use a comb drive actuator to generate lateral forces and a parallel plate actuator to create vertical forces [2, 29-33]. The same capacitive arrangements are used to detect both horizontal and vertical motion. In the following sections, both electrostatic forcing and capacitor sensing theories are presented for the interdigitated comb finger and parallel plate configurations.

2.2.1 Electrostatic Forces

The electrostatic force between the two charged conductors shown in Figure 2.6 may be determined using Lagrange's energy formulation [10, 38]. For these conductors, the potential energy may be expressed as

$$V_p = \frac{1}{2}CV^2 \qquad (2.46)$$

where,

V = voltage between the conductors, and

C = the capacitance between the conductors. It may be a function of x.
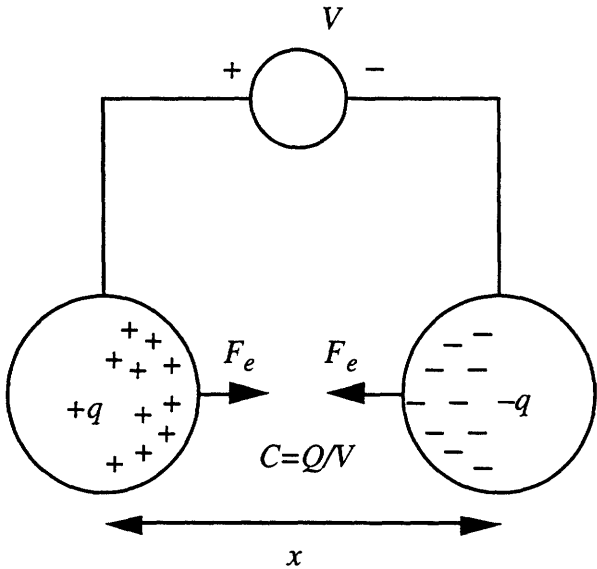
Figure 2.6. Force and Capacitance Between Two Charged Conductors

The force applied for is the derivative of the potential energy with respect to position, as shown in Equation 2.2

$$\mathbf{F} = \nabla V_p \qquad (2.47)$$

41

If the voltage is independent of the generalized coordinates, but the capacitance is not, then the vertical and horizontal forces due to electrostatic potential energy are

$$F_{e,x} = \frac{\partial V_p}{\partial x} = \frac{1}{2}\frac{\partial C}{\partial x}V^2 \qquad (2.48)$$

$$F_{e,y} = \frac{\partial V_p}{\partial y} = \frac{1}{2}\frac{\partial C}{\partial y}V^2 \qquad (2.49)$$

These force are not directly dependent on the charge stored on the conductors, but vary with the capacitance spatial derivative and the square of the voltage. The implications of these equations will be investigated in detail in the following sections.

2.2.2 Interdigitated Comb Actuators

A comb actuator consists of overlapping tines from two different oscillator elements, such as the stator and rotor shown in Figure 2.7. In this figure, the ground plane is shown under one comb interaction only. In an actual device, each comb would have a ground plane below it. These combs are designed to generate horizontal forces. However, there are also capacitors between the combs and the substrate, and these capacitors create vertical forces on the proof mass [29, 30]. The analysis of the interdigitated comb drive actuator will be twofold [15]. First, the combs will be analyzed without the contributions of the substrate. The ground plane on the substrate will then be introduced, and finite element analysis will be used to determine the capacitances and their spatial derivatives for this more detailed configuration.

2.2.2.1 Generation of Lateral Forces by Comb Drive

The comb drive, consisting of interdigitated capacitors, generates the lateral motion of a micromechanical resonator. A set of engaged fingers includes a stationary comb, known as the stator, and a comb on the rotor, or proof mass, which is free to move both horizontally and vertically (out of the plane). There are two sets of interdigitated capacitors: the drive comb is used to generate horizontal rotor motion, and the sense comb is used to detect this motion. A ground plane may be located under the comb fingers to eliminate electrostatic pull-down force to the substrate [10, 29, 30]. However, the ground plane may also be used to generate forces to control rotational and vertical motions of the proof mass, as shown in Chapter 5. In the derivations that follow, the subscripts s, r, and p will be used to denote the stator fingers, rotor fingers and ground plane, respectively. The stator-rotor-ground plane interaction is investigated with finite element analysis in Section 2.2.3.3.

42
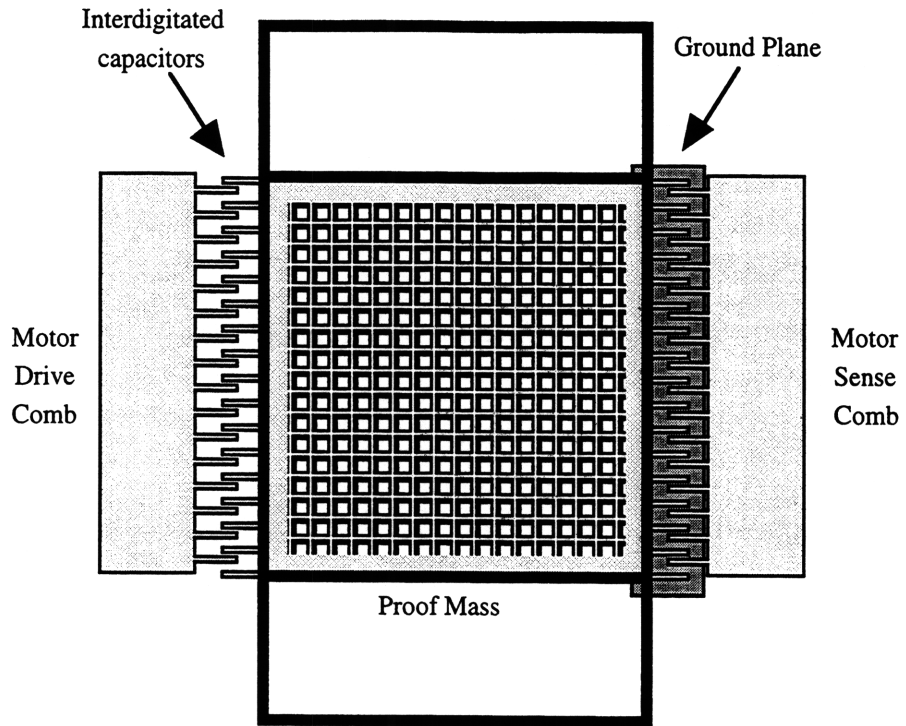
Figure 2.7. Location of Drive and Sense Interdigitated Capacitors
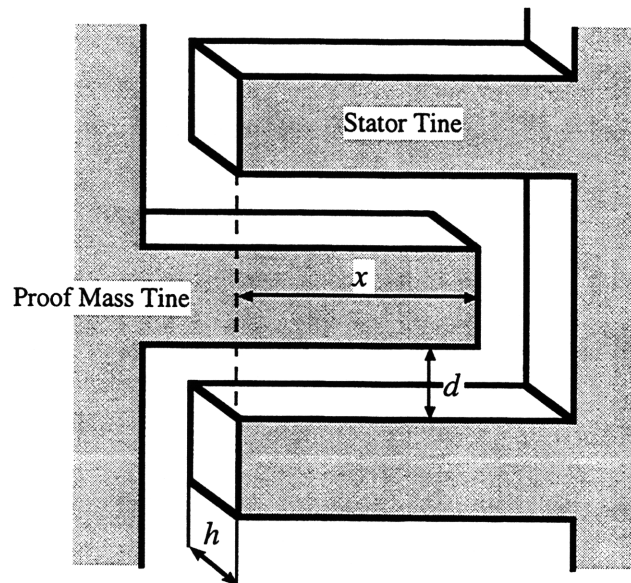
Figure 2.8. Interaction Between Two Stator Tines and One Rotor Tine

Figure 2.8 shows two stator tines and one proof mass tine. Without including the effects of the ground plane, the capacitance between one proof mass tine and one stator tine may be modeled as a simple parallel plate capacitor,

$$C_t = \alpha \frac{\varepsilon_0 h x}{d} \qquad (2.50)$$

where,

ε_0 = the permittivity of free space = 8.854 x 10^{-12} F/m or C^2/N-m^2

h = the thickness of the tines

d = the gap between a rotor and stator tine

x = the time varying overlap between comb fingers, and

α = the fringing coefficient to account for edge effects of the capacitance.

For N total tine interactions[4], the total capacitance between two combs is

$$C = \alpha N \frac{\varepsilon_0 h x}{d} \qquad (2.51)$$

From Equation 2.48, the mechanical force between the stator and proof mass combs is

$$F = \frac{1}{2} \frac{\partial C}{\partial x} (V_s - V_r)^2 = \alpha N \frac{\varepsilon_0 h}{2d} (V_s - V_r)^2 \qquad (2.52)$$

where,

V_s = the voltage on the stator, and

V_r = the voltage on the rotor.

If the proof mass is grounded ($V_r = 0$), then the electrostatic force due to the comb drive is simply

$$F = \frac{1}{2} \frac{\partial C}{\partial x} V_s^2 = \alpha N \frac{\varepsilon_0 h}{2d} V_s^2 \qquad (2.53)$$

where, from Equation 2.51 above,

$$\frac{\partial C}{\partial x} = \alpha N \frac{\varepsilon_0 h}{d} = \text{constant} \qquad (2.54)$$

Since this derivative is constant, the force acting on the proof mass created by applying a voltage to the drive stator depends only on the voltage. The two most common choices for generating a force at the resonant frequency of the system are [31-33]

---

[4]There is one fewer tine interaction than tines, i.e., $N = M - 1$, where M is the total number of tines on one side (stator+rotor).

$$V = A\sin\frac{1}{2}\omega_n t \qquad (2.55)$$

$$V = A\sin\omega_n t + B \qquad (2.56)$$

where ω_n is the natural frequency of the proof mass. If either of these are inserted into Equation 2.53, the resulting electrostatic forces are

$$F = \frac{1}{4}\frac{\partial C}{\partial x}A^2(1 - \cos\omega_n t) \qquad (2.57)$$

$$F = \frac{1}{2}\frac{\partial C}{\partial x}\left[2AB\sin\omega_n t + B^2 + \frac{A^2}{2}(1 - \cos2\omega_n t)\right] \qquad (2.58)$$

Both of these forces have a component at the resonant frequency and a DC component. For a lightly damped system, the response of the system to the second harmonic in Equation 2.58 will be negligible when compared to the resonant frequency amplitude response.

2.2.2.2 Capacitance with z-axis Variation

In the previous section, it was assumed that the drive comb capacitance was dependent on x only. However, both the basic and SEO dynamic models include an additional translational degree of freedom: vertical motion. Also, even though the SEO has been designed to minimize z-axis motion, the effects of small z=displacements on the drive capacitance should be examined by looking at a tine with both vertical and z-axis displacement. From Figure 2.9, the overlap height of the proof mass tine and stator tine may be redefined from h to $h-|y|$, since any vertical motion, positive or negative, will reduce the overlap area. For the capacitance between the proof mass tine and upper stator tine of Figure 2.10, the distance between the two decreases for positive z-motion, so that the gap may be expressed as $(d-z)$. Conversely, for the lower stator tine, the gap may be defined as $(d+z)$.
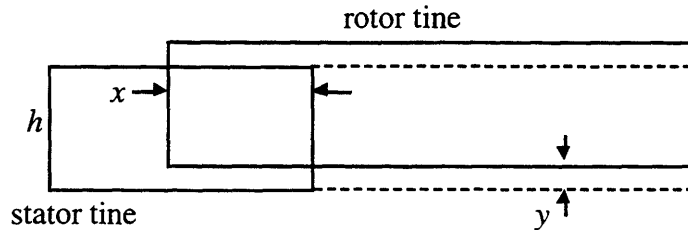
Figure 2.9. Comb Capacitance for a Vertical Displacement of the Proof Mass

45
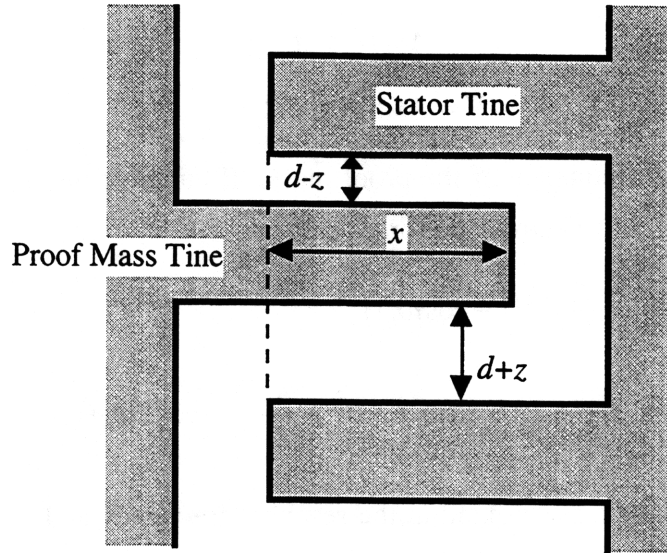
Figure 2.10. Comb Capacitance for z-axis Displacement of Proof Mass

The capacitances for these two tine interactions may be written as

$$C_u = \alpha_u \frac{\varepsilon_0(h - |y|)x}{d - z} \tag{2.59}$$

$$C_l = \alpha_l \frac{\varepsilon_0(h - |y|)x}{d + z} \tag{2.60}$$

where the subscript u represents the upper capacitor, and the subscript l represents the lower capacitor. For small z, the sum of these two capacitances is

$$
\begin{aligned}
C_u + C_l &= \frac{\varepsilon_0(h - |y|)x}{d}\left(\alpha_u(1 + \frac{z}{d}) + \alpha_l(1 - \frac{z}{d})\right) \\
&= 2\alpha \frac{\varepsilon_0(h - |y|)x}{d}
\end{aligned}
\tag{2.61}
$$

where α_u is assumed to be equal to α_l. Therefore, the total capacitance between two stator tines and one proof mass tine is independent of z, for small z, and decreases with any vertical displacement.

2.2.2.3 Comb Drive with Ground Plane

By including the ground plane below the engaged combs, the derivation of the force equation is more complex [9, 10]. Here, there are several considerations. First, as shown in Figure 2.11, there are three distinct regions of interaction. In Region I, only the rotor tines and ground plane (or control plate) interact. In Region II, the stator, rotor, and

ground plane are all engaged. In the third region, only the stator and ground plane overlap.
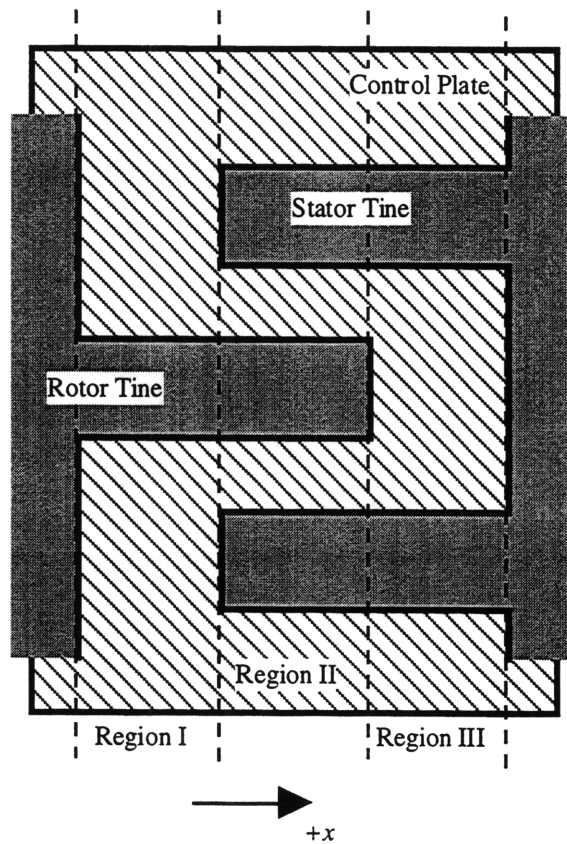
Figure 2.11. Three Regions of Tine-Control Plate Interaction

Three separate capacitor schematics may be drawn to show the interaction of the three capacitors: C_{rs}, C_{rp}, and C_{sp}. The first, shown in Figure 2.12a, represents Region I. Figure 2.12b shows the engaged fingers and ground plane of Region II. Finally, in Figure 2.12c, the interaction between the stator and ground plane is shown. The comb tines are designed to be about 20 times longer than the gap between the combs and the control plate, with an initial overlap of 50% of the tine length.

As the rotor oscillates, the lengths of the three regions of engagement vary in size, and this change affects the fringing coefficients of the capacitances. In order to determine the magnitude and significance of the proof mass oscillation, the values of the capacitors as a function of x may be determined by using finite element analysis. The results of the finite element analysis are discussed in Section 2.2.3.
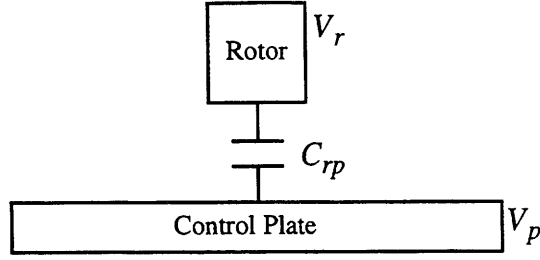
Figure 2.12a. Schematic of Capacitances in Region I
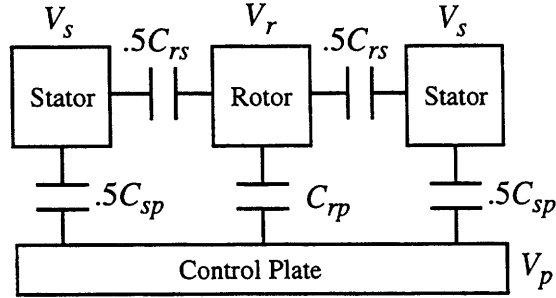
Figure 2.12b. Schematic of Capacitances in Region II
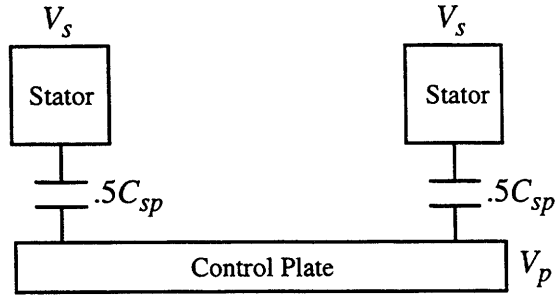
Figure 2.12c. Schematic of Capacitances in Region III

2.2.2.4 Comb Drive with Ground Plane Lateral Force

For a system of n conductors and p forces, the total electrostatic potential energy may be expressed as [10]

$$V_p = \frac{1}{2} \sum_{i=1}^{n} C_i V_i^2 \qquad (2.62)$$

where V_i and C_i are the respective voltages and capacitances associated with the ith conductor.

The potential energy of the three conductor comb drive shown in Figure 2.12b may be written as

$$V_p = \frac{1}{2} C_{rs}(V_s - V_r)^2 + \frac{1}{2} C_{rp}(V_r - V_p)^2 + \frac{1}{2} C_{sp}(V_s - V_p)^2 \qquad (2.63)$$

48

where q_s, q_r, and q_p are the charge per unit length for the stator, rotor, and control plate respectively. The capacitances in Figures 2.12a-2.12c are given per tine per unit length: c_{rs} for the rotor-stator capacitance, c_{rp} for the rotor-ground plane capacitance, and c_{sp} for the stator-ground plane capacitance. Using these definitions and integrating Equation 2.63 yields the electrostatic force (with units of force)

$$F_{e,x} = \frac{1}{2}\frac{\partial C_{rs}}{\partial x}(V_s - V_r)^2 + \frac{1}{2}\frac{\partial C_{sp}}{\partial x}(V_s - V_p)^2 + \frac{1}{2}\frac{\partial C_{rp}}{\partial x}(V_r - V_p)^2 \qquad (2.64)$$

which has the associated charges per unit length

$$q_s = (c_{sp} + c_{rs})V_s - c_{rs}V_r - c_{sp}V_p \qquad (2.65)$$

$$q_r = -c_{rs}V_s + (c_{rp} + c_{rs})V_r - c_{rp}V_p \qquad (2.66)$$

$$q_p = -c_{sp}V_s - c_{rp}V_r + (c_{sp} + c_{rp})V_p \qquad (2.67)$$

The capacitances must include the effects from each of the three regions. In this design, Region I is either non-existent or very small and may be neglected. Region III consists of the stator and ground plane only, and the sizes of Regions II and III vary with x. To first order, the capacitances in Equation 2.64 may be expressed as

$$C_{rs} = Nc_{rs}(L_0 + x) \qquad (2.68)$$

$$C_{sp} = N\left[c_{sp,e}(L_0 + x) + c_{sp,u}(L_0 - x)\right] \qquad (2.69)$$

$$C_{rp} = N\left[c_{rp,e}(L_0 + x) + c_{rp,u}(L_0 - x)\right] \qquad (2.70)$$

where,

L_0 = the overlap of tines when proof mass is at rest (assumes a 50% overlap)

x = the horizontal displacement, and

N = the total number of rotor tines.

The subscripts u and e are used to represent unengaged and engaged tines of the stator and rotor. Since these capacitances are, to first order, linear functions of x, the horizontal force is independent of x.

If the rotor is grounded ($V_r = 0$), then the comb drive horizontal force becomes

$$F_{e,x} = \frac{1}{2}\frac{\partial C_{rs}}{\partial x}V_s^2 + \frac{1}{2}\frac{\partial C_{sp}}{\partial x}(V_s - V_p)^2 + \frac{1}{2}\frac{\partial C_{rp}}{\partial x}V_p^2 \qquad (2.71)$$

where the first term makes the largest contribution to horizontal motion. These partial derivatives may depend on both x and y if the variations in fringing coefficients are large.

2.2.2.5 Comb Drive Vertical Force

This approach may also be used to determine the vertical force generated by the comb drive. The y-axis equivalent (for $V_r = 0$) to Equation 2.71 is

$$F_{e,y} = \frac{1}{2}\frac{\partial C_{rs}}{\partial y}V_s^2 + \frac{1}{2}\frac{\partial C_{sp}}{\partial y}(V_s - V_p)^2 + \frac{1}{2}\frac{\partial C_{rp}}{\partial y}V_p^2 \qquad (2.72)$$

In this equation, the variation of the capacitances with respect to the gap between the tines and the ground plane is required. The capacitance between the rotor and the ground plane depends greatly on the vertical displacement of the proof mass, as shown in the finite element analysis of Section 2.2.3 [29, 30].

2.2.3 Finite Element Models of Capacitors and Their Derivatives

Finite element analysis provides a method to model accurately both the comb capacitors and their derivatives as a function of the vertical position of the proof mass by including the fringing field effects. For smaller capacitors, in terms of the length to width ratios, the fringing fields are a significant portion of the total capacitance. The finite element approach yields both the electric field and the potential (voltage) of the arrangement. From these results, it is possible to extract both the charge on a plate and the force exerted on a capacitive element. By repeating the analysis for several applied voltages, it is possible to do a least squares fit to determine the capacitors and their spatial derivatives. Because of the symmetry of the combs, the electric field is also symmetric, such that it is possible to model the interaction between one rotor tine and two stator tines, and then to extrapolate this result over an entire comb. By neglecting the fringing effects at the tips of the tines, two dimensional finite element analysis may be used to yield accurate models of the comb capacitors.

By extending the symmetry arguments further, it is possible to define the region of interest for the comb capacitors as shown in Figure 2.13, which is a cross-section of the combs. In this schematic, the y-axis is up, the z-axis is to the right, and the drive, or x-axis, is into the page. Here, an entire rotor tine is flanked on both sides by one half of a stator tine. Beneath all of the tines is the control plate. Both stators have the same voltage applied to them, and the rotor and control plate are permitted to have independent voltages. It is assumed that each rotor tine will have the same electric field, such that the total capacitance of the comb drive is simply the product of the capacitance of one rotor tine times the total number of rotor tines.

50
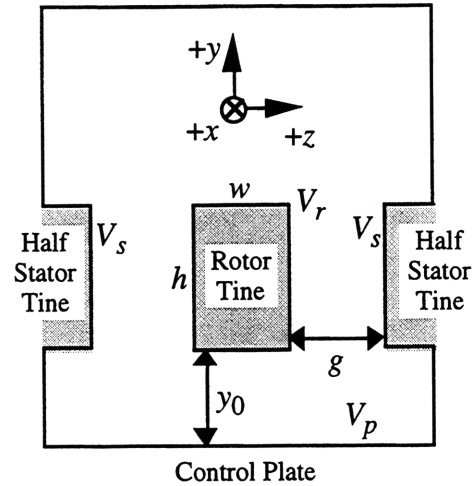
Figure 2.13. Region of Interest for Finite Element Analysis of Tine Interaction

In this figure,

V_s = the voltage applied to the stator

V_r = the voltage applied to the rotor

V_p = the voltage applied to the control plate

w = the width of the rotor and stator tines

h = the height of the tines

g = the gap between a rotor and stator tine, and

y_0 = the gap between a tine and the control plate.

These values may be varied to determine the effects of either different voltage or design configurations on the forces generated on the rotor.

2.2.3.1 Finite Element Analysis of Electrostatic Forces

In order to determine the electric field for this capacitive relationship, a governing differential equation is required, and its boundary conditions must be defined for the entire region. On the tines and control plate, the boundary conditions are defined by the voltage applied to the surface. On the boundaries of the region that are not part of the oscillator, the voltage is free. The governing equation for the electric field is

$$\nabla \cdot \mathbf{E} = 0 \tag{2.73}$$

where,

∇ = the divergence operator, and

$\mathbf{E} = -\varepsilon_0 \nabla V$ = the electric field.

Here,

$$\nabla = \begin{bmatrix} \dfrac{\partial}{\partial x} & \dfrac{\partial}{\partial y} & \dfrac{\partial}{\partial z} \end{bmatrix} = \text{the gradient operator, and}$$

V = the voltage between the tines.

Once the region, its boundary conditions, and the governing differential equation have been defined, the finite element software package PDEase™ may be used to numerically determine the electric field and potential distribution for various applied voltages and vertical displacements[5]. Typical results from this program are shown in Figures 2.14 through 2.17. For these plots, the applied voltages are $V_s = 1$ V, $V_r = 0$ V, and $V_p = 0$ V.

The distribution of the potential is shown in the contour plot of Figure 2.14. The first significant observation is that the voltage distribution is symmetric about the rotor, as assumed earlier. The symmetry of the potential permits the construction of the entire comb electric field. Between the tines, the voltage is very concentrated, implying a constant and large electric field, with significant energy storage between the tines. Along the top of the tines, the potential distribution is symmetric and rounded. This behavior generates the fringing effect that was represented by α in Equation 2.50. The fringing coefficient can be determined directly by dividing the capacitance determined through finite element analysis by the capacitance derived from the parallel plate equation.

The contour of the electric field in Figure 2.15 has been divided by ε_0 to increase the magnitude of the scale of the contour plot. Between the tines, the electric field has a nearly constant value around $0.5\varepsilon_0$, ranging from ε_0 at the stator to 0 at both the rotor and the control plate[6]. Slightly above the tines (about 2 μm), the electric field is nearly constant at $0.1\varepsilon_0$. The electric field bends from the stator-control plate region to the stator-rotor region because both the rotor and control plate are at the same potential, such that the field distribution between these and the stator should be identical. However, the effects of the bend of the electric field will be quite significant.

As expected, the electric field flows from high potential to low potential, as shown in Figure 2.16. This vector plot emphasizes that, except for the corners, the electric field flows directly from the stator to the rotor and the control plate. From the top of the stator, the electric field bends towards the rotor. From the bottom corner of the stator, the electric field travels either to the rotor or to the control plate.

Finally, the energy density plot in Figure 2.17 emphasizes the concentrations of energy[7]. Most of the electrostatic energy is stored between the stator and the rotor, with

---

[5]PDEase is provided by Macsyma, Inc. of Arlington, MA.

[6]The accuracy of the finite element analyses are about $0.001\varepsilon_0$.

[7]Similar to Figure 2.15, the contour labels are hard to discern. The b-contour is on the rotor, and the c-contour is on the stator. The value in the stator-rotor gap is 0.125. Again, the values at the stator corners have significant energy concentrations.

some stored between the control plate and the stator. The energy density plot suggests that most of the drive force will be generated by the rotor-stator interaction, and that the stator-control plate and rotor-control plate overlaps contribute secondary drive forces.

After determining the potential, the electric field, and the energy density for a particular geometry and voltage configuration, the Maxwell stress tensor may be calculated, which, in turn, leads to the force generated on either the rotor or the stator tine. From Appendix B, the stress tensors for a two-dimensional field are [38]

$$T_{11} = \frac{\varepsilon}{2} E_1^2 \tag{2.74a}$$

$$T_{12} = 0 \tag{2.74b}$$

$$T_{22} = \frac{\varepsilon}{2} E_2^2 \tag{2.74c}$$

where the subscript "11" represents the x-force exerted on the x-face; "12", the y-force on the x-face, and vice versa; and "22", the y-force on the y-face. These values may then be integrated over the surface to yield the mth component of the force per unit length,

$$f_m = \oint_S T_{mn} n_n da \tag{2.75}$$

From this equation it is possible to determine the total electric force on a volume by knowing only the electric fields on the surface of the volume.
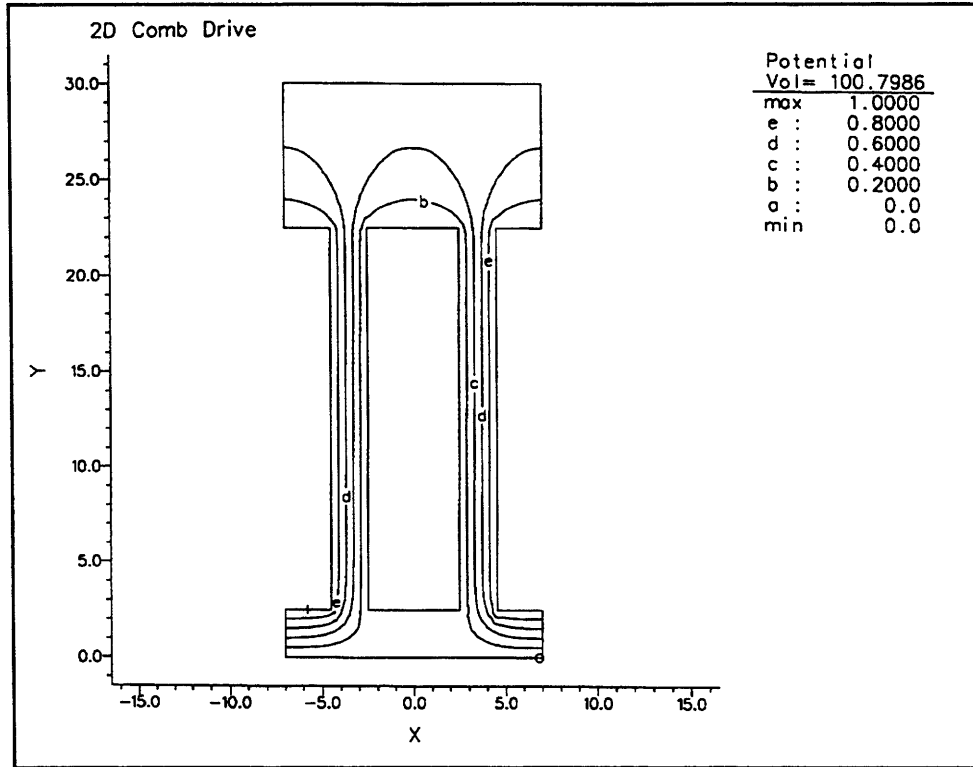
Figure 2.14. Voltage Potential Contour Plot for Zero Proof Mass Displacement
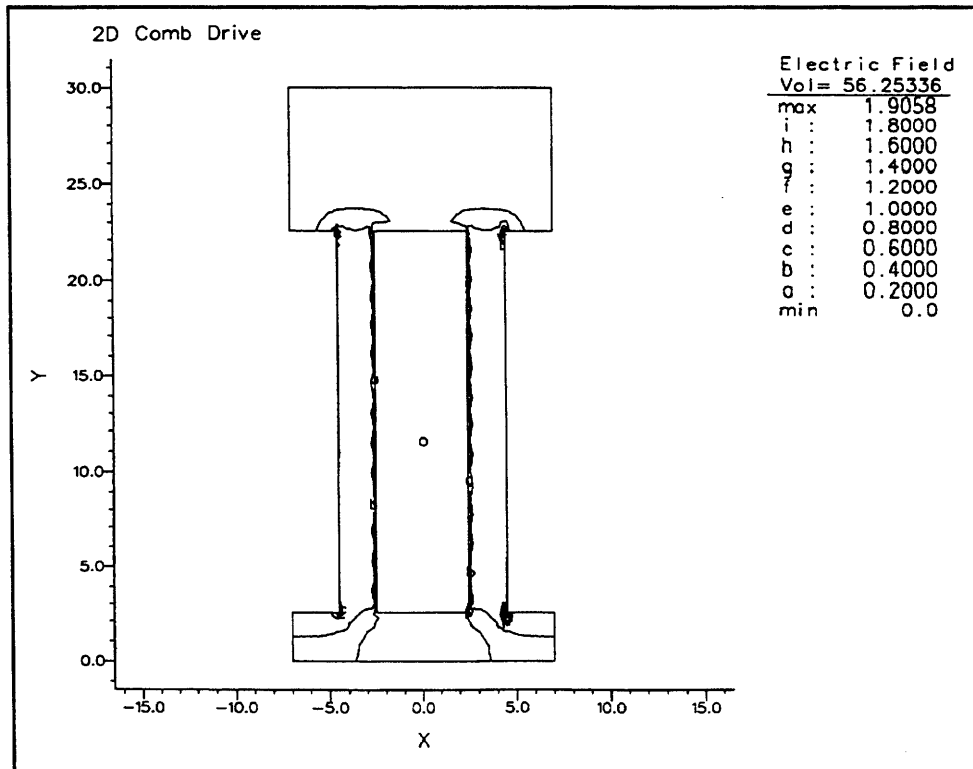
Figure 2.15. Electric Field Contour for Zero Proof Mass Displacement
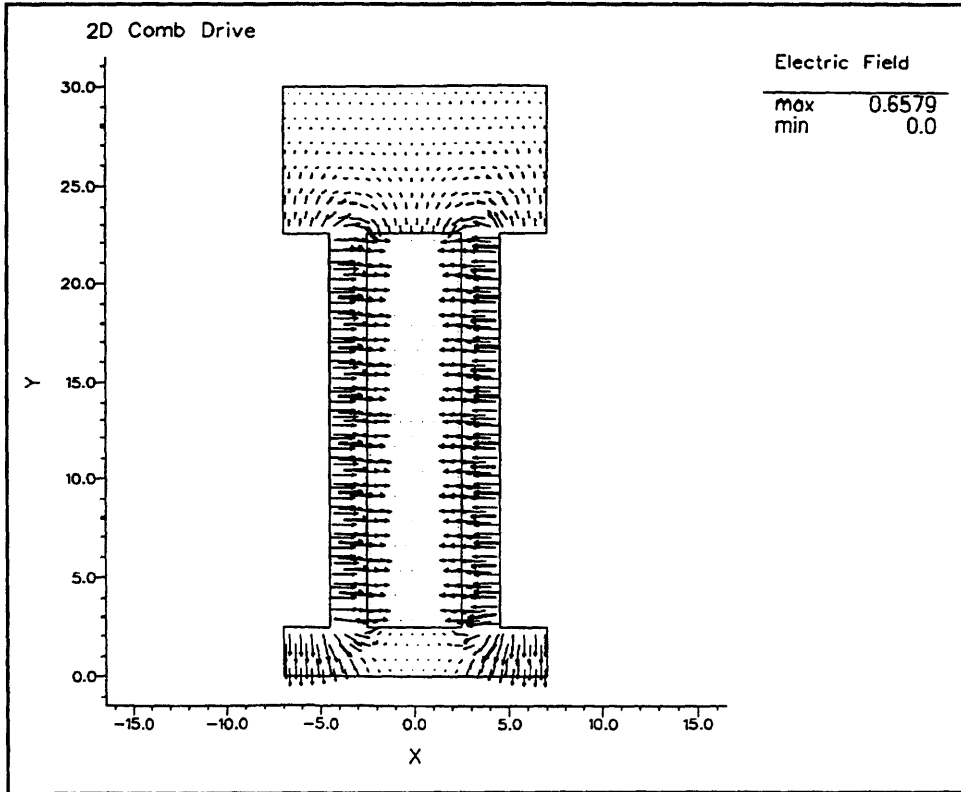
Figure 2.16. Electric Field Vector Plot for Zero Proof Mass Displacement
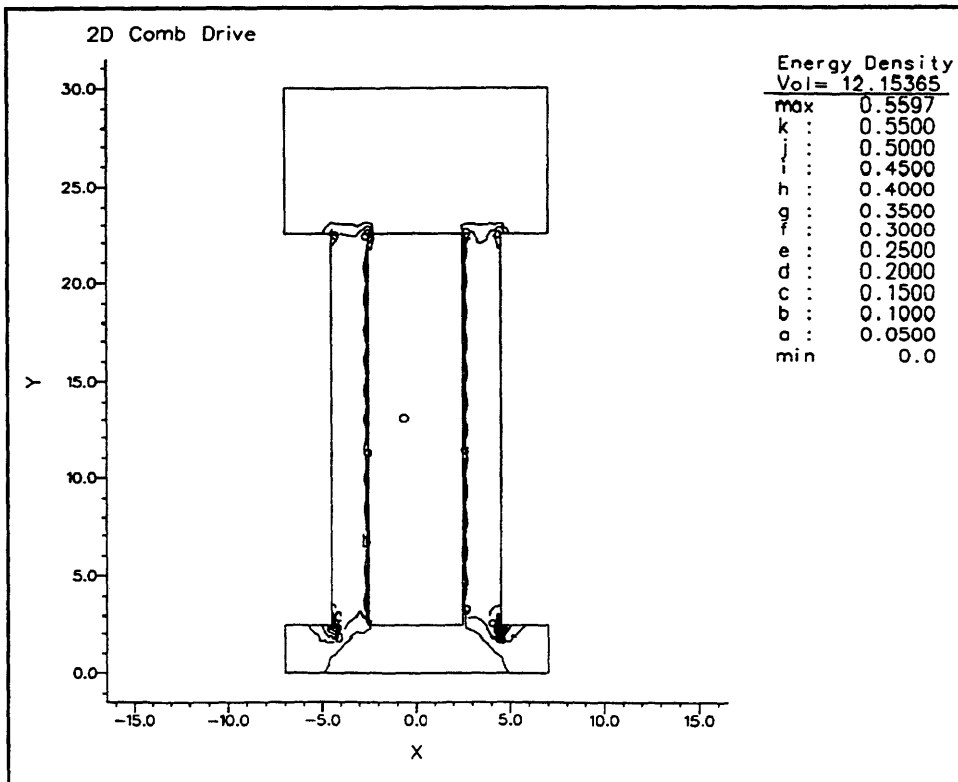
Figure 2.17. Energy Density Contour for Zero Proof Mass Displacement

2.2.3.2 Charge and Force per Unit Length

Because the charge and force problems have been stated in two dimensions, it is more convenient to recast the problems such that the surface integrals become contour integrals, and both the charge and force are expressed as charge per unit length and force per unit length, respectively. In this case, the charge may be found from [38]

$$q = \oint_C \sigma \cdot dl \qquad (2.76)$$

where,

$$\sigma = \mathbf{D} \cdot \mathbf{n} \qquad (2.77)$$

$\mathbf{D}$ = the electric displacement, and

$\mathbf{n}$ = the normal to the surface.

The net charges on the rotor and ground plane are found by integrating over the surface of each element.

The force may be written as

$$f_m = \oint_C T_{mn} n_n dl \qquad (2.78)$$

where the contour C is defined for the stator and the rotor in Figure 2.18. The rotor contour (C_r) is closed within the region, but the stator contour (C_s) must be closed by assuming electrostatic symmetry about a comb tine. Also in Figure 2.18, the normals ($\mathbf{n}$) to each surface are shown. The vertical force on the rotor is determined by finding the electric field density on the top and bottom surfaces, and differencing them to yield a net force.
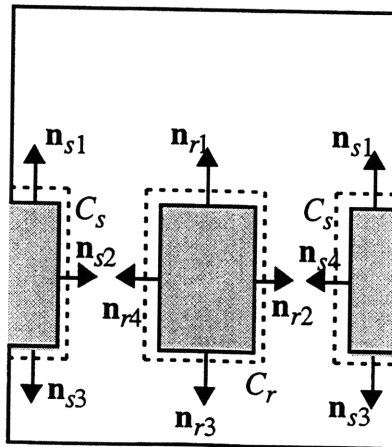
Figure 2.18. Surface Contours and Normal Vectors for Finite Element Analysis

Because the problem has been stated in two dimensions, only the y- and z-axis forces may be determined from this method. However, this assumption also permits a method of calculating the x-axis force. By integrating the energy density over the entire surface of the region, the result will be in units of energy per length. The total energy stored in the combs may then be found by summing these infinitesimal slices over the entire length of the comb overlap. Since the overlap occurs along the x-axis and the drive force is the gradient of the stored energy along the drive axis, the drive force may be expressed as

$$F_x = \frac{\partial E_C}{\partial x} = \frac{1}{2} \oint_S \varepsilon \mathbf{E} \cdot \mathbf{E} dA \tag{2.79}$$

Therefore, by assuming constant energy density at each comb cross-section, the energy density may be integrated over the entire surface of the region to determine the drive force. This is a very powerful result that will complete the estimates of the tine capacitors and their derivatives.

2.2.3.3 Determining Capacitors and Their Derivatives

Once the force and charge are determined from the finite element analysis and subsequent integration, the results are fitted to the analytic definitions of the charge and force

$$q_r = c_{rs}(V_r - V_s) + c_{rp}(V_r - V_p) \tag{2.80a}$$

$$q_s = c_{rs}(V_s - V_r) + c_{sp}(V_s - V_p) \tag{2.80b}$$

$$f_y = \frac{1}{2}\frac{\partial c_{rs}}{\partial y}(V_r - V_s)^2 + \frac{1}{2}\frac{\partial c_{rp}}{\partial y}(V_r - V_p)^2 + \frac{1}{2}\frac{\partial c_{sp}}{\partial y}(V_s - V_p)^2 \tag{2.81a}$$

$$F_x = \frac{1}{2}\frac{\partial C_{rs}}{\partial x}(V_r - V_s)^2 + \frac{1}{2}\frac{\partial C_{rp}}{\partial x}(V_r - V_p)^2 + \frac{1}{2}\frac{\partial C_{sp}}{\partial x}(V_s - V_p)^2 \tag{2.81b}$$

where the lower case variables represent quantities per unit length per finger and the upper case variables represent the quantities in the proper units per finger. For example, q_r, the charge per unit length per rotor finger, is expressed in terms of the capacitance per unit length per finger. On the other hand, the drive force, F_x, has units of force and is expressed in terms of the partial spatial derivatives of the capacitances, which have units of Farads per meter. The capacitances and their derivatives need to be determined in all three regions shown in Figure 2.11.

For the SEO, which has a thickness of 20 μm, a tine width of 5 μm, a tine gap of 2 μm, a tine-control plate gap of 2.5 μm, and an overlap of 25 μm, the capacitor results are plotted in Figures 2.19 through 2.21 and are shown in Table 2.1 for zero vertical

57

displacement of the proof mass. In this table, the raw values of the quantities, with their units, are listed for each of the three regions. The signs of the C_{sp} x-derivative arises from the its x-dependency in Equation 2.69. Using Equations 2.68 through 2.70 and assuming that $x = 0$, the net values in the fourth column are calculated. From these calculations, an observation from Figures 2.14 through 2.17 may be confirmed. The capacitance between the rotor and the stator, c_{rs}, is the largest; a conclusion that is expected based on the large thickness and small gap between these tines. In fact, this capacitance is about 9 times greater than the remaining two capacitors. As a result of this, most of the horizontal force is generated by the stator-rotor interaction.

Table 2.1. Finite Element Analysis Estimates of Capacitors and Derivatives

Quantity	Region I	Region II	Region III	Net Values
C_{rs}	0	4.7329 fF/finger	0	4.7329 fF/finger
C_{rp}	0.853 fF/finger	0.5583 fF/finger	0	1.4113 fF/finger
C_{sp}	0	0.5975 fF/finger	0.9092 fF/finger	1.5067 fF/finger
$\dfrac{\partial C_{rs}}{\partial y}$	0	56.301 pF/m/finger	0	56.301 pF/m/finger
$\dfrac{\partial C_{rp}}{\partial y}$	-460.978 pF/m/finger	-453.284 pF/m/finger	0	-914.262 pF/m/finger
$\dfrac{\partial C_{sp}}{\partial y}$	0	58.956 pF/m/finger	0	58.956 pF/m/finger
$\dfrac{\partial C_{rs}}{\partial x}$	0	190.970 pF/m/finger	0	190.970 pF/m/finger
$\dfrac{\partial C_{rp}}{\partial x}$	-35.69 pF/m/finger	23.347 pF/m/finger	0	-12.343 pF/m/finger
$\dfrac{\partial C_{sp}}{\partial x}$	0	24.244 pF/m/finger	-36.367 pF/m/finger	-12.123 pF/m/finger

One significant result may be seen in the partial derivatives of the capacitances with respect to y. Here, the derivative of c_{rp} is negative, suggesting that a potential difference between these two plates will generate a downward force. However, the other two capacitor derivatives will push the rotor up, not down. Because a potential difference does exist between the stator and rotor, there is force coupling between the horizontal and vertical axes. With the control plate grounded and 25 μm of tine overlap, the ratio of the horizontal to vertical forces is 3.4. The significant increase in c_{sp} in Region III occurs

because the electric field is not constrained by the rotor, and the field goes from the entire length of the stator to the control plate.

From these results, it is possible to determine the fringing coefficients for each of the three capacitors. For C_{rs}, α is 1.07; for C_{rp}, 1.26; and for C_{sp}, 1.35. The rotor-stator fringing coefficient is the smallest because the tines are thick enough that the fringing effects at the top are small when compared to the capacitance between the tines themselves.

The results of this analysis are shown in Figures 2.19 through 2.25. In Figure 2.19, the capacitors for all three regions are shown in per finger values with an assumed overlap of 25 μm. From here, it is clear that the rotor-stator capacitance is the largest. Also, in Figure 2.20, the partial derivatives of the capacitances with respect to x shows that C_{rs} also contributes the largest component to the horizontal force of the comb drive. From Figure 2.21, the rotor-ground plane capacitance has the largest vertical partial derivative, with a value of -9500 pF/m/finger at -2 μm vertical displacement. This term pulls the proof mass towards the substrate. As the rotor moves towards the ground plane, the vertical force increases, since the partial derivative of C_{rp} with respect to y becomes more negative. However, by chosing the proper ground plane voltage, this effect can be minimized.
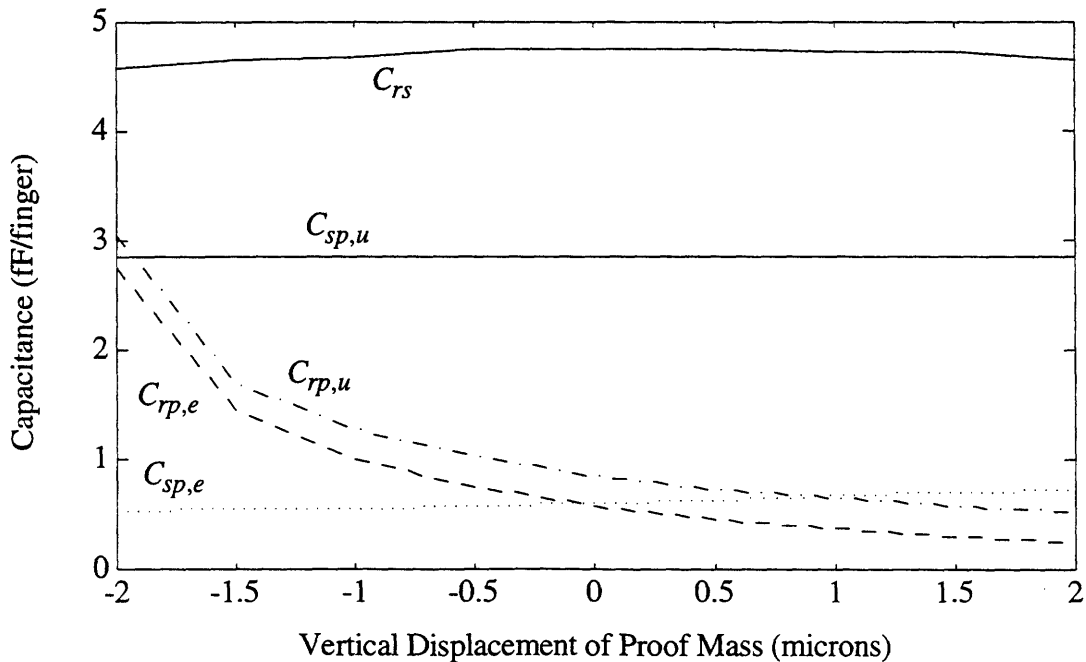
Figure 2.19. Comb Finger Capacitances versus Rotor Vertical Position
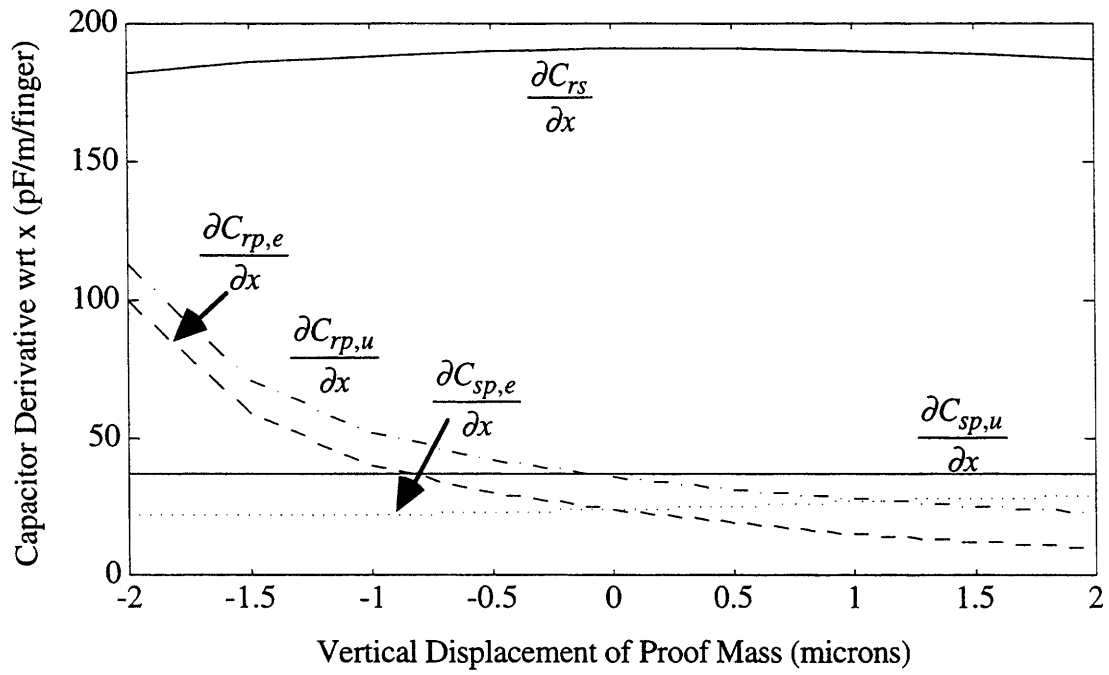
Figure 2.20. Comb Capacitor Derivatives wrt x versus Rotor Vertical Position
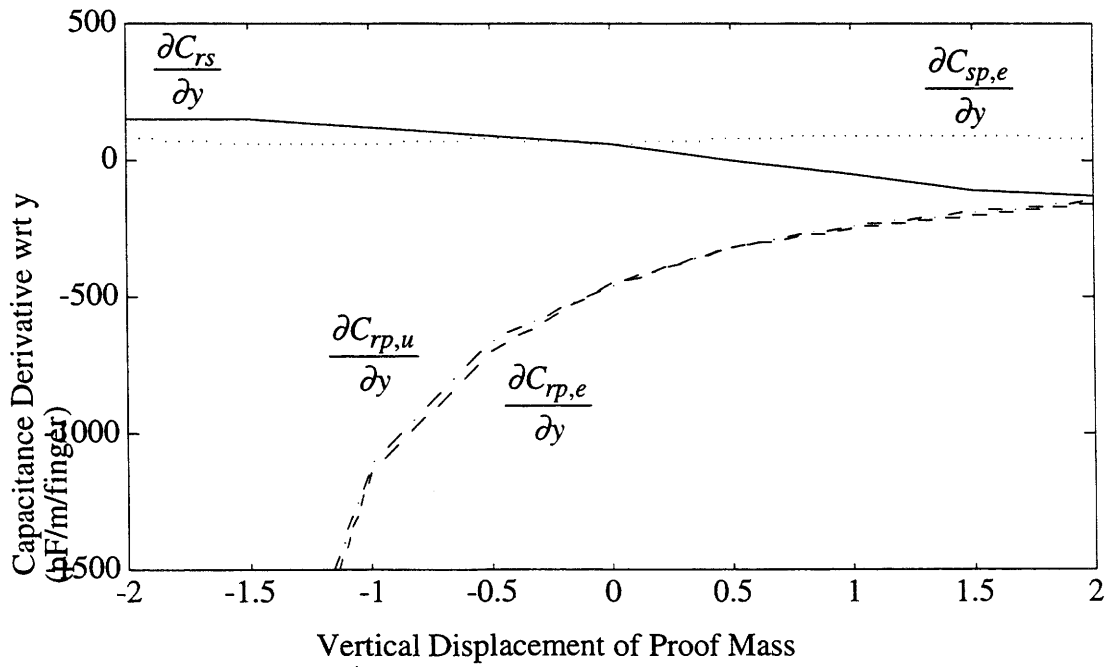
Figure 2.21. Comb Capacitor Derivatives wrt y versus Rotor Vertical Position
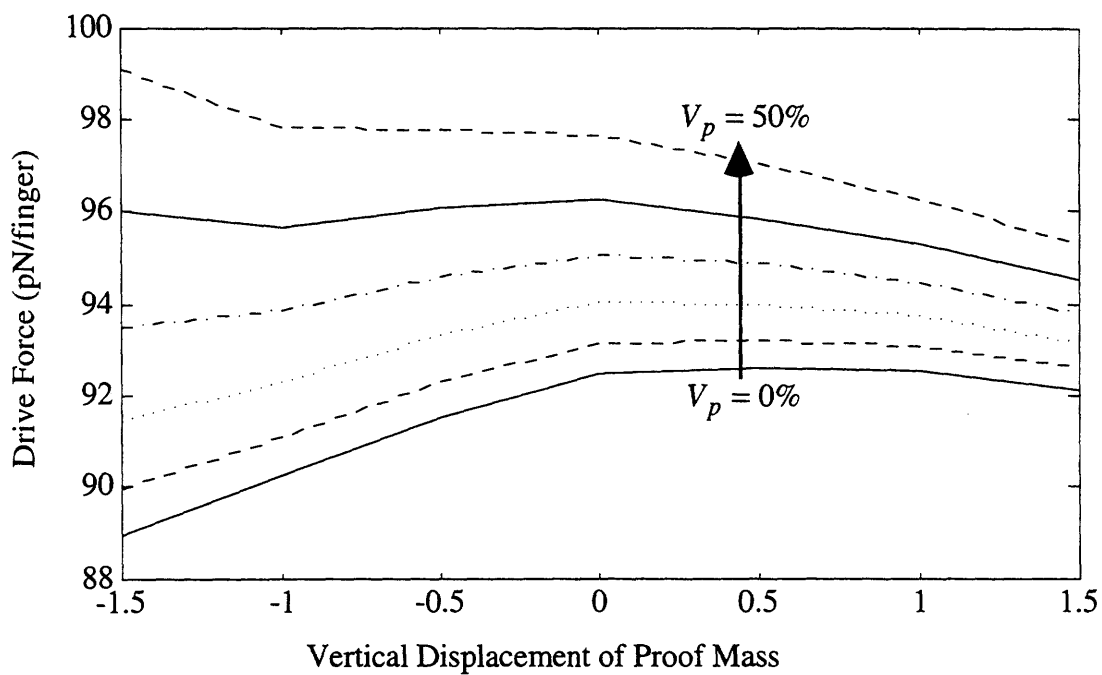
Figure 2.22. Drive Force versus Rotor Vertical Position and Ground Plane Voltage
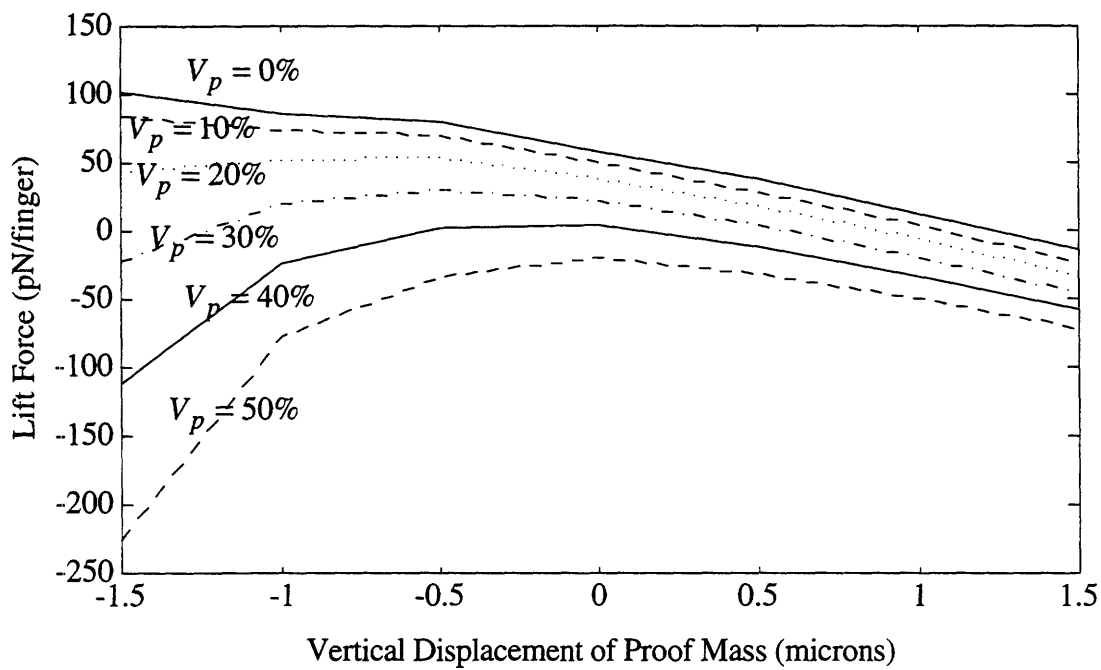
Figure 2.23. Lift Force versus Rotor Vertical Position and Ground Plane Voltage
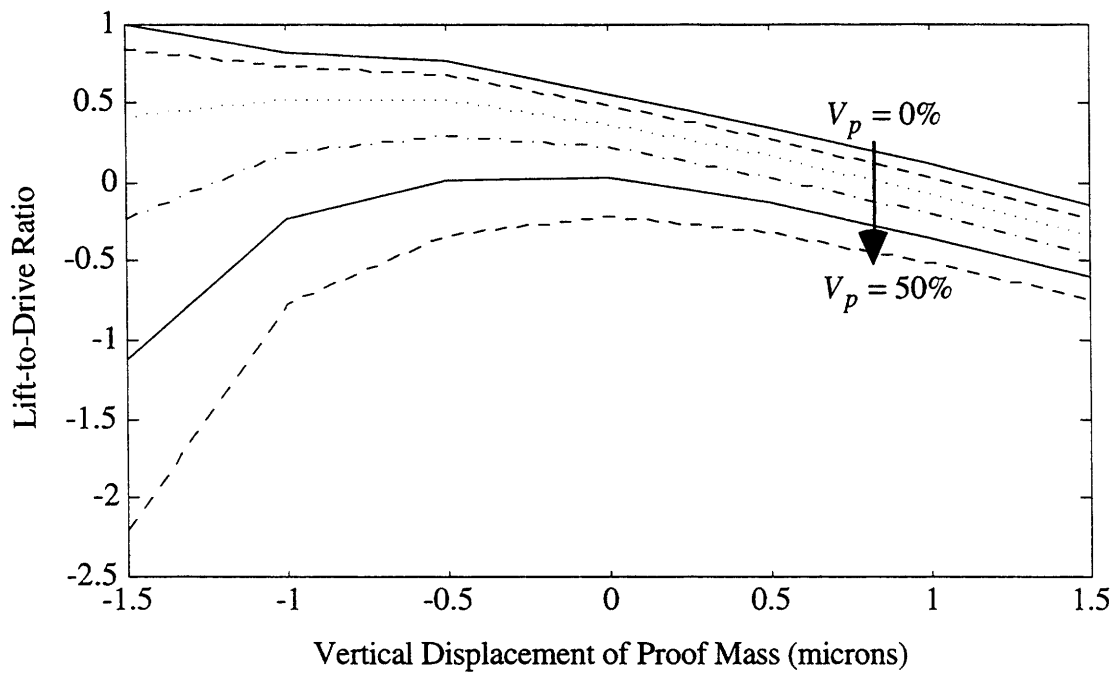
Figure 2.24. Comb Drive Lift-to-Drive Ratio
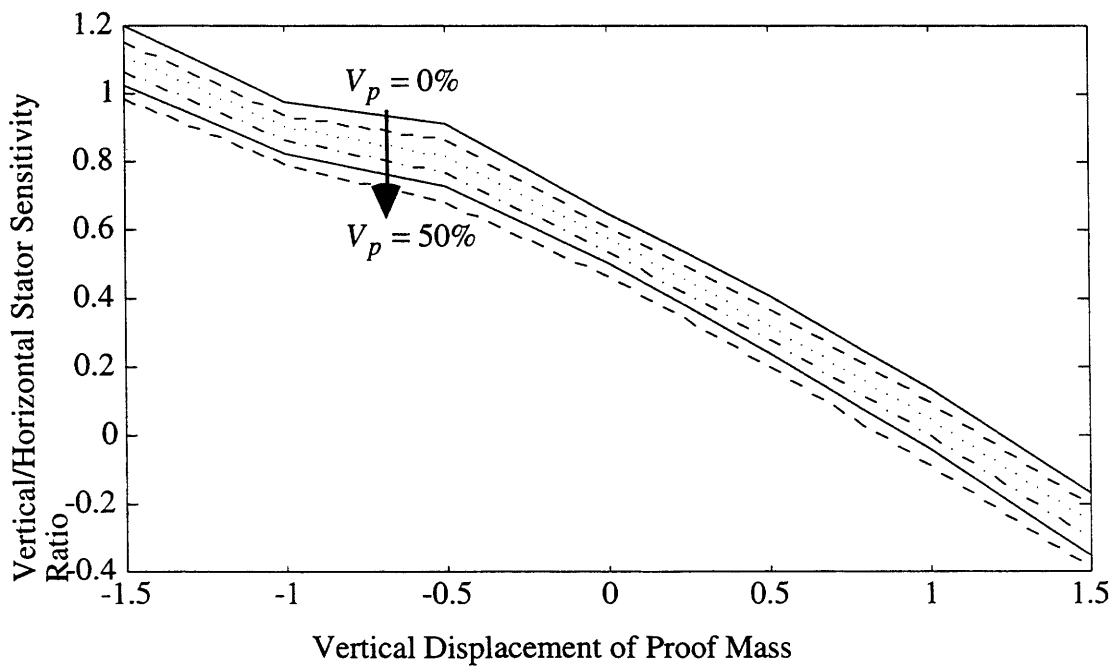
Figure 2.25. Stator Comb Vertical-Horizontal Sensitivity Ratio

From the force expressions in Equations 2.81a and 2.81b, the horizontal and vertical forces may be determined for various voltages. These forces are plotted in Figures 2.22 and 2.23, respectively. In these plots, the ground plane voltage, V_p, was varied from 0% to 50% of the stator voltage in 10% increments. The horizontal force in Figure 2.22 is relatively insensitive to the ground plane voltage, with a force of about 100 pN/finger for all applied forces. However, in Figure 2.23, the vertical force varies significantly with the ground plane voltage. As the voltage increases, the C_{rp} derivative becomes the dominant factor in determining the force. Figure 2.24 shows the ratio between the vertical and horizontal forces in 10% increments of V_p. From this plot, a ground plane voltage may be chosen that minimizes the lift-to-drive ratio.

The vertical-to-horizontal-sensitivity ratio of the stator comb is plotted for various V_p and rotor vertical displacements in Figure 2.25. From this plot, the sensitivity ratio is clearly a function of the ground plane voltage. The larger the ground plane voltage, the lower the sensitivity ratio is. This phenomemon needs to be balanced with the lift-to-drive ratio in order to permit closed-loop operation of the horizontal axis of the oscillator. When the proof mass moves up, the capacitance between the stator and the control plate increases, as seen in Figure 2.19. This occurs because, as the rotor moves, more of the electric field travels from the stator to the control plate, instead of to the rotor.

In Figures 2.26 and 2.27, the rotor is displaced upwards by 1.75 μm. The potential distribution has bulged under the rotor since more of the stator is exposed directly to the control plate. As shown in Figure 2.27, the electric field is much stronger under the rotor. Since both the rotor and the control plate are at the same potential, this increase in the electric field must be attributed to the stator and control plate interaction. Here the voltage and distance between the stator and control plate remain unchanged, so that the growth in the electric field must be caused by an increase in the stored charge, which implies that the capacitance between the stator and control plate is larger when the proof mass is displaced upwards. Similarly, when the proof mass moves towards the control plate, the stator-control plate capacitance decreases.
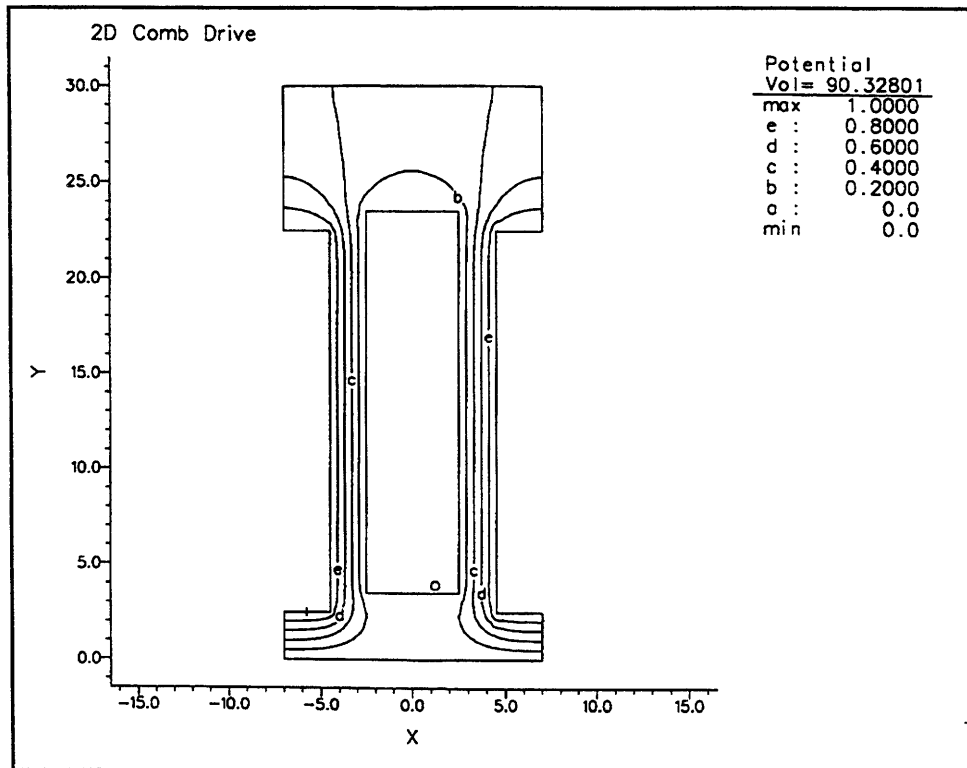
Figure 2.26. Potential Distribution for Vertically Displaced Proof Mass
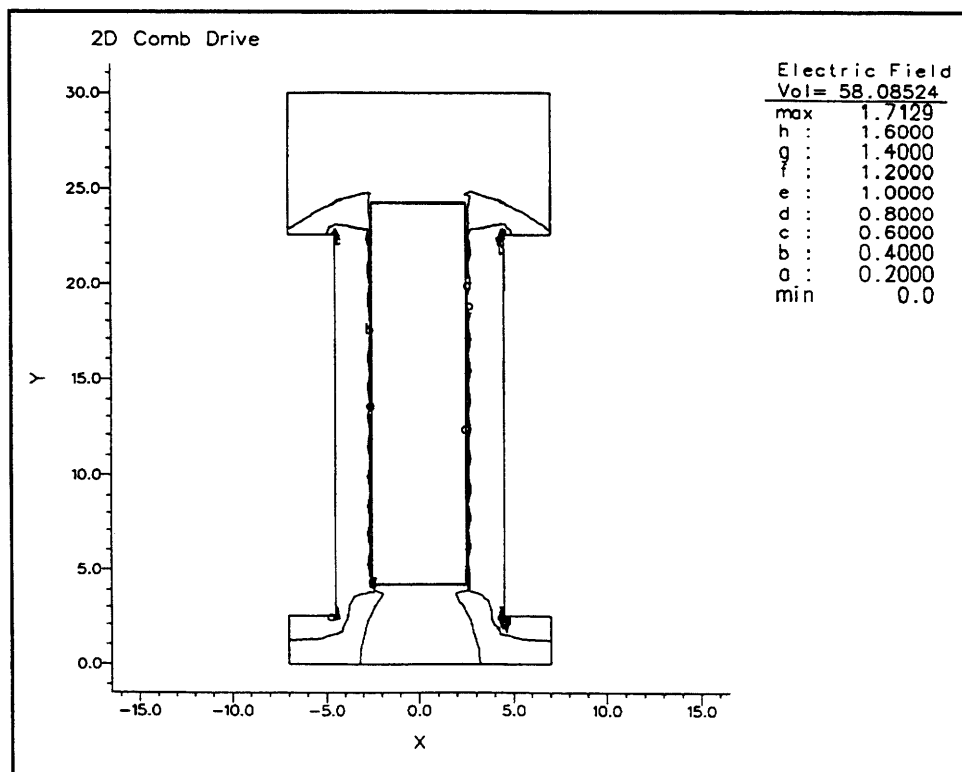
Figure 2.27. Electric Field Distribution for Vertically Displaced Proof Mass

64

2.2.3.4 Implications of Finite Element Analysis

The results of the finite element analysis have some implications for micromechanical oscillators in general. First, the fact that the application of a voltage on the stator generates both vertical and horizontal forces on the proof mass means that there is intrinsic coupling of the motions in a comb drive. The ratio of the vertical to horizontal force for the SEO is 0.3. The second major effect is on the detection of proof mass horizontal motion, as shown in Figure 2.25. As discussed in Section 2.2.5.1, the x-displacement of the rotor is determined by integrated the total charge leaving the motor sense comb. The differential charge may be expressed as

$$\Delta q = \left[\left(\frac{\partial C_{rs}}{\partial x} + \frac{\partial C_{sp}}{\partial x} \right) \Delta x + \left(\frac{\partial C_{rs}}{\partial y} + \frac{\partial C_{sp}}{\partial y} \right) \Delta y \right] V_s \qquad (2.82)$$

where both the motor sense control plate, V_p, and the rotor, V_r, are grounded. Therefore, the ratio of the detection coefficient of vertical to horizontal motion, assuming a 25 µm tine overlap, is about 1.

2.2.4 Parallel Plate Actuators

In addition to the forces generated by the comb interactions, an electrostatic force may also be created between two parallel plates, as shown in Figure 2.28. In this figure, one plate is the sense plate, which is fixed to the substrate, and the other is the proof mass, which is free to move. The capacitance between these two plates may be expressed as

$$C = \gamma \frac{\varepsilon_0 lw}{y} \qquad (2.83)$$

where,

C = total capacitance (Farads)

γ = the fringing coefficient

ε_0 = permittivity of free space

l = length of plate

w = width of plate, and

y = distance between plates.
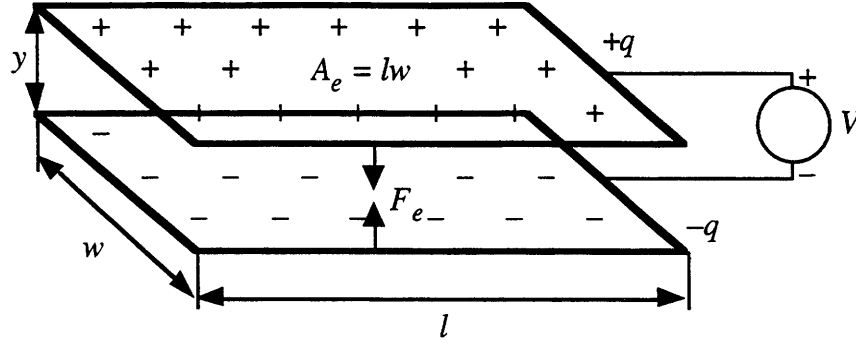
Figure 2.28. Parallel Plate Capacitance

It is helpful at this point to redefine the gap as a variation, y, about the nominal gap, y_0, such that the capacitance is now

$$C_y = \gamma \frac{\varepsilon_0 lw}{y_0 + y} = \gamma \frac{\varepsilon_0 lw}{y_0} \frac{1}{\left(1 + \dfrac{y}{y_0}\right)} \tag{2.84}$$

From a development similar to that in Section 2.2.1, the force generated along the y-axis may now be expressed as the partial derivative of the capacitance with respect to y

$$F_y = \frac{1}{2} \frac{\partial C_y}{\partial y} V^2 = -\gamma \frac{\varepsilon_0 lw}{2(y_0 + y)^2} V^2 = -\gamma \frac{\varepsilon_0 lw}{2y_0^2} \frac{V^2}{\left(1 + \dfrac{y}{y_0}\right)^2} \tag{2.85}$$

For $y/y_0 \ll 1$, the capacitance and force may be expressed using Taylor series expansions

$$C_y \approx \gamma \frac{\varepsilon_0 lw}{y_0} \left(1 - \frac{y}{y_0} + \left(\frac{y}{y_0}\right)^2 - \left(\frac{y}{y_0}\right)^3 + \ldots\right) \tag{2.86}$$

$$F_y \approx -\gamma \frac{\varepsilon_0 lw}{2y_0^2} \left(1 - 2\frac{y}{y_0} + 3\left(\frac{y}{y_0}\right)^2 - 4\left(\frac{y}{y_0}\right)^3 + \ldots\right) V^2 \tag{2.87}$$

It is important to note that the force generated by the parallel plates is proportional not only to the voltage squared, but also to y, and the capacitance has a DC component in addition to the y-dependent term.

2.2.4.1 Electrostatic Spring Softening

The force in Equation 2.87 makes a significant contribution to the vertical dynamics of the proof mass. This force not only generates a vertical force, but also reduces the

spring constant along the vertical axis [10, 36]. If a typical mass-spring-damper, second-order equation is driven by the first-order approximation of the electrostatic force, F_y,

$$m\ddot{y} + b\dot{y} + k_y y = -\gamma \frac{\varepsilon_0 lw}{2y_0^2}\left(1 - 2\frac{y}{y_0}\right)V^2 \tag{2.88}$$

then the system takes on some very interesting characteristics. Collecting the terms linear in y yields the equation

$$m\ddot{y} + b\dot{y} + \left(k_y - \gamma \frac{\varepsilon_0 lw}{y_0^3}V^2\right)y = -\gamma \frac{\varepsilon_0 lw}{2y_0^2}V^2 \tag{2.89}$$

This equation now has a spring constant that includes the mechanical spring, k_m, and an electric spring with

$$k_e = -\gamma \frac{\varepsilon_0 lwV^2}{y_0^3} \tag{2.90}$$

For small y, the resonant frequency of this system is therefore

$$\omega_y^2 = \frac{\left(k_y - \gamma \frac{\varepsilon_0 lw}{y_0^3}V^2\right)}{m} \tag{2.91}$$

If either a positive or negative voltage is applied to the stationary plate, then the resonant frequency along this axis decreases. When a large enough voltage is applied, the resonant frequency of the system will go to zero, and the two plates will come into contact for any increase in the applied voltage. This is called the snapdown voltage, and it is defined as the voltage for which both the net force and net spring are equal to zero. This occurs because of spring softening, i.e., the net spring constant has changed from positive to negative, so that the total spring force is no longer a restoring force, but is instead an attractive force. If $k = 0$, then any voltage would cause the plates to come together. Figure 2.29 is a plot of the resonant frequency versus the voltage normalized by the snapdown voltage. For V near zero, the resonant frequency is nearly quadratic with the voltage. As the potential increases, the frequency is a nonlinear function of the voltage, as the displacement becomes significant and the Taylor series expansions are no longer valid. In order to prevent this instability, the voltages applied to the stationary plate should remain well below the snapdown voltage.
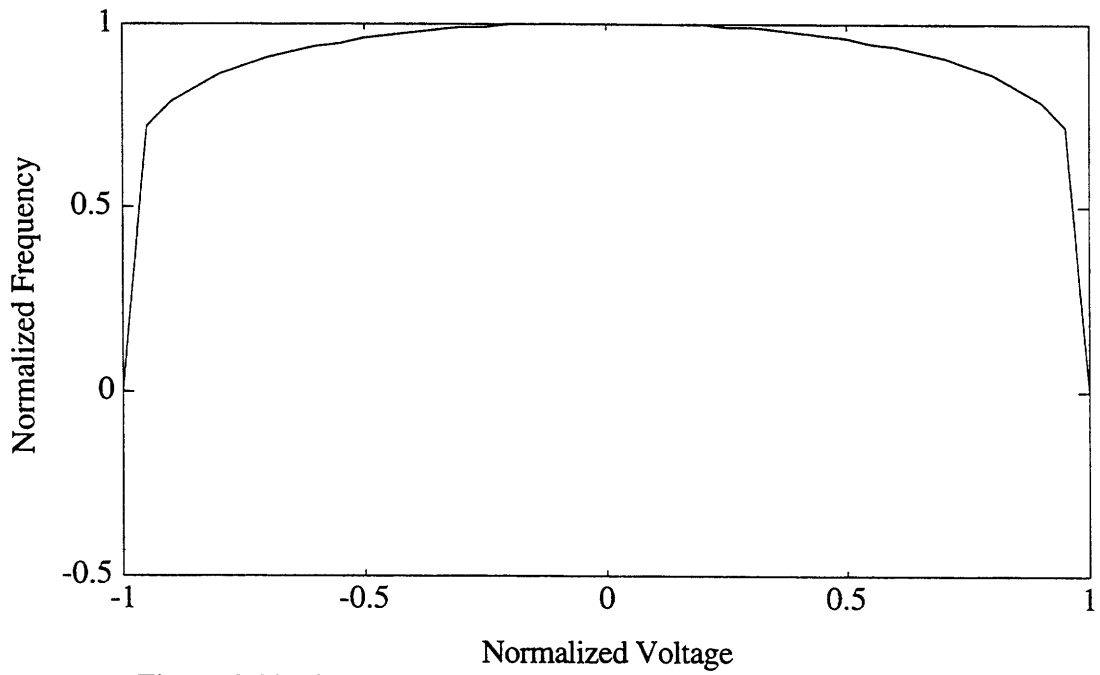
Figure 2.29. Sense Axis Resonant Frequency vs. Sense Plate Voltage
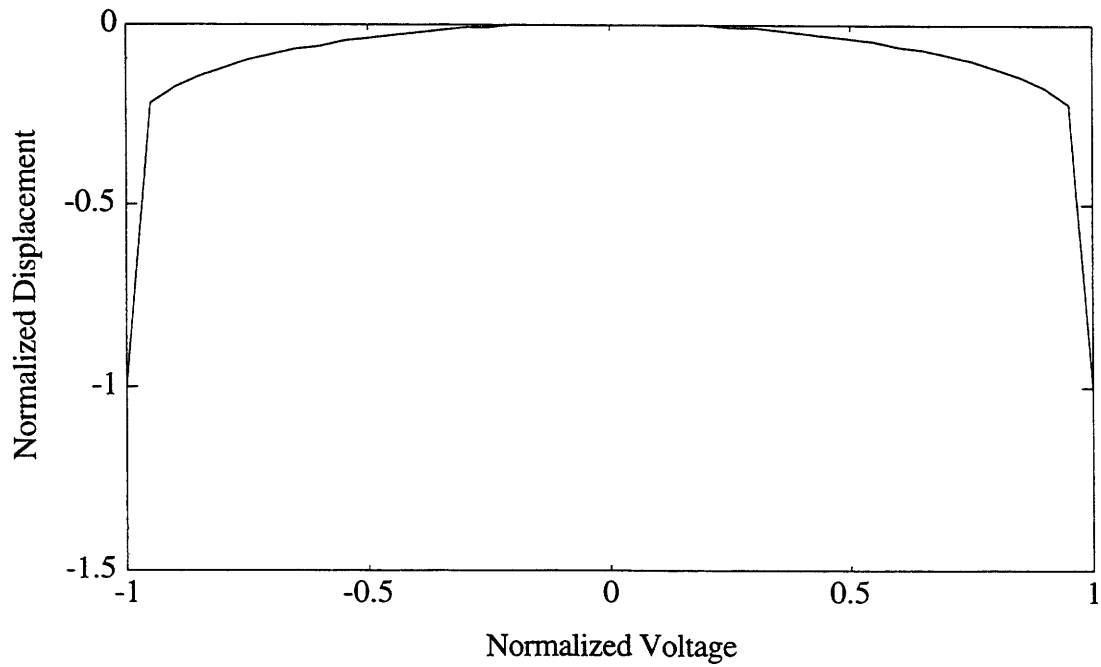
Figure 2.30. Sense Axis Displacement vs. Sense Plate Voltage

As the resonant frequency of the y-axis decreases, the small displacement assumption for y is no longer valid. Therefore, in order to determine when the spring constant goes to zero, the electrostatic spring constant must first be derived from Equation 2.92.

$$k_e(y) = -\frac{\partial F_e}{\partial y} = -\gamma \frac{\varepsilon_0 wl}{(y+y_0)^3} V_s^2 \qquad (2.92)$$

When this term equals the mechanical spring constant, the resonant frequency of the system is zero, and the snapdown voltage may be derived. This requirement yields a voltage

$$V_{snap} = \sqrt{\frac{8k_y y_0^3}{27\gamma\varepsilon_0 wl}} = \sqrt{\frac{8k_y y_0^2}{27C_{y0}}} \qquad (2.93)$$

where C_{y0} is the nominal sense plate capacitance. Snapdown also requires a critical displacement

$$y_{crit} = -\frac{y_0}{3} \qquad (2.94)$$

If the resonant frequency goes to zero, then the proof mass will snap down when the displacement has reduced the gap by one-third of its nominal value. For displacements less than this, the proof mass is marginally stable. This dramatic behavior is seen in both Figures 2.29 and 2.30. In Figure 2.30, for a normalized voltage near 1, the vertical displacement moves rapidly from -0.33 to -1 as the voltage increases. Similarly, as seen in Figure 2.29, the sense frequency drops to zero. This behavior places a strict limit on the magnitude of voltages that may be used to control the vertical and rotational motion of the proof mass.

2.2.5 Electrostatic Position Sensing

An essential element in any control system is measuring the variables to be controlled. If the displacement and velocity of the structure are unknown, then it is impossible to determine the magnitude of its vibration, or even whether or not the system is resonating. In micromechanical systems, the electrostatic behavior used to create forces is used in a slightly different way to measure the position of the proof mass. By exploiting the behavior of capacitors, both vertical and horizontal displacements may be detected in a micromechanical system.

2.2.5.1 Comb Drive Motion Detection

A typical micromechanical resonator has two sets of stationary combs associated with each proof mass, as shown in Figure 2.1. One comb is used to force a horizontal oscillation of the proof mass, and the other comb is used to detect that lateral motion [37]. By applying a constant voltage on the sense comb, proof mass oscillations cause the total capacitance between the rotor and the stator combs to vary, injecting a time varying charge (current) onto the sense comb that is integrated to determine proof mass position.

The total capacitance between two set of combs from Section 2.2.2.1 is repeated here

$$C = \alpha \frac{N\varepsilon_0 hx}{d} \tag{2.51}$$

The total charge on the detection stator may then be written as

$$q = CV = \alpha \frac{N\varepsilon_0 hx}{d} V_{ms} \tag{2.95}$$

where,

V_{ms} = DC voltage applied to stationary detection comb.

As the proof mass moves, the net charge varies, creating a current on the sense comb,

$$i = \frac{dq}{dt} = \frac{d}{dt}(CV) = \alpha \frac{N\varepsilon_0 h V_{ms}}{d} \frac{dx}{dt} = V_{ms} \frac{\partial C}{\partial x} \frac{dx}{dt} \tag{2.96}$$

With a DC voltage, the current depends only on the velocity of the proof mass. This current may then be integrated with an ideal op-amp, as shown in the schematic in Figure 2.31, high-pass filtered, and finally amplified by a factor of g_1. The ideal voltage output[8] is equal to

$$V_{out} = \frac{g_1}{C_{fb}} \int i dt = \frac{g_1}{C_{fb}} \int V_{ms} \frac{\partial C}{\partial x} dx = g_1 \frac{V_{ms}}{C_{fb}} \frac{\alpha N\varepsilon_0 h}{d} x \tag{2.97}$$

In this solution, the effects of the control plate seen in Equation 2.82 have been ignored. Therefore, the output voltage from the integrator is a scaled version of the proof mass position. This scale factor may be estimated either through direct measurement or by calculation, so that the displacement of the rotor can be determined.

---

[8]In Section 3.2.1.2, the effects of noise, the blocking capacitor, and the gain stage are studied in more detail.
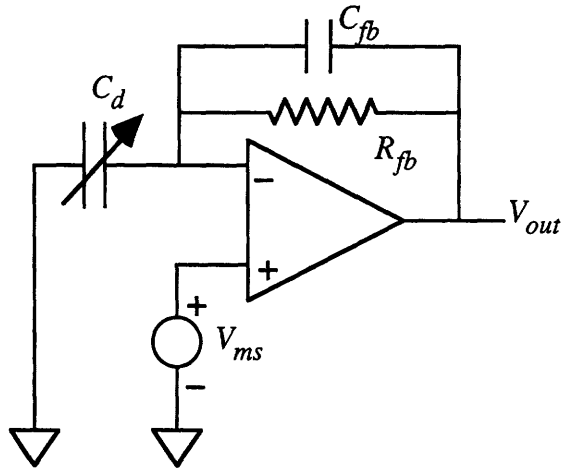
Figure 2.31. Integrator for Drive Motion Detection

The inclusion of the ground plane and the sensitivity to vertical motion, as shown in Equation 2.82, yields an output

$$V_{out} = g_1 \frac{V_{ms}}{C_{fb}} \left[\left(\frac{\partial C_{rs}}{\partial x} + \frac{\partial C_{sp}}{\partial x} \right) x + \left(\frac{\partial C_{rs}}{\partial y} + \frac{\partial C_{sp}}{\partial y} \right) y \right] \qquad (2.97)$$

In steady-state operation, the vertical motion may be neglected, since the horizontal motion is significantly larger. However, for modeling oscillator startup, as in Chapter 3, both sensitivity terms should be included.

2.2.5.2 Parallel Plate Motion Detection

Measurement of vertical motion of the proof mass is analogous to the measurement of horizontal motion. In this case, however, the voltage is applied to the stationary plate, and the proof mass itself is connected to the integrator. The proof mass is held at a virtual ground, as shown in Figure 2.32, and, analogous to the motor axis, the output signal is high-passed and gained to yield a signal linear with position.
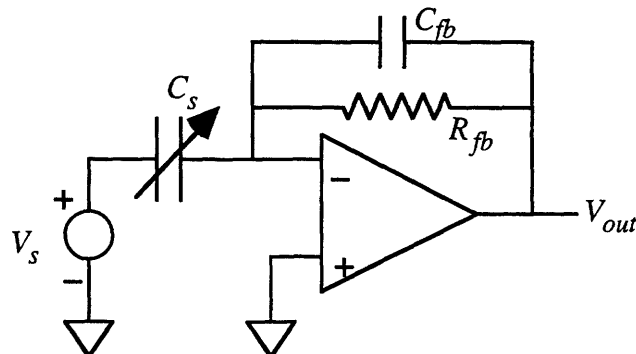
Figure 2.32. Integrator for Vertical Motion Detection

71

The capacitance between the proof mass and the stationary plate is now

$$C = \gamma \frac{\varepsilon_0 lw}{y + y_0} \qquad (2.84)$$

and the total charge on the proof mass is

$$q = CV = \gamma \frac{\varepsilon_0 lw}{y + y_0} V_s \qquad (2.98)$$

Here, the voltage will not be assumed to be constant, but will instead have both a DC and an AC component, in order to derive a more general solution. As the proof mass moves vertically, the current generated on the proof mass is

$$i = \frac{dq}{dt} = \frac{d}{dt}(CV) = V\frac{dC}{dt} + C\frac{dV}{dt} = -\gamma \frac{\varepsilon_0 lw}{(y + y_0)^2} V_s \frac{dy}{dt} + \gamma \frac{\varepsilon_0 lw}{(y + y_0)} \frac{dV_s}{dt} \qquad (2.99)$$

This current may also be integrated using an ideal op-amp, and then high-passed and amplified by g_s, so that the output voltage becomes

$$V_{out} = \frac{g_s}{C_{fb}} \int i \, dt = \frac{g_s V_s}{C_{fb}} \frac{\gamma \varepsilon_0 lw}{(y + y_0)} \qquad (2.100)$$

For small vertical motion with respect to the gap between the plates and a constant sense voltage, the output voltage may be approximated as

$$V_{out} \approx g_s \frac{\varepsilon_0 lw}{C_{fb} y_0} V_s \left(1 - \frac{y}{y_0}\right) = g_s \frac{C_{y0}}{C_{fb}} V_s \left(1 - \frac{y}{y_0}\right) \qquad (2.101)$$

The output voltage is approximately a DC value plus a small AC term that varies directly with the proof mass vertical motion. In Section 3.2.1.2, real op-amps are discussed, and the effects of noise on the minimum detectable signal are presented.

2.3 Micromechanical Resonator Total Lumped Parameter Model

Having examined in detail both the dynamics and electrostatics for the micromechanical resonator, the non-dimensional, coupled, nonlinear, differential equations of motion may be stated as

$$\ddot{\tilde{x}} + \frac{1}{Q}\dot{\tilde{x}} + \tilde{x} + \tilde{k}_{x_2}\tilde{x}^2 + \tilde{k}_{x_3}\tilde{x}^3 + \tilde{\omega}_{xy}^2\tilde{y} + \frac{1}{Q_{xy}}\dot{\tilde{y}} - 2\tilde{\Omega}\dot{\tilde{y}} \qquad (2.102)$$

$$= \frac{1}{2k_x x_0}\left[\frac{\partial C_{rs}}{\partial x}V_s^2 + \frac{\partial C_{rp}}{\partial x}V_p^2 + \frac{\partial C_{sp}}{\partial x}(V_s - V_p)^2\right]$$

$$\ddot{\tilde{y}} + \frac{\tilde{\omega}_y}{Q_y}\dot{\tilde{y}} + \tilde{\omega}_y^2\tilde{y} + \tilde{k}_{y_2}\tilde{y}^2 + \tilde{k}_{y_3}\tilde{y}^3 + \tilde{\omega}_{xy}^2\tilde{x} + \frac{1}{Q_{xy}}\dot{\tilde{x}} + 2\tilde{\Omega}\dot{\tilde{x}} \qquad (2.103)$$

$$= \tilde{F}_y + \frac{1}{2k_x x_0}\left[\frac{\partial C_{rs}}{\partial y}V_s^2 + \frac{\partial C_{rp}}{\partial y}V_p^2 + \frac{\partial C_{sp}}{\partial y}(V_s - V_p)^2\right]$$

This model incorporates the nonlinear springs, the coupling effects of the comb drive, and the coupling of both dissipative and restoring forces. The additional vertical force not due to the combs will be used in Chapter 5 as the vertical control force, which does not couple into the horizontal axis.

A capacitor model of a single element oscillator[9] is shown in Figure 2.33. In this figure, the proof mass is connected to the pre-amplifier with the output $V_{out,y}$, and the motor sense comb to $V_{out,x}$. Each of the circular nodes may be set either to ground or to a potential for capacitor measurements, as done in Chapter 6.
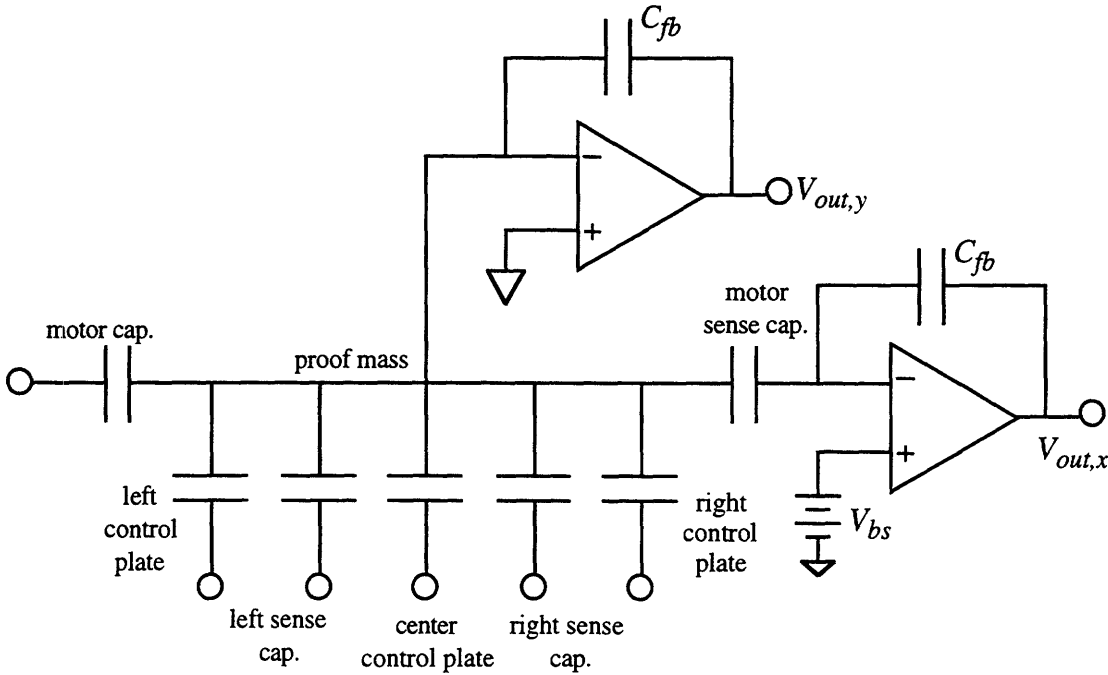
Figure 2.33. Capacitor Model for Single Element Oscillator

---

[9]See Figure 4.2 for an optical micrograph of the SEO.

There are seven capacitors for the SEO. Models for all of these capacitors were presented in Chapter 2. The motor and motor sense capacitors are interdigitated comb capacitors; the left and right control plates are ground planes; and the left and right sense and center control electrodes are parallel plate capacitors. These control plates will be examined in more detail in Chapters 4 and 5 as control actuators for the vertical and rotational motion control.

Chapter 3

Sustained Oscillations in Micromechanical Resonators

3.0 Introduction

Because the micromechanical resonator is a second-order system, it is possible to generate steady-state oscillations, i.e., limit cycles, by closing the loop of the system with an integrator and a relay. Significant analyses of these types of systems were performed in the 1960s [13, 19]. The techniques that emerged from this era include describing function analysis and stability criteria for nonlinear closed-loop systems. These tools are used extensively here to characterize the performance and behavior of a closed-loop micromechanical oscillator. After introducing the describing functions used for modeling the resonator, the behavior of the amplitude regulator loop is studied. Next, the stability of the closed oscillator loop is demonstrated, and perturbation analysis is used to examine the transient behavior of the system in response to parameter variations.

3.1 Describing Function Analysis

From Chapter 2, it is clear that the oscillator itself possesses a nonlinear element: the cubic spring. In order to close the loop on this system, the relay, another nonlinear element, is required. If the transfer functions of both of these elements can be linearized, then quasilinear techniques may be used to analyze the closed-loop behavior. In a steady-state oscillation, the dominant signals in the system are sinusoids; this fact will permit the application of describing functions to linearize the system.

3.1.1 Theory of Describing Function Analysis

The principle of superposition permits straightforward analysis of linear system behavior. This principle states that,

If the input $r_1(t)$ produces the response $c_1(t)$, and the input $r_2(t)$ yields the response $c_2(t)$, then for all a and b the response to the input $ar_1(t) + br_2(t)$ will be $ac_1(t) + bc_2(t)$; and this must be true for all inputs [13].

This means that linear elements may be studied one input at a time, and the response from these inputs may be used to extrapolate the response for all other inputs. A system that does not satisfy the superposition principle is defined to be nonlinear. For these systems, the output cannot be generalized given the response of the system for a particular input.

The first step in simplifying the analysis of a nonlinear feedback control system is to express the system as a single loop with both linear and nonlinear components, as shown in Figure 3.1 [13]. Nonlinearities may occur in any of the elements, but they most often occur in the actuator or in the feedback element.
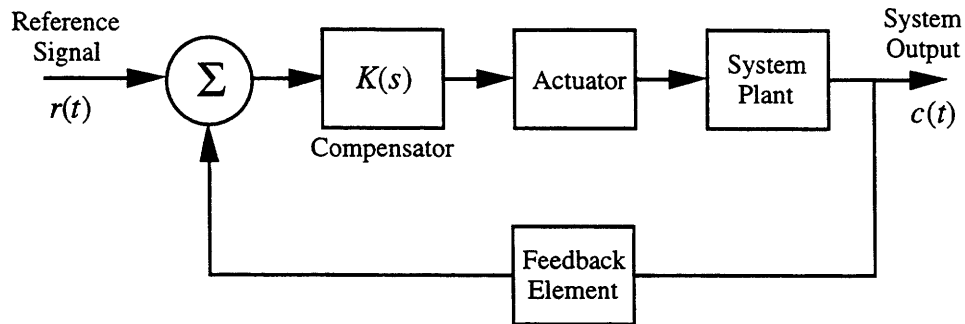
Figure 3.1. Typical Nonlinear Feedback Loop

For linearization, several different methods may be used. The most common approaches are power series expansion, perturbation techniques, and describing function analysis. In describing function analysis, a general form of the input to a nonlinear element is assumed, and from there, a solution may be derived for this particular input. The most common describing function inputs are a bias, a sinusoid, and a gaussian process. Quasilinear approximations to the nonlinear element response based on these inputs are called describing functions. The closer the actual input is to the assumed input shape, then the more accurate the describing function analysis will be. For a sinusoidal describing function approach to be meaningful, three essential criteria must be met:

1. The nonlinear element must be time-invariant.
2. No subharmonics may be generated by the non-linearity in response to a sinusoidal input.

3. There must be a low-pass filter somewhere in the system, so that the fundamental frequency is fedback, and higher harmonics are attenuated. This is known as the filter hypothesis [13].

For the SEO, all three requirements are satisfied for sinusoidal describing functions. The linear plant for each degree of freedom is a high-Q resonator that acts as a low-pass filter with large gain at resonance and -40 dB/decade roll-off above the natural frequency of the system. It will be shown that, in the electronics, sufficient low-pass filters exist to attenuate the higher-order harmonics from the system throughout the closed loop.

3.1.2 General Solutions for Sinusoidal Describing Functions

The three nonlinearities typically encountered in a closed-loop micromechanical resonator are a cubic spring, a relay with hysteresis, and an ideal relay. Here, the sinusoidal describing functions for these elements are derived. The output of a nonlinear element, $y(x, \dot{x})$, may be written as a Fourier series for a sinusoidal input. By the conditions defined above for the describing function, the significant quantity of the output will be at the first harmonic of the series, so that, for the input

$$x = A\sin\psi \tag{3.1}$$

where,

A = real amplitude of input

ψ = $\tilde{\omega}\tau + \varphi$

$\tilde{\omega}$ = non-dimensional input frequency

τ = non-dimensional time, and

φ = real phase shift,

the output is

$$y(A\sin\psi, A\tilde{\omega}\cos\psi) = \sum_{n=1}^{\infty} A_n(A, \tilde{\omega})\sin[n\tilde{\omega}\tau + \varphi_n(A, \tilde{\omega})] \tag{3.2}$$

From this equation for y, the describing function of the nonlinear element may be expressed as

$$N(A, \tilde{\omega}) = \frac{\text{output component at } \tilde{\omega}}{\text{input component at } \tilde{\omega}}$$

$$= \frac{A_1(A, \tilde{\omega})}{A} e^{j\varphi_1(A, \tilde{\omega})} \tag{3.3}$$

Equations for A_1 and φ_1 may be defined by solving Equation 3.2 for the Fourier coefficient and phase at $n = 1$. Substituting this result into Equation 3.3 yields a solution for $N(A, \tilde{\omega})$ in terms of the nonlinearity, y,

$$N(A, \tilde{\omega}) = \frac{j}{\pi A} \int_0^{2\pi} y(A \sin \psi, A \tilde{\omega} \cos \psi) e^{-j\psi} d\psi \tag{3.4}$$

This representation of $N(A, \tilde{\omega})$ may be expanded into real and imaginary parts

$$N(A, \tilde{\omega}) = \frac{1}{\pi A} \int_0^{2\pi} y(A \sin \psi, A \tilde{\omega} \cos \psi) \sin \psi d\psi + \frac{j}{\pi A} \int_0^{2\pi} y(A \sin \psi, A \tilde{\omega} \cos \psi) \cos \psi d\psi$$
$$= n_p(A, \tilde{\omega}) + j n_q(A, \tilde{\omega}) \tag{3.5}$$

where $n_p(A, \tilde{\omega})$ and $n_q(A, \tilde{\omega})$ are the in-phase and quadrature gains of the nonlinearity output, respectively. This representation will useful for the analyses performed in Sections 3.3.3 through 3.3.5.

3.1.2.1 Describing Function for the Cubic Spring

For many real mechanical systems, the forces exerted by the springs have significant nonlinearities. Typically, nonlinear terms depend on the magnitude of the displacement. A third-order restoring force may be written as

$$\tilde{k}_1 \xi + \tilde{k}_2 \xi^2 + \tilde{k}_3 \xi^3 \tag{3.6}$$

where ξ is a generalized coordinate (either x or y) and the $\tilde{k}_i$ are non-dimensional spring constants. In steady-state operation, both x and y will be sinusoidal, so ξ may be defined as $A \sin \psi$ where A is the non-dimensional amplitude and ψ is the non-dimensional argument of the trigonometric function defined earlier. If this definition is substituted into Equation 3.6, then

$$\tilde{k}_1 A \sin \psi + \tilde{k}_2 A^2 \sin^2 \psi + \tilde{k}_3 A^3 \sin^3 \psi$$
$$= \tilde{k}_1 A \sin \psi + \tilde{k}_2 \frac{A^2}{2}(1 - \cos 2\psi) + \tilde{k}_3 \frac{A^3}{4}(3 \sin \psi - \sin 3\psi) \tag{3.7}$$

Collecting like terms yields

$$\frac{1}{2}\tilde{k}_2 A^2 + \left(\tilde{k}_1 + \frac{3}{4}\tilde{k}_3 A^2\right) A \sin \psi - \tilde{k}_2 \frac{A^2}{2} \cos 2\psi - \frac{1}{4}\tilde{k}_3 A^3 \sin 3\psi \tag{3.8}$$

The filter hypothesis allows the non-fundamental frequency terms to be neglected, so that the approximate output for the quadratic and cubic spring becomes

78

$$\frac{1}{2}\tilde{k}_2 A^2 + \left(\tilde{k}_1 + \frac{3}{4}\tilde{k}_3 A^2\right) A \sin \tau \qquad (3.9)$$

which is similar to the results of Section 2.1.3.2, in that the quadratic spring contributes a DC component to the system. If the quadratic term is set equal to zero, such as the case for the drive axis, then the describing function for the cubic spring is

$$N(A, \tilde{\omega}) = \frac{3}{4}\tilde{k}_3 A^2 \qquad (3.10)$$

This describing function is dependent only on the amplitude of the oscillation. The linearization of the cubic spring by describing function analysis is identical to that by perturbation methods in Chapter 2. By using this describing function, the non-dimensional resonant frequency of the system may be written as

$$\tilde{\omega}^2 = 1 + \frac{3}{4}\tilde{k}_3 A^2 \qquad (3.11)$$

For small $\tilde{k}_3$, the resonant frequency may be approximated by

$$\tilde{\omega} \approx 1 + \frac{3}{8}\tilde{k}_3 A^2 \qquad (3.12)$$

The increase in the resonant frequency due to the cubic spring depends on the square of the amplitude, as shown in Section 2.1.3.

3.1.2.2 Describing Function for Relays

The typical response for a relay element with hysteresis is shown in Figure 3.2. In this figure, the input signal is x, and the output is y. Physically, if y is equal to $-D$, then, as x becomes greater than δ, y will switch its value from $-D$ to $+D$. The output will remain at $+D$ until x decreases below $-\delta$. Because the output depends on its previous state, the hysteretic relay is known as an odd, static, symmetric, frequency-independent, nonlinear element with memory. As $\delta \rightarrow 0$, this element becomes an ideal relay, which is a memoryless, odd, static, symmetric nonlinearity. To determine the describing function for the relay, it is best to include the hysteresis, and then let $\delta \rightarrow 0$ to find the describing function for the ideal relay.

The response of a relay to a sinusoidal input is a square wave with phase shift. A typical square wave response is shown in Figure 3.3 for an input magnitude greater than the delay, δ. The phase shift of the output square wave due to the hysteresis is clearly seen between the input and output signals because the output signal does not switch until after the input has changed signs. For the ideal relay, there is no phase shift.
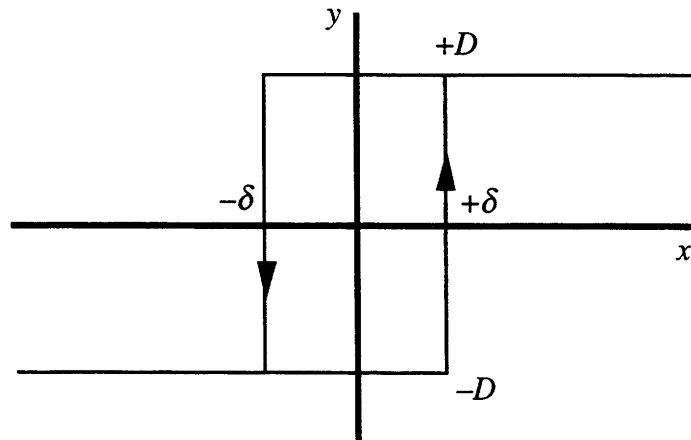
Figure 3.2. Relationship Between Input and Output for a Relay with Hysteresis
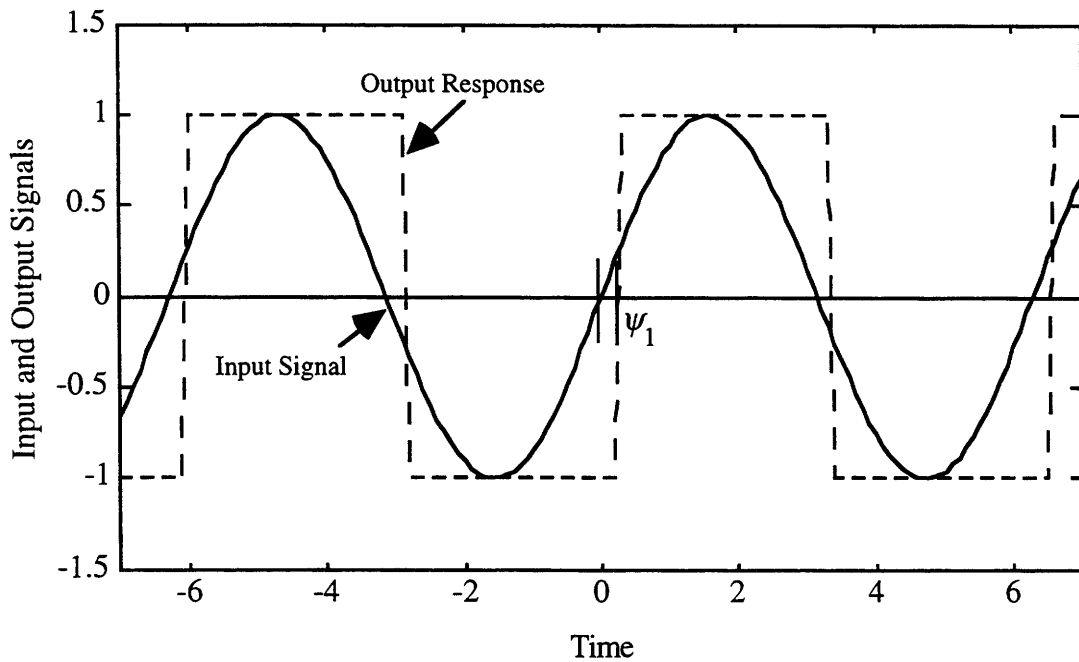
Figure 3.3. Response of Relay with Hysteresis to a Sinusoidal Input

The describing function for the hysteretic relay may be found by solving the describing function equation for an odd static nonlinearity

$$N(A) = \frac{2j}{\pi A} \int_0^\pi y(A\sin \psi)e^{-j\psi}d\psi \qquad (3.13)$$

From Figure 3.3, it is clear that this system may be divided into two separate integrals for each region of the relay output, for $A > \delta$,

$$N_{HR}(A) = \frac{2j}{\pi A}\left[\int_0^{\psi_1} -De^{-j\psi}d\psi + \int_{\psi_1}^{\pi} De^{-j\psi}d\psi\right]$$

$$= \frac{4D}{\pi A}e^{-j\psi_1} \tag{3.14}$$

where,

D = magnitude of relay output

ψ_1 = phase shift due to hysteresis = $\sin^{-1}(\delta/A)$,

and the subscript HR stands for hysteretic relay.

This describing function may also be expressed as a complex number
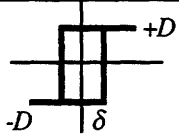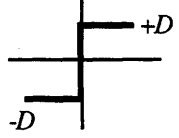
$$N_{HR}(A) = \frac{4D}{\pi A}\sqrt{1 - \left(\frac{\delta}{A}\right)^2} - j\frac{4D\delta}{\pi A^2} \tag{3.15}$$

By letting $\delta \to 0$, the describing function for the ideal relay is

$$N_{IR}(A) = \frac{4D}{\pi A} \tag{3.16}$$

where the subscript IR means ideal relay. Therefore, the hysteretic relay introduces both gain and phase shift, while the ideal relay is a pure gain element. Both of these describing functions are independent of frequency, a fact that greatly simplifies later analyses. The describing functions derived in this section are summarized in Table 3.1.

Table 3.1. Describing Functions Encountered in Closed-Loop Oscillator

Nonlinear Function	Description	Describing Function $N(A,\tilde{\omega})$
Cubic spring	$\tilde{k}_3\xi^3$	$\dfrac{3}{4}\tilde{k}_3 A^2$
Relay with hysteresis	$\begin{array}{c}+D\\ -D \quad \mid\delta\end{array}$	$\dfrac{4D}{\pi A}\sqrt{1 - \left(\dfrac{\delta}{A}\right)^2} - j\dfrac{4D\delta}{\pi A^2}$
Ideal relay	$\begin{array}{c}+D\\ -D\end{array}$	$\dfrac{4D}{\pi A}$

3.2 A Closed-Loop Micromechanical Oscillator

A typical closed loop for generating steady-state oscillations is shown in Figure 3.4. Two control loops are required for self-exciting the SEO and maintaining a constant amplitude: the oscillator loop and the amplitude regulator loop. The oscillator loop consists of the micromechanical resonator, a preamplifier and gain stage, a 90° phase shifter, and a hard limiter. The amplitude regulator loop contains the resonator plant, an absolute value operation, a low-pass filter that eliminates the resulting second harmonic, a summing element that compares the amplitude of the oscillation to a desired value, and a compensation block with a proportional plus integral gain that determines the voltage necessary to maintain the desired amplitude.
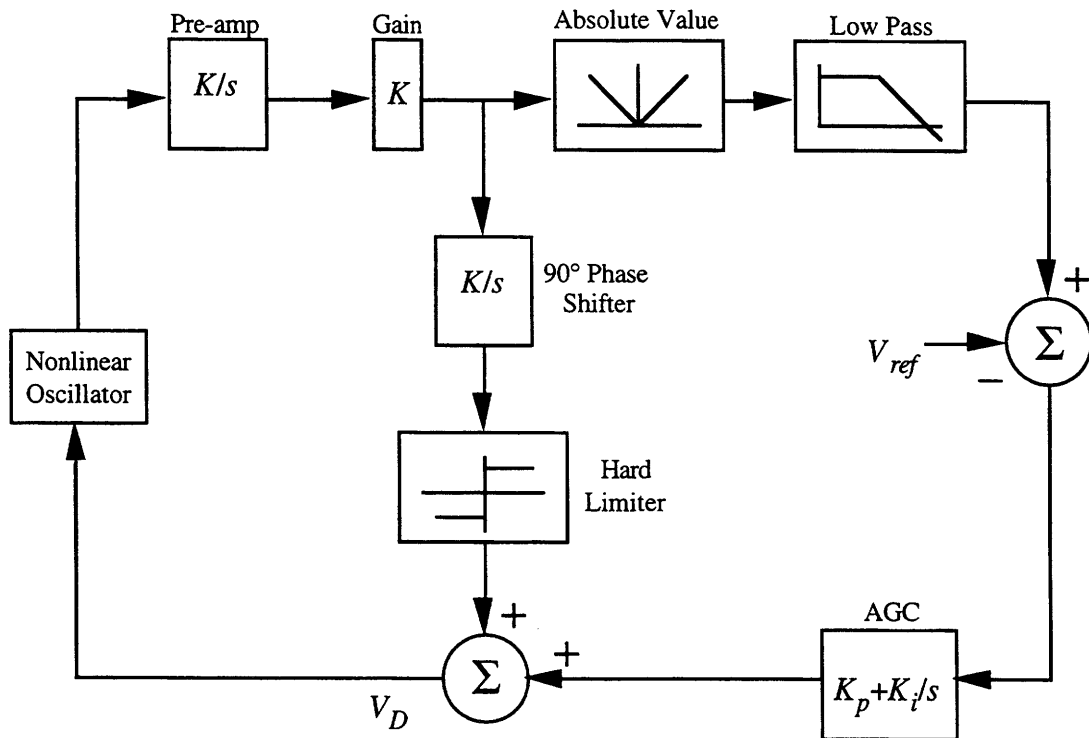
Figure 3.4. Block Diagram of Self-Exciting Motor Axis Control Loop

The outputs from each of these loops are then summed together and applied to the drive comb of the oscillator as V_D, a voltage that consists of a signal in-phase with the velocity of the proof mass and a DC term equal to the gain required to maintain the oscillation amplitude. Through the comb interaction, this voltage creates a force that is in-phase with the proof mass velocity. This force eliminates the effects of damping and sustains the oscillation. These two loops are related; the oscillation loop determines the frequency of the force, and the regulator determines the magnitude of the applied force.

3.2.1 Components of the Oscillator Loop

The self-exciting oscillator loop consists of the inner loop shown in Figure 3.4. Each of these blocks represents a component with unique behavior. It is useful to examine each of the individual elements in detail with a state-space approach. For this discussion, it is assumed that a steady-state oscillation exists at the resonant frequency of the system (with the cubic spring effects included). In Section 3.3.3, it is proven that a stable limit cycle exists for any hard spring. Here, each block of the oscillator loop is examined in detail. First, the resonator dynamics are expressed in state-space form by using the cubic spring describing function. Next, each of the components in the oscillator loop is discussed. Finally, a state-space model for the self-excitation loop is given.

3.2.1.1 State-Space Model for the SEO

It is possible to express the nonlinear, second-order, differential equations (2.9 and 2.10) of the SEO from Chapter 2 in state-space form by using the describing function for the cubic spring from Equation 3.10

$$
\frac{d}{d\tau}\begin{bmatrix}\dot{\tilde{x}}\\ \tilde{x}\\ \dot{\tilde{y}}\\ \tilde{y}\end{bmatrix} = -\begin{bmatrix} \dfrac{1}{Q} & 1+\dfrac{3}{4}\tilde{k}_{x_3}A_x^2 & \dfrac{1}{Q_{xy}} & \tilde{\omega}_{xy}^2 \\ -1 & 0 & 0 & 0 \\ \dfrac{1}{Q_{xy}} & \tilde{\omega}_{xy}^2 & \dfrac{\tilde{\omega}_y}{Q_y} & \tilde{\omega}_y^2+\dfrac{3}{4}\tilde{k}_{y_3}A_y^2 \\ 0 & 0 & -1 & 0 \end{bmatrix}\begin{bmatrix}\dot{\tilde{x}}\\ \tilde{x}\\ \dot{\tilde{y}}\\ \tilde{y}\end{bmatrix} + \begin{bmatrix}1 & \alpha\\ 0 & 0\\ \beta & 1\\ 0 & 0\end{bmatrix}\begin{bmatrix}\tilde{F}_x\\ \tilde{F}_y\end{bmatrix} \qquad (3.17)
$$

By writing the SEO dynamics in state-space form, it is much simpler to analyze the behavior of the system, to determine a stability criterion, and to simulate the startup and steady-state behavior of the system. The force coupling coefficients, α and β, were determined from the finite element analysis of Section 2.2.3, and the actual values depend on the voltages applied to the stator, rotor, and ground plane. Here, the coefficients will be used to simplify the description of the force cross-coupling effects.

3.2.1.2 Preamplifier and Gain Stages

The preamplifier and gain stage can be modeled as shown in Figure 3.5. Here, the drive capacitance, C_d, is represented by a variable capacitance due to the proof mass oscillations, and the op-amp feedback elements are a capacitor and a resistor connected in parallel. The positive input to the op-amp has both the DC bias of the sense comb and the input noise of the pre-amp. The noise capacitance is modeled by C_N, and the gain stage is simply represented by g_1.

By modeling the capacitors as impedance elements, Kirchoff's current law states

$$-s(V_{bs} + V_N)(C_d + C_N) = C_{fb}\left(s + \frac{1}{R_{fb}C_{fb}}\right)(V_{bs} + V_N - V_{out}) \qquad (3.18)$$

where,

V_{bs} = DC bias on motor sense comb

V_N = preamplifier noise

C_{fb} = feedback capacitor

R_{fb} = feedback resistor

C_d = capacitance between proof mass and sense comb

V_{out} = output voltage from pre-amplifier, and

C_N = stray capacitance.
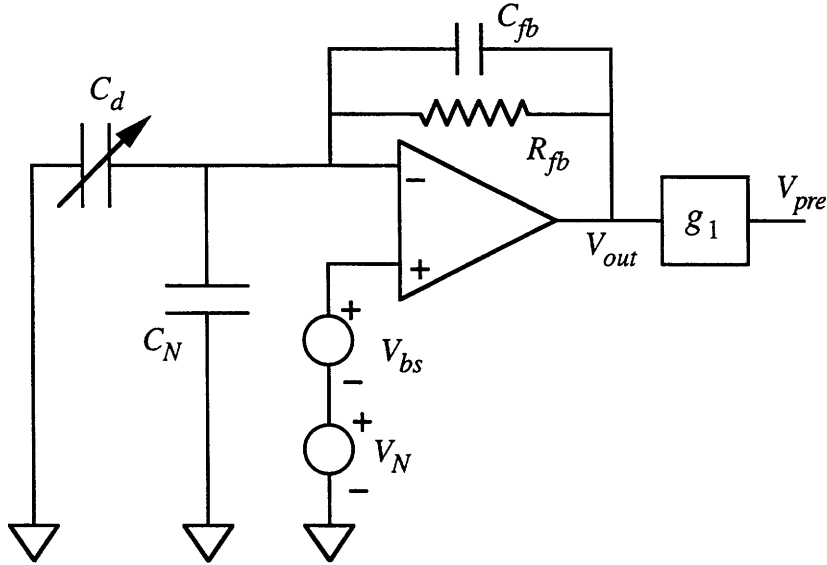
Figure 3.5. Schematic of Motor Sense Comb Output Integrator with Noise

To find the transfer function of this system, first define x^*, with units of Volts, to be a combination of the output voltage, sense comb bias, and noise of the pre-amp,

$$x^* = V_{out} - (V_{bs} + V_N)\left(1 + \frac{C_N}{C_{fb}}\right) \qquad (3.19)$$

Substituting this definition into Equation 3.18, and assuming $V_{bs} >> V_N$, yields the differential equation

$$\dot{x}^* = \frac{V_{bs}}{C_{fb}}\frac{\partial C_d}{\partial x}\dot{x} - \omega_{pre}\left(x^* + \frac{C_N}{C_{fb}}(V_{bs} + V_N)\right) \qquad (3.20)$$

where $\omega_{pre} = 1/R_{fb}C_{fb}$. This equation may then be non-dimensionalized by making the time and displacement normalizations from Equation 2.8,

$$\dot{x}* = \frac{V_{bs}x_0}{C_{fb}} \frac{\partial C_d}{\partial x} \tilde{\dot{x}} - \tilde{\omega}_{pre}\left(x* + \frac{C_N}{C_{fb}}(V_{bs} + V_N)\right) \qquad (3.21)$$

The gain stage also includes a blocking capacitor to remove the V_{bs} term from the output voltage. Therefore, the transfer function from V_{out}, the output of the preamplifier expressed in terms of $x*$, to V_{pre}, the output of the gain stage, is

$$V_{pre} = -\frac{R_g}{R_b} \frac{\tilde{s}}{\tilde{s} + \tilde{\omega}_b}\left(x* + (V_{bs} + V_N)\left(1 + \frac{C_N}{C_{fb}}\right)\right) \qquad (3.22)$$

where,

R_g = the feedback resistor in the gain op-amp

R_b = the resistor for the high-pass filter

$\tilde{\omega}_b$ = the cut off frequency of the high-pass circuit; $\tilde{\omega}_b = 1/(R_bC_b\omega_n)$, and

C_b = the blocking capacitor for the high-pass filter.

For the DC term, V_{bs}, the gain of the high-pass transfer function is 0. For $x*$ and V_N, the transfer function approaches 1 for $\tilde{\omega}_b \ll 1$. Therefore, in Equations 3.21 and 3.22, the V_{bs} term in the sum $V_{bs} + V_N$ may be ignored. These three equations then become

$$x* = V_{out} - V_N\left(1 + \frac{C_N}{C_{fb}}\right) \qquad (3.23)$$

$$\dot{x}* = \frac{V_{bs}x_0}{C_{fb}} \frac{\partial C_d}{\partial x} \tilde{\dot{x}} - \tilde{\omega}_{pre}\left(x* + \frac{C_N}{C_{fb}}V_N\right) \qquad (3.24)$$

$$V_{pre} = -\frac{R_g}{R_b}\left(x* + V_N\left(1 + \frac{C_N}{C_{fb}}\right)\right) \qquad (3.25)$$

The transfer function between the preamplifier output and the input noise, before the gain stage, is, from Equation 3.18

$$\frac{V_{out}}{V_N} = \left(1 + \frac{C_d + C_N}{C_{fb}}\right)\frac{s + \dfrac{1}{R_{fb}\left(C_{fb} + C_d + C_N\right)}}{s + \dfrac{1}{R_{fb}C_{fb}}} \qquad (3.26)$$

For very low frequencies, the gain of this transfer function is 1, and for very high frequencies, the gain is

$$1 + \frac{C_d + C_N}{C_{fb}} = \frac{\Sigma C}{C_{fb}} \tag{3.27}$$

Therefore, the high frequency noise is amplified by this arrangement, and will limit the position measurement accuracy. The non-dimensional position equivalent noise may be expressed approximately as

$$\sigma_{\tilde{x}} = \frac{C_{fb} + C_d + C_N}{V_{bs} x_0 \frac{\partial C_d}{\partial x}} \sigma_N \tag{3.28}$$

where σ_N is the square root of the input noise density. For an assumed input noise density of 10^{-16} V²/Hz, the noise on the drive position measurement is 115×10^{-9} 1/√Hz, which is equivalent to 0.0115 Å/√Hz. For amplitudes on the order of microns, the noise is insignificant in the steady-state signal.

From Section 2.2.3.4, it was shown that there exists cross-sensing at the motor comb. Including this effect in the preamplifier model changes Equation 3.24 to

$$\dot{x}^* = \frac{V_{bs} x_0}{C_{fb}} \left(\frac{\partial C_d}{\partial x} \dot{\tilde{x}} + \frac{\partial C_d}{\partial y} \dot{\tilde{y}} \right) - \tilde{\omega}_{pre} \left(x^* + \frac{C_N}{C_{fb}} V_N \right) \tag{3.29}$$

where both partial derivatives include the total effects of the interactions between the stator, rotor, and ground plane.

3.2.1.3 90° Phase Shifter and Hard Limiter

The 90° phase shifter adds 90° of phase shift to the position signal so that it is now in-phase with the proof mass velocity. This phase shift is necessary in order to generate a force that is proportional to velocity and therefore maintain a steady-state oscillation. In practice, the sinusoidal position signal is integrated and multiplied by -1 to achieve the correct phase shift. The phase shifter may simply be modeled as a non-dimensional differential equation

$$\dot{V}_{ps} = V_{pre} - \tilde{\omega}_{int} V_{ps} \tag{3.30}$$

where,

V_{ps} = the phase shifted voltage, and

$\tilde{\omega}_{int}$ = non-dimensional break frequency of integrator = $0.001 \tilde{\omega}_n$.

86

With such a low break frequency, the phase of this low-pass filter will approach 90° (89.94°) at the resonant frequency of the system. Also, at a non-dimensional resonant frequency of 1, the gain of this filter is very close to 1 (1-5x10^{-7}).

The hard limiter behaves as shown in Figure 3.2. A typical hard limiter has hysteresis, such that the transition between +1 and -1 does not occur as soon as the input voltage changes from positive to negative. The hard limiter may be modeled with an algorithm, as shown in Equation 3.31, or by using the describing function of Equation 3.15.

$$V_{hl} = \begin{cases} +1, & \text{if } V_{ps} > \delta \text{ and } V_{hl} = -1 \\ -1, & \text{if } V_{ps} < -\delta \text{ and } V_{hl} = +1 \end{cases} \qquad (3.31)$$

where,

V_{hl} = the output of the hard limiter, and

δ = half-width of the hard limiter hysteresis.

During startup, the hard limiter must be modeled using Equation 3.31, since the input to the relay is not sinusoidal. Describing function analysis may be used for the hard limiter in the steady-state because, at that point, the input to the limiter will be sinusoidal.

The elements of the oscillator loop sustain limit cycles because there is a total of 360° of phase shift in this loop. The resonator itself contributes -90°, the phase shifter contributes another -90°, and the negative feedback adds the remaining 180°. This configuration is a very straightforward implementation of a relay controller used to generate steady-state oscillations.

3.2.2 Amplitude Regulator Loop

In addition to the self-excitation loop, the oscillator electronics have an amplitude control loop. In Figure 3.4, the regulator loop is the outer control loop, and it consists of the peak detector, the low-pass filter, the addition of a reference voltage, a proportional plus integral controller, the addition of the oscillating drive signal, and the oscillator itself. At the drive voltage summation, the oscillator and amplitude control loops are reunited to generate a signal that controls both the frequency and the amplitude of the oscillation. By automatically monitoring the amplitude of the oscillation, the system can be driven at a reasonable amplitude that balances the nonlinear effects of the cubic spring against the need for a large signal-to-noise ratio. As with most amplitude regulators, the magnitude of the oscillation is found and compared to a reference value. The error between the actual and desired amplitudes is then passed through a proportional plus integral controller, and the resulting voltage is applied to the oscillator loop.

The magnitude is found by multiplying the sinusoidal output of the preamplifier after the gain, V_{pre}, by a square wave generated by a hard limiter with V_{pre} as the input. The resulting output signal is then the absolute value of V_{pre}, as shown in Equation 3.32,

$$V_{pre} = K_s x = K_s A \sin \tilde{\omega}\tau$$

$$V_{pre} \operatorname{sqr} \tilde{\omega}\tau = \frac{4}{\pi} K_s A \sin \tilde{\omega}\tau \left(\sin \tilde{\omega}\tau + \frac{1}{3} \sin 3\tilde{\omega}\tau + \ldots \right) \approx \frac{2}{\pi} K_s A (1 - \cos 2\tilde{\omega}\tau) \tag{3.32}$$

where,

$\tilde{\omega}$ = non-dimensional drive axis resonant frequency (may include spring hardening)

K_s = the preamplifier gain, and

A = the non-dimensional amplitude of the proof mass oscillation.

This signal is low-pass filtered to produce a nearly constant signal that is proportional to the amplitude of the proof mass oscillation.

The reference voltage, V_{ref}, is calculated analytically by using the oscillator dynamic model and the preamplifier model

$$V_{ref} = \frac{2}{\pi} K_s = \frac{2}{\pi} \frac{g_{pre} V_{bs} x_0}{C_{fb}} \frac{\partial C_d}{\partial x} \tag{3.33}$$

where g_{pre} is the gain stage amplification. For a desired amplitude of 10 μm and a preamplifier gain of 10, the reference voltage is approximately 0.39 Volts.

The error between the amplitude of V_{pre} and V_{ref} is passed through a PI controller to generate the control voltage, V_A,

$$V_A = \left(K_P + \frac{K_I}{s} \right) \left(V_{ref} - \frac{2}{\pi} K_s A \right) \tag{3.34}$$

where K_P is the proportional gain and K_I is the integral gain.

This DC value is added to the hard limiter output, yielding a drive control voltage

$$V_d = V_A + V_{DC} \operatorname{sqr}(\tilde{\omega}\tau) \tag{3.35}$$

where $\operatorname{sqr}(\tilde{\omega}\tau)$ is a square wave at the resonant frequency and in-phase with a sinusoid[1]. This voltage is then applied to the stator comb, resulting in a drive force

$$F_d = \frac{1}{2} \frac{\partial C}{\partial x} V_d^2 = \frac{1}{2} \frac{\partial C}{\partial x} \left(2 V_A V_{DC} \operatorname{sqr}(\tilde{\omega}\tau) + V_A^2 + V_{DC}^2 \right) \tag{3.36}$$

The constant forces are offset by the DC voltage on the sense comb, and, in steady-state, the AC component of the force is at the resonant frequency of the oscillator.

---

[1] csqr(ωt) will be a square wave at ω that is in-phase with a cosinusoid. See Appendix A for details on square wave relationships.

88

The behavior of the amplitude regulator loop may be studied by using the slowly varying parameter approach introduced by Krylov and Bogoliubov [17]. Here, the shape of the signal is assumed to be $A(t)\sin(\omega_0\tau+\varphi(t))$, where both the amplitude, A, and phase, φ, are time varying. If the amplitude control element is assumed to be an integral plus proportional controller, then the nonlinear elements of the frequency modulation and low-pass may be simplified to the closed-loop block diagram shown in Figure 3.6, where x_vel is a square wave in phase with the proof mass velocity.
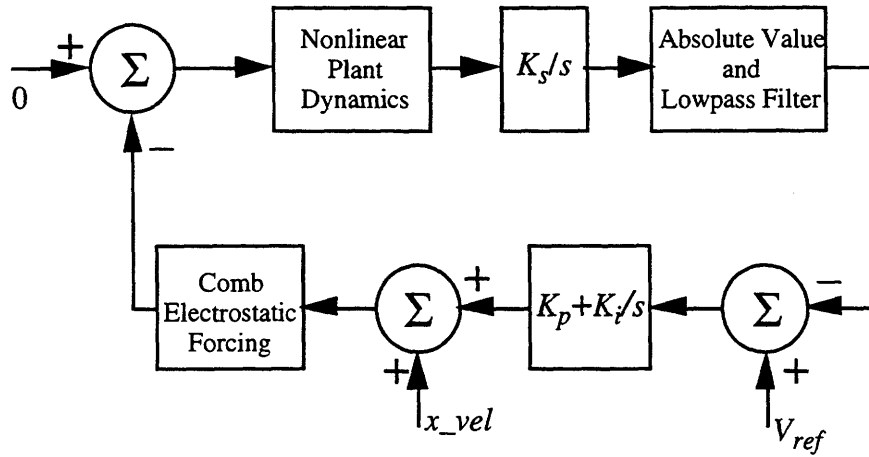
Figure 3.6. Simplified Block Diagram of Amplitude Regulator Loop

If it is also assumed that the oscillator loop has locked onto the natural frequency of the drive axis, then the dynamic model for the amplitude control loop is

$$\ddot{\tilde{x}} + \frac{\dot{\tilde{x}}}{Q} + \tilde{x} + \tilde{k}_3\tilde{x}^3 = K_{f,A}\frac{4}{\pi}V_A\frac{\dot{\tilde{x}}}{A} \tag{3.37}$$

where,

$$V_A = \left(K_P + \frac{K_I}{s}\right)\left(V_{ref} - \frac{2K_s}{\pi}A\right) \tag{3.38a}$$

$$\tilde{x} = A\sin(\tau + \varphi) \tag{3.38b}$$

$$\dot{\tilde{x}} = \dot{A}\sin(\tau + \varphi) + (1 + \dot{\varphi})A\cos(\tau + \varphi) \tag{3.38c}$$

$$\ddot{\tilde{x}} = \left(\ddot{A} - (1 + \dot{\varphi})^2 A\right)\sin(\tau + \varphi) + \left(\ddot{\varphi}A + 2\dot{A}(1 + \dot{\varphi})\right)\cos(\tau + \varphi) \tag{3.38d}$$

$K_{f,A}$ = forcing coefficient for the amplitude control loop = $\dfrac{V_{DC}}{k_x x_0}\dfrac{\partial C_d}{\partial x}$

K_s = sensing coefficient for amplitude control loop (defined in Equation 3.33)

K_P = G_{AR} = the proportional gain of the PI compensator = 0.0179

K_I = $G_{AR}\tilde{\omega}_z$ = the integral gain of the PI compensator = 1.424 x 10⁻⁷

89

g_1 = gain after preamplifier

G_{AR} = gain of amplitude regulation loop

ω_z = location of zero in PI controller = 1 rad/sec. It is non-dimensionalized for K_I,

and V_A is the varying control voltage discussed previously. This voltage is passed through a saturation function with limits equal to zero or the positive supply voltage, i.e., 10 Volts, such that V_A is always positive and less than or equal to 10 Volts.

In Equation 3.37, the nonlinear plant is driven by a sinusoidal force that is in-phase with the proof mass velocity and has a magnitude determined by the amplitude regulator. Substituting the derivatives (Equations 3.38c and 3.38d) into Equation 3.37 and collecting the trigonometric coefficients yields

$$0 = \left(\left(\ddot{A} - (1+\dot{\varphi})^2 A \right) + \frac{\dot{A}}{Q} + A + \frac{3}{4}\tilde{k}_3 A^3 - \frac{4K_{f,A}}{\pi} V_A \frac{\dot{A}}{A} \right) \sin(\tau+\varphi)$$
$$+ \left(\left(\ddot{\varphi}A + 2\dot{A}(1+\dot{\varphi}) \right) + \frac{(1+\dot{\varphi})A}{Q} - \frac{4K_{f,A}}{\pi} V_A(1+\dot{\varphi}) \right) \cos(\tau+\varphi)$$

(3.39)

Since this system is assumed to be slowly varying, the first derivatives of both the amplitude and phase will be quite small. Therefore, in this equation, second derivatives and products of first derivatives may be neglected. For lightly damped systems, $1/Q$ will be very small, as will $K_{f,A}$. Neglecting second derivatives, products of first derivatives, and products between first derivatives and $1/Q$ or $K_{f,A}$, leads to the simplified result[2]

$$0 = \left(-2\dot{\varphi}A + \frac{3}{4}\tilde{k}_3 A^3 \right)\sin(\tau+\varphi) + \left(2\dot{A} + \frac{A}{Q} - \frac{4K_{f,A}}{\pi} V_A \right)\cos(\tau+\varphi) \quad (3.40)$$

Setting the coefficients of the trigonometric terms equal to zero and using the definition of V_A from Equation 3.38a yields

$$\dot{\varphi} = \frac{3}{8}\tilde{k}_3 A^2 \tag{3.41}$$

$$\dot{A} + \frac{1}{2Q}A = \frac{2K_{f,A}}{\pi} V_A \tag{3.42}$$

$$\ddot{A} + \left(\frac{1}{2Q} + \frac{4K_P K_s K_{f,A}}{\pi^2} \right)\dot{A} + \frac{4K_I K_s K_{f,A}}{\pi^2} A = \frac{2K_{f,A}K_I}{\pi} V_{ref} \tag{3.43}$$

Equation 3.41 is exactly the solution that is expected for the change in frequency due to the cubic spring, as shown in Section 2.1.3, and it is valid for all values of V_A. The next two equations describe the growth of the amplitude of the limit cycle once the self-

---

[2]These assumptions were verified by simulating and comparing both Equations 3.39 and 3.40.

exciting electronics have locked onto the resonant frequency. Equation 3.42 is used when the control voltage V_A exceeds the saturation limits of 0 Volts and 10 Volts. For V_A less than 0 Volts, V_A is held at zero by the negative supply voltage, and the amplitude decays exponentially from its present value towards zero with time constant $2Q$. For V_A greater than 10 Volts, V_A is 10 Volts, and the amplitude decays as $(1-e^{(-t/\tau)})$ from its present value to the value defined by the right hand side of Equation 3.42. For $0<V_A<10$ Volts, the second-order response of Equation 3.43 may be used. By numerically integrating these equations and Equation 3.38a, and by including the saturation limits for V_A, the behavior of the amplitude during startup may be determined.

3.2.2.1 Simulation of Amplitude Regulator Loop

Typical responses of the amplitude regulator loop components are shown in Figures 3.7 through 3.10 for a Q of 150,000. The amplitude of the oscillation is plotted in Figure 3.7. Here, it is clear that there are three distinct regions of operation, which are defined by the value of V_A. In the steady-state, the amplitude does reach the desired value of 1. The corresponding control voltage is plotted without and with the saturation limits in Figures 3.8a and 3.8b, respectively. The nominal steady-state value for V_A occurs when the applied force is equal and opposite to the damping force and the time derivative of the amplitude is zero,

$$V_{A,ss} = \frac{\pi}{4QK_{f,A}}$$

(3.44)

This yields a nominal value of 0.196 Volts. In Figure 3.8, the simulated, unsaturated, steady-state value is 0.204 Volts. The saturated control voltage is shown in Figure 3.9. In Region 1, V_A is 10 Volts, and the amplitude increases rapidly. When the amplitude exceeds 1, V_A begins to decrease, and soon becomes negative, saturating to a value of 0 Volts. In Region 2, the overshoot of the response decays exponentially towards zero with time constant $2Q$. When the amplitude falls below 1, the control voltage becomes positive, but less than 10 Volts. In Region 3, the amplitude behaves according to the second-order system of Equation 3.43, which has a steady-state amplitude of 1. The frequency of the limit cycle oscillation, $\dot{\varphi}$, is plotted in Figure 3.10. Since the resonant frequency is a function of the amplitude squared, its appearance is similar to Figure 3.7. The three regions of amplitude behavior can now be examined in more detail.

In Region 1, the amplitude is quickly driven past the desired value of 1, since the error between the reference voltage and preamplifier voltage is quite large, and the control voltage has saturated. In this region, the time constant is $2Q$, and the amplitude

grows as $51(1-e^{(-t/2Q)})$, where 51 is the magnitude of the right-hand side of Equation 3.42. The control signal shoots rapidly to the saturation value of 10 Volts, resulting in the maximum drive force, i.e. overforcing. Despite the slow time constant, the amplitude exceeds 1 in 0.047 seconds. Once the proof mass amplitude is greater than the reference amplitude, the control voltage decreases because the error is less than zero. The control voltage will briefly re-enter the linear region of controller before becoming negative and saturating to an output of zero. As V_A decreases, the amplitude continues to grow, hence the overshoot of the desired amplitude of unity in Region 1.

Region 2 begins at about 0.1 seconds, with the negative control voltage saturating to zero Volts. Here, the amplitude decays with a time constant of $2Q$ from a peak of 1.4 to a nearly steady-state value of one. At about 1.1 seconds, the amplitude is at 0.9. Throughout this region, no force is applied by the closed loop; it simply permits the free decay of the oscillator amplitude towards 1. The amplitude undershoots the steady-state value because the amplitude continues to decay while V_A is increasing towards zero.

In Region 3, the amplitude increases towards a steady-state value of one as the second-order system in Equation 3.43. The amplitude and control voltage for Region 3 are shown in Figures 3.11 and 3.12, respectively. The amplitude is the sum of an exponential of the form $(1-e^{(-t/\tau)})$ with an exponentially decaying sinusoid. Because the control voltage is a function of the amplitude, it is also an exponentially decaying sinusoid. In the steady-state, the amplitude is 1, and the control voltage is 0.204 Volts.
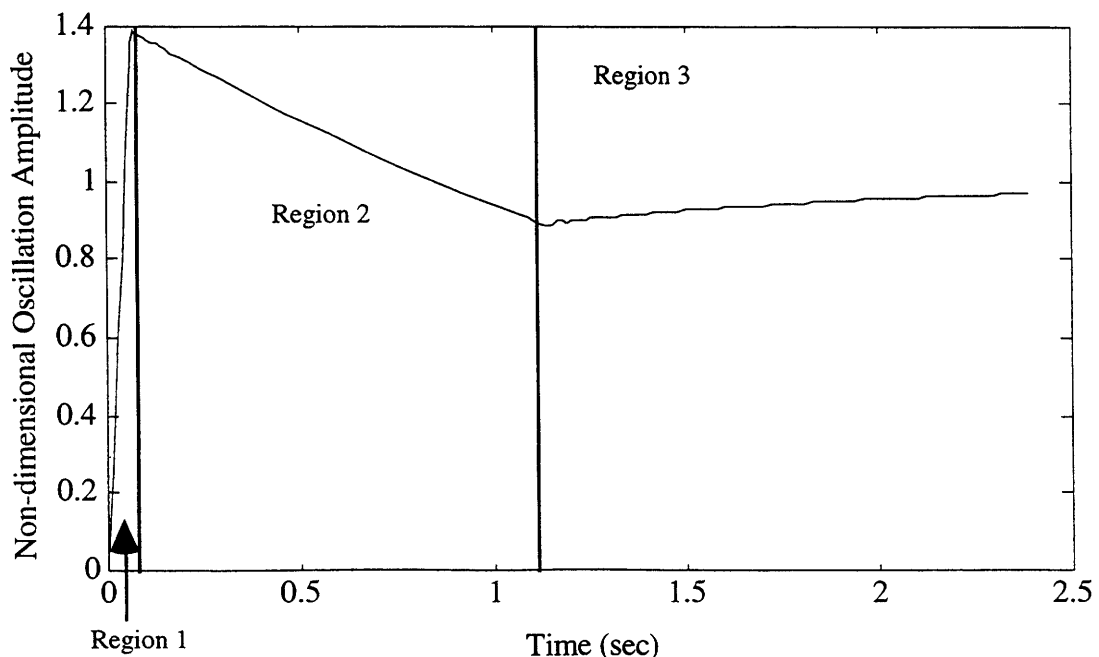
Figure 3.7. Displacement Response of Amplitude Regulator

92
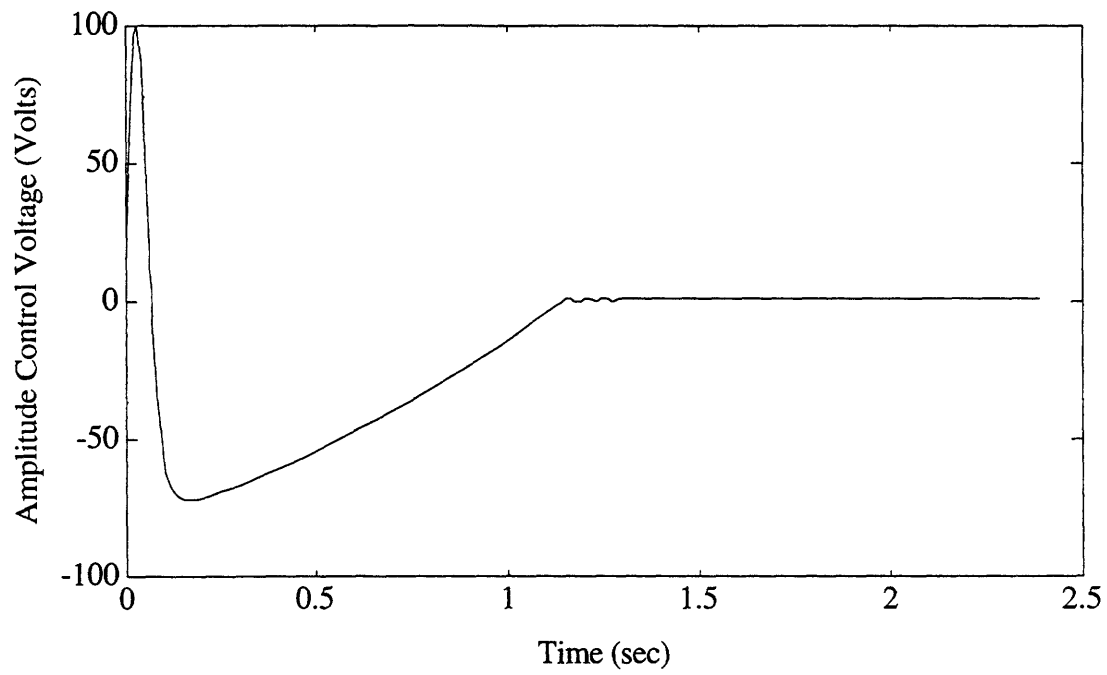
Figure 3.8. Control Voltage for Amplitude Regulator
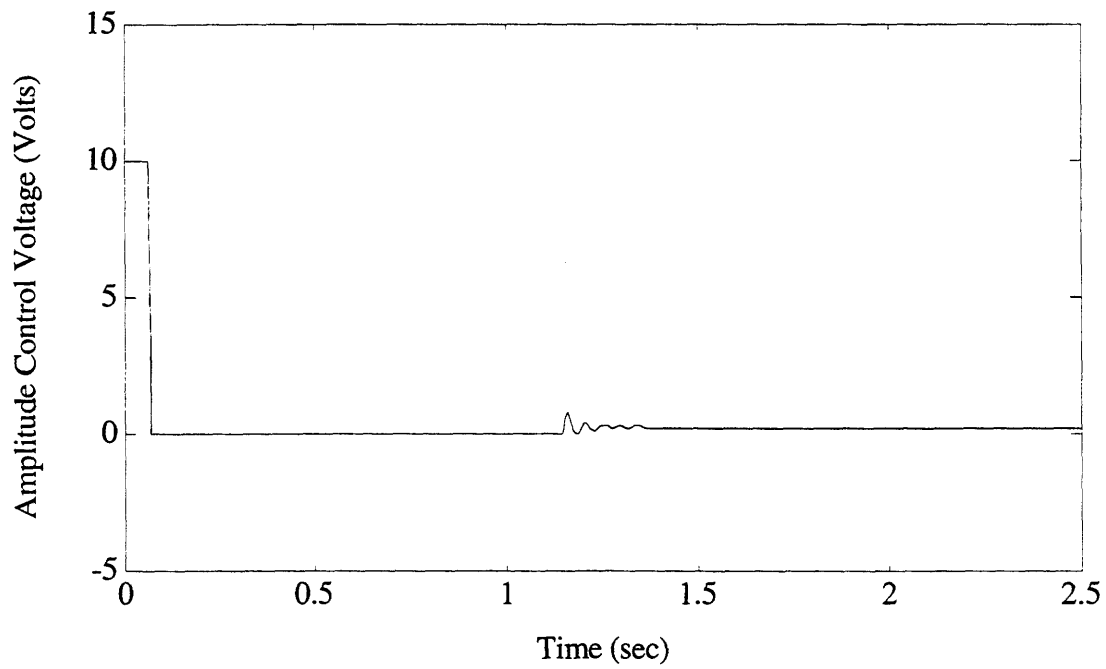
Figure 3.9. Saturated Control Voltage for Amplitude Regulator

93
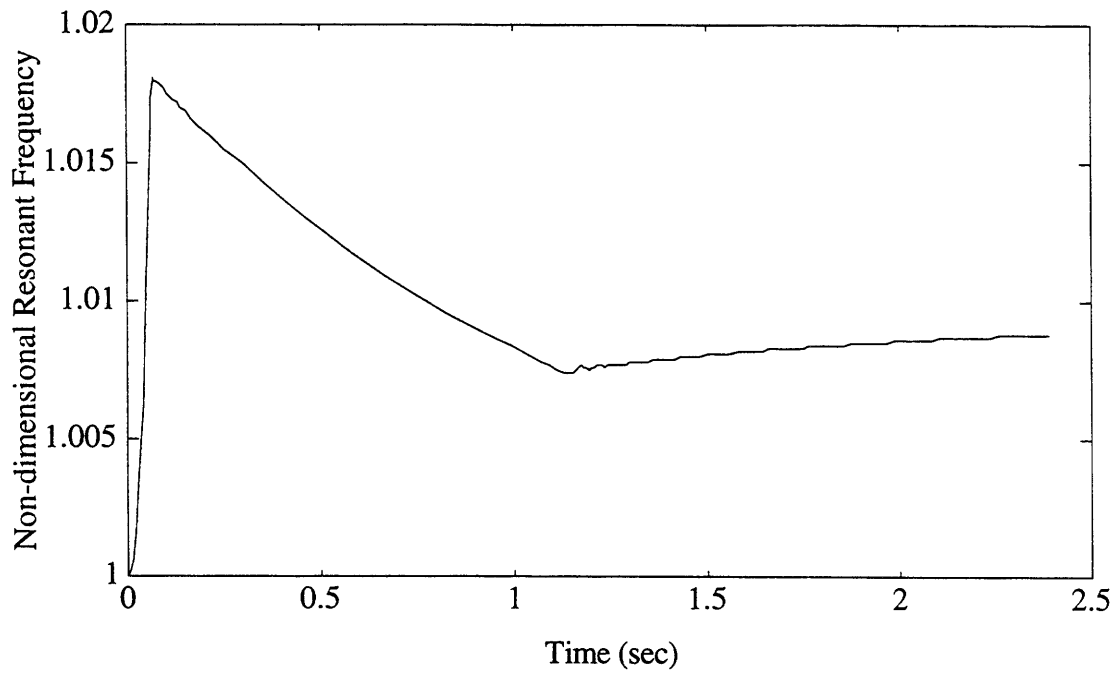
Figure 3.10. Resonant Frequency of Oscillator During Startup
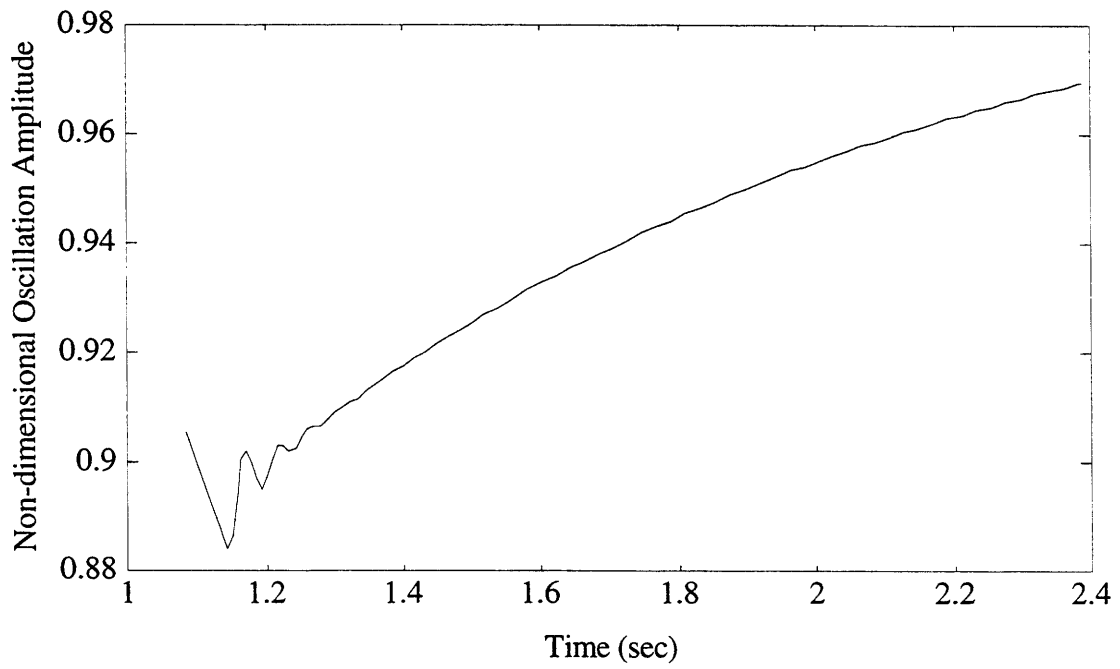
Figure 3.11. Amplitude of Oscillation in Region 3

94
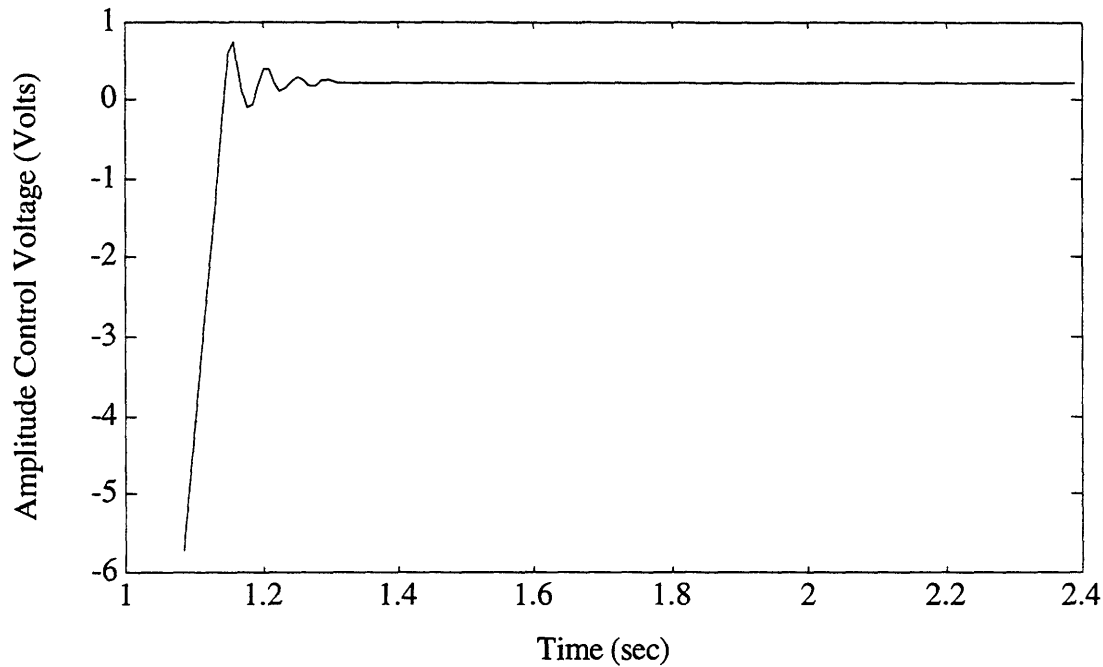
Figure 3.12. Amplitude Control Voltage in Region 3

If the Q of the system is reduced, then the system will reach steady-state quicker. Figures 3.13 through 3.16 show the amplitude and control voltage for a Q of 30,000 for all three regions and for Region 3. Here, the system reaches the desired steady-state amplitude of 1 and a control voltage[3] of 0.979. Since there is more damping in this example, the amplitude decays more rapidly towards its steady-state value. The three regions of operation still exist, but both Regions 2 and 3 are significantly shorter in time. Region 1 is nearly identical, but the maximum amplitude for Q = 30,000 is less than that for Q = 150,000. The results indicate that higher Q systems require more time to reach steady-state than lower Q systems, since the reduced damping makes the proof mass more sensitive to changes in the applied force. However, the lower Q needs more control voltage to generate a larger force, and the smallest Q for which a 10 μm amplitude is feasible is about 3000, at which point the control voltage is 10 Volts, and the control electronics have saturated.

---

[3] The lower Q requires more voltage to maintain a given amplitude.
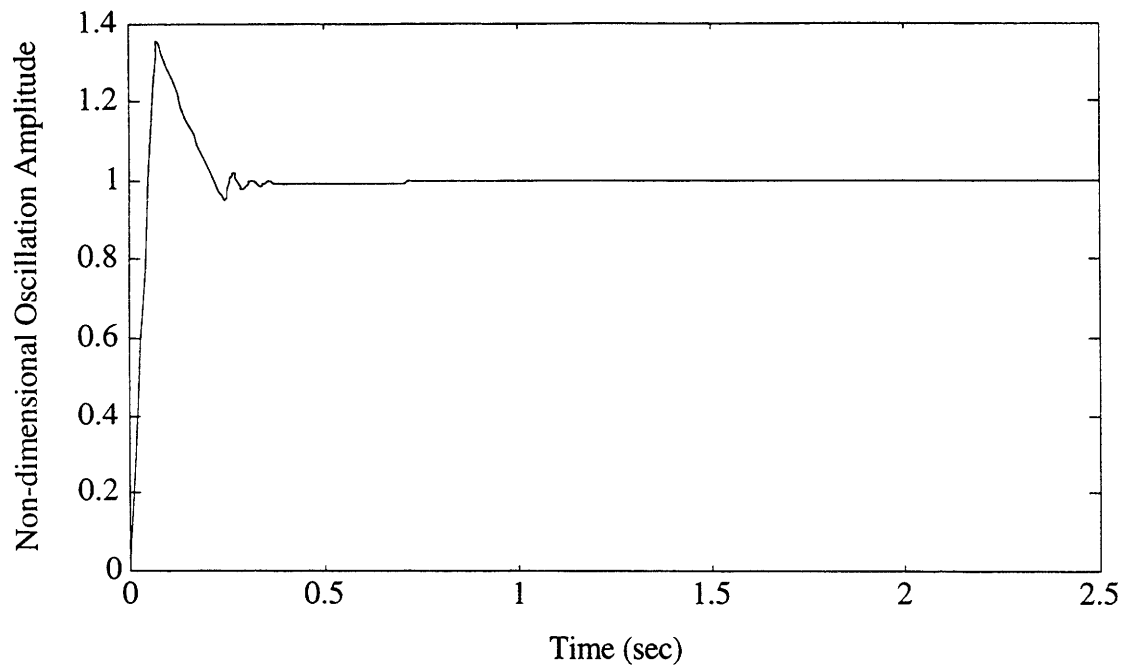
Figure 3.13. Amplitude of Startup with Lower Q
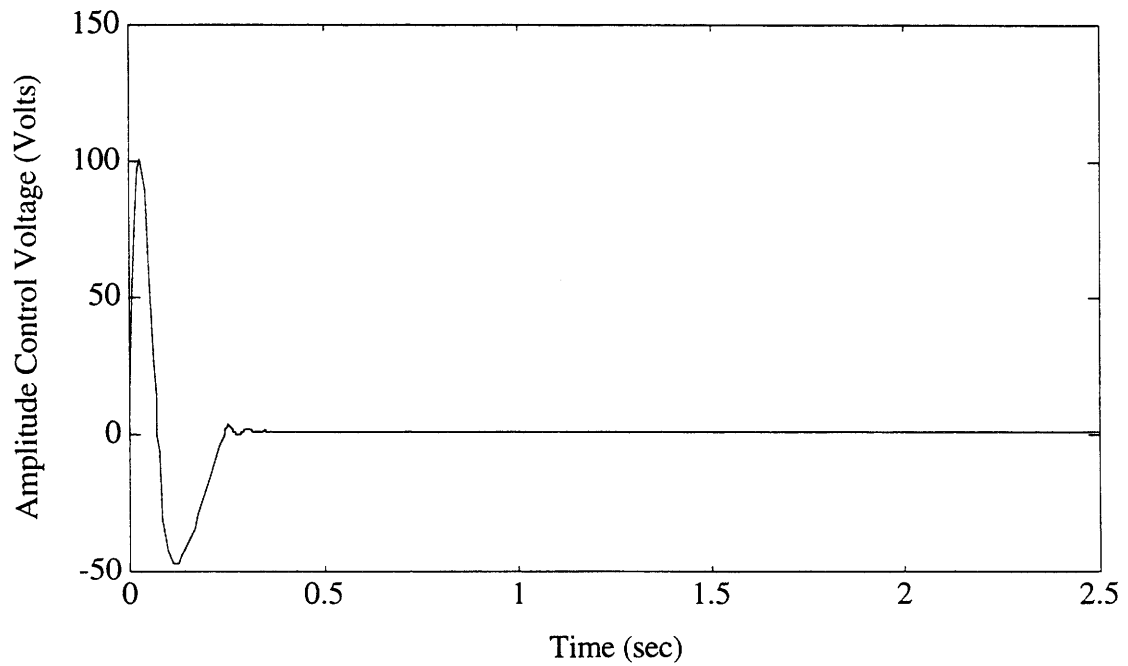
Figure 3.14. Amplitude Control Voltage for Lower Q
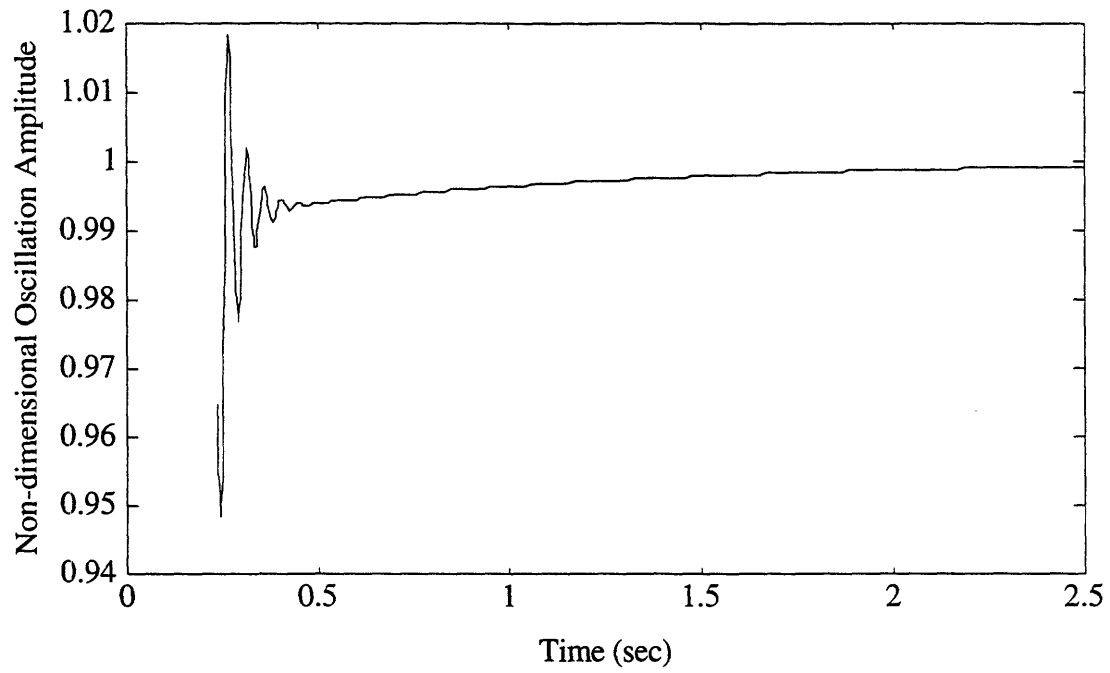
Figure 3.15. Oscillation Amplitude for Lower Q in Region 3
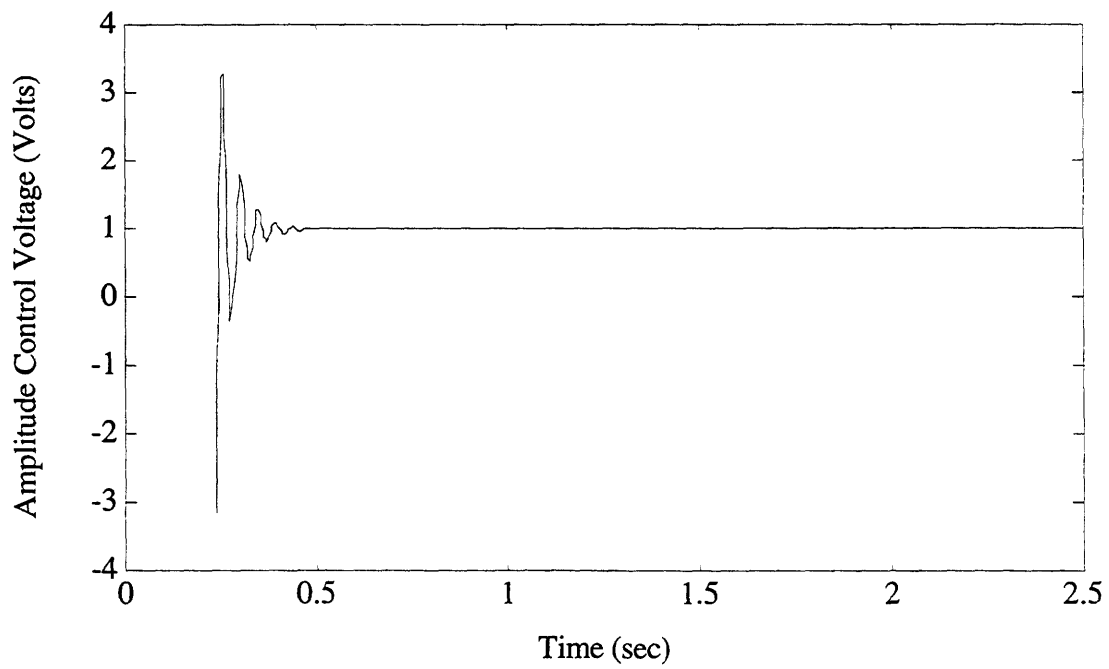
Figure 3.16. Amplitude Control Voltage for Lower Q in Region 3

97

The oscillation amplitude of the reduced-Q example enters Region 3 in about 0.25 seconds, instead of the nearly 1 second required for a higher Q. For the lower-Q case, the amplitude has a rapidly decaying sinusoidal response for less than 0.25 seconds, and the amplitude is with 0.5% of its steady-state value in 0.5 seconds, compared to almost 3 seconds for the higher-Q example. The control voltage is also at its steady-state value in 0.5 seconds, but it overshoots the steady-state value by 2 Volts, compared to about 0.6 Volts in the first example. Although the lower-Q amplitude reaches steady-state faster, the control voltage has more overshoot and a larger steady-state value. One significant trade-off in designing low pressure resonators is startup time versus the magnitude and overshoot of the control voltage.

3.2.3 Electronics Operation

The self-starting electronics operate in the following manner. At initial turn-on, the oscillator is at rest, and the pre-amplifier output is broadband noise, as shown in Figure 3.17. This noise passes through the gain stage, the 90° phase shifter, and the hard limiter; it is simultaneously passed through the absolute value and low-pass filter. The low-pass filter output is compared to a reference voltage, and the resulting error is integrated in the automatic gain control (AGC) stage.
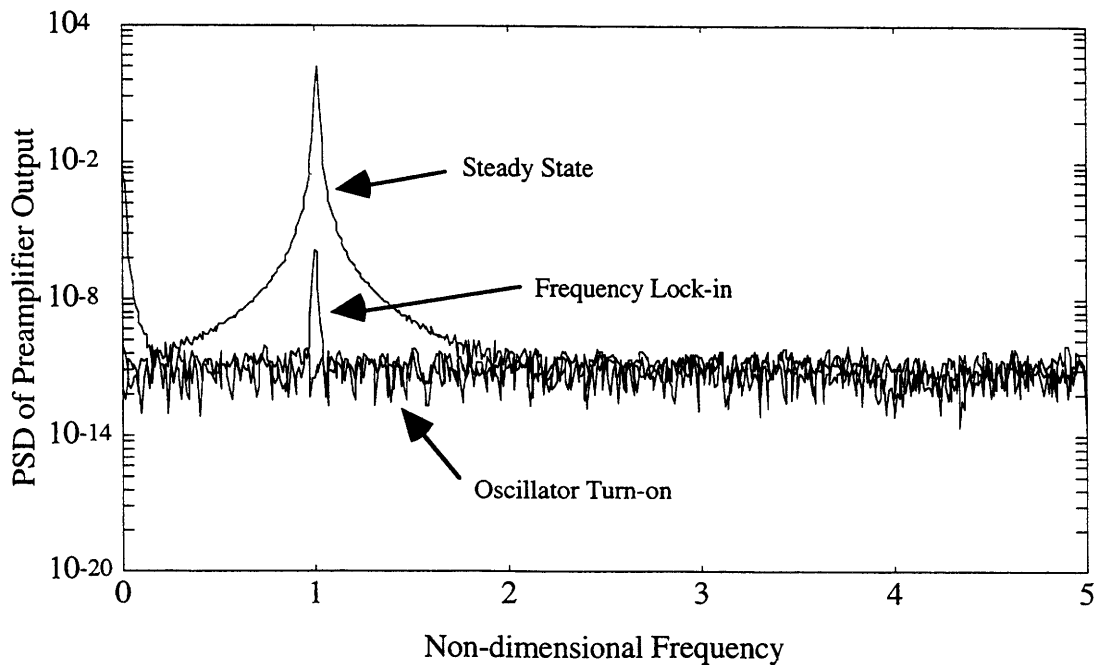
Figure 3.17. PSD of Preamplifier Output During Oscillator Startup

At startup, the only input to the amplitude regulator is noise, so the resulting error is quite large, causing the drive voltage to reach its positive limit. This value is then added to the output of the hard limiter, which in turn is applied to the drive comb of the oscillator. Through the interaction of the combs, a force proportional to the voltage squared is generated. At this point, the force is the largest possible, and the voltage spectrum is broad band. However, since the oscillator is a very high-Q system, the noise around the resonant frequency of the oscillator is amplified, and higher frequencies are attenuated. This output signal is then integrated and amplified.

Because of the high-Q, the output signal is concentrated at the natural frequency, and the oscillation of the SEO grows, as shown in Figure 3.17. This growth continues until the output from the oscillator is large enough that the hard limiter begins to switch back and forth at the resonant frequency of the oscillator; frequency lock-in [37]. Once this happens, the amplitude control loop varies the DC voltage until the error between the position signal amplitude and the reference voltage is zero, as discussed in Section 3.2.2. Now the oscillator may be considered to be in steady-state operation.

In Figure 3.17, a system with an assumed cubic spring nonlinearity of 2.5% is shown. This results in a shift of the non-dimensional resonant frequency by 9.375×10^{-3}. The dominant signal in both loops is the sinusoidal position signal. The noise from the pre-amplifier, crucial for exciting the oscillator, may now be neglected in the analysis of the steady-state behavior of the loops.

3.3 Determination of Limit Cycles

In Section 3.2, the two loops of the micromechanical resonator were examined. In that analysis, it was assumed that a limit cycle could be established. Here, the existence of a limit cycle is demonstrated. It is then shown that this oscillation is stable for all linear and hard spring systems. Finally, a perturbation analysis is performed to determine the response of the closed loop to possible variations in the system parameters.

3.3.1 Nonlinear State-Space Model of Oscillator Loop

In order to determine whether or not a limit cycle exists in the single element oscillator, a nonlinear representation of the motor loop is necessary [34]. A simplified version of Figure 3.4 is shown in Figure 3.18.
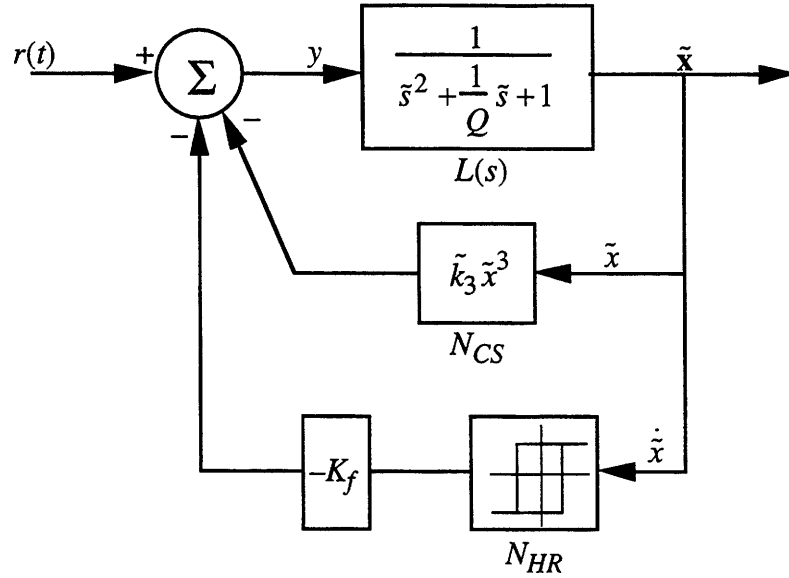
Figure 3.18. Simplified Motor Axis Control Loop

This limit cycle loop does not include the amplitude regulator because it is assumed to have no effect on the oscillation of the system when reasonable steady-state amplitudes are commanded, i.e., no greater than 15 microns. The amplitude regulator affects the magnitude of $\tilde{K}_f$, not its sign[4]. It will be shown that the magnitude of $\tilde{K}_f$ is not critical to the stability of the system. In this figure, there are two nonlinear elements: the cubic spring, whose output depends on the displacement of the proof mass, $\tilde{x}$; and the hysteretic relay, whose output varies with the velocity of the proof mass[5], $\dot{\tilde{x}}$. The minus sign on the outer feedback loop constant gain is necessary to make the applied force in-phase with the velocity, not 180° out of phase. The input to the linear oscillator plant for a non-dimensional frequency, $L(\tilde{s})$, can be approximated as

$$y = \tilde{K}_f N_{HR} \dot{\tilde{x}} - N_{CS} \tilde{x} \tag{3.45}$$

where,

N_{HR} = describing function of hysteretic relay (Equation 3.15)

N_{CS} = describing function of cubic spring (Equation 3.10), and

$\tilde{K}_f$ = non-dimensional forcing constant (for a non-dimensional amplitude of 1).

The closed-loop differential equation for the self-excitation loop may be expressed as

$$\ddot{\tilde{x}} + \frac{\dot{\tilde{x}}}{Q} + \tilde{x} = \tilde{K}_f N_{HR} \dot{\tilde{x}} - N_{CS} \tilde{x} \tag{3.46}$$

[4]The tilde is added to K_f to signify that, in the following sections, this constant is non-dimensional.

[5]In practice, the displacement is integrated, gained by -1 and fedback. From an electronics viewpoint, this is a better approach. For a non-dimensional sinusoidal system, this will yield a signal that has the same magnitude and phase as the velocity signal. Therefore, in this analysis, the velocity signal is used directly.

100

where $Q \gg 1$, so that the system may be considered lightly damped[6]. This system may then be expressed in state-space form with $y_1 = \dot{\tilde{x}}$, $y_2 = \tilde{x}$,

$$\frac{d}{d\tau}\begin{bmatrix} y_1 \\ y_2 \end{bmatrix} = -\begin{bmatrix} \dfrac{1}{Q} - \tilde{K}_f N_{HR} & 1 + N_{CS} \\ -1 & 0 \end{bmatrix}\begin{bmatrix} y_1 \\ y_2 \end{bmatrix} \tag{3.47}$$

To solve this system of equations, define

$$y_1 = A_1 \sin(\tilde{\omega}\tau + \theta_1) \tag{3.48a}$$

$$y_2 = A_2 \sin(\tilde{\omega}\tau + \theta_2) \tag{3.48b}$$

where $\tilde{\omega}$ is some non-dimensional frequency and τ is a non-dimensional time. It is assumed for now that A_1 and A_2 are independent. It will be shown shortly that these amplitudes are related through differentiation. For this assumed solution, let $\theta_2 = 0°$, i.e., the displacement will be used as the reference signal. Inserting Equations 3.48a and 3.48b into Equation 3.47 yields the coupled equations

$$A_1\tilde{\omega}\cos(\tilde{\omega}\tau + \theta_1) = -\left(\frac{1}{Q} - \tilde{K}_f N_{HR}\right)A_1 \sin(\tilde{\omega}\tau + \theta_1) - (1 + N_{CS})A_2 \sin(\tilde{\omega}\tau) \tag{3.49a}$$

$$A_2\tilde{\omega}\cos(\tilde{\omega}\tau) = A_1 \sin(\tilde{\omega}\tau + \theta_1) \tag{3.49b}$$

Examination of Equation 3.49b leads to the solutions

$$\theta_1 = \frac{\pi}{2}$$
$$A_1 = \tilde{\omega}A_2 \tag{3.50}$$

The solution for A_1 is expected since the derivative of y_2 is equal to y_1. Inserting θ_1 and the describing functions determined in Section 3.1 into Equation 3.49a and expanding the trigonometric terms with standard identities yields the following two equations for the coefficients of $\cos(\tilde{\omega}\tau)$ and $\sin(\tilde{\omega}\tau)$, respectively:

$$0 = -\frac{A_1}{Q} + \frac{4\tilde{K}_f}{\pi}\sqrt{1 - \left(\frac{\tilde{\delta}}{A_1}\right)^2} \tag{3.51a}$$

$$-A_1\tilde{\omega} = -A_2 - \frac{3}{4}\tilde{k}_3 A_2^3 + \frac{4\tilde{K}_f}{\pi}\frac{\tilde{\delta}}{A_1} \tag{3.51b}$$

where,

---

[6] It will therefore meet the filter hypothesis requirement for describing function analysis.

$$\tilde{\delta} = \frac{C_{fb}}{g_1 \frac{\partial C}{\partial x} V_{bs} x_0} \delta.$$

By manipulating these equations, solutions for A_1, A_2, and $\tilde{\omega}$ may be derived:

$$A_1^2 = 8\left(\frac{\tilde{K}_f Q}{\pi}\right)^2 \left(1 \pm \sqrt{1 - \left(\frac{\pi \tilde{\delta}}{2 K_f Q}\right)^2}\right) \tag{3.52a}$$

$$A_2^2 = \frac{2}{3\tilde{k}_3}\left((\tilde{\omega}^2 - 1) \pm \sqrt{(1 - \tilde{\omega}^2)^2 + \frac{12\tilde{\delta}\tilde{K}_f \tilde{k}_3}{\pi\tilde{\omega}}}\right) \tag{3.52b}$$

$$\tilde{\omega} = \frac{A_1}{A_2} \tag{3.52c}$$

Assuming $\delta^2 \ll 1$ and $\delta/Q \ll 1$ and requiring a non-dimensional steady-state amplitude of 1 for A_1 yields the real, non-trivial solutions

$$\tilde{K}_f = \frac{\pi}{4Q} \tag{3.53}$$

$$A_1^2 = 1 \tag{3.54a}$$

$$A_2^2 = \frac{2\left(\sqrt{1 + 3\tilde{k}_3} - 1\right)}{3\tilde{k}_3} \tag{3.54b}$$

$$\tilde{\omega}^2 = \frac{1}{2}\left(1 + \sqrt{1 + 3\tilde{k}_3}\right) \tag{3.54c}$$

For $\tilde{k}_3 \ll 1$, these solutions may be approximated by Taylor series expansions as

$$A_1 = 1 \tag{3.55a}$$

$$A_2 \approx 1 - \frac{3}{8}\tilde{k}_3 \tag{3.55b}$$

$$\tilde{\omega} \approx 1 + \frac{3}{8}\tilde{k}_3 \tag{3.55c}$$

These are the steady-state values for the limit cycle. The amplitude of the oscillation is A_2 and the frequency of the oscillation is $\tilde{\omega}$. Here, A_2 is nearly 1, and $\tilde{\omega}$ has been increased by the hard spring, as predicted in Sections 2.1.3 and 3.1.2.

As mentioned earlier, amplitude regulation is not considered here. If it was, then the ratio of the steady-state velocity and position amplitudes must be equal to the ratio of A_1 to A_2 in order to satisfy the limit cycle condition. The amplitude is controlled by

changing the value of $\tilde{K}_f$, which appears in the solution for A_1, which in turn affects the amplitude A_2.

If these solutions are inserted into the original nonlinear state-space equation, then, for small $\tilde{\delta}$, the eigenvalues of the system are

$$\lambda \approx \pm j\left(1 + \frac{3}{8}\tilde{k}_3\right)$$ (3.56)

which are purely imaginary, and an oscillation will exist. The open-loop small-amplitude eigenvalues of this system are

$$\lambda = -\frac{1}{2Q} \pm j\sqrt{1 - \frac{1}{4Q^2}}$$ (3.57)

Therefore, by closing the loop on this system with the hysteretic relay, the poles are moved from a complex left-half-plane pair to a purely imaginary pair.

3.3.2 Graphical Solution to Limit Cycle

The steady-state limit cycle for Figure 3.18 may also be found by examining the magnitude-phase plots for both the linear and nonlinear elements. The characteristic equation of the system is

$$1 + L(\tilde{s})\left[-\tilde{s}\tilde{K}_f N_{HR}(A,\tilde{\omega}) + N_{CS}(A,\tilde{\omega})\right] = 0$$ (3.58)

where A and $\tilde{\omega}$ describe the amplitude and frequency of the horizontal sinusoidal motion. This equation must hold true at the location of a limit cycle. Hence, a limit cycle exists when

$$L(\tilde{s}) = -\frac{1}{N_{CS}(A,\tilde{\omega}) - j\tilde{\omega}\tilde{K}_f N_{HR}(A,\tilde{\omega})}$$ (3.59)

If the functions on both sides of the equation are plotted in a magnitude-phase diagram, then limit cycles would exist at the intersections of these curves.

It is clear that the linear transfer function depends on the frequency of the oscillation. However, it is not as obvious that the nonlinear transfer function only depends on the amplitude of the oscillation. This is true because the input to the hysteretic relay is the velocity of the proof mass, which has an amplitude equal to $A\tilde{\omega}$, and the describing function must be expressed in terms of this amplitude. By then rewriting the describing function as the product of a derivative and the hysteretic relay describing function, the $\tilde{\omega}$ in the denominator of the describing function will cancel that in the numerator from the

103

derivative, as will be shown in Section 3.3.3.1. The frequency term that remains both in the square root and in the imaginary term are both negligible because $\tilde{\delta}$ is assumed to be small. Numerical simulation verified that these frequency terms do not affect the conclusions drawn here, i.e., the nonlinear transfer function depends on amplitude only.

The linear transfer function $L(\tilde{s})$ and the negative inverse of the sum of the nonlinear elements (Equation 3.59) may be drawn on a magnitude-phase plot, as shown in Figure 3.19, where the solid line is the linear response and the dashed line is the nonlinear response. In this plot, the phase of the linear system changes dramatically from $0°$ to $-180°$ due to the high Q of the resonator. The nonlinear plot starts at $-90°$ for small amplitude and moves toward $-180°$ for increasing oscillation amplitude. From this plot, it is clear that there is only one limit cycle, since there is only one intersection of the two curves. The location of the limit cycle is shown in the expanded plot of Figure 3.20. The point of intersection $(A, \tilde{\omega})$ is very close to the values found in Section 3.3.1. For an assumed cubic spring constant of 0.025, the graphical and analytical locations of the limit cycle are shown in Table 3.2.

Table 3.2. Location of Stable Limit Cycle

Limit Cycle	Graphical	Analytical	Error
A	0.99	0.9906	0.06%
$\tilde{\omega}$	1.0091482	1.009375	0.02%

The errors between the graphical and analytical solutions are less than 0.1%, suggesting that the analytic approach provides a solution that is nearly identical to that of the graphical approach, but much more straightforward to compute. The narrow range of the phase (0.025°) in Figure 3.20 suggests that determining the exact location of the curve intersection can be very time consuming.

The stability of the limit cycle point may be determined graphically from Figure 3.20. If the $-1/N$ point is considered to be equivalent to the Nyquist critical point of -1, then stability of the limit cycle may be determined with Nyquist-like arguments. If the amplitude is increased from A to $(A + \Delta A)$, the location of the critical point will move to the left of the linear curve along the nonlinear curve. Using Nyquist arguments, it may be shown that the response to the perturbation is stable when the linear curve passes to the right of the critical point, i.e., it will not encircle the new critical point. If the linear curve is to the left of the equivalent critical point, then the system is unstable because it
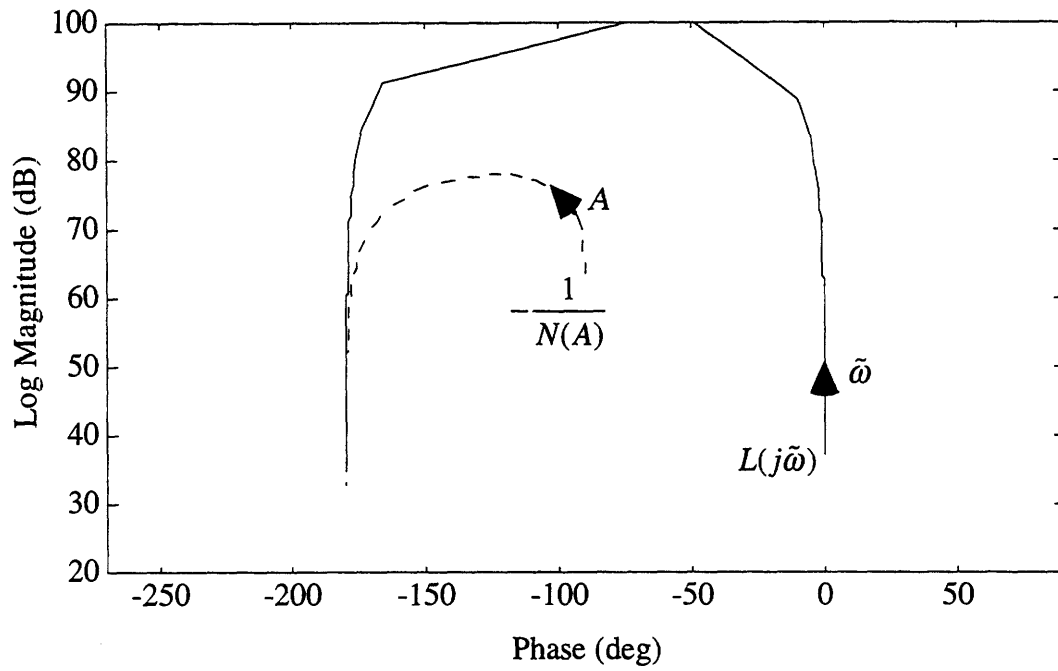
Figure 3.19. Graphical Limit Cycle Determination for Closed-Loop Oscillator
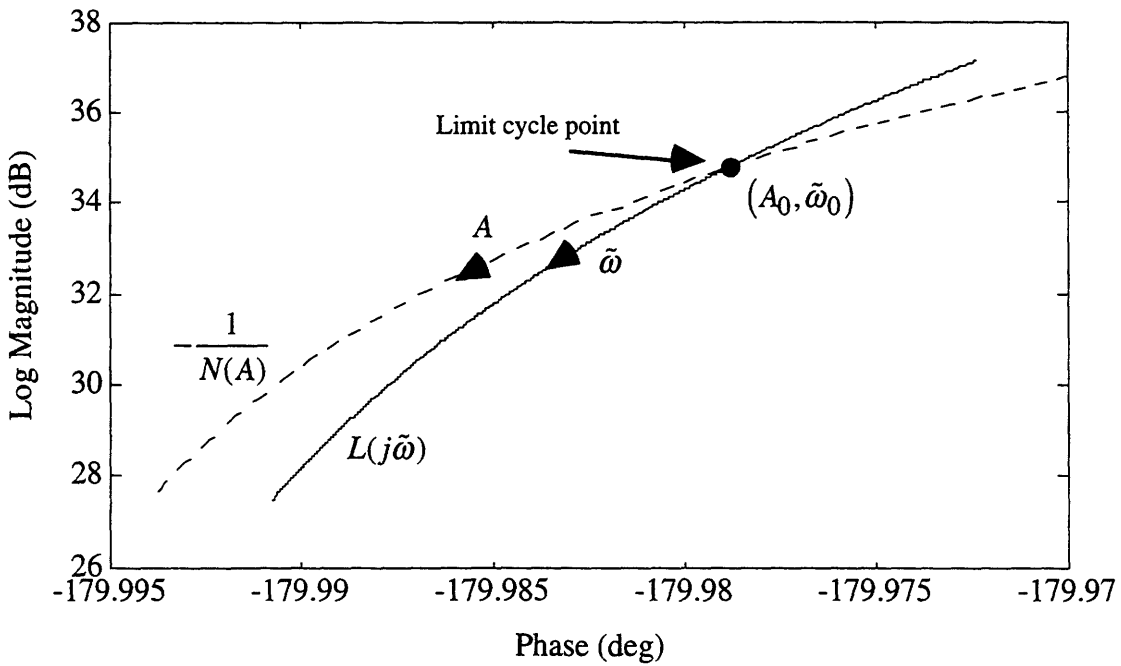
Figure 3.20. Limit Cycle Location for Closed-Loop Oscillator

105

encircles this critical point. Therefore, if the amplitude is increased, then the system is stable, and the amplitude will decay to the steady-state value. On the other hand, if the amplitude is decreased, then the system will be unstable, and the amplitude will grow until it returns to the steady-state value of $(A_0, \tilde{\omega}_0)$.

3.3.3 Stability Analysis of Oscillator Loop

Having determined that a limit cycle solution exists for the motor loop, the next step is to verify analytically the stability of this solution by examining the characteristic equation of the system,

$$1 + L(j\tilde{\omega}_0)\left[-j\tilde{\omega}_0 \tilde{K}_f N_{HR}(A_{10}, \tilde{\omega}_0) + N_{CS}(A_{20}, \tilde{\omega}_0)\right] = 0 \tag{3.60}$$

where A_{10}, A_{20}, and $\tilde{\omega}_0$ are the amplitudes (velocity and position, respectively) and frequency of the equilibrium limit cycle. The additional term of $j\tilde{\omega}_0$ is necessary because the input to this non-linearity is the derivative of position, and the relay describing function must be rewritten to derive the characteristic equation. It is helpful to make the substitution $A_1 = \tilde{\omega} A_2$ from Equation 3.52c, so that the characteristic equation is defined in terms of A_2 and $\tilde{\omega}$ only. Equation 3.60 can now be rewritten in complex form as

$$U(A_0, \tilde{\omega}_0) + jV(A_0, \tilde{\omega}_0) = 0 \tag{3.61}$$

where U and V may be found through straightforward manipulation of Equation 3.60 and A_0 now represents A_{20}. If A_0 and $\tilde{\omega}_0$ are perturbed slightly, such that

$$\begin{aligned} A_0 &\to A_0 + \Delta A \\ \tilde{\omega}_0 &\to \tilde{\omega}_0 + \Delta \tilde{\omega} + j\Delta\sigma \end{aligned} \tag{3.62}$$

where $\Delta\sigma = -\dot{A}/A$, then the stability of the steady-state limit cycle may be determined [13][7]. By first substituting these perturbations into Equation 3.61, then by performing a Taylor series expansion about the equilibrium point $(A_0, \tilde{\omega}_0)$, and finally by removing the quiescent terms (Equation 3.61), the first-order differential terms may be derived

$$\frac{\partial U}{\partial A}\Delta A + \frac{\partial U}{\partial \tilde{\omega}}(\Delta\tilde{\omega} + j\Delta\sigma) + j\frac{\partial V}{\partial A}\Delta A + j\frac{\partial V}{\partial \tilde{\omega}}(\Delta\tilde{\omega} + j\Delta\sigma) = 0 \tag{3.63}$$

where the partial derivatives are evaluated at the equilibrium point. To satisfy this equation, both the real and imaginary terms must equal zero. If $\Delta\tilde{\omega}$ is eliminated from

---

[7]In [13] page 122, "the perturbation of the rate of change of amplitude has been associated with the frequency term, a device which becomes clear upon thinking of the limit cycle in the form $A_0\exp(j\omega_0 t)$." In the next section, σ will be defined as the positive ratio of the rate of change of amplitude to the amplitude.

both of these terms, then a relationship for the stability of the equilibrium point is derived:

$$\left(\frac{\partial U}{\partial A}\frac{\partial V}{\partial \tilde{\omega}} - \frac{\partial U}{\partial \tilde{\omega}}\frac{\partial V}{\partial A}\right)\Delta A = \left[\left(\frac{\partial U}{\partial \tilde{\omega}}\right)^2 + \left(\frac{\partial V}{\partial \tilde{\omega}}\right)^2\right]\Delta\sigma \qquad (3.64)$$

In order for an oscillation to be stable, a positive change in ΔA must cause a positive change in $\Delta\sigma$, and, similarly, a negative change in ΔA must create a negative $\Delta\sigma$. From the definition of $\Delta\sigma$, this means that $\dot{A}$ must always vary in the opposite direction of A, i.e., drive A back towards its steady-state value. In order for this to be true, Equation 3.64 may be rewritten as the necessary condition:

$$\frac{\partial U}{\partial A}\frac{\partial V}{\partial \tilde{\omega}} - \frac{\partial U}{\partial \tilde{\omega}}\frac{\partial V}{\partial A} > 0 \qquad (3.65)$$

For the motor excitation loop of the SEO, the characteristic equation is, with the substitution for A_1 having been made,

$$1 - \tilde{\omega}_0^2 + \frac{j\tilde{\omega}_0}{Q} + \left[-\frac{4\tilde{K}_f}{\pi A_0}\left(j\sqrt{1-\left(\frac{\tilde{\delta}}{A_0\tilde{\omega}_0}\right)^2} + \frac{\tilde{\delta}}{A_0\tilde{\omega}_0}\right) + \frac{3}{4}\tilde{k}_3 A_0^2\right] = 0 \qquad (3.66)$$

Further manipulation of this equation yields the form of Equation 3.61, (i.e., $U+jV$) by using Equation 3.53 for $\tilde{K}_f$

$$\left[1 - \tilde{\omega}_0^2 + \frac{3}{4}\tilde{k}_3 A_0^2 - \frac{\tilde{\delta}}{A_0^2\tilde{\omega}_0 Q}\right] + j\left[\frac{\tilde{\omega}_0}{Q} - \frac{1}{A_0 Q}\sqrt{1-\left(\frac{\tilde{\delta}}{A_0\tilde{\omega}_0}\right)^2}\right] = 0 \qquad (3.67)$$

Inserting these values of U and V into the stability equation, and then substituting the steady-state limit cycle values of A_0 and $\tilde{\omega}_0$ (Equations 3.55b and 3.55c) yields the necessary condition for small $\tilde{k}_3$, large Q, and $\tilde{\delta}^2 \ll 1$,

$$2 + \frac{15}{4}\tilde{k}_3 > 0 \qquad (3.68)$$

which implies a stable system for $\tilde{k}_3 > -0.533$. As $\tilde{k}_3$ increases, this criterion is no longer valid because of the Taylor series approximation. It has been shown through numerical simulation that the stability criterion is met for all non-negative values of $\tilde{k}_3$, i.e., for all linear and hard springs. This is a conservative conclusion that acknowledges the

existence of an instability at some negative $\tilde{k}_3$ value[8]. In Figure 3.21, the stability criterion derived from Equation 3.67 is plotted for $\tilde{k}_3 \geq 0$, without a Taylor series approximation.
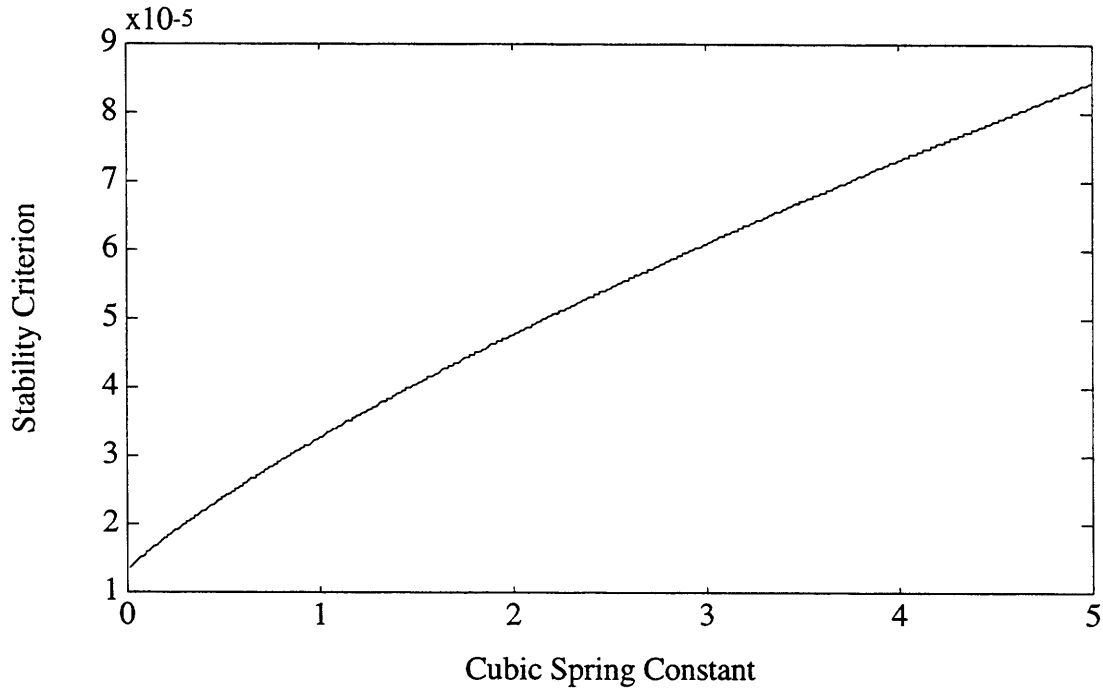
Figure 3.21. Stability Criterion for Closed-Loop Oscillation

This value is greater than zero for all positive $\tilde{k}_3$. Therefore, the closed-loop limit cycle is stable. It is interesting to note that the stability of the system does not depend on the quality factor. Therefore, pressure does not dictate the stability of the closed-loop drive axis. Since Q only appears in the denominator of the stability criterion and is positive, it only affects the magnitude of the criterion. Large Q will decrease the value of the test function, but will never force it to be less than zero. The value of the cubic spring is the only system parameter that determines closed-loop stability.

In practice, the amplitude of the oscillation is directly related to Q, and, as shown in Section 3.2.2, the system cannot reach the desired amplitude for Q less than 3000. However, the system may still maintain an oscillation at a degraded magnitude. At a sufficiently low Q, no oscillation can be maintained because the force cannot overcome the viscous damping, and the amplitude of the oscillation is of the same order as the noise. This occurs for Q on the order of 100.

[8]In this thesis, limit cycles are studied for hard springs only, the exact location and behavior of this instability are not examined in detail. This is a topic of future investigations.

3.3.3.1 An Alternative Approach to Stability Analysis

A second approach to the stability problem is to assume that the hysteretic relay nonlinearity also includes a 90° phase shift with the position signal as the input. The input to the hysteretic relay is the velocity of the proof mass, which has an amplitude of $A\tilde{\omega}$. However, in order to determine the characteristic equation, it is necessary to rewrite this nonlinearity so that its input is the position. The derivative, which is expressed as $\tilde{s}\tilde{x}$, may be written explicitly, as in Section 3.3.3, or incorporated implicitly into the describing function, as it is done here. In this case, the describing function is

$$N_{HRS}(A,\tilde{\omega}) = j\tilde{\omega}N_{HR}(A\tilde{\omega}) = \frac{4\tilde{\delta}}{\pi A^2 \tilde{\omega}} + j\frac{4}{\pi A}\sqrt{1-\left(\frac{\tilde{\delta}}{A\tilde{\omega}}\right)^2} \qquad (3.69)$$

where the subscript HRS represents the hysteretic relay with phase shift. The differences between this describing function and N_{HR} are that the signs of both terms of N_{HRS} are positive, and the imaginary term contains the square root. In Equation 3.69, the describing function depends on both the frequency and amplitude of the position, whereas, in Section 3.3.3, N_{HR} depended only on the amplitude of the velocity.

From Figure 3.18, the transfer function from y to $\tilde{x}$ is clearly $L(\tilde{s})$. Also, the time-domain relationship between x and y across the non-linearities is

$$y(t) = -\left[-\tilde{K}_f N_{HRS}(t) + N_{CS}(t)\right]\tilde{x}(t) \qquad (3.70)$$

These two relationships lead to the characteristic equation

$$1 + L(j\tilde{\omega})\left[-\tilde{K}_f N_{HRS}(A,\tilde{\omega}) + N_{CS}(A,\tilde{\omega})\right] = 0 \qquad (3.71)$$

By defining U and V as in Section 3.5.2 and following the procedure from above, the necessary condition for stability at the equilibrium point $(A_0, \tilde{\omega}_0)$ (Equation 3.55b and 3.55c) for small $\tilde{k}_3$, small $\tilde{\delta}$, and large Q is

$$2 + \frac{15}{4}\tilde{k}_3 > 0 \qquad (3.72)$$

Once again, as in Section 3.3.3, it can be shown that for positive $\tilde{k}_3$, the system is always stable. Therefore, either by using the describing function state-space approach or by redefining the non-linearity to have an input $\tilde{x}$, the motor loop has been shown to be stable for all linear and hard spring cases. The existence of an instability for a negative $\tilde{k}_3$ value is acknowledged, but not investigated, in this thesis.

3.3.4 Analysis of Transient Oscillations

The modification to the hysteretic relay to include a 90° phase shift was an important step towards a straightforward analysis of transient oscillations in the system. A transient oscillation is meant "to imply a function of time which is oscillatory in nature and which can be described as a sinusoid with slowly changing amplitude and frequency [13]". By performing this study, the behavior of the system for changes in its physical parameters can be better understood. Specifically, it would be quite useful to understand how the amplitude of the oscillation will vary with changes in the spring constants, damping, forcing, or hysteresis behavior of a micromechanical resonator.

If the shape of the output signal $\tilde{x}(t)$ is defined as

$$\tilde{x}(t) = A(t)e^{j\psi(t)} \tag{3.73}$$

then its time derivative is

$$\frac{d\tilde{x}}{dt} = \dot{A}e^{j\psi} + j\dot{\psi}Ae^{j\psi}$$

$$= \left(\frac{\dot{A}}{A} + j\dot{\psi}\right)Ae^{j\psi} \tag{3.74}$$

From here, a clever definition of variables leads to an elegant solution [13, p. 215]. Let

$$\sigma = \frac{\dot{A}}{A} \tag{3.75a}$$

$$\tilde{\omega} = j\dot{\psi} \tag{3.75b}$$

$$s = \sigma + j\tilde{\omega} \tag{3.75c}$$

where σ and $\tilde{\omega}$ both vary with time, and s is used as a variable [13]; *it is not a Laplace transform!* By using this new variable, the derivatives of x may be rewritten as

$$\frac{d\tilde{x}}{dt} = s\tilde{x} = \left(\sigma + j\tilde{\omega}\right)\tilde{x} \tag{3.76a}$$

$$\frac{d^2\tilde{x}}{dt^2} = s\dot{\tilde{x}} + \dot{s}\tilde{x}$$

$$= \left(s^2 + \dot{s}\right)\tilde{x} = \left(\sigma^2 - \tilde{\omega}^2 + 2j\sigma\tilde{\omega} + \dot{\sigma} + j\dot{\tilde{\omega}}\right)\tilde{x} \tag{3.76b}$$

Higher derivatives may be calculated in a similar fashion, but they are not necessary here. Also, time derivatives of the product Nx can be determined as

$$\frac{d(N\tilde{x})}{dt} = \left(Ns + \dot{N}\right)\tilde{x} \tag{3.77a}$$

$$\frac{d^2(N\tilde{x})}{dt^2} = Ns\dot{\tilde{x}} + N\dot{s}\tilde{x} + \dot{N}s\tilde{x} + \dot{N}\dot{\tilde{x}} + \ddot{N}\tilde{x}$$

$$= \left[N\left(s^2 + \dot{s}\right) + 2\dot{N}s + \ddot{N}\right]\tilde{x} \tag{3.77b}$$

This expansion will not be used in this thesis.

By inserting the definitions for the first and second derivatives from Equations 3.73 to 3.76 into Equation 3.46, and by replacing the describing function N_{HR} in Equation 3.46 with the describing function N_{HRS} of Equation 3.69, a complex equation is derived[9], which may be separated into real and imaginary parts:

$$R(\sigma,\tilde{\omega},A,\dot{\tilde{\omega}}) = \dot{\sigma} + 1 - \tilde{\omega}^2 + \sigma^2 + \frac{\sigma}{Q} + \frac{3}{4}\tilde{k}_3 A^2 - \frac{4\tilde{\delta}\tilde{K}_f}{\pi A^2 \tilde{\omega}} = 0 \tag{3.78a}$$

$$I(\sigma,\tilde{\omega},A,\dot{\tilde{\omega}}) = \dot{\tilde{\omega}} + \frac{\tilde{\omega}}{Q} + 2\tilde{\omega}\sigma - \frac{4\tilde{K}_f}{\pi A}\sqrt{1 - \left(\frac{\tilde{\delta}}{A\tilde{\omega}}\right)^2} = 0 \tag{3.78b}$$

This solution is a more general version of the slowly varying parameter approach of Krylov and Bogoliubov [17]. In Equations 3.78a and 3.78b, the dependencies on $\dot{\sigma}, \dot{\tilde{\omega}}$ and higher powers of σ have not been eliminated. By allowing $\tilde{\omega}_0$ to be non-zero and perhaps time varying, a wide range of dynamic systems can be studied.

3.3.4.1 Determination of Limit Cycle Values

Equations 3.78a and 3.78b are a more exact solution, and they will be used in the subsequent analysis. The quasi-static solution for this system may be found by setting σ and its derivatives and the derivatives of $\tilde{\omega}$ equal to zero in Equations 3.78a and 3.78b. Here the limit cycle quantities are

$$\tilde{\omega}^2 = \frac{1}{2}\left(1 + \sqrt{1 + 3\tilde{k}_3}\right) \tag{3.79a}$$

$$A^2 = \frac{2\left(\sqrt{1 + 3\tilde{k}_3} - 1\right)}{3\tilde{k}_3} \tag{3.79b}$$

which are identical to the solutions found in Equations 3.54b and 3.54c.

---

[9]Before making this substitution, the Laplace transform of the plant transfer function $L(s)$ should be rewritten in the time domain so that the derivatives are clearly seen.

3.3.4.2 Limit Cycle Amplitude Transients with Small-σ Analysis

The steady-state behavior of the perturbed limit cycle of this system can be approximated in order to examine the effects of disturbances on the system. If the amplitude and frequency are indeed slowly varying such that the changes over one period are very small, i.e.,

$$\frac{|\dot{A}|}{A}\frac{2\pi}{\tilde{\omega}} = 2\pi\frac{|\sigma|}{\tilde{\omega}} << 1$$

$$\frac{|\dot{\tilde{\omega}}|}{\tilde{\omega}}\frac{2\pi}{\tilde{\omega}} = 2\pi\frac{|\dot{\tilde{\omega}}|}{\tilde{\omega}^2} << 1$$

$$(3.80)$$

then the small-σ solution may be used to determine an approximate steady-state response to system variations [13]. The first step of this approach is to drop the derivatives of σ and $\tilde{\omega}$ and powers of σ greater than two in the equation of reals (Equation 3.75a). From this equation, solve for $\tilde{\omega}(\sigma, A)$ by substituting for Equation 3.53 $\tilde{K}_f$ and by assuming $\tilde{\delta}/Q << 1$,

$$\tilde{\omega}^2 = 1 + \frac{\sigma}{Q} + \sigma^2 + \frac{3}{4}\tilde{k}_3 A^2$$

$$(3.81)$$

Next, differentiate this expression with respect to time and drop the derivatives of σ to get a solution for $\dot{\tilde{\omega}}(\sigma, A)$,

$$\dot{\tilde{\omega}} = \frac{3\tilde{k}_3 \sigma A^2}{4\tilde{\omega}(\sigma, A)}$$

$$(3.82)$$

The derivatives of σ are neglected because, from Equation 3.80, σ is a small value, and it is assumed to be slowly varying, since it is a function of A.

Third, in the equation of imaginaries (Equation 3.75b), drop the derivatives of σ and the second and higher derivatives of $\tilde{\omega}$. Insert Equations 3.81 and 3.82 and then solve for σ(A). After the substitutions, the resulting equation is

$$(QA)^2\left[2\sigma^3 + \frac{3}{Q}\sigma^2 + 2\left(\frac{9}{8}\tilde{k}_3 A^2 + 1\right)\sigma + \frac{1}{Q}\left(1 + \frac{3}{4}\tilde{k}_3 A^2\right)\right]^2 = \tilde{\omega}^2$$

$$(3.83)$$

If this equation is then expanded and powers of σ greater than two are neglected, the quadratic equation for σ is

112

$$\left(\frac{81}{16}\tilde{k}_3^2 A^6 + 9\tilde{k}_3 A^4 + 4A^2 - \frac{1}{Q^2}\right)\sigma^2$$

$$+\left(\frac{27}{8}\tilde{k}_3^2 A^6 + \frac{15}{2}\tilde{k}_3 A^4 + 4A^2 - \frac{1}{Q^2}\right)\frac{\sigma}{Q} \quad (3.84)$$

$$+\frac{1}{Q^2}\left[\frac{9}{16}\tilde{k}_3^2 A^6 + \frac{3}{2}\tilde{k}_3 A^4 + A^2\left(1 - \frac{3}{4}\tilde{k}_3\right) - 1\right] = 0$$

Here, the quantity of interest is $\dot{A}$, which is equal to $A\sigma$. The solution to Equation 3.84 for small $\tilde{k}_3$ and $Q \gg 1$ may be expressed in terms of A as

$$\dot{A} = A\sigma = \frac{2}{Q}\frac{\sqrt{\left(3\tilde{k}_3 A^2 + 1\right)}}{\left(9\tilde{k}_3 A^2 + 4\right)} - \frac{A}{4Q}\frac{\left(15\tilde{k}_3 A^2 + 8\right)}{\left(9\tilde{k}_3 A^2 + 4\right)} \quad (3.85)$$

The Taylor series expansion of this solution is

$$\dot{A} = A\sigma = \frac{1}{2Q}(1 - A) \quad (3.86)$$

which, when plotted as $A\sigma$ vs. A, appears as a straight line. Because $\tilde{k}_3$ is small, there is very little difference between the series expansion and exact solutions for A near 1. The approximation of Equation 3.85 may be fitted to the curve

$$\dot{A} = mA + n \quad (3.87)$$

From here, the amplitude may be estimated from the exponential equation

$$A = 1 - e^{-\frac{t}{2Q}} \quad (3.88)$$

While this is an adequate approximation to the behavior of the amplitude in steady-state, it neglects one important aspect. In the startup sequence of the oscillator, the forcing coefficient $\tilde{K}_f$ is not a constant. When the amplitude of the proof mass is very small, the error between the actual and desired amplitudes is very large, generating much larger forces than the steady-state force assumed here. Therefore, this analysis is not useful for analyzing the startup of the resonator. However, the significance of this solution will become apparent in the next section, in which the time constant for the transfer functions between the amplitude or frequency and system parameters will also be $2Q$. A derivation of the startup model with an amplitude-varying forcing constant was performed in Section 3.2.2.

113

3.3.5 Limit Cycle Amplitude Variation

As a parameter in the system, such as the pressure, damping, spring constant, etc. changes, a transient variation is induced in the amplitude of the limit cycle. Since the SEO will be operating with an amplitude controller, it may be assumed that $\dot{A}$ will not depart very far from zero during steady-state operation. The time derivative of the amplitude may therefore be approximated as a linear function of the amplitude, i.e., [13]

$$\dot{A} = \left. \frac{d\dot{A}}{dA} \right|_{\dot{A}=0} (A - A_0) \tag{3.89}$$

for which the exponential solution has the time constant

$$\tau = -\left[\left. \frac{d\dot{A}}{dA} \right|_{\dot{A}=0} \right]^{-1} = -\left[A_0 \left. \frac{d\sigma}{dA} \right|_{\sigma=0} \right]^{-1} \tag{3.90}$$

which leads to a transfer function between a change in a parameter and the change in limit cycle amplitude [13]

$$\frac{\Delta A}{\Delta P} = \frac{(\Delta A/\Delta P)_{ss}}{\tau \tilde{s} + 1} \tag{3.91}$$

where both τ and $(\Delta A/\Delta P)_{ss}$ must be derived. If τ is positive, then the nonlinear system is stable, since variations in system parameters will generate exponentially decaying responses. A negative τ indicates an unstable limit cycle.

3.3.5.1 Derivation of Time Constant

In order to solve for the time constant, the real and imaginary terms from Equations 3.78a and 3.78b are needed to obtain $d\sigma/dA$. In a manner similar to the small-σ solution above, it is permissible to drop the derivatives of σ, the derivatives of $\tilde{\omega}$ of higher order than one, and the powers of σ greater than 1, such that

$$R\left(\sigma,\tilde{\omega},A,\dot{\tilde{\omega}}\right) = 0 = 1 - \tilde{\omega}^2 + \frac{3}{4}\tilde{k}_3 A^2 - \frac{4\tilde{\delta}\tilde{K}_f}{\pi A^2 \tilde{\omega}} \tag{3.92a}$$

$$I\left(\sigma,\tilde{\omega},A,\dot{\tilde{\omega}}\right) = 0 = \frac{\tilde{\omega}}{Q} + 2\tilde{\omega}\sigma + \dot{\tilde{\omega}} - \frac{4\tilde{K}_f}{\pi A}\sqrt{1 - \left(\frac{\tilde{\delta}}{A\tilde{\omega}}\right)^2} \tag{3.92b}$$

The first differentials of the real and imaginary equations, in general, are

114

$$\frac{\partial R}{\partial \sigma} d\sigma + \frac{\partial R}{\partial \tilde{\omega}} d\tilde{\omega} + \frac{\partial R}{\partial A} dA + \frac{\partial R}{\partial \dot{\tilde{\omega}}} d\dot{\tilde{\omega}} = 0 \qquad (3.93a)$$

$$\frac{\partial I}{\partial \sigma} d\sigma + \frac{\partial I}{\partial \tilde{\omega}} d\tilde{\omega} + \frac{\partial I}{\partial A} dA + \frac{\partial I}{\partial \dot{\tilde{\omega}}} d\dot{\tilde{\omega}} = 0 \qquad (3.93b)$$

The equation of reals may now be solved for $d\tilde{\omega}$, and the time derivative of the resulting equation may be written as

$$\dot{\tilde{\omega}} = \frac{d\tilde{\omega}}{dt} = -\left(\frac{\partial R}{\partial \tilde{\omega}}\right)^{-1}\left(\frac{\partial R}{\partial \sigma}\frac{d\sigma}{dt} + \frac{\partial R}{\partial A}\frac{dA}{dt} + \frac{\partial R}{\partial \dot{\tilde{\omega}}}\frac{d\dot{\tilde{\omega}}}{dt}\right)$$

$$= -\left(\frac{\partial R}{\partial \tilde{\omega}}\right)^{-1}\left(\frac{\partial R}{\partial A}A\sigma\right) \qquad (3.94)$$

where $\dot{\sigma}$ and $\ddot{\tilde{\omega}}$ have been neglected in these equations. In the steady-state ($\sigma = 0$), this equation becomes

$$d\dot{\tilde{\omega}} = -\left(\frac{\partial R}{\partial \tilde{\omega}}\right)^{-1}\frac{\partial R}{\partial A}A_0 d\sigma \qquad (3.95)$$

Equations 3.94 and 3.95 may be inserted into the equation of imaginaries (Equation 3.93b). This result may then be solved for $d\sigma/dA$

$$\frac{d\sigma}{dA} = -\frac{\dfrac{\partial I}{\partial A} - \dfrac{\partial I}{\partial \dot{\tilde{\omega}}}\left(\dfrac{\partial R}{\partial \tilde{\omega}}\right)^{-1}\dfrac{\partial R}{\partial A}}{\dfrac{\partial I}{\partial \sigma} - \dfrac{\partial I}{\partial \dot{\tilde{\omega}}}\left(\dfrac{\partial R}{\partial \tilde{\omega}}\right)^{-1}\dfrac{\partial R}{\partial A}A_0 - \dfrac{\partial I}{\partial \tilde{\omega}}\left(\dfrac{\partial R}{\partial \tilde{\omega}}\right)^{-1}\left[\dfrac{\partial R}{\partial \sigma} - \dfrac{\partial R}{\partial \dot{\tilde{\omega}}}\left(\dfrac{\partial R}{\partial \tilde{\omega}}\right)^{-1}\dfrac{\partial R}{\partial A}A_0\right]} \qquad (3.96)$$

which, when inserted into Equation 3.90, yields the time constant

$$\tau = \frac{\dfrac{1}{A_0}\dfrac{\partial I}{\partial \sigma} - \dfrac{\partial I}{\partial \dot{\tilde{\omega}}}\left(\dfrac{\partial R}{\partial \tilde{\omega}}\right)^{-1}\dfrac{\partial R}{\partial A} - \dfrac{\partial I}{\partial \tilde{\omega}}\left(\dfrac{\partial R}{\partial \tilde{\omega}}\right)^{-1}\left[\dfrac{1}{A_0}\dfrac{\partial R}{\partial \sigma} - \dfrac{\partial R}{\partial \dot{\tilde{\omega}}}\left(\dfrac{\partial R}{\partial \tilde{\omega}}\right)^{-1}\dfrac{\partial R}{\partial A}\right]}{\dfrac{\partial I}{\partial A} - \dfrac{\partial I}{\partial \tilde{\omega}}\left(\dfrac{\partial R}{\partial \tilde{\omega}}\right)^{-1}\dfrac{\partial R}{\partial A}} \qquad (3.97)$$

To find the steady-state time constant, the limit cycle values may be inserted: $\sigma = 0$, $\tilde{\omega} = \tilde{\omega}_0$, $A = A_0$, $\dot{\tilde{\omega}} = 0$. As will be shown in Section 3.3.5.3, the time constant is $2Q$, which has been demonstrated several times in this chapter. Therefore, this limit cycle is stable, confirming the conclusions of Section 3.3.3.

3.3.5.2 Amplitude-Parameter Transfer Functions

The steady-state amplitude/parameter relationships required for Equation 3.91 may be determined by evaluating the real and imaginary equations when $\sigma = 0$ and $\dot{\tilde{\omega}} = 0$. In this case, Equations 3.78a and 3.78b become functions of the amplitude A, the frequency $\tilde{\omega}$, and any system parameter P, where P may be chosen from the set of $[Q, \tilde{k}_3, \tilde{K}_f, \tilde{\delta}]$.

$$R(A, \tilde{\omega}, P) = 0 = 1 - \tilde{\omega}^2 + \frac{3}{4}\tilde{k}_3 A^2 - \frac{4\tilde{\delta}\tilde{K}_f}{\pi A^2 \tilde{\omega}} \qquad (3.98a)$$

$$I(A, \tilde{\omega}, P) = 0 = \frac{\tilde{\omega}}{Q} - \frac{4\tilde{K}_f}{\pi A}\sqrt{1 - \left(\frac{\tilde{\delta}}{A\tilde{\omega}}\right)^2} \qquad (3.98b)$$

The differential relating changes in P to changes in A may be written in a manner similar to that of Equations 3.90 and 3.90b

$$\frac{\partial R}{\partial A}dA + \frac{\partial R}{\partial \tilde{\omega}}d\tilde{\omega} + \frac{\partial R}{\partial P}dP = 0 \qquad (3.99a)$$

$$\frac{\partial I}{\partial A}dA + \frac{\partial I}{\partial \tilde{\omega}}d\tilde{\omega} + \frac{\partial I}{\partial P}dP = 0 \qquad (3.99b)$$

By eliminating $d\tilde{\omega}$ from these equations, the relationship between A and P may be expressed as

$$\frac{dA}{dP} = -\frac{\dfrac{\partial I}{\partial P} - \dfrac{\partial I}{\partial \tilde{\omega}}\left(\dfrac{\partial R}{\partial \tilde{\omega}}\right)^{-1}\dfrac{\partial R}{\partial P}}{\dfrac{\partial I}{\partial A} - \dfrac{\partial I}{\partial \tilde{\omega}}\left(\dfrac{\partial R}{\partial \tilde{\omega}}\right)^{-1}\dfrac{\partial R}{\partial A}} \qquad (3.100)$$

where the partial derivatives are evaluated in the steady-state, with $\sigma = 0$ and all derivatives of σ and $\tilde{\omega}$ equal to zero. Additionally, the relationship between the limit cycle frequency $\tilde{\omega}$ and P may be expressed as

$$\frac{d\tilde{\omega}}{dP} = -\frac{\dfrac{\partial I}{\partial P} - \dfrac{\partial I}{\partial A}\left(\dfrac{\partial R}{\partial A}\right)^{-1}\dfrac{\partial R}{\partial P}}{\dfrac{\partial I}{\partial \tilde{\omega}} - \dfrac{\partial I}{\partial A}\left(\dfrac{\partial R}{\partial A}\right)^{-1}\dfrac{\partial R}{\partial \tilde{\omega}}} \qquad (3.101)$$

A cursory examination of Equations 3.97, 3.100 and 3.101 shows that the same partial derivatives are used in all three cases. Once the time constant and dA/dP have been derived, the transfer function between A and any P may be determined from Equation 3.91.

3.3.5.3 Parameter Variation for SEO Model

The sensitivity of the limit cycle amplitude to parameter variations for the SEO may now be derived from the approach discussed above. From Section 3.5.3, the real and imaginary parts of the characteristic equation are as listed in Equations 3.78a and 3.78b:

$$R\left(\sigma, \tilde{\omega}, A, \dot{\tilde{\omega}}\right) = 0 = \dot{\sigma} + \sigma^2 + \frac{\sigma}{Q} + 1 - \tilde{\omega}^2 + \frac{3}{4}\tilde{k}_3 A^2 - \frac{4\tilde{\delta}\tilde{K}_f}{\pi A^2 \tilde{\omega}} \tag{3.78a}$$

$$I\left(\sigma, \tilde{\omega}, A, \dot{\tilde{\omega}}\right) = 0 = \frac{\tilde{\omega}}{Q} + 2\tilde{\omega}\sigma + \dot{\tilde{\omega}} - \frac{4\tilde{K}_f}{\pi A}\sqrt{1 - \left(\frac{\tilde{\delta}}{A\tilde{\omega}}\right)^2} \tag{3.78b}$$

where it may be noted that, since the partial derivatives will be evaluated at the steady-state limit cycle, it is not necessary in that case to redefine R and I for dA/dP, since the steady-state values of σ and $\dot{\tilde{\omega}}$ will be equal to zero. The relevant partial derivatives are

$$
\begin{aligned}
\frac{\partial I}{\partial \sigma} &= 2\tilde{\omega} & \frac{\partial R}{\partial \sigma} &= 2\sigma + \frac{1}{Q} \\
\frac{\partial I}{\partial \tilde{\omega}} &\approx 2\sigma + \frac{1}{Q} & \frac{\partial R}{\partial \tilde{\omega}} &= -2\tilde{\omega} + \frac{4\tilde{K}_f\tilde{\delta}}{\pi\tilde{\omega}^2 A^2} \\
\frac{\partial I}{\partial A} &\approx \frac{4\tilde{K}_f\left[(A\tilde{\omega})^2 - \tilde{\delta}^2\right]}{\pi A^4 \tilde{\omega}^2} & \frac{\partial R}{\partial A} &= \frac{3}{2}\tilde{k}_3 A + \frac{8\tilde{K}_f\tilde{\delta}}{\pi\tilde{\omega}A^3} \\
\frac{\partial I}{\partial \dot{\tilde{\omega}}} &= 1 & \frac{\partial R}{\partial \dot{\tilde{\omega}}} &= 0 \\
\frac{\partial I}{\partial Q} &= -\frac{\tilde{\omega}}{Q^2} & \frac{\partial R}{\partial Q} &= -\frac{\sigma}{Q^2} \\
\frac{\partial I}{\partial \tilde{\delta}} &\approx \frac{4\tilde{K}_f\tilde{\delta}}{\pi A^3 \tilde{\omega}^2} & \frac{\partial R}{\partial \tilde{\delta}} &= -\frac{4\tilde{K}_f}{\pi\tilde{\omega}A^2} \\
\frac{\partial I}{\partial \tilde{k}_3} &= 0 & \frac{\partial R}{\partial \tilde{k}_3} &= \frac{3}{4}A^2 \\
\frac{\partial I}{\partial \tilde{K}_f} &\approx -\frac{4}{\pi A} & \frac{\partial R}{\partial \tilde{K}_f} &= -\frac{4\tilde{\delta}}{\pi\tilde{\omega}A^2}
\end{aligned} \tag{3.102}
$$

which, when inserted into Equation 3.97 and evaluated at the steady-state values ($\sigma = 0$, $A = A_0$, $\tilde{\omega} = \tilde{\omega}_0$) yields the time constant

$$\tau = \frac{4\left(3\tilde{k}_3 + 4\right)}{\left(9\tilde{k}_3 + 8\right)}Q \approx 2Q \tag{3.103}$$

It should be noted that for small $\tilde{k}_3$, the time constant is exactly that derived in the small-σ solution, which estimates the behavior of the system near steady-state. For linear and hard springs, τ will always be greater than zero.

The steady-state gains between the amplitude and the system parameters $\tilde{k}_3$, $\tilde{\delta}$, Q, and $\tilde{K}_f$ may be evaluated for $\tilde{\delta}^2 \ll 1$, $\tilde{k}_3 \ll 1$, from the development of Section 3.3.1[10]

$$A_0 = 1 - \frac{3}{8}\tilde{k}_3 \tag{3.55b}$$

$$\tilde{\omega}_0 = 1 + \frac{3}{8}\tilde{k}_3 \tag{3.55c}$$

$$\tilde{K}_f = \frac{\pi}{4Q} \tag{3.53}$$

where $\tilde{K}_f$ is defined for a non-dimensional amplitude of 1. With these first-order approximations of A_0 and $\tilde{\omega}_0$, the Taylor series expansions of the partial derivatives are

$$\frac{\partial A}{\partial \tilde{k}_3} \approx -\frac{3A_0^4}{8\omega_0 + 6A_0^3\tilde{k}_3} = \frac{3}{2}\frac{3\tilde{k}_3 - 2}{9\tilde{k}_3 + 8} \approx -\frac{3}{8} \tag{3.104a}$$

$$\frac{\partial A}{\partial \tilde{\delta}} \approx \frac{2A_0 - 4\tilde{\delta}Q}{A_0\omega_0\left(4\omega_0 + 3A_0^3\tilde{k}_3\right)Q} = \frac{8 + 3\tilde{k}_3}{2\left(9\tilde{k}_3 + 8\right)Q} - \frac{8\tilde{\delta}}{9\tilde{k}_3 + 8} = \frac{1}{2Q} - \delta \tag{3.104b}$$

$$\frac{\partial A}{\partial Q} \approx \frac{4A_0^2\omega_0^2}{\left(4\omega_0 + 3A_0^3\tilde{k}_3\right)Q} = \frac{8}{\left(9\tilde{k}_3 + 8\right)Q} \approx \frac{1}{Q} \tag{3.104c}$$

$$\frac{\partial A}{\partial \tilde{K}_f} \approx \frac{16A_0\omega_0 Q}{\pi\left(4\omega_0 + 3A_0^3\tilde{k}_3\right)} = \frac{32Q}{\pi\left(9\tilde{k}_3 + 8\right)} \approx \frac{4Q}{\pi} \tag{3.104d}$$

The final approximations of these derivatives are based on $\tilde{k}_3 \ll 1$. The physical importance of these gains can be interpreted in the context of the amplitude control loop that maintains a constant amplitude. First, it is assumed that the amplitude regulator will not adjust the force to maintain the amplitude, i.e., the applied force remains as a constant. Comments are then made on the impact of these derivatives on the behavior of the amplitude regulator loop, i.e., how these variations change the amplitude control voltage.

If the nonlinear spring is made harder, i.e., $\tilde{k}_3$ increases, then the amplitude will decrease, as shown in Equation 3.104a and suggested by Equation 3.55b. Since the force varies with the velocity of the proof mass, an increase in $\tilde{k}_3$ will increase the resonant frequency. However, the velocity amplitude is kept at 1, so the displacement amplitude must decrease to satisfy Equation 3.52c. For larger $\tilde{k}_3$, the Taylor series expansions are no longer valid, and a more general solution must be derived. In this case, the amplitude

---

[10]These equations are repeated here so that the reader does not have to refer to Section 3.3.1.

regulator loop would supply more voltage to increase the force in order to maintain the non-dimensional amplitude of the proof mass at 1.

In Equation 3.104b, an increase in $\tilde{\delta}$ will also decrease the resulting amplitude for a constant magnitude force. Likewise, the amplitude regulator loop will increase the voltage to compensate for the increase in the hysteresis of the relay. As the hysteresis of the relay is increased, the real gain of the relay decreases and the imaginary gain increases, as suggested by Equation 3.15, which is repeated here with $D = 1$:

$$N_{HR}(A) = \frac{4}{\pi A}\sqrt{1 - \left(\frac{\tilde{\delta}}{A}\right)^2} - j\frac{4\tilde{\delta}}{\pi A^2} \tag{3.15}$$

Therefore, increasing $\tilde{\delta}$ not only lowers the in-phase gain, but also increases the quadrature gain, which in turn generates a force that is in-phase with proof mass displacement, not velocity. At a certain point, not relevant here, the size of the hysteresis will prevent the system from oscillating. This value is not determined here because the relays used are nearly ideal, with hystereses on the order of mV, and input signals on the order of Volts.

By increasing the quality factor of the system, i.e., by reducing damping, the amplitude of the proof mass will increase if the applied force is held at a constant magnitude, as shown in Equation 3.104c. As the damping of the system is decreased, the Q of the system goes up, so that less force is required to overcome the damping in the system. In this case, the amplitude control loop will lower the applied voltage because less force is required to maintain the desired amplitude. On the other hand, if the damping is increased, perhaps by increasing the pressure around the oscillator, then the amplitude will decrease and more voltage is required in order to keep the amplitude at its reference value. By integrating this equation, it is clear that the amplitude grows as the natural logarithm of the quality factor.

Finally, if the forcing constant itself is increased, then the amplitude will also grow because the amplitude is directly proportional to the forcing constant. Once again, the amplitude regulator will use less voltage to achieve a non-dimensional amplitude of 1 because the applied voltage is more efficient in generating an electrostatic force, i.e., there is more "bang for the buck." In practice, the forcing constant is varied by changing the DC value in the drive voltage or by modifying the design to affect the comb drive capacitor derivatives with respect to x. By varying the shape of the stator comb fingers or the distance between them and the rotor fingers and ground plane, the forcing constant may be changed.

For typical non-dimensional oscillator values,

119

$$\tilde{K}_f = 5.236 \times 10^{-6}$$

$$\tilde{\delta} = 0.0103$$

$$Q = 150,000$$

$$\tilde{k}_3 = 0.025$$

The nominal values of the partial derivatives of Equation 3.104 are shown in Table 3.3. For these calculations, the second to last equations for the partial derivatives are used to include the effects of the cubic spring.

Table 3.3. Typical Values of Steady-state Amplitude Gains

Steady-state Gain	Value
$\dfrac{\partial A}{\partial \tilde{k}_3}$	-0.3511
$\dfrac{\partial A}{\partial Q}$	6.48×10^{-6}
$\dfrac{\partial A}{\partial \tilde{\delta}}$	-0.0100
$\dfrac{\partial A}{\partial \tilde{K}_f}$	1.858×10^5

Although some of these gains seem to be either quite large or quite small, in reality these values are quite reasonable. For example, although the partial derivative of the amplitude with respect to $\tilde{K}_f$ seems quite large, the forcing constant is unlikely to change more than 10^{-5}, such that the amplitude will change, at most, by twice its value. Similarly, a change in Q will be on the order of 10^3 to 10^4, such that the amplitude will change by 0.006 or 0.06. In fact, the solution for A as a function of Q is the natural logarithm, suggesting that, after a certain point, increasing Q will not increase the amplitude of the system by a significant amount. Therefore, once an adequate package pressure has been designated, improvements beyond that value are not required. On the other hand, for low Q, small changes will have a great impact on the amplitude of the limit cycle.

From Equation 3.101, the partial derivatives of the frequency with respect to the system parameters may be found under the same assumptions as the amplitude derivatives:

$$\frac{\partial \omega}{\partial \tilde{k}_3} \approx -\frac{3}{4}\left(\frac{3\tilde{k}_3 - 4}{9\tilde{k}_3 + 8}\right) \qquad\qquad (3.105a)$$

$$\frac{\partial \omega}{\partial \tilde{\delta}} \approx -\frac{2}{\left(3\tilde{k}_3 + 4\right)Q} \qquad\qquad (3.105b)$$

$$\frac{\partial \omega}{\partial Q} \approx \frac{6\tilde{k}_3}{\left(9\tilde{k}_3 + 8\right)Q} \qquad\qquad (3.105c)$$

$$\frac{\partial \omega}{\partial \tilde{K}_f} \approx \frac{24Q\tilde{k}_3}{\pi\left(9\tilde{k}_3 + 8\right)} \qquad\qquad (3.105d)$$

Once again, a physical understanding of these steady-state gains is necessary in order to evaluate the usefulness of this approach. From Equation 3.55c, it is obvious that as $\tilde{k}_3$ increases, the resonant frequency of the system will also increase. As shown in Equation 3.105a, the frequency does in fact increase as $\tilde{k}_3$ goes up. To first order, the partial derivative is exactly equal to that obtained by differentiating Equation 3.55c with respect to $\tilde{k}_3$. Changes in $\tilde{\delta}$ do not affect the frequency of the system. Because the relay determines the magnitude of the force, not its frequency, it is logical that the resonant frequency is independent of variations in the hysteresis. The contributions that the relay make are limited to amplitude and phase. In addition, changes in Q have little effect on the frequency. Varying damping, to first order, affects the amplitude of the system only. As the damping becomes larger, the Taylor series approximation is no longer valid, and the damping may affect the frequency of the system. Finally, for similar reasons, the forcing constant also has a small effect on the frequency.

Table 3.4. Typical Values of Steady-state Frequency Gains

Steady-state Gain	Value
$\dfrac{\partial \omega}{\partial \tilde{k}_3}$	0.3579
$\dfrac{\partial \omega}{\partial Q}$	1.216×10^{-7}
$\dfrac{\partial \omega}{\partial \tilde{\delta}}$	-3.27×10^{-6}
$\dfrac{\partial \omega}{\partial \tilde{K}_f}$	3.48×10^3

For the typical system parameters given earlier, the steady-state frequency gains are shown in Table 3.4. Here, the dependence on $\tilde{k}_3$ is nearly equal to 0.375, as expected. However, the other three values are significantly less than the amplitude gains, verifying that the frequency is essentially independent of these system parameters.

From this approach, transfer functions have been derived for both the amplitude and frequency with respect to the system parameters; both the time constant τ and the steady-state gains, $(\Delta A/\Delta P)_{ss}$ and $(\Delta \omega/\Delta P)_{ss}$, have been calculated. A typical response to a variation in a parameter may be determined using Equation 3.91. Figure 3.22 is a plot of the time response of the amplitude and frequency where $\tilde{k}_3 = 0.025$, $Q = 15,000$, and $\Delta Q = 1000$. The value for Q was chosen this low for a reasonable time constant.
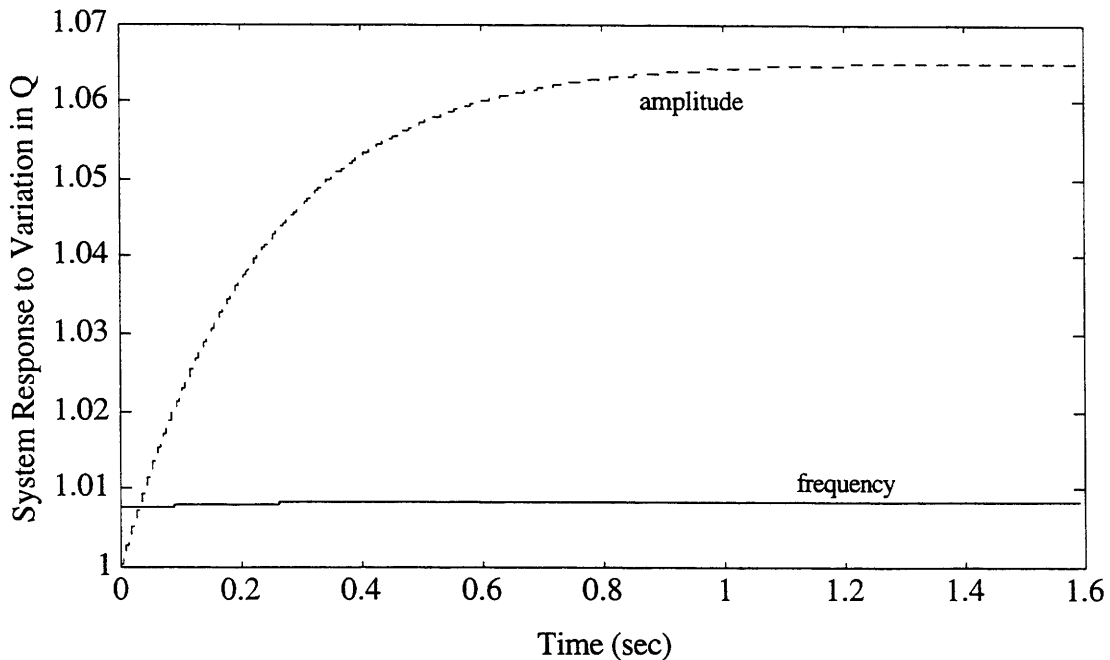
Figure 3.22. Amplitude and Frequency Response for $\Delta Q = 1000$

In this plot, it is clear that variations in the damping affect the amplitude more than the frequency. The amplitude changes by 6% for a variation of 6.66% in the damping. However, the frequency variation is only 0.09%. Similar analyses may be made for variations in the other system parameters.

3.3.6 Summary of Transient Response Analysis

In the previous sections, Equations 3.78a and 3.78b were used to derive various transient characteristics of the closed-loop system. These two equations were determined with the hysteretic relay describing function that included differentiation (Equation 3.69).

122

Table 3.5 summarizes the approaches taken. The first column lists the section, the second shows the quantity that is derived, the third column states the approach taken, and the fourth column summarizes the assumptions. The steady-state assumption means that σ and its derivatives are equal to zero, $\tilde{\omega} = \tilde{\omega}_0$, $A = A_0$, and $\dot{\tilde{\omega}} = 0$.

Table 3.5. Transient Response Analysis Summary

Section	Derivation	Approach	Assumptions
3.3.4.1	limit cycle	steady-state sol'n	steady-state values
3.3.4.2	$A(\tau)$	small-σ solution	drop $\dot{\sigma}$, $\dot{\tilde{\omega}}$, $\sigma^n, n > 2$
3.3.5.1	τ	first differential	steady-state values
3.3.5.2	$[A, \tilde{\omega}]/P$ Xfer Fcns	first differential	steady-state values

3.4 Simulation of Motor Loop Operation

The closed loop, non-dimensionalized, two-dimensional, lumped parameter mechanical model was simulated using FORTRAN [36]. The nonlinear, coupled, second-order equations were separated into four first-order differential equations. The oscillator was represented by the state-space model of Equation 3.17. The preamplifier and gain stages were modeled using Equations 3.23 through 3.25. An integrator was used for the phase shifter, and the relay was implemented according to Equation 3.31. The elements of the amplitude regulator are shown in Figure 3.6, where an absolute value function was used to represent the peak detector. The MATLAB™ and FORTRAN code are shown in Appendix C[11]. Two cases were run to examine the startup and steady-state behavior of the two-dimensional model.

3.4.1 Amplitude Regulator Simulation

In the first case, all cross-coupling terms were set equal to zero, so that only x-axis motion is present. The horizontal displacement is shown versus time in Figure 3.23[12]. As the oscillator starts, the initial displacement is zero. Once the excitation loop has locked onto the resonant frequency, the amplitude initially exceeds the nominal value of 1, and this overshoot quickly settles out, as shown in Figure 3.24. The phase-plane plot of Figure 3.25 demonstrates that the system starts from rest at the origin, and slowly increases to a steady-state non-dimensional position of 1.

---

[11]MATLAB™ is provided by The Mathworks, Inc. of Natick, MA.

[12]In this plot, the data is aliased, so the observed sinusoidal motion is actually at a much lower frequency than that occurring in the simulation.

123
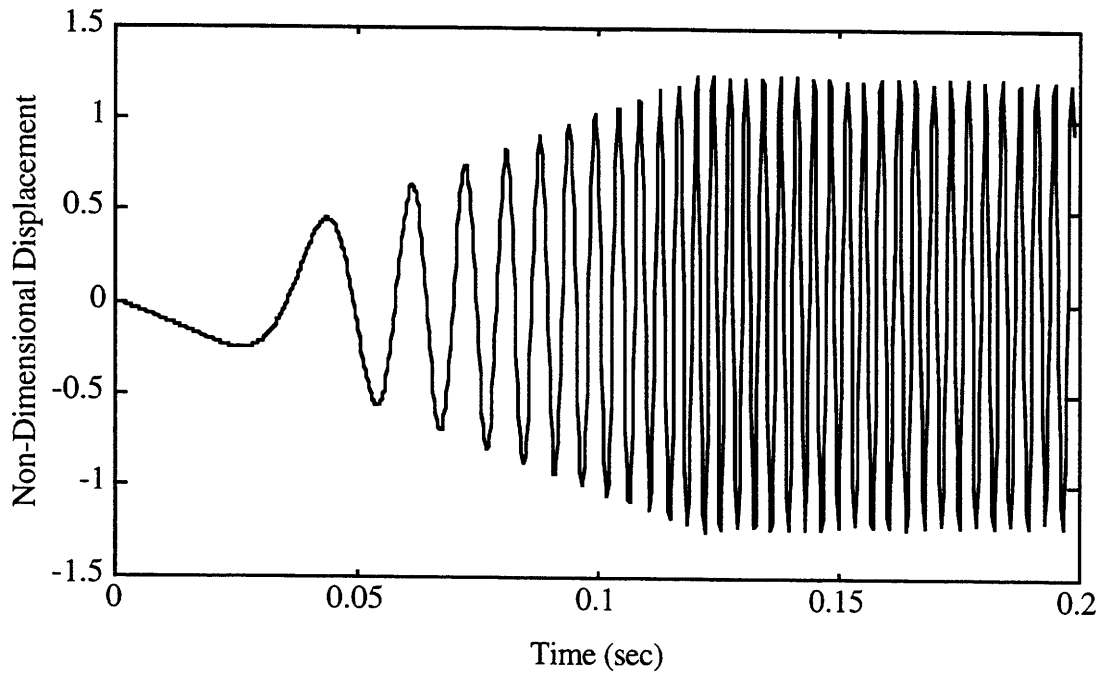
Figure 3.23. Simulation of Startup Response for SEO
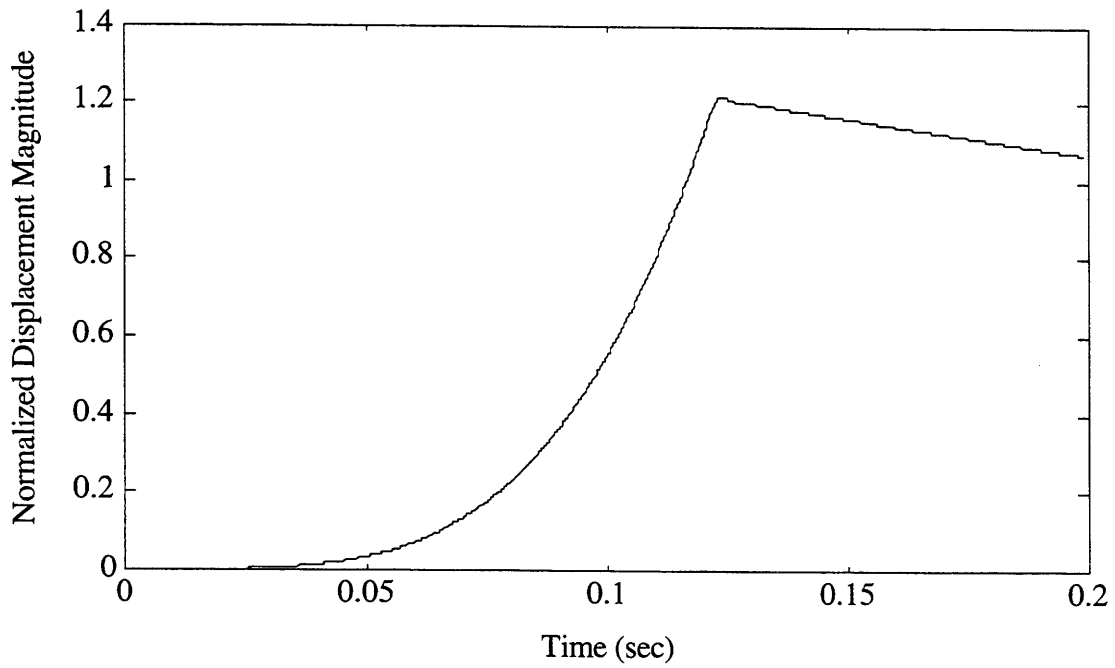
Figure 3.24. Magnitude of Response of Horizontal Axis for SEO
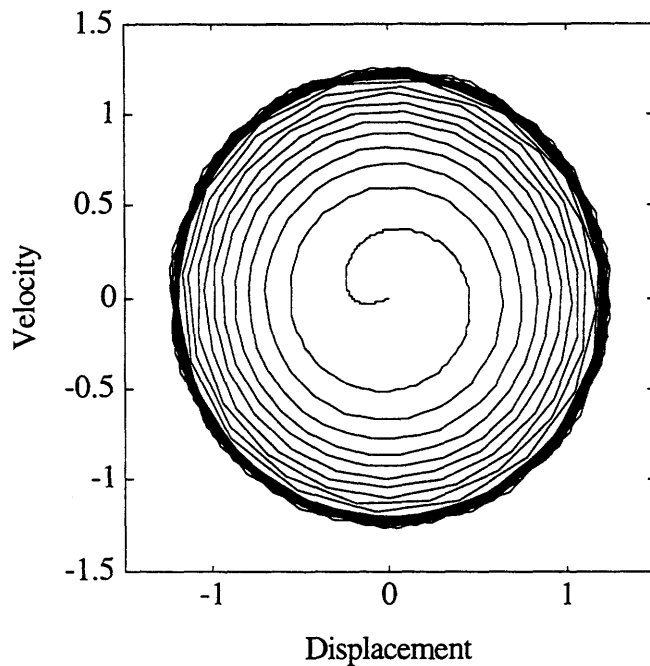
Figure 3.25. Phase Plane of SEO Startup Simulation

In Figure 3.24, the amplitude of the drive motion grows as predicted in Section 3.2.2. Here, the amplitude is quickly driven beyond the desired amplitude. The control voltage then goes to zero and allows the motion to decay below the steady-state value. At this point, the control voltage is again non-zero, and the amplitude increases towards a steady-state value of 1. In Figures 3.26 and 3.27, the length of the simulation was increased to examine the amplitude behavior. Figure 3.26 shows the simulated (solid) and predicted (dashed) amplitudes of the oscillation. The predicted behavior of the amplitude is quite close to the simulated response. The slight differences arise due to the complexity of the simulation and the fact that the system does not immediately lock onto the correct frequency. Also, the simulated behavior has some low-pass filters that do not have a gain of exactly one, and that difference will vary the response. In addition, the second derivative of the amplitude is ignored in the prediction, and, during startup, that may affect the estimates slightly.

125
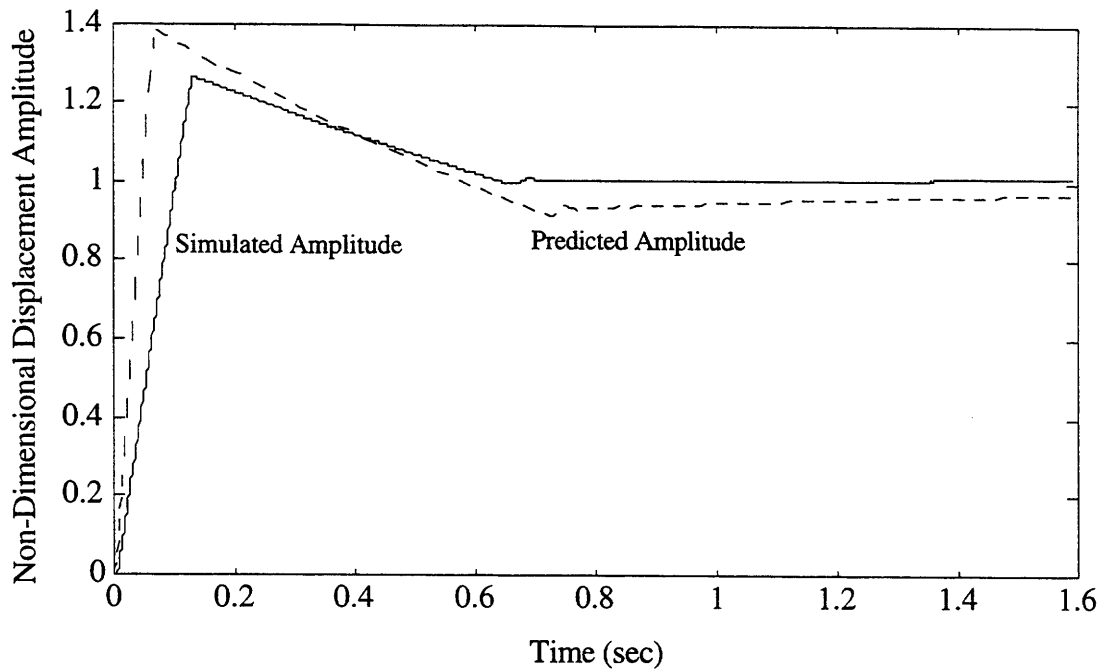
Figure 3.26. Predicted vs. Simulated Behavior of Amplitude Regulator
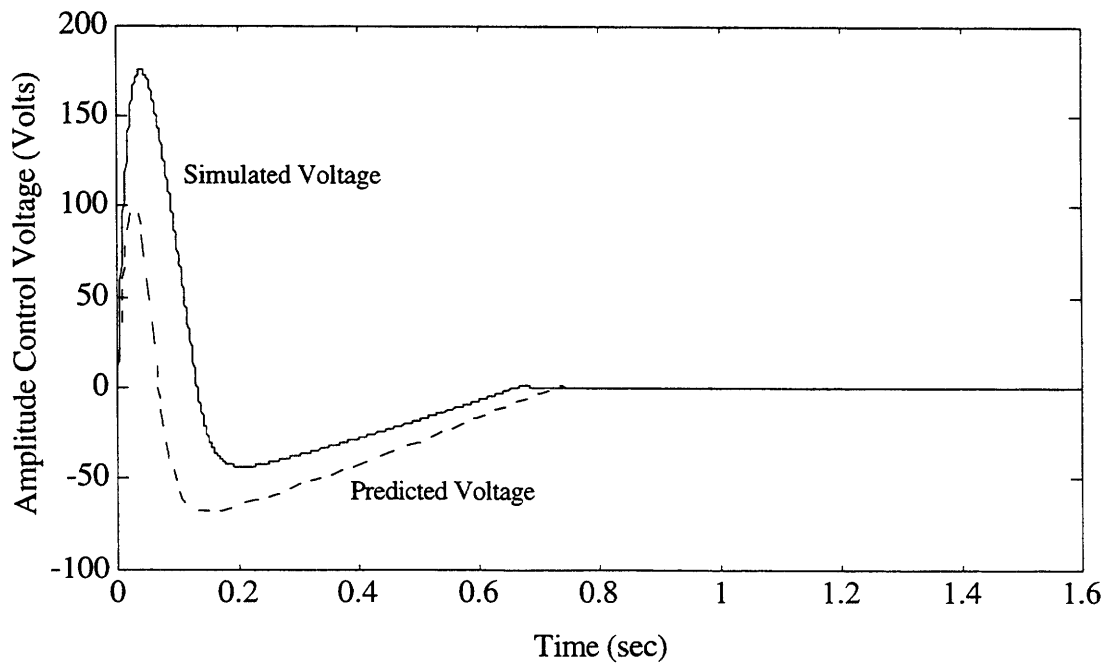
Figure 3.27. Predicted vs. Simulated Amplitude Control Voltage

126

Figure 3.27 shows the non-limited control voltages for both the simulation (solid) and the prediction (dashed) based on Section 3.2.2. Here, both signals have very similar behavior. Initially, both voltages exceed the +10 Volt saturation point and continue to increase for about 0.1 seconds. At that point, the signal decreases, until it is below the 0 Volt saturation point. At about 0.8 seconds, both voltages become positive again, and head towards the desired steady-state values. The slight errors in the prediction occur because at start up, the higher-order derivatives of the amplitude cannot be ignored. However, the impact of this assumption does not reduce the utility of the methodology which predicted, in a very simple way, the behavior of the amplitude control loop.

3.4.2 Oscillator Simulation with Cross-Coupling

In the next case, the cross-coupling terms were included to show that the cross-coupling of the x-motion and x-force can induce significant motion into the y-axis. The resulting x- and y-motions are shown in Figures 3.28 and 3.29. The horizontal motion is essentially unchanged from the previous case, verifying that the cross-coupling forces do not couple back into the original axis. The vertical motion is clearly coupled to the horizontal motion. Both degrees of freedom have very similar shapes, but with different amplitudes. The y-motion amplitude is about 4% of the non-dimensional nominal sense gap of 0.25. This large vertical motion is the motivation for designing vertical control.
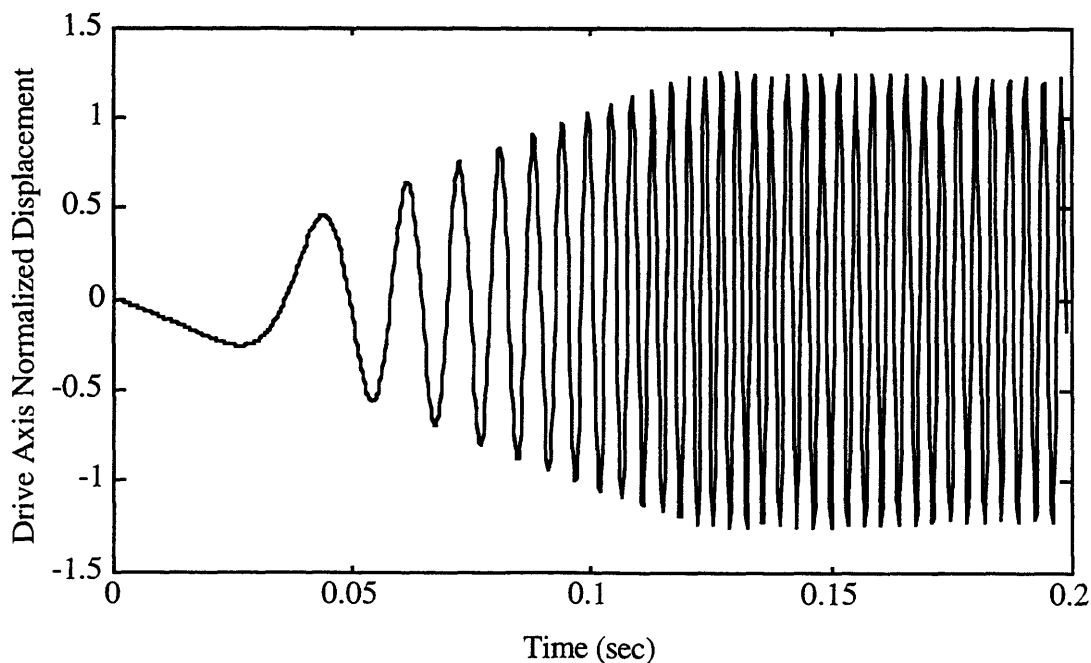
Figure 3.28. Startup Response of Horizontal Axis for SEO

127
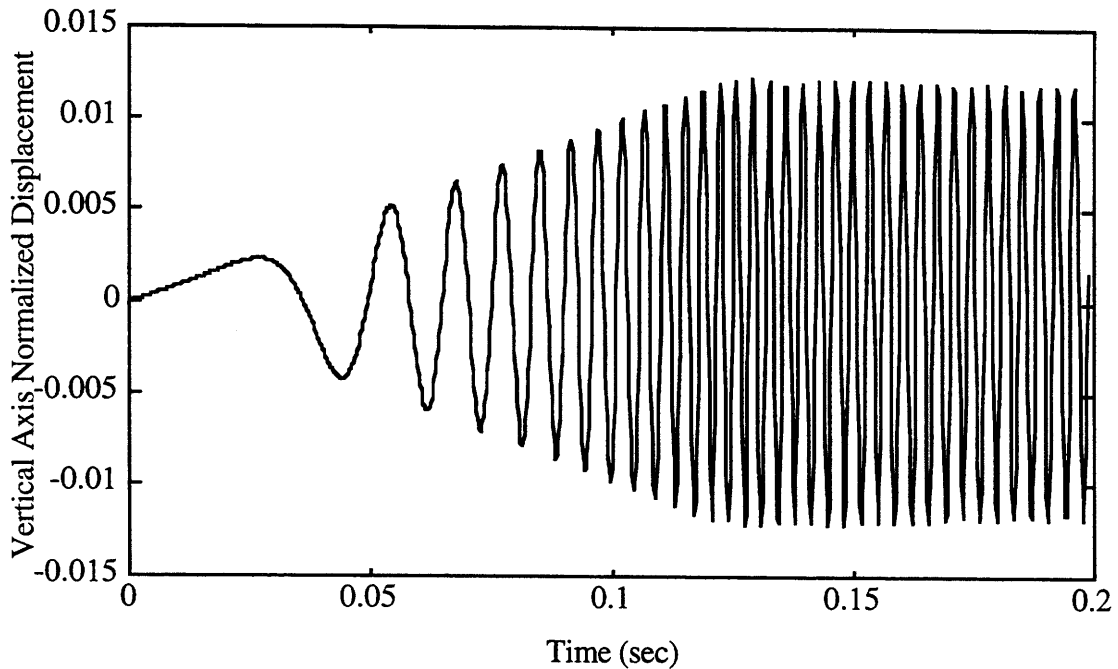
Figure 3.29. Startup Response of Vertical Axis for SEO

Comparisons between experiments and simulations of oscillator start-up, performed independently of the work reported in this thesis, suggest that the simulation is quite accurate. The behavior of the amplitude, the time to steady-state behavior, and the values of the control voltages were verified experimentally; the results agree with the simulations. For example, the time-to-steady-state was simulated as about 1 second (from Figure 3.26), and typical times-to-steady-state are on the order of 1 second. The control voltage for an assumed Q of 150,000 was about 1 Volt, which is often seen in resonators sealed in low pressure containers [2, 3, 37]. Actual performance depends on the parameters of the oscillator, and the simulation will adequately predict behavior, given the characteristics of the device. This simulation of the basic model will be expanded and used to implement the third degree of freedom and vertical and rotational control systems of Chapters 4 and 5.

128

Chapter 4

Silicon Element Oscillator
Lumped Parameter Model and Design

4.0 Introduction

The two degree of freedom dynamic model developed in Chapters 2 and 3 is adequate for most analyses of micromechanical oscillators. However, in real systems, the proof mass may rotate about the z-axis because of cross-coupling with both the lateral and vertical motions. A third degree of freedom, θ, may be added to the dynamic model to study the extent to which this occurs. With this expanded model, the magnitude of the rotational motion may be determined through open-loop frequency response analysis. The addition of θ also requires revisiting the electrostatic model to include the effects of rotation in the capacitor models.

In this chapter, the design of the silicon element oscillator (SEO) is presented. This design includes modifications that are necessary to observe and to control vertical and rotational motions, and will be examined in both Chapters 4 and 5. In Chapter 4, the three degree of freedom dynamic model is derived, and the vertical and rotational motion detection schemes are presented. In addition, the design of both vertical control force plates and rotational control torque plates for the SEO is discussed, and the magnitude of the error signals is analyzed. Simulations are performed to demonstrate the stability and behavior of this dynamic model. In Chapter 5, control systems are designed to minimize both vertical and rotational motion.

4.1 Design and Layout of Single Element Oscillator

In order to study the impact of rotation on the micromechanical resonator and to control both vertical and rotational motions of the proof mass, several changes to the basic oscillator layout had to be made. First, control torque plates are located under both

sets of combs so that the torque, which can be applied from either plate, is maximized. A vertical force control plate is under the center line of the proof mass to generate vertical control forces.

In order to place these control plates under the proof mass, the sense plate must be split in two, as shown in Figure 4.1. This reduces the total sense plate area, and decreases the sensitivity to vertical motion, which is proportional to the sense plate area. In this design, each sense plate is 209.5 μm by 424 μm for a two sense plate total area of 177,656 μm^2, compared to the Chapter 2 design of a 474 μm by 424 μm sense plate with an area of 200,976 μm^2. The vertical control force plate is 40 μm by 424 μm, and each rotational control torque plate is 48 μm by 424 μm. Although the overall sensitivity is reduced, the dual sense plate design permits simultaneous detection of both vertical and rotational motions, which is a significant advantage, as shown in Section 4.3.3.
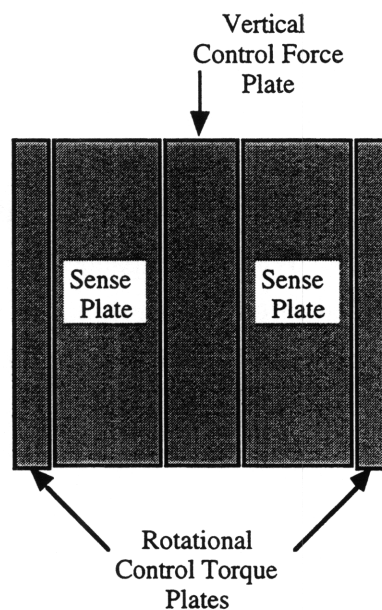
Figure 4.1. Sense and Control Plate Metallization Pattern for a Typical SEO

The proof mass and the stationary combs of the SEO are unchanged from the Chapter 2 micromechanical resonator. One set of combs generates horizontal motion, and the other set detects this motion. The SEO was designed to be 20 μm thick, with a total proof mass size (including the 50 μm fingers on each side) of 550 μm (x-axis) by 400 μm (z-axis). There are 28 tines on each side of the proof mass and on each stator. The fingers are 50 μm long, 5 μm wide with 2 μm spacing between a rotor and stator finger. An optical microscope picture of a typical SEO structure is shown in Figure 4.2. Here, the comb fingers on both the stators and the rotors are clearly seen on the left and right sides

of the image. The motor drive comb is on the left side of the picture, and the motor sense comb is on the right side of the device. The control torque plates are situated under the interdigitated comb fingers. For typical oscillators, gold leads travel from both the silicon components and the surface plates to bond pads not shown in the picture. In this figure, the gold is white, and both the silicon and glass are gray.
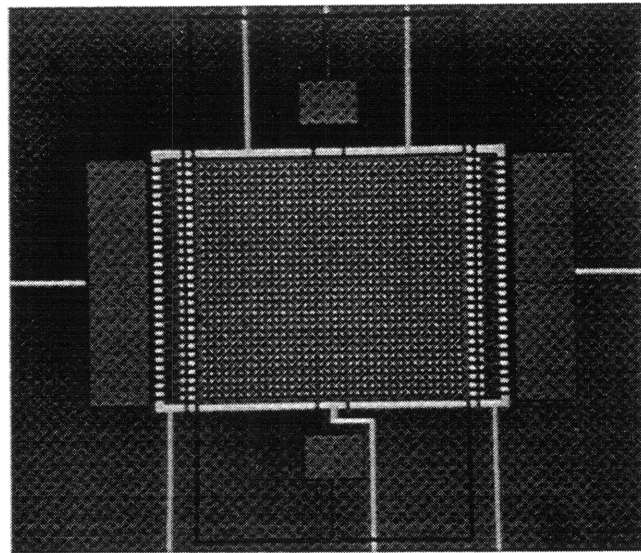
Figure 4.2. Optical Micrograph of a Typical Single Element Oscillator
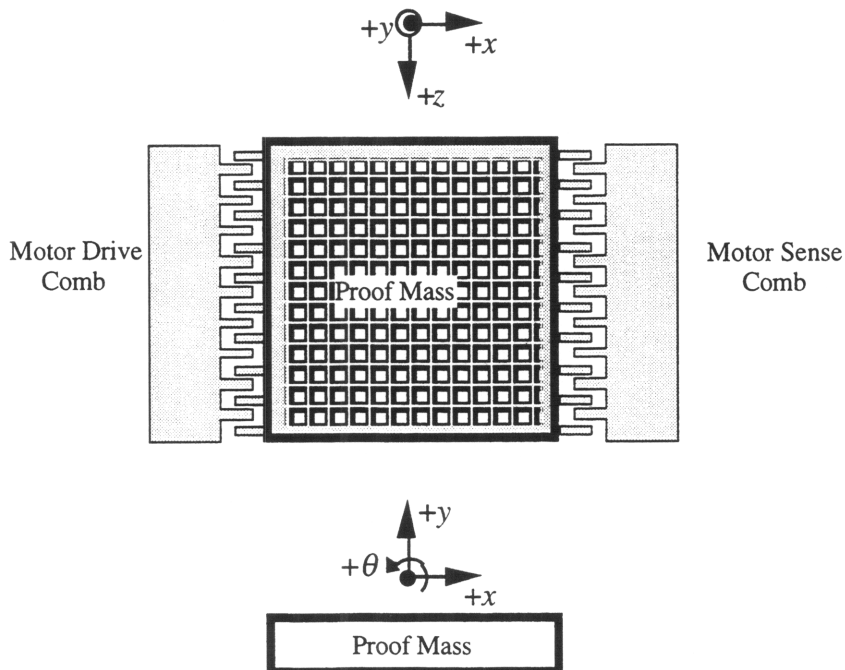
Figure 4.3. Coordinate System for Three Degrees of Freedom

4.2 Expanded SEO Dynamic Model

For the single element oscillator, a three degree of freedom model is a more accurate representation of the system than the traditional two degree of freedom model. Here the generalized coordinates are x, y, and θ, as shown in Figure 4.3. A folded-flexure structure was used to inhibit motion along the z-axis and rotation about the x- and y-axes, so these degrees of freedom are neglected in the dynamic model analysis.

With no vertical displacement, the largest proof mass rotation is $\tan^{-1}(y_0/L_0)$. For a typical resonator, $|\theta_{max}| < 0.521°$, where y_0 is the nominal sense gap and L_0 is the distance along the x-axis from the center of the rotor to the end of a rotor comb finger. For larger rotations, the proof mass will contact the substrate. If the proof mass has been displaced vertically, then θ_{max} decreases.

4.2.1 Lagrangian Derivation of Three DOF Model

From Section 2.1.1, the Lagrange equation for a system of n generalized coordinates with viscous damping was

$$\frac{d}{dt}\left(\frac{\partial L}{\partial \dot{\xi}_i}\right) - \frac{\partial L}{\partial \xi_i} + \frac{\partial D_v}{\partial \dot{\xi}_i} = \Xi_{ext,i} \quad \text{for } i = 1,...,n \tag{2.1}$$

with the terms defined in Chapter 2.

Inserting the three generalized coordinates of the SEO into the kinetic energy, potential energy, and viscous damping equations and including an angular rate, Ω, about the z-axis yields

$$T^* = \frac{1}{2}m(\dot{x} - \Omega y)^2 + \frac{1}{2}m(\dot{y} + \Omega x)^2 + \frac{1}{2}I_\theta(\dot{\theta} + \Omega)^2 \tag{4.1a}$$

$$V = \frac{1}{2}k_x x^2 + \frac{1}{3}k_{x_2} x^3 + \frac{1}{4}k_{x_3} x^4$$

$$+ \frac{1}{2}k_y y^2 + \frac{1}{3}k_{y_2} y^3 + \frac{1}{4}k_{y_3} y^4 \tag{4.1b}$$

$$+ \frac{1}{2}k_\theta \theta^2 + \frac{1}{3}k_{\theta_2} \theta^3 + \frac{1}{4}k_{\theta_3} \theta^4$$

$$+ k_{xy} xy + k_{x\theta} x\theta + k_{y\theta} y\theta + \frac{1}{2}CV^2$$

$$D_v = \frac{1}{2}b_x \dot{x}^2 + \frac{1}{2}b_y \dot{y}^2 + \frac{1}{2}b_\theta \dot{\theta}^2 + b_{xy}\dot{x}\dot{y} + b_{x\theta}\dot{x}\dot{\theta} + b_{y\theta}\dot{y}\dot{\theta} \tag{4.1c}$$

where,

I_θ = moment of inertia about z-axis = mR^2

R = radius of gyration about z-axis

b_θ = torsional damping about z-axis

k_θ, $k_{\theta2}$, $k_{\theta3}$ = linear, quadratic, and cubic torsional springs about z-axis

$b_{x\theta}$, $b_{y\theta}$ = cross-damping between translational and rotational modes, and

$k_{x\theta}$, $k_{y\theta}$ = spring cross-coupling between translational and rotational modes.

The effects of the electrostatic potential energy will be addressed in significant detail in Section 4.3.

If, for now, the electrostatic forces are defined along the x-axis as F_x, along the y-axis as F_y, and about the z-axis as T_θ, then, by inserting Equations 4.1a, 4.1b and 4.1c into Equation 2.1, the equations of motion become, assuming here that Ω is a constant,

$$m\ddot{x} + b_x\dot{x} + k_x x + k_{x_2} x^2 + k_{x_3} x^3 + k_{xy}y + \left(b_{xy} - 2m\Omega\right)\dot{y} + k_{x\theta}\theta + b_{x\theta}\dot{\theta} = F_x \quad (4.2a)$$

$$m\ddot{y} + b_y\dot{y} + k_y y + k_{y_2} y^2 + k_{y_3} y^3 + k_{xy}x + \left(b_{xy} + 2m\Omega\right)\dot{x} + k_{y\theta}\theta + b_{y\theta}\dot{\theta} = F_y \quad (4.2b)$$

$$I_\theta\ddot{\theta} + b_\theta\dot{\theta} + k_\theta\theta + k_{\theta_2}\theta^2 + k_{\theta_3}\theta^3 + k_{x\theta}x + b_{x\theta}\dot{x} + k_{y\theta}y + b_{y\theta}\dot{y} = T_\theta \quad (4.2c)$$

These equations are significantly more complex than those of Section 2.1.1, even though only one degree of freedom has been added. There are four new dynamic coupling terms and two new force coupling terms, the details of which will be addressed in Section 4.3. The equation for each degree of freedom now has ten terms, including one forcing term that includes the effects of all external forcing. However, through careful analysis, it is shown that the basic behavior of this model is very similar to that of Chapter 2.

4.2.2 Non-dimensionalization of Equations of Motion

Once again, it is useful to non-dimensionalize these equations [36]. The first step in the normalization is to use the non-dimensional time and two non-dimensional displacements from Section 2.1.2 (θ does not need to be normalized, since it is non-dimensional by definition, i.e., its units are radians). After substituting these three values into Equations 4.2a through 4.2c, the x- and y-equations are divided by $m\omega_n^2 x_0$, and the θ equation is divided by $m\tilde{R}^2\omega_n^2 x_0^2$, to yield the non-dimensional equations:

$$\ddot{\tilde{x}} + \frac{1}{Q}\dot{\tilde{x}} + \tilde{x} + \tilde{k}_{x_2}\tilde{x}^2 + \tilde{k}_{x_3}\tilde{x}^3 + \tilde{\omega}_{xy}^2\tilde{y} + \left(\frac{1}{Q_{xy}} - 2\tilde{\Omega}\right)\dot{\tilde{y}} + \tilde{\omega}_{x\theta}^2\theta + \frac{1}{Q_{x\theta}}\dot{\theta} = \tilde{F}_x \quad (4.3a)$$

$$\ddot{\tilde{y}} + \frac{\tilde{\omega}_y}{Q_y}\dot{\tilde{y}} + \tilde{\omega}_y^2\tilde{y} + \tilde{k}_{y_2}\tilde{y}^2 + \tilde{k}_{y_3}\tilde{y}^3 + \tilde{\omega}_{xy}^2\tilde{x} + \left(\frac{1}{Q_{xy}} + 2\tilde{\Omega}\right)\dot{\tilde{x}} + \tilde{\omega}_{y\theta}^2\theta + \frac{1}{Q_{y\theta}}\dot{\theta} = \tilde{F}_y \quad (4.3b)$$

$$\ddot{\theta} + \frac{\tilde{\omega}_\theta}{Q_\theta}\dot{\theta} + \tilde{\omega}_\theta^2\theta + \tilde{k}_{\theta_2}\theta^2 + \tilde{k}_{\theta_3}\theta^3 + \frac{\tilde{\omega}_{x\theta}^2}{\tilde{R}^2}\tilde{x} + \frac{1}{\tilde{R}^2 Q_{x\theta}}\dot{\tilde{x}} + \frac{\tilde{\omega}_{y\theta}^2}{\tilde{R}^2}\tilde{y} + \frac{1}{\tilde{R}^2 Q_{y\theta}}\dot{\tilde{y}} = \tilde{T}_\theta \quad (4.3c)$$

where, from Section 2.1.2 and Equations 4.2a through 4.2c above,

$$Q = \frac{m\omega_n}{b_x} \qquad \tilde{\omega}_y = \sqrt{\frac{k_y}{k_x}} \qquad \tilde{\omega}_\theta = \sqrt{\frac{k_\theta}{\tilde{R}^2 x_0^2 k_x}} \qquad \tilde{\omega}_{xy}^2 = \frac{k_{xy}}{k_x} \qquad (4.4)$$

$$\tilde{k}_{x_3} = \frac{k_{x_3} x_0^2}{k_x} \qquad Q_y = \frac{m\omega_y}{b_y} \qquad Q_\theta = \frac{m\tilde{R}^2 x_0^2 \omega_\theta}{b_\theta} \qquad Q_{xy} = \frac{m\omega_n}{b_{xy}}$$

$$\tilde{k}_{x_2} = \frac{k_{x_2} x_0}{k_x} \qquad \tilde{k}_{y_2} = \frac{k_{y_2} x_0}{k_x} \qquad \tilde{k}_{\theta_2} = \frac{k_{\theta_2}}{\tilde{R}^2 x_0^2 k_x} \qquad \tilde{\omega}_{x\theta}^2 = \frac{k_{x\theta}}{k_x x_0}$$

$$\tilde{F}_x = \frac{F_x}{k_x x_0} \qquad \tilde{k}_{y_3} = \frac{k_{y_3} x_0^2}{k_x} \qquad \tilde{k}_{\theta_3} = \frac{k_{\theta_3}}{\tilde{R}^2 x_0^2 k_x} \qquad Q_{x\theta} = \frac{m\omega_n x_0}{b_{x\theta}}$$

$$\tilde{R} = \frac{R}{x_0} \qquad \tilde{F}_y = \frac{F_y}{k_x x_0} \qquad \tilde{T}_\theta = \frac{T_\theta}{\tilde{R}^2 x_0^2 k_x} \qquad \tilde{\omega}_{y\theta}^2 = \frac{k_{y\theta}}{k_x x_0}$$

$$Q_{y\theta} = \frac{m\omega_n x_0}{b_{y\theta}}$$

The term R is the radius of gyration about the z-axis of the proof mass. Since each cross-coupling term in the θ equation is divided by the radius of gyration, their impact on the rotational mode is reduced. As in Chapter 2, the cross-coupling frequencies $\tilde{\omega}_{xy}^2$, $\tilde{\omega}_{x\theta}^2$, and $\tilde{\omega}_{y\theta}^2$, and the cross-quality factors Q_{xy}, $Q_{x\theta}$, and $Q_{y\theta}$ may be negative. These terms were defined to keep the appearance of the equations consistent, i.e., Q terms represents viscous damping constants, and $\tilde{\omega}$ terms represent spring restoring constants, whether on- or off-axis. In Chapter 6, values for the significant parameters are measured experimentally for the SEO. Magnitude analysis was performed on these results, and a reduced-order model that retains only the critical terms is presented in Chapter 6.

4.2.3 State-Space Representation of System

These non-dimensional equations of motion may be linearized and then expressed in the state-space form of Equation 4.5. Here, the forces are assumed to be the control forces applied for each axis. As discussed in Chapter 2, the drive voltage generates vertical forces in addition to the desired horizontal force, resulting in the cross-coupling term β_x. Similarly, the control signals for the vertical and rotational motion may also couple into other modes. A detailed analysis of the forces in Section 4.3.1.3 gives explicit values for the cross-coupling between generalized coordinates. In Equation 4.5, α_i, β_i, and γ_i represent the magnitude of the force coupling into the x, y, and θ degrees of freedom, respectively.

$$\frac{d}{d\tau}\begin{bmatrix}\dot{\tilde{x}}\\ \tilde{x}\\ \dot{\tilde{y}}\\ \tilde{y}\\ \dot{\theta}\\ \theta\end{bmatrix} = \begin{bmatrix}1 & \alpha_y & \alpha_\theta\\ 0 & 0 & 0\\ \beta_x & 1 & \beta_\theta\\ 0 & 0 & 0\\ \gamma_x & \gamma_y & 1\\ 0 & 0 & 0\end{bmatrix}\begin{bmatrix}\tilde{F}_x\\ \tilde{F}_y\\ \tilde{T}_\theta\end{bmatrix} - $$

$$\begin{bmatrix}
\dfrac{1}{Q} & 1+\dfrac{3}{4}\tilde{k}_{x3}A_x^2 & \dfrac{1}{Q_{xy}} & \tilde{\omega}_{xy}^2 & \dfrac{1}{Q_{x\theta}} & \tilde{\omega}_{x\theta}^2\\[6pt]
-1 & 0 & 0 & 0 & 0 & 0\\[6pt]
\dfrac{1}{Q_{xy}} & \tilde{\omega}_{xy}^2 & \dfrac{\tilde{\omega}_y}{Q_y} & \tilde{\omega}_y^2+\dfrac{3}{4}\tilde{k}_{y3}A_y^2 & \dfrac{1}{Q_{y\theta}} & \tilde{\omega}_{y\theta}^2\\[6pt]
0 & 0 & -1 & 0 & 0 & 0\\[6pt]
\dfrac{1}{\tilde{R}^2 Q_{x\theta}} & \dfrac{\tilde{\omega}_{x\theta}^2}{\tilde{R}^2} & \dfrac{1}{\tilde{R}^2 Q_{y\theta}} & \dfrac{\tilde{\omega}_{y\theta}^2}{\tilde{R}^2} & \dfrac{\tilde{\omega}_\theta}{Q_\theta} & \tilde{\omega}_\theta^2+\dfrac{3}{4}\tilde{k}_{\theta3}A_\theta^2\\[6pt]
0 & 0 & 0 & 0 & -1 & 0
\end{bmatrix}\begin{bmatrix}\dot{\tilde{x}}\\ \tilde{x}\\ \dot{\tilde{y}}\\ \tilde{y}\\ \dot{\theta}\\ \theta\end{bmatrix} \quad (4.5)$$

This expanded state-space model was added to the simulation introduced in Chapter 3. In Section 4.4, results from this simulation are shown. As shown in Section 2.1.3.2, the effects of the quadratic and cubic springs on the vertical and rotational axes have been incorporated in the cubic springs. The cubic spring describing function has then been used to linearize the model. In Section 4.3, the forces and torques will be analyzed and separated into coupled forces, similar to those found in Chapter 2. The state-space representation will also be useful in designing the open-loop tests used in Chapter 6 to evaluate the parameters of this system.

4.3 Electrostatics for Three DOF SEO

Adding θ to the SEO dynamic model requires re-evaluating the electrostatic capacitor and forcing models. Proof mass rotation changes the configuration not only between the stator and rotor combs, but also between the proof mass and the sense plates. Both positive and negative rotations decrease the overlap area between the rotor and stator combs and vary the distance between the rotor and the control plate. With a rotating proof mass, the gap between the proof mass and sense plate also changes, increasing the capacitance for one sense plate and decreasing it for the other. The capacitor models for both the combs and parallel plates can be recalculated by considering the effects of proof mass rotation. These expanded models yield new electrostatic forcing models for the SEO.

135

4.3.1 Interdigitated Comb Capacitors for Three DOF Model

If a stationary proof mass is permitted to rotate, then the effective area between the rotor and stator tines is reduced. The magnitude of this effect can be determined through two approaches. The first model is derived from geometry, which means that the fringing fields are either ignored or assumed to be constant. In the second model, the finite element results of Chapter 2 are modified to construct first-order estimates of the capacitance as a function of the rotation of the proof mass.

4.3.1.1 Geometric Model for Drive Comb Capacitance

With the addition of θ, the comb capacitor model becomes more complicated. In Figure 4.4, a stator tine is shown (in an unscaled diagram) with the proof mass rotated through an angle θ, and displaced both along y and x. For any rotation, the overlap area between the proof mass and stator tines is decreased. The dashed box represents the stationary position of the proof mass. In this case, the effects of the substrate are not included here. They are investigated in Section 4.3.1.2 because when the proof mass rotates, the rotor tine moves closer to the substrate, and that increases the magnitude of C_{rp}, an effect not considered in this section. In this figure,

The values given here are nominal values for the SEO only. The numerical results in both Chapters 4 and 5 are based upon these dimensions. The actual dimensions, determined by experiment, are presented in Chapter 6.

Through geometric analysis of the overlap area, it can be shown that the total capacitance between the motor drive stator and the proof mass is

$$C_{m,d} = N\alpha \frac{\varepsilon_0(l_0 - x)}{d}\left(h - \left|y - \left(L_0 - \frac{(l_0 - x)}{2}\right)\theta\right|\right) \tag{4.6}$$

Similarly, the capacitance for the motor sense stator may be expressed as

$$C_{m,s} = N\alpha \frac{\varepsilon_0(l_0 + x)}{d}\left(h - \left|y + \left(L_0 - \frac{(l_0 + x)}{2}\right)\theta\right|\right) \tag{4.7}$$

where,

L_0 = the distance from the center of the proof mass to end of its tine = 275 μm

l_0 = the nominal overlap between the proof mass and stator tines = 25 μm

d = the gap between the rotor and stator tine = 2 μm

h = the thickness of both the tines and the proof mass = 20 μm

A_e = the effective area of overlap between the proof mass and stator tines, and

136
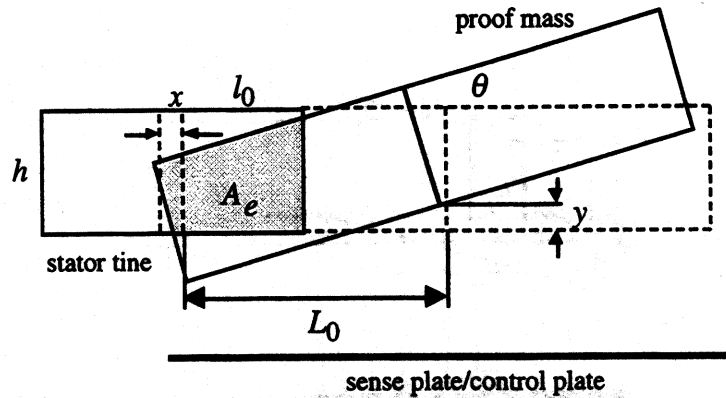
Figure 4.4. Stator-Rotor Comb Finger Interaction for Rotating Proof Mass

the signs in the absolute value have changed to reflect that θ changes the overlap area in different directions at both stators, i.e., positive θ moves the proof mass down with respect to the drive stator and moves it up with respect to the sense stator. If y and θ are very small, then both of these equations reduce to Equation 2.51, the general equation for the capacitance between two comb tines. For a typical oscillator, θ is very small, and y is at most 13% of h. For $\theta = 0.1°$, the rotation reduces the capacitance by 2.29%. At $\theta_{max} = 0.52°$, the point at which the end of the proof mass would contact the substrate, the capacitance is 88.1% of its nominal value. Therefore, even for the largest possible rotation, the drive capacitance is not significantly reduced. For a typical θ on the order of a milliradian, the capacitance is about 98.6% of its nominal value. This geometric model does not include variations in the fringing fields due to rotation; these effects are included in the next section.

4.3.1.2 Finite Element Model for Drive Comb Capacitance

A finite element approach is more accurate than an analytic method because the fringing effects are included in the capacitor estimates. From the 2-D results in Chapter 2, a first-order finite element model of the capacitance with rotation may be derived by assuming again that the electric field is only two-dimensional, i.e., there are no three-dimensional fringing effects at the ends of the tines. Therefore, all interactions between the stator, rotor, and ground plane must be considered.

In Figure 4.5, a vertical cross-section of a proof mass comb, perpendicular to the ground plane, has been highlighted. Under this interaction a sense or control plate is shown. The actual electrode depends on how the metallization is designed. For the SEO, this is a control torque plate. As the proof mass rotates, the area of this cross-section increases, since a longer cut is necessary to generate the perpendicular section. Its area is

137
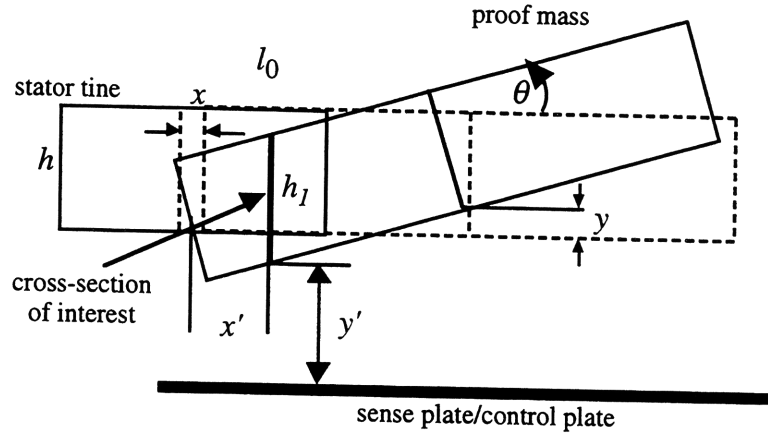
Figure 4.5. Location of Stator-Rotor Cross-section for Finite Element Analysis
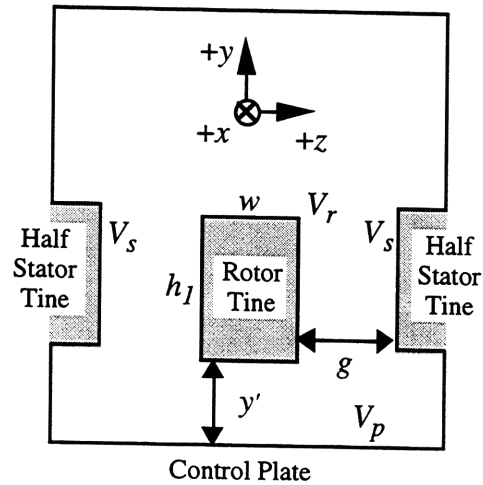
Figure 4.6. Cross-section of Stator-Rotor for Finite Element Analysis

h_1 by w, where h_1 is the height of the cross-section and w is the width of the comb, as shown in Figure 4.6. For any θ, with no vertical displacement, h_1 is related to the thickness of the tine, h, by

$$h_1 = \frac{h}{\cos\theta} \qquad (4.8)$$

For small θ, h_1 is about equal to h, so that the finite element results from Chapter 2 may be used here. The rotation may be assumed to be just a vertical displacement of the cross-section of the rotor tine. In this figure, the distance between the rotor and the control torque plate is

$$y' = y - (L_0 - x')\theta \qquad (4.9)$$

138

where,

y = vertical displacement of the proof mass

L_0 = length from center of proof mass to end of combs

y' = distance from control plate to bottom of cross-section, and

x' = distance from cross-section to the end of the tine.

The total capacitance of a rotated tine may be determined by integrating over the length of the tine. At each cross-section along the rotor tine, the capacitance and its derivative are defined by the height of that section above the control plate. The vertical displacement of each point may be determined from Equation 4.8, and this result may be integrated over the entire length of the rotor-stator tine interaction in order to generate capacitance estimates as a function of θ

$$C_T = \int_{-L}^{-L-(l_0-x)} C(x')dx' \tag{4.10}$$

where L is the distance from the center of the substrate to the edge of the stator comb and each $C(x')$ depends on the rotation angle. With this integral, all three capacitors and their derivatives at the comb interactions may be determined from the finite element results.

For a rotation of $0.1°$, the height of a rotor tine cross-section above the substrate ranges from 2.02 μm at the end of the rotor tine to 2.064 μm at the inner edge of the control plate. At $\theta = 0.01°$, the gaps range from 2.452 μm to 2.456 μm. These small variations permit a linearization of the capacitance for a given rotation. The integrand of Equation 4.10 is a line whose slope and intercept may be found by curve-fitting the capacitor cross-section values at each end of the range. Table 4.1 summarizes the capacitances between the stator and the rotor from the finite element analysis for various θ. In this table, the stator-rotor capacitance is given for θ, assuming that $x = y = 0$.

Table 4.1. Stator-Rotor Total Comb Capacitance versus θ

θ	Geometric	Finite Element
0° (Nominal)	0.24792 pF	0.27352 pF
0.001°	0.24786 pF	0.27358 pF
0.01°	0.24734 pF	0.27355 pF
0.1°	0.24224 pF	0.27245 pF

From this table, the fringing coefficient for C_{rs} is about 1.10. As θ rotates from 0° through 0.1°, C_{rs} changes by about 0.4%, an insignificant amount. The nominal value at

$0°$ is slightly different from that of $0.001°$ because of numerical limitations in the finite element software package.

Figures 4.7 through 4.9 show the three capacitors[1], C_{rs}, C_{rp}, and C_{sp}; and their partial derivatives with respect to x and y, as functions of θ. A kink occurs at $0.01°$ because only the four values of θ listed in Table 4.1 were used to generate this plot. These values were calculated using the approach discussed with Equation 4.10. If the maximum angle is less than $0.01°$, then the effects of the rotation may be neglected for both the motor drive and motor sense combs because the capacitors and their derivatives are virtually constant.

The lift and drive forces versus rotation angle for zero vertical displacement are shown in Figures 4.10 and 4.11, assuming that 0%, 20%, 40%, and 60% of a one Volt drive voltage is applied to the control plate. The drive force changes by 0.75% for a grounded control plate as θ changes from $0.001°$ to $0.1°$. The lift force can change by as much as 50% over this range of θ, with great dependence on the control plate voltage, as shown in Figure 4.11. For θ less than $0.01°$, the effect of rotation on the drive force is negligible (0.07% maximum). For a grounded control plate and rotation between $0°$ and $0.001°$, the drive force variations are about 0.1%, and the lift force variations are 0.45%.
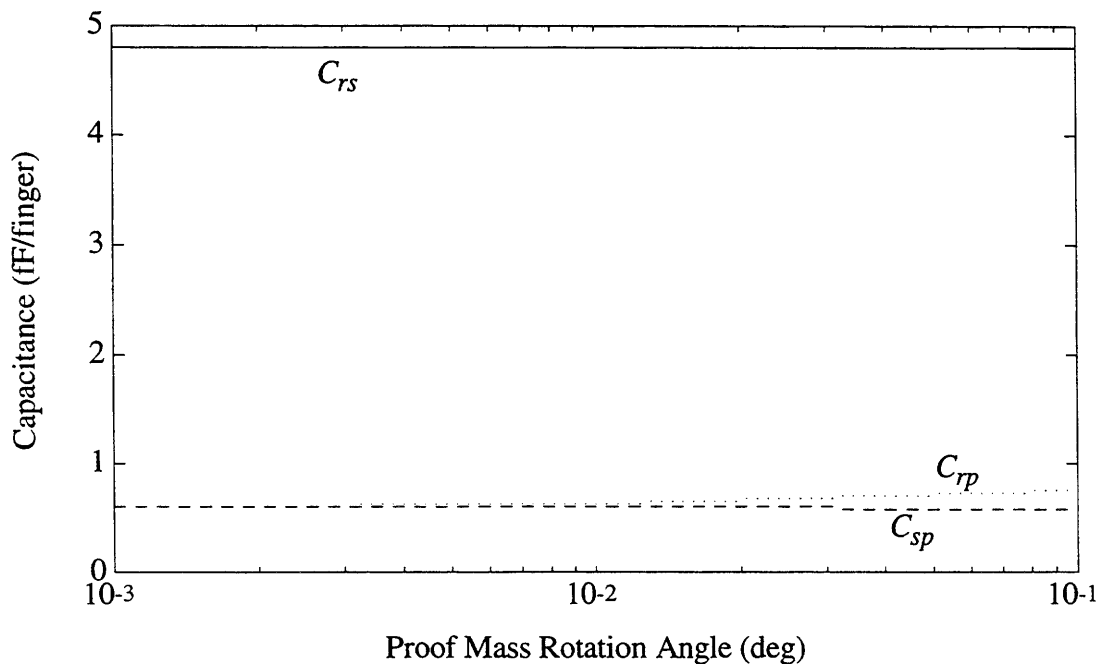
Figure 4.7. Comb Capacitances for Various Proof Mass Rotations

---

[1] There is some bend in these plots at the second point because only three rotation angles ($0.001°$, $0.01°$, and $0.1°$) were used.
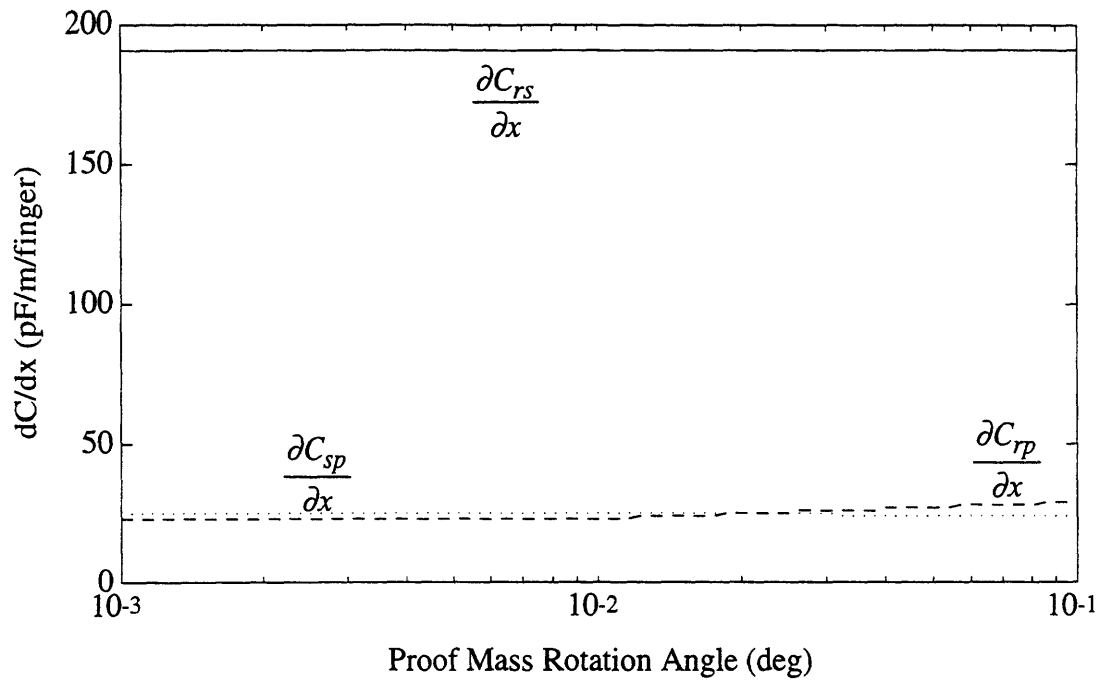
Figure 4.8. Comb Capacitor x-Derivatives for Various Proof Mass Rotations
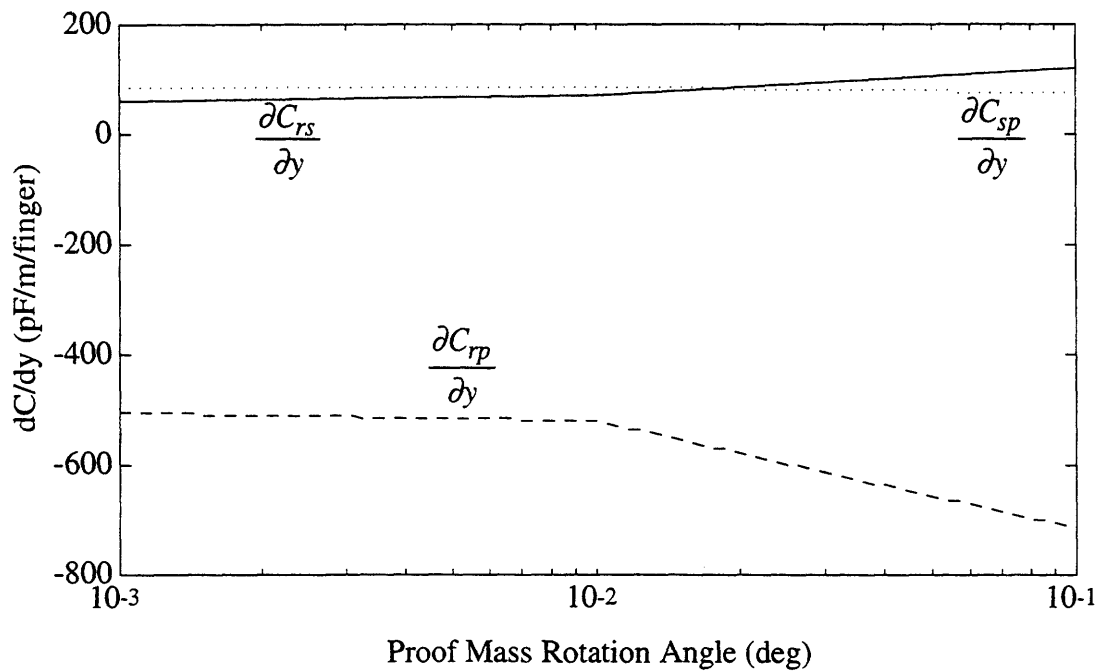
Figure 4.9. Comb Capacitor y-Derivatives for Various Proof Mass Rotations
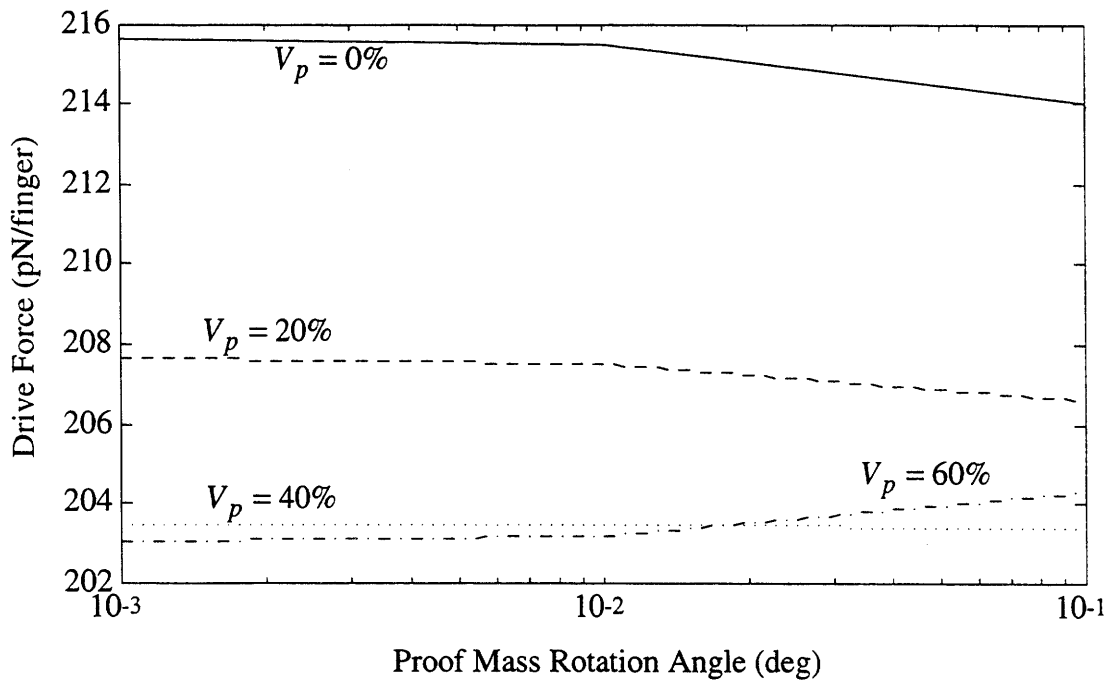
Figure 4.10. Comb Drive Force versus Proof Mass Rotation and V_p
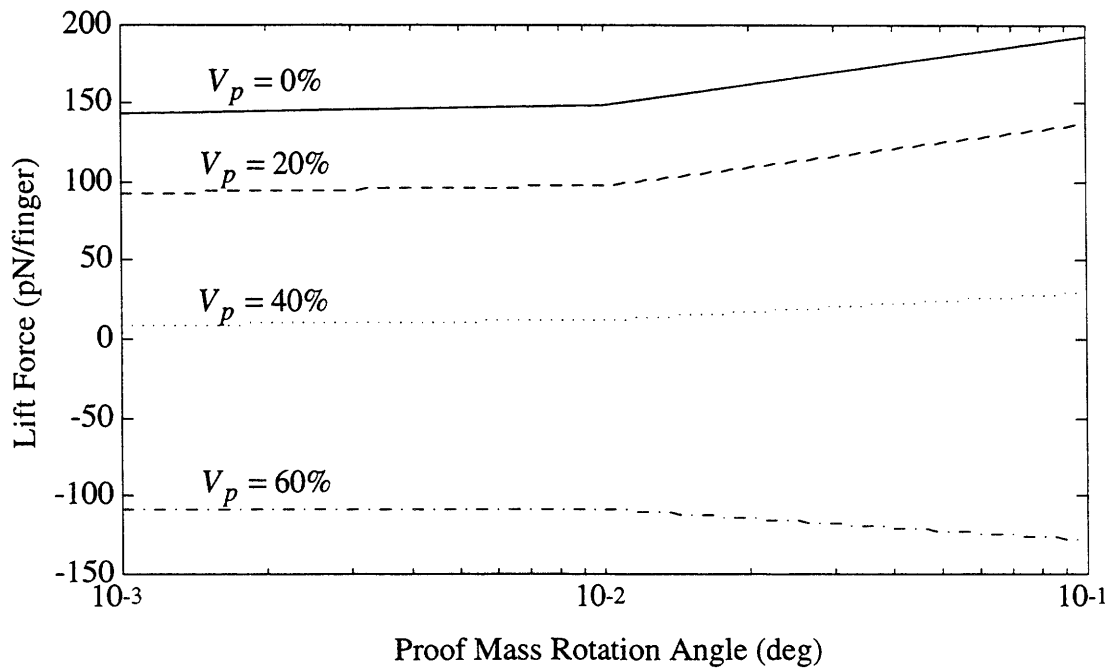
Figure 4.11. Comb Lift Force versus Proof Mass Rotation and V_p
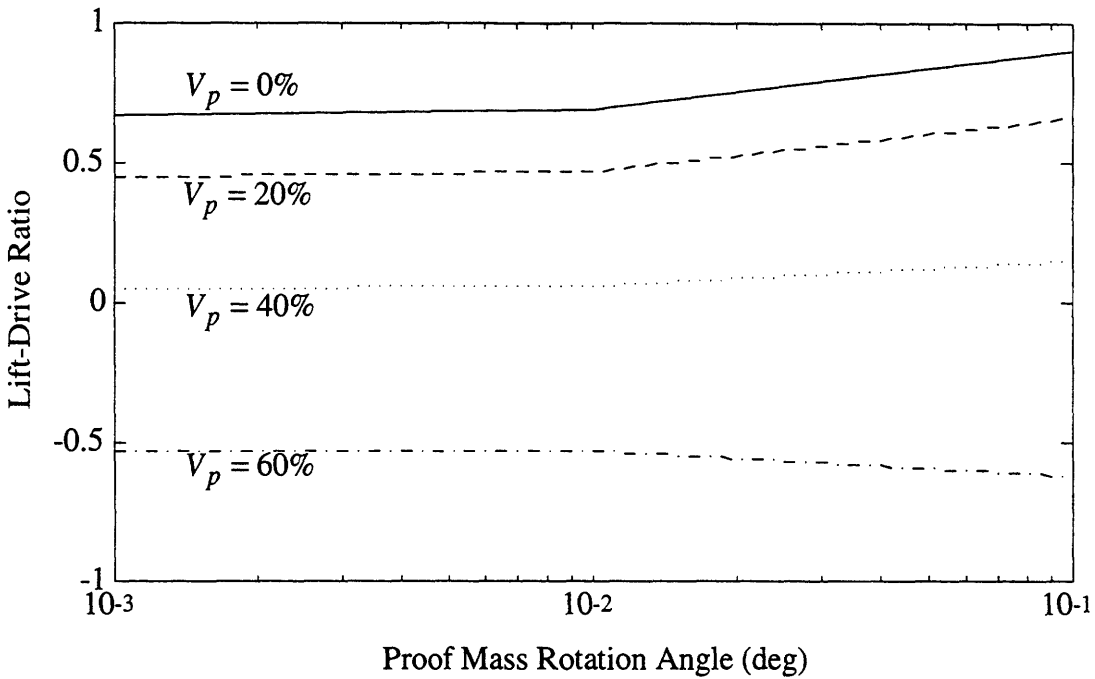
Figure 4.12. Lift-Drive Ratio versus Proof Mass Rotation and V_p

For the comb model derived above, it is clear that the effects of rotation are not significant for θ less than 0.01°. For certain control plate voltages, the lift-to-drive ratio may be reduced significantly, as shown in Figure 4.12, further reducing the effects of rotation on the SEO dynamics. Because the tines are thick, the rotations, even at θ_{max}, do not change the capacitance significantly. Therefore, both the comb drive horizontal and vertical forces may be assumed to be insensitive to the rotation of the proof mass, and the comb capacitor models derived in Chapter 2 may be used as approximations to the more detailed models developed here.

4.3.1.3 Forcing Models for Comb Actuators

Both the horizontal and vertical comb forces generate torque on the proof mass, as shown in Figure 4.13. Because the vertical force is applied at the end of the proof mass, it will always contribute a torque. For the horizontal force, a torque is created only if the force is not applied along the center of mass of the rotor. In Sections 4.3.2 and 5.2.1, the torque is derived based on Lagrange's equation.

143
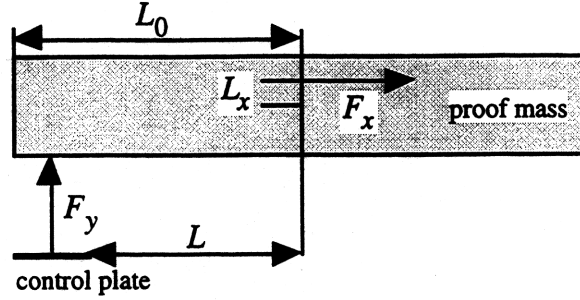
Figure 4.13. Forces and Moment Arms for SEO

where,

L_0 = distance from center of proof mass to end of rotor tine, and

L = distance from center of substrate to inner edge of control plate.

The moment arm for the control plate vertical force, assuming a stationary proof mass, is $(L_0+L)/2$. For the horizontal force, the moment arm is defined as L_x, and is equal to the distance between the rotor center of mass and the plane of the lateral force. All of the external torques are generated by either lateral or vertical forces, and these forces may be determined directly from the comb force equations for the x- and y-axes.

The lateral and vertical force models are unchanged by small rotations of the proof mass, i.e., less than $0.01°$. Typical magnitudes for θ are on the order of a milliradian, so the small angle assumption is valid. Therefore, the coupling of the forces into torques on the rotational axis may be approximated by neglecting the effects of rotation:

$$T_\theta = \gamma_x F_x + \gamma_y F_y =$$

$$\frac{L_x}{2}\left[\frac{\partial C_{rs}}{\partial x}(V_s - V_r)^2 + \frac{\partial C_{rp}}{\partial x}(V_r - V_p)^2 + \frac{\partial C_{sp}}{\partial x}(V_s - V_p)^2\right]$$

$$+\frac{L_0 + L}{4}\left[\frac{\partial C_{rs}}{\partial y}(V_s - V_r)^2 + \frac{\partial C_{rp}}{\partial y}(V_r - V_p)^2 + \frac{\partial C_{sp}}{\partial y}(V_s - V_p)^2\right] \qquad (4.11)$$

where γ_x and γ_y are the cross-coupling coefficients from Equation 4.5. These coefficients are the moment arms for the drive and lift forces. The magnitude of the torque depends both on the voltages and on the misalignment of the proof mass. The voltages here include the control torque voltage, V_p, that can be applied for rotational control. In the current SEO design, with the control torque plates directly under the combs, the desired control plate torque also creates undesired lift forces. The vertical control system must also compensate for this additional excitation.

144
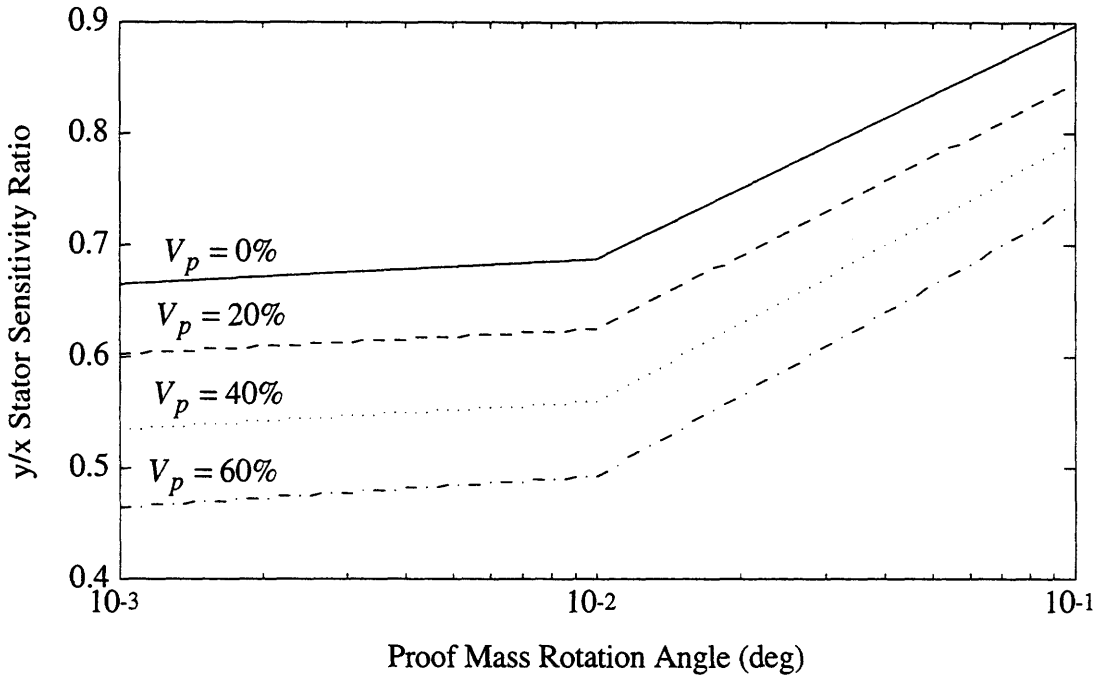
Figure 4.14. Vertical to Horizontal Stator Charge Sensitivity Ratio
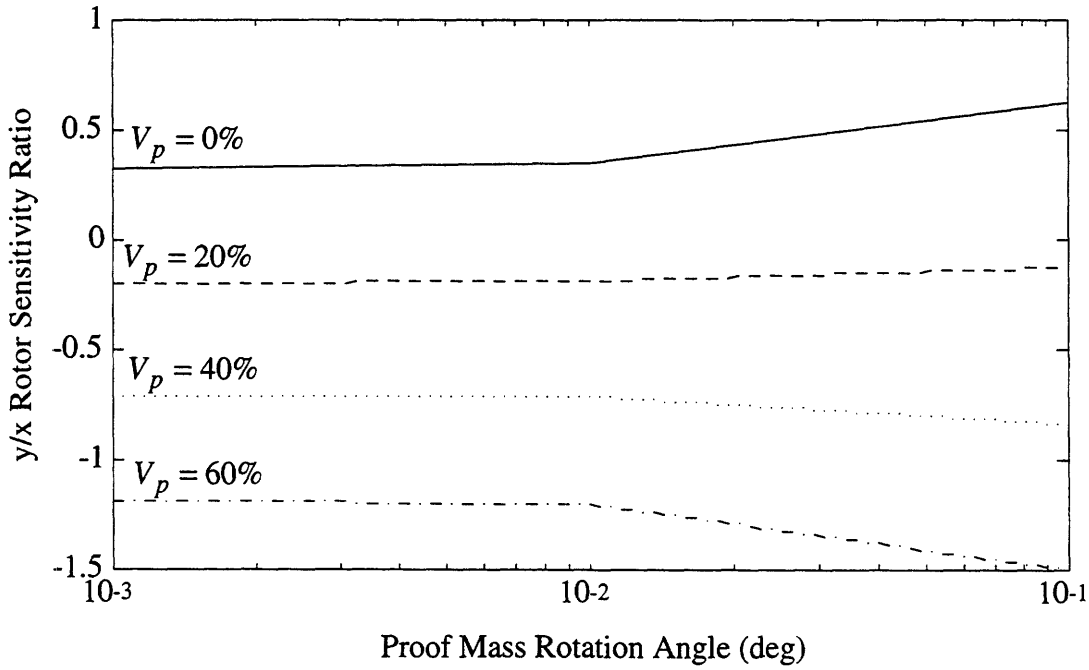
Figure 4.15. Vertical to Horizontal Rotor Charge Sensitivity Ratio

4.3.1.4 Sensing Models for Interdigitated Comb Fingers

Although the lateral comb forces are assumed to be independent of θ, it is important to examine the effects of rotation on motion detection. The plots in Figures 4.14 and 4.15 show the ratio of vertical to horizontal sensitivity for both the stator and rotor for various control plate voltage percentages and rotation angles. As in Section 4.3.1.2, the kinks are due to the limited data points. For rotation angles less than or equal to 0.01°, the rotor sensitivity ratios change by 1% with the control plate grounded and by as little as 0.1% with applied control plate voltages. The stator sensitivity ratios vary from 3.5% to 5.6%, depending on the control plate voltage. The variations from 0° to 0.001° are on the order of 1%.

Since the comb drive is relatively insensitive to proof mass rotation, the comb sensor detected motions may be assumed to be only the vertical and horizontal modes presented in Chapter 2. Based on this analysis, rotational motion does not interfere with the self-excitation loop, because it is not observed, so the electronics cannot lock onto this mode.

4.3.2 Parallel Plate Capacitor Model for Three DOF SEO

For a rotating proof mass, the gap between the proof mass and the substrate electrodes varies over the length of the rotor. With only one sense plate, it is impossible to determine whether the sensed motion is vertical or rotational. In this case, it is useful to separate the sense electrodes into two separate plates. This design modification is important because it permits simultaneous detection of both vertical and rotational motions. There are two approaches to observe y and θ at the same time, and both are presented in Section 4.3.3.

The two control torque plates generate torque on the proof mass. First-order torquing models are derived in Section 4.3.2.2, and, from these models, the rotational snapdown voltage is derived. Just as along the vertical axis, the substrate electrodes decrease the rotational restoring force, and, for some voltage, snap an end of the proof mass to the substrate.

4.3.2.1 Derivation of Parallel Plate Capacitor Model

The capacitance between a stationary proof mass and each sense plate may be expressed by analyzing Figure 4.16 and integrating over the width of each sense plate. The sense plate capacitance for a laterally oscillating proof mass is derived in Section 5.2.2. In Figure 4.16, the shaded vertical area represents a three dimensional differential capacitance.

146
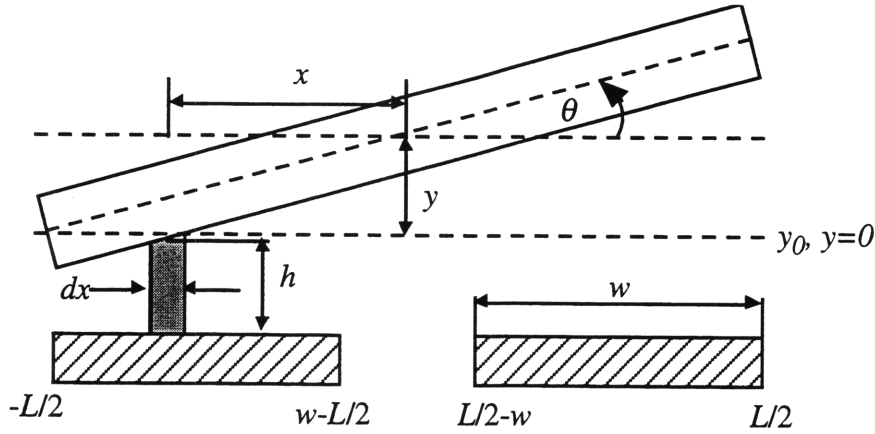
Figure 4.16. Capacitance Between Rotating Proof Mass and Sense Plates

The width of this region is dx, and its height is h. The length of this region into the page, i.e., the length of the sense plate, is l. The width of the sense plate is w, and the outer ends of the sense plates are located at a distance $L/2$ from the center of the proof mass. In this picture, the proof mass has been rotated through an angle θ and displaced a height y from the nominal sense gap y_0.

The differential capacitance between a sense plate and the proof mass is expressed as

$$dC = \gamma \frac{\varepsilon_0 l}{h} dx \qquad (4.12)$$

where,

$$h = y + y_0 + x \tan \theta \qquad (4.13)$$

and γ is the fringing coefficient.

For the left sense plate capacitance, the integral is

$$C_L = \int_{-L/2}^{w-L/2} \frac{\gamma \varepsilon_0 l}{y + y_0 + x \tan \theta} dx$$
$$= \gamma \frac{\varepsilon_0 l}{\tan \theta} \ln \frac{y + y_0 + (w - L/2) \tan \theta}{y + y_0 - L/2 \tan \theta} \qquad (4.14)$$

Similarly, the capacitance between the right sense plate and the proof mass is

$$C_R = \int_{L/2-w}^{L/2} \frac{\gamma \varepsilon_0 l}{y + y_0 + x \tan \theta} dx$$
$$= \gamma \frac{\varepsilon_0 l}{\tan \theta} \ln \frac{y + y_0 + L/2 \tan \theta}{y + y_0 - (w - L/2) \tan \theta} \qquad (4.15)$$

147

For small displacements in both θ and y, these capacitances may be expressed as truncated Taylor series expansions:

$$C_L = \gamma \frac{\varepsilon_0 wl}{y_0} \left[1 - \left(1 + \frac{(L-w)}{2y_0}\theta\right)\frac{y}{y_0} + \left(\frac{y}{y_0}\right)^2 + \frac{(L-w)}{2y_0}\theta \right] \qquad (4.16a)$$

$$C_R = \gamma \frac{\varepsilon_0 wl}{y_0} \left[1 - \left(1 - \frac{(L-w)}{2y_0}\theta\right)\frac{y}{y_0} + \left(\frac{y}{y_0}\right)^2 - \frac{(L-w)}{2y_0}\theta \right] \qquad (4.16b)$$

Since θ_{max} is less than 0.52° (0.01 radians), θ may always be assumed small. The derivations for the left and right capacitances may be used for both the sense plates and the control torque plates. The values of L (the distance between the outer edges of the two plates) and w (the width of a single plate) for both plates are shown in Table 4.2.

Table 4.2. Dimensions for Sense and Torque Plates

	L (μm)	w (μm)
Sense Plate	474	209.5
Torque Plate	580	48

From these values, it is clear that the sense plate capacitor derivative with respect to θ is about 132 times greater than the derivative with respect to a non-dimensional y. For the torque plate, the ratio is 266. The sense plate is more sensitive to rotation than to vertical displacement, and the torquer plate is capable of generating much larger torques than vertical forces.

For the vertical control force plate, the integral is derived in exactly the same manner, as stated in Equation 4.14. The boundary conditions on the integral are changed to $-L/2$ and $L/2$, where L here is the width of the control plate (40 μm):

$$C = \int_{-L/2}^{L/2} \frac{\gamma \varepsilon_0 l}{y + y_0 + x \tan\theta} dx$$

$$= \gamma \frac{\varepsilon_0 l}{\tan\theta} \ln \frac{y + y_0 + L/2 \tan\theta}{y + y_0 - L/2 \tan\theta} \qquad (4.17)$$

The truncated Taylor series expansion of this capacitance is

$$C = \gamma \frac{\varepsilon_0 Ll}{y_0} \left(1 - \frac{y}{y_0} + \left(\frac{y}{y_0}\right)^2 \right) \qquad (4.18)$$

148

which is simply the sum of the left and right capacitances from Equations 4.16a and 4.16b. From this equation, it is clear that the vertical control plate capacitance is independent of θ to first order. This is a very important result, because an applied vertical force does not depend on the rotation of the proof mass to first order, and therefore y-axis motion may be controlled independent of θ.

4.3.2.2 Snapdown Voltage and Forcing Models for Parallel Plates

The torque created by the control torque plates also decreases the rotational restoring force. As in Chapter 2, both snapdown voltage and spring softening issues exist for both the vertical and rotational degrees of freedom. To determine the magnitude of these effects, force and torque models are developed and examined for both the torque and force control plates.

Neglecting cross-coupling and nonlinear spring terms, the dynamics of the rotational mode are

$$\ddot{\theta} + \frac{\tilde{\omega}_\theta}{Q_\theta}\dot{\theta} + \tilde{\omega}_\theta^2\theta = \tilde{T}_\theta \tag{4.19}$$

The torque on a stationary proof mass from the control torque plates may be written from Lagrange's energy formulation as

$$\tilde{T}_\theta = \frac{1}{2k_x x_0^2 \tilde{R}^2}\left(\frac{\partial C_R}{\partial\theta}V_R^2 + \frac{\partial C_L}{\partial\theta}V_L^2\right) \tag{4.20}$$

The partial derivatives of the left and right capacitances with respect to θ are

$$\frac{\partial C_L}{\partial\theta} = \gamma\varepsilon_0 l\left\{\frac{w(L-w)}{2y_0^2}\left(1-2\frac{y}{y_0}\right)-\left[\frac{L}{2y_0}-\frac{w\left(3L^2-6Lw+4w^2\right)}{12y_0^3}\right]\theta\right\} \tag{4.21a}$$

$$\frac{\partial C_R}{\partial\theta} = \gamma\varepsilon_0 l\left\{-\frac{w(L-w)}{2y_0^2}\left(1-2\frac{y}{y_0}\right)-\left[\frac{L}{2y_0}+\frac{w\left(3L^2-6Lw+4w^2\right)}{12y_0^3}\right]\theta\right\} \tag{4.21b}$$

If, for now, it is assumed that voltage is applied to the left control plate only, and that there is no vertical displacement of the proof mass, then the dynamic model is

$$\ddot{\theta} + \frac{\tilde{\omega}_\theta}{Q_\theta}\dot{\theta} + \tilde{\omega}_\theta^2\theta = \gamma\frac{\varepsilon_0 wl}{y_0^2}\frac{(L-w)}{4k_x x_0^2 \tilde{R}^2}\left\{1+\left[\frac{\left(3L^2-6Lw+4w^2\right)}{6y_0(L-w)}+\frac{Ly_0}{w(L-w)}\right]\theta\right\}V_L^2 \tag{4.22}$$

The equivalent rotational natural frequency is

$$\tilde{\omega}_{\theta,eq}^2 = \tilde{\omega}_\theta^2 - \frac{\partial \tilde{T}}{\partial \theta} = \tilde{\omega}_\theta^2 - \gamma \frac{\varepsilon_0 l}{24 k_x x_0^2 \bar{R}^2 y_0^3} \left[w\left(3L^2 - 6Lw + 4w^2\right) + 6Ly_0^2 \right] V_L^2 \quad (4.23)$$

This frequency and the net torque will both be equal to zero at the rotational snapdown voltage, which is equal to

$$V_{snap}^2 = \frac{24 y_0^3}{\gamma \varepsilon_0 l \left[w\left(3L^2 - 6Lw + 4w^2\right) + 6Ly_0^2 \right]} k_\theta \quad (4.24)$$

For the SEO control torque plates, the rotational snapdown voltage for a rotational resonant frequency of $1.25\omega_n$ is 41.78 Volts.

From Chapter 2, the vertical snapdown voltage for the vertical control force plate is

$$V_{snap} = \sqrt{\frac{8 k_m y_0^3}{27 \gamma \varepsilon_0 w l}} \quad (4.25)$$

For the 40 μm by 424 μm control force plate and no vertical displacement, the snapdown voltage is calculated as 37.84 Volts, assuming a sense frequency of $1.09\omega_n$.

The maximum vertical control force is limited by the largest voltage that may be applied to the control plate[2]. Similar to the drive axis, the applied voltage is the sum of a DC and an AC term. The DC value is constant, while the amplitude of the AC signal varies, depending on the required force. The supplies of the electronics have been set to 10 Volts, so that the maximum vertical control force is defined by

$$F_{max} = \frac{1}{2} \frac{\partial C}{\partial y} \left(V_{DC} + V_{AC,max}\right)^2$$
$$= \frac{1}{2} \frac{\partial C}{\partial y} \left(V_{DC}^2 + V_{AC,max}^2 + 2 V_{DC} V_{AC,max}\right) \quad (4.26)$$

The DC force generates a steady-state offset of the proof mass. However, this term does not control vertical motion; the $2V_{DC}V_{AC}$ term is the only one that may be used to eliminate y-axis displacements at the drive axis resonant frequency. If the capacitance derivative with respect to y from Equation 4.18 is used, and V_{DC} is set equal to 5 Volts, then the maximum AC force is about 1.3 μN. The DC force in this case is 1.5 μN. It should be noted that the voltages applied here are significantly less than the snapdown voltage, and that snapdown is not a concern in the SEO control system design.

---

[2] The maximum control force is based on the limits of the op-amp outputs and the area of the control plate.

The maximum control torque may similarly be evaluated from Equation 4.19 by assuming that the left and right control voltages have equal DC terms and equal and opposite AC terms, such that they create a force couple,

$$T_{\theta,max} = \frac{L-w}{4}\left(\frac{\partial C_R}{\partial y}\left(V_{DC} + V_{AC,max}\right)^2 - \frac{\partial C_L}{\partial y}\left(V_{DC} - V_{AC,max}\right)^2\right)$$

$$= (L-w)\frac{\partial C}{\partial y}V_{DC}V_{AC,max}$$

(4.27)

For the SEO, the maximum control torque is 0.844 nN-m. Another benefit of this approach is that there is no DC offset of θ, i.e., for equal and opposite AC voltages on the control plates, no net displacement of θ occurs. If a constant torque is necessary to offset a steady-state displacement, then either the DC or AC voltages may be modified to accommodate both the steady-state and sinusoidal disturbances. By creating an imbalance in the applied DC torque, but keeping the AC torques equal, the proof mass is tilted, but does not rock. During proof mass rotation, the torque equations become more complicated, as will be shown in Chapter 5.

4.3.3 Sensing Models for the SEO

As discussed in Section 2.2.5, proof mass motion is detected by measuring the change in charge either on the motor sense comb or on the proof mass itself. For vertical motion, the charge on the proof mass is typically monitored. With the SEO, both vertical and rotational motions, which occur at the lateral resonant frequency, must be measured by applying voltages to the sense plates and measuring the charge either from the proof mass or from the sense plates themselves.

From the capacitances for the left and right sense plates (Equations 4.16a and 4.16b), it is clear that vertical motion is a common mode, and that rotational motion is a differential mode. Common mode motion is defined as motion that has no phase difference between the left and right sense plates, i.e. each sense plate "sees" the same motion. A differential mode is one in which each plate "sees" motion 180° out of phase, i.e., as one plate sees an increase, the other sees an equal and opposite decrease. To demonstrate this, two cases will be examined. First, if the same voltage is applied to both sense plates, and small displacements are assumed, then the total charge on the proof mass may be expressed as

$$q = V(C_L + C_R) = 2V\frac{\gamma\varepsilon_0 wl}{y_0}\left(1 - \frac{y}{y_0}\right)$$

(4.28)

151

Notice that, to first order, the charge is a function of y only. For an assumed input noise density of 10^{-16} V²/Hz, the non-dimensional vertical position equivalent noise[3] is 0.0069 Å/√Hz.

However, if equal and opposite voltages are applied to the plates, then the total charge on the proof mass is

$$q = V(C_L - C_R) = V \frac{\gamma \varepsilon_0 wl(L-w)}{y_0^2} \theta \left(1 + \frac{y}{y_0}\right) \qquad (4.29)$$

Here, to first order, the charge depends only on the rotation of the proof mass. The rotational equivalent noise is 523.26 picoradians/√Hz. Since the vertical motion is common mode with respect to the two plates, it is canceled by applying equal and opposite voltages. The rotational motion is differential with respect to the sense plates, so it is detected with the equal and opposite voltages, but it is not seen when equal voltages are applied to both sense plates.

4.3.3.1 Simultaneous Vertical and Rotational Motion Detection

For the SEO, both vertical and rotational motion must be measured. Equations 4.28 and 4.29 suggest that the SEO must be designed to obtain both the sum and difference of the charge from each sense plate. There are two major considerations for simultaneous detection of both vertical and rotational motion. First, there is only one proof mass, so that any vertical or rotational motion that varies the gap between the two plates will generate a current on the proof mass. Therefore, it is impossible, without careful design, to determine whether the change in output voltage from the sense preamplifier is due to vertical or rotational motion. Second, both of these motions will be occurring at the resonant frequency of the horizontal axis. Because energy is only being put into the system at this frequency, all cross-coupling of errors and control forces into the vertical and rotational modes will occur at the horizontal resonant frequency. Both modes will therefore generate outputs at the same frequency, requiring a methodology to distinguish the signals. This problem is two-fold: the motions must both be observable, and one output signal must be used to sense both vertical and rotational motion. There are two ways to separate these signals and simultaneously measure the vertical and rotational motions.

If the stationary sense plate is split into a left and right half, as shown in Figure 4.17a, then, as the proof mass moves, the two sense plates "see" different things. As the proof mass rotates counterclockwise (positive θ), as shown in Figure 4.17b, the left sense plate

---

[3]By an analysis similar to that performed in Section 3.2.1.2.

"sees" an increase in capacitance while the right sense plate "sees" a decrease in capacitance, i.e., differential motion. However, as the proof mass moves up (positive y), both sense plates "see" an equal decrease in capacitance; and, as the proof mass moves down, both "see" an equal increase, i.e., common mode motion, as shown in Figure 4.17c. The gray box outline in Figures 4.17b and 4.17c represent the stationary position of the proof mass.
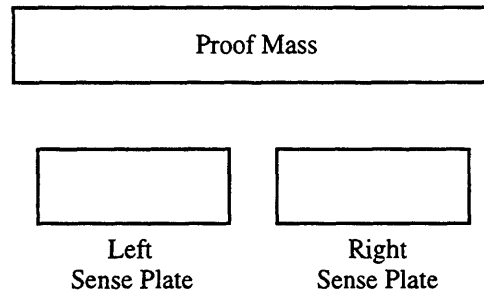
Figure 4.17a. Split Sense Plate Design for SEO
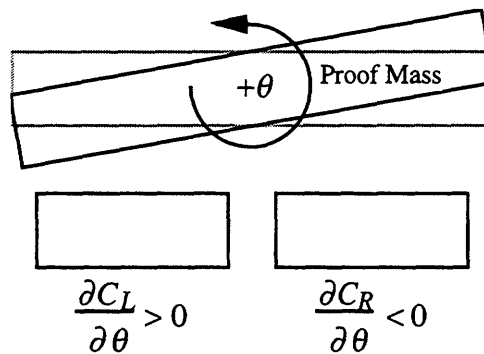
Figure 4.17b. Positive Rotation of Proof Mass with Split Sense Plate
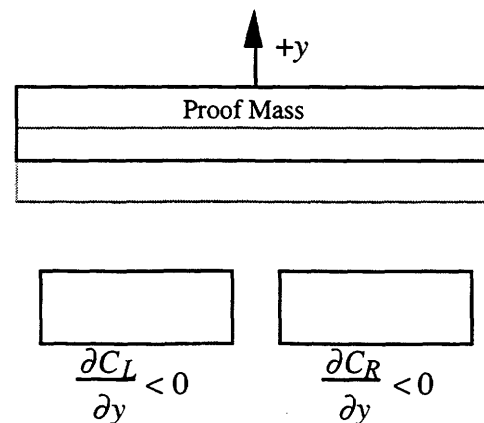
Figure 4.17c. Vertical Displacement of SEO with Split Sense Plate

4.3.3.2 Motion Detection Using DC and AC Biases

By splitting the sense plate, it is straightforward to detect both rotational and vertical motion using the charge injected onto the proof mass. By applying the same AC carrier voltage to both sense plates, and equal and opposite DC voltages to the sense plates, it is possible to measure y from the carrier signal and to measure θ from the DC signal. Using a development analogous to that for the single sense plate, the voltage after the integrator and gain stage will be, for small displacements of y and θ,

$$
\begin{aligned}
V_{out} &= \frac{(C_L + C_R)}{C_{fb}} V_{car} + \frac{(C_L - C_R)}{C_{fb}} V_{DC} \\
&= 2 g_s \frac{C_{y0}}{C_{fb}} \left(V_{DC} \left(\frac{(L-w)}{2y_0} \theta \right) - V_{car} \left(\frac{y}{y_0} \right) \right)
\end{aligned}
\tag{4.30}
$$

where the nominal sense axis capacitance is

$$
C_{y0} = \frac{\gamma \varepsilon_0 w l}{y_0}
\tag{4.31}
$$

and w and l are the width and length, respectively, of one of the split sense plates.

The scheme for obtaining y and θ is shown in Figure 4.18, in which V_{out} is separated and filtered to yield each signal. The rotational motion may be obtained by low-pass filtering the voltage of Equation 4.30. To distinguish the vertical motion, V_{out} must first be demodulated by the carrier signal to reduce the y information to a baseband frequency. From there, the signal is low-pass filtered to yield the y motion.
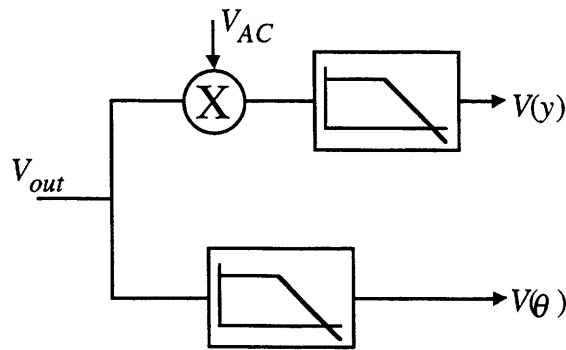
Figure 4.18. Demodulation and Low-pass to Obtain y and θ

Therefore, by separating the sense plate into a right and left plates, and, by applying common and differential mode voltages to the plates (one at DC, one at a carrier), it is possible to detect simultaneously the rotational and vertical motions from the same signal, even though the displacements both occur at the motor resonant frequency.

154

4.3.3.3 Motion Detection Using DC Bias and Two Preamplifiers

A second approach is very similar to that above. In this scheme, a DC bias is applied to each sense plate, and the charge injected onto each sense plate, instead of that injected into the proof mass, is integrated separately and then summed and differenced to yield y and θ. In this case, to first order, the charge on each plate is

$$q_L = V_L C_{y0}\left(1 - \frac{y}{y_0} + \frac{(L-w)}{2y_0}\theta\right) \tag{4.32a}$$

$$q_R = V_R C_{y0}\left(1 - \frac{y}{y_0} - \frac{(L-w)}{2y_0}\theta\right) \tag{4.32b}$$

If these charges are integrated by a preamplifier, amplified by a gain stage, and high-pass filtered by a blocking capacitor, then the resulting output voltages are

$$V_{L,out} = g_s \frac{C_{y0}}{C_{fb}}\left(-\frac{y}{y_0} + \frac{(L-w)}{2y_0}\theta\right)V_L \tag{4.33a}$$

$$V_{R,out} = g_s \frac{C_{y0}}{C_{fb}}\left(-\frac{y}{y_0} - \frac{(L-w)}{2y_0}\theta\right)V_R \tag{4.33b}$$

The sum and difference of these voltages are

$$\Sigma V = \frac{g_s}{y_0}\frac{C_{y0}}{C_{fb}}\left(-(V_L + V_R)y + (V_L - V_R)\frac{(L-w)}{2}\theta\right) \tag{4.34a}$$

$$\Delta V = \frac{g_s}{y_0}\frac{C_{y0}}{C_{fb}}\left(-(V_L - V_R)y + (V_L + V_R)\frac{(L-w)}{2}\theta\right) \tag{4.34b}$$

These equations demonstrate, that, as long as the sense plate bias voltages are of equal magnitude, then the sum will yield either y or θ, and that the difference will yield the other quantity. For the SEO, V_L is assumed to be a positive voltage, V_s; and V_R is $-V_s$; such that the sum and difference become

$$\Sigma V = 2g_s \frac{V_s}{y_0}\frac{C_{y0}}{C_{fb}}\frac{(L-w)}{2}\theta \tag{4.35a}$$

$$\Delta V = -2g_s \frac{V_s}{y_0}\frac{C_{y0}}{C_{fb}}y \tag{4.35b}$$

Therefore, the sum of the sense plate charge integrals yields θ, and the difference gives $-y$. The minus sign may be eliminated by choosing the proper inputs for the differencing op-amp. For the design and analysis of the SEO, the two preamplifier/sense plate approach (Equations 4.35a and 4.35b) was chosen.

155

4.4 Stability and Simulation of Three Degree of Freedom System

In the development of the three degree of freedom SEO model, no claims were made on the stability of the system. Both the vertical and rotational modes are basic second-order, damped oscillator systems. With the natural frequency and quality factor of each degree of freedom greater than zero, both modes are open-loop stable. The only remaining concerns for stability are the cross-coupling of the modes and forces. The force coupling is not a significant concern, because this coupling is based on the drive axis voltage, which couples through the combs, the effects of which can be reduced or eliminated through electronic and design modifications. It was shown earlier that the motor sense comb does not detect small rotations, so the self-excitation loop is insensitive to rotational motion. The cross-coupling of modes could be a concern if coupling of x motion into another mode is fedback to the drive axis as an increasing disturbance. However, the cross-coupling terms are symmetric, and any coupling back into the original axis generates a negligible error force compared to the desired x-axis forces.

The simulation used in Chapter 3 was modified to include the θ dynamic model as well as the cross-coupling between all three modes. Simulations were then run to verify that the new system behaves as expected, with the horizontal motion self-exciting and the remaining modes acting as sinusoidally-forced, second-order systems. The non-dimensional parameters used in these simulations are shown in Table 4.3[4]. The nonlinear spring effects were not included in either the vertical or rotational degrees of freedom.

In Figure 4.19, the horizontal position is shown versus time. Even with the additional mode, the oscillator loop locks onto the drive axis resonance, and the amplitude regulator drives the magnitude to the desired non-dimensional value of 1. The response of the vertical motion is shown in Figure 4.20. Since this axis is driven only by the force and compliance cross-coupling from the drive axis and, to second order, by θ, its response closely resembles that of the drive axis, with an amplitude of 0.018. The DC displacement of the vertical axis has been removed from this simulation to focus analysis on its oscillatory behavior, not the magnitude of its steady-state offset.

Similarly, the rotational motion has a startup profile with characteristics similar to those of the drive axis, as shown in Figure 4.21. The amplitude of the θ oscillation is 79.5 µradians. These simulations were performed to demonstrate that the system is stable and that the behavior of the drive axis is not affected by the additional cross-coupling terms. These results also show that the drive motion and its force are capable of generating significant disturbances on the other degrees of freedom. In these plots, the

---

[4]A complete list of parameters used may be found in Appendix C.

156

noise from the preamplifiers is not immediately apparent, since, for all three motions, the noise is significantly smaller than the observed outputs, as discussed earlier.

Table 4.3. Dynamic Model Parameters for Simulation

	Parameter	Value
x-axis	$\tilde{\omega}_x$	1
	$\tilde{k}_{x_3}$	0.025
	Q_x	150,000
y-axis	$\tilde{\omega}_y$	1.09
	Q_y	30,000
θ-axis	$\tilde{\omega}_\theta$	1.25
	Q_θ	30,000
	$\tilde{R}^2$	117
x-y coupling	$\tilde{\omega}_{xy}^2$	0.003
	Q_{xy}	5,000,000
	α_y	0
	β_x	0.5
x-θ coupling	$\tilde{\omega}_{x\theta}^2$	0.005
	$Q_{x\theta}$	2000
	α_θ	0
	γ_x	12.925
y-θ coupling	$\tilde{\omega}_{y\theta}^2$	0.001
	$Q_{y\theta}$	6,000,000
	β_θ	0
	γ_y	0

In this simulation, the vertical and rotational motions were detected using the DC bias with two preamplifiers approach from Section 4.3.3.3. In Chapter 5, the measured motions will be demodulated by the position and velocity clocks of the drive axis to estimate the quadrature and in-phase components, respectively, of both y and θ. These values will be used to generate control signals that eliminate the undesired out-of-plane motion.

157
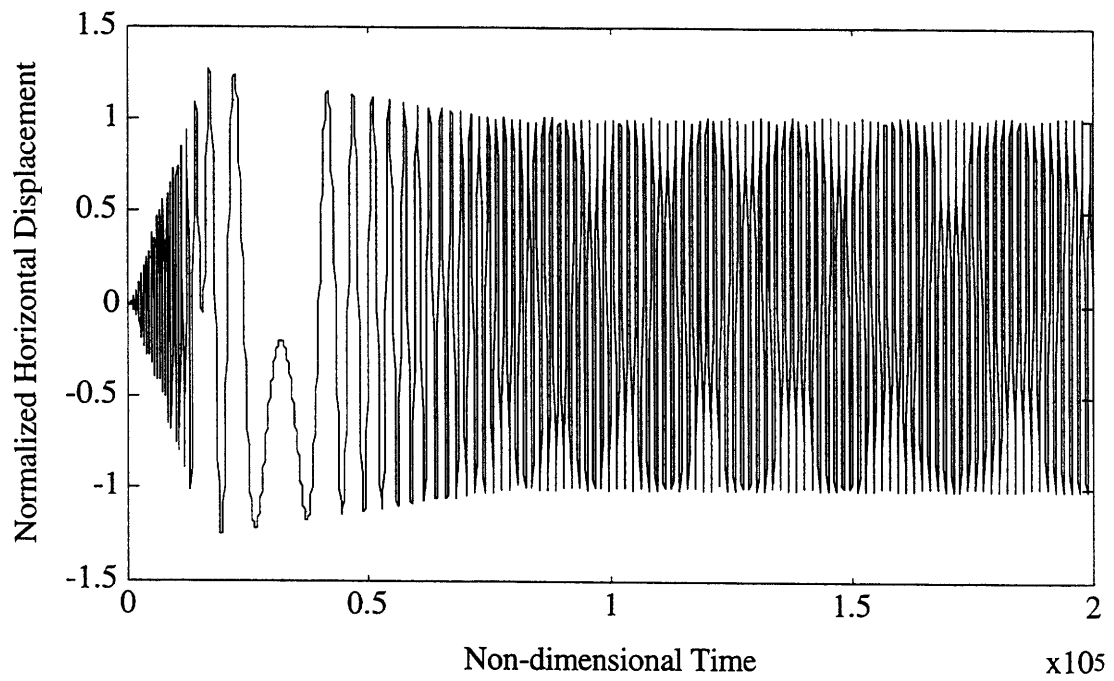
Figure 4.19. Horizontal Displacement vs. Time for 3 DOF Model
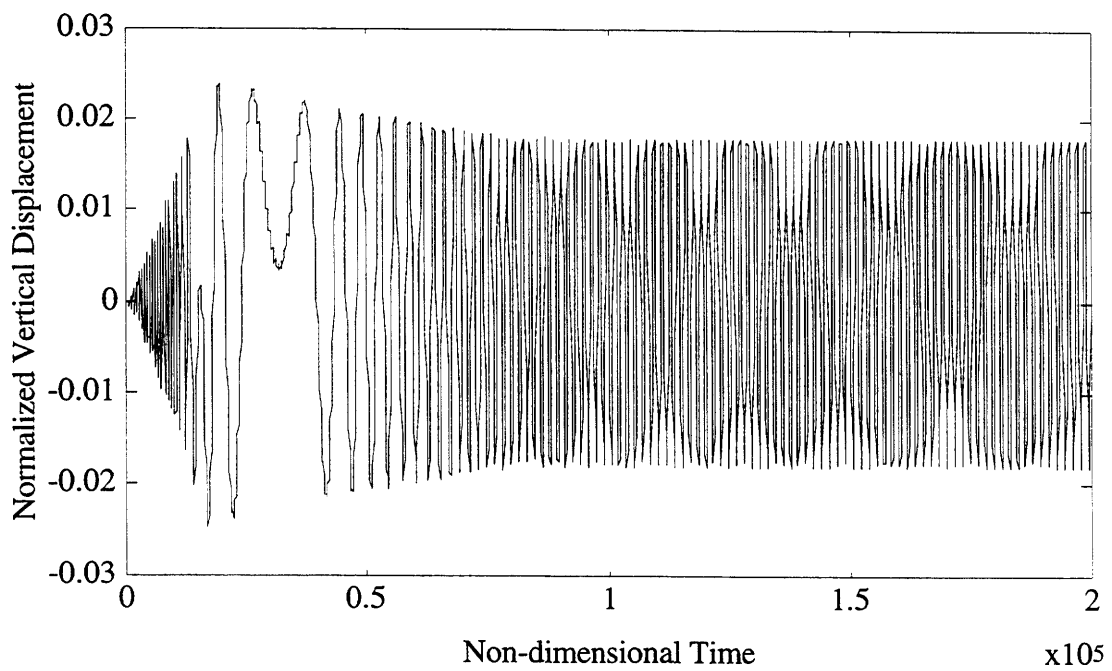
Figure 4.20. Vertical Displacement vs. Time for 3 DOF Model
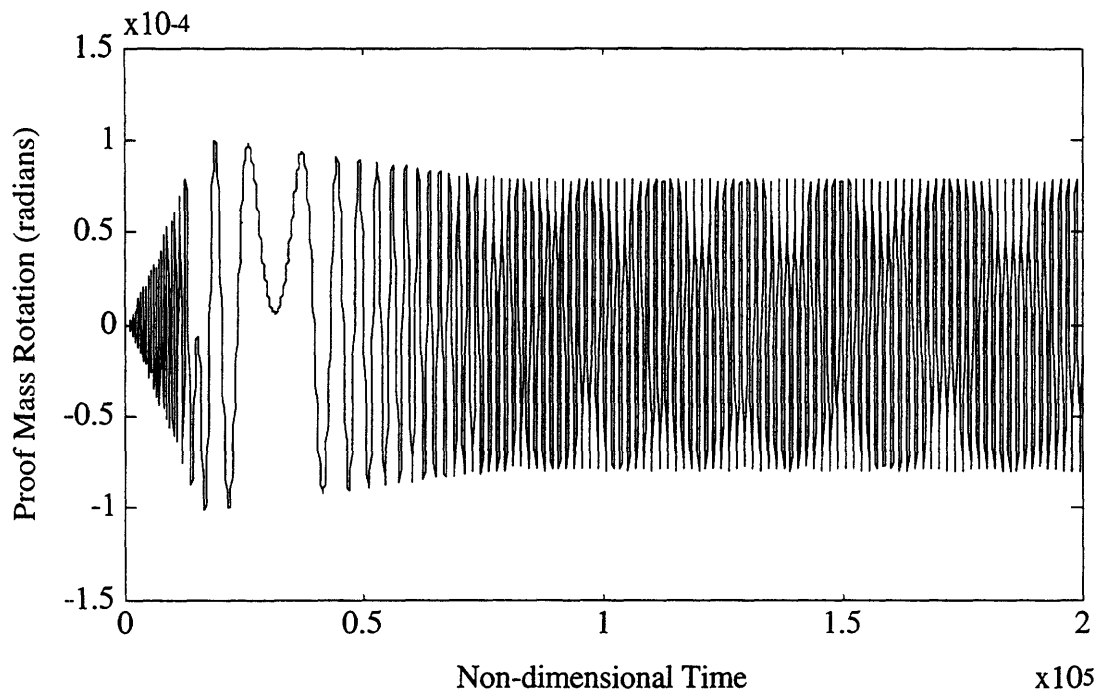
Figure 4.21. Rotation Angle vs. Time for 3 DOF Model

4.5 Complete Three DOF Model for SEO

From the analyses performed in this chapter, several conclusions on proof mass rotation emerge. First, the magnitude of the force couplings among all three modes may be reduced by careful electronic and mechanical design of the torque control plate configuration. Second, both the motor drive and motor sense combs are insensitive to rotations less than 1 milliradian. Therefore, the comb forcing and sensing models developed in Chapter 2 may be used for analyzing the three degree of freedom dynamic system. Third, snapdown effects exist for the rotational mode, but voltages near the snapdown voltage are not applied. Finally, for small θ, the sense plate capacitance varies linearly with both y and θ. This fact is exploited to develop two schemes for simultaneously detecting both vertical and rotational motions. In Chapters 5 and 6, the DC bias/two preamplifier method is used for both simulation of the control systems and experimental measurement of the SEO parameters.

159

Chapter 5

Closed-Loop Control of
Vertical and Rotational Motion

5.0 Introduction

In the expanded three degree of freedom model developed in Chapter 4, the cross-couplings of the dynamics and forces generate undesirable vertical and rotational motion. In order to eliminate these motions, closed-loop force rebalance systems may be designed for each of these degrees of freedom. With this approach, both the in-phase and quadrature components of y and θ may be determined through demodulations at the appropriate phase. In this chapter, a closed-loop control system for each coordinate is presented and linearized to permit linear compensator design. Each control system is then simulated to verify performance. For the θ control system, configurations are presented for the current SEO design and for future modifications to the metallization pattern.

The two main goals in developing the control systems are simple design and information output. First, because micromechanical devices can be produced on the order of hundreds of thousands, and complicated control electronics will increase the per unit cost, so simple solutions are desired to minimize cost. Second, instead of simply reducing the undesired y and θ motion, it would be useful to have the magnitude of the in-phase and quadrature components for both coordinates. The in-phase signal of the vertical motion contains information about angular rates applied about the z-axis. Because of feedthrough and noise concerns, the sensed outputs for both y and θ should not be fedback directly, since both the feedthrough and noise can corrupt the control signal to the extent that the desired displacement information is much smaller than the disturbances themselves.

By using a force rebalance approach, the feedthrough problem may be avoided and the desired quadrature and in-phase information may be obtained. By demodulating the output signals with two clocks, one in-phase with drive axis position and one with drive

161

axis velocity, the in-phase and quadrature components of the vertical and rotational motion may be isolated, passed through a PI controller, and then remodulated with the same clocks to generate control signals. These reconstructed signals will be much cleaner, since off-frequency disturbances have been eliminated by the demodulation and resulting low-pass filtering. In addition, the desired quadrature and in-phase magnitudes for both y and θ have been obtained. Since the modulations are nonlinear, it is necessary to linearize the motion detection and actuation of the system in order to analyze the stability of the control system.

5.1 Vertical Motion Rebalance Loop Analysis

For both y and θ, the induced motions come mostly from coupling with the horizontal dynamics. A control system is assumed for the y-axis and is also applicable to the θ motion. From here, the modulators are linearized to yield a baseband transfer function. This baseband model is then used to design a force rebalance control loop for the vertical axis. Finally, the simulation expanded in Chapter 4 is modified further to include the control systems, and results are presented for various control implementations.

5.1.1 Analysis and Linearization of Vertical Motion Control Loop

As the proof mass oscillates horizontally at the drive axis resonant frequency, manufacturing imperfections (suggested by Equation 4.5) can generate error oscillations in both the vertical and rotational coordinates

$$F_{err_y} = F_{y_0} \sin\left(\tau + \varphi_y\right) \tag{5.1}$$

$$T_{err_\theta} = T_{\theta_0} \sin\left(\tau + \varphi_\theta\right) \tag{5.2}$$

These models are valid for small couplings and some mode separation. With adequate spacing between the resonant modes of the drive, vertical, and rotational axes, the induced motion will be at the drive axis natural frequency, that is, the energy will not "spill" into the resonant mode of either coordinate. By defining the drive-axis steady-state motion as $\tilde{x} = \cos \tau$, the resulting open-loop motions of both $\tilde{y}$ and θ may be expressed as the sum of scaled components of the drive axis displacement and velocity

$$\tilde{y} = \tilde{A}_y \cos \tau + \tilde{B}_y \sin \tau \tag{5.3}$$

$$\theta = A_\theta \cos \tau + B_\theta \sin \tau \tag{5.4}$$

For the forcing shown in Equation 5.1 and a lightly damped second-order plant, the steady-state motion amplitudes of $\tilde{y}$ (a similar result exists for θ), may be written as
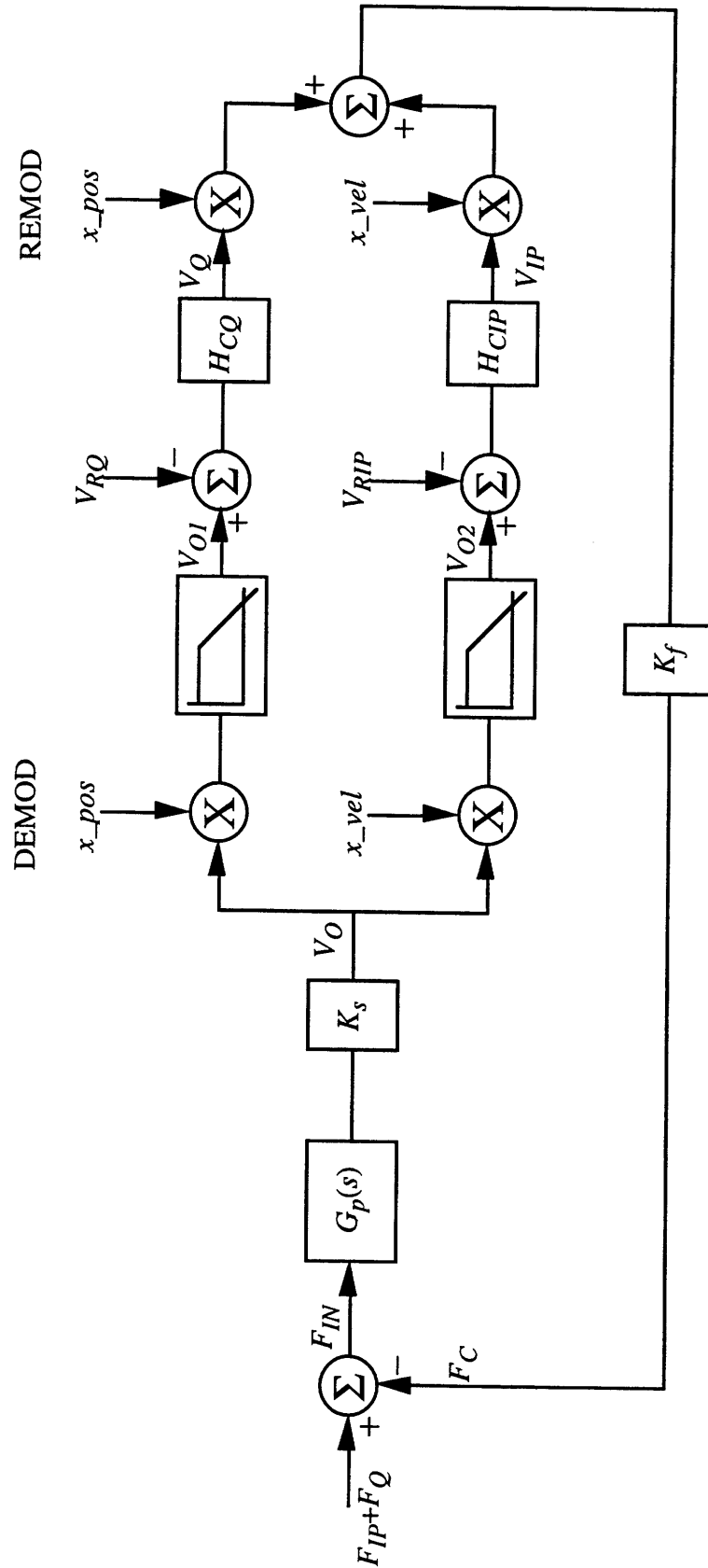
Figure 5.1. Block Diagram for Vertical and Rotational Motion Control

163

$$\tilde{A}_y = \tilde{F}_{y_0} \left(\frac{\left(\tilde{\omega}_y^2 - 1\right)\sin\varphi_y - \dfrac{\tilde{\omega}_y}{Q_y}\cos\varphi_y}{\left(\tilde{\omega}_y^2 - 1\right)^2 + \left(\dfrac{\tilde{\omega}_y}{Q_y}\right)^2} \right) \tag{5.5a}$$

$$\tilde{B}_y = \tilde{F}_{y_0} \left(\frac{\left(\tilde{\omega}_y^2 - 1\right)\cos\varphi_y + \dfrac{\tilde{\omega}_y}{Q_y}\sin\varphi_y}{\left(\tilde{\omega}_y^2 - 1\right)^2 + \left(\dfrac{\tilde{\omega}_y}{Q_y}\right)^2} \right) \tag{5.5c}$$

where $\tilde{\omega}_y$ and Q_y are the resonant frequency and quality factor for the vertical motion, and φ_y is the phase shift in the force with respect to the horizontal displacement. For large Q_y, which exists for the SEO, these equations may be reduced to

$$\tilde{A}_y = \frac{\tilde{F}_{y_0}\sin\varphi_y}{\left(\tilde{\omega}_y^2 - 1\right)} \tag{5.6}$$

$$\tilde{B}_y = \frac{\tilde{F}_{y_0}\cos\varphi_y}{\left(\tilde{\omega}_y^2 - 1\right)} \tag{5.7}$$

Therefore, in a high-Q system, there is very little cross-coupling between the in-phase (with respect to drive-axis velocity) and quadrature error forces.

A suitable feedback control system is shown in Figure 5.1. In this figure, $G_p(s)$ is the plant of the SEO for the given coordinate[1], in this case, the y-axis. The sensing constant K_s is determined by the sense capacitor arrangement and the preamplifier gain. The forcing constant K_f is also defined by the gain stages and forcing capacitor layout. The force F_{IN} is the net input force to the vertical dynamics of the system. The voltage V_O is the output from the SEO for the given coordinate. The signal x_pos is a square wave that is in-phase with the drive axis position signal (in quadrature with the velocity), and x_vel is a square wave that is in-phase with the drive-axis velocity signal. The value V_{O1} is the demodulated quadrature signal consisting of two sinusoids: one at very low frequency with an amplitude equal to $0.5A_y$, and another at twice the drive axis resonant frequency also at an amplitude of $0.5A_y$. Similarly, the signal V_{O2} is the demodulated in-phase signal composed of a low-frequency sinusoid and a second harmonic signal both with

---

[1] Here, each coordinate will be analyzed separately, since, as shown above, the motions of x, y, and θ are sinusoidal with phase shift, and their contribution may be lumped into the error forces.

164

amplitude $0.5B_y$. The low-pass filters along both paths are used to eliminate the second harmonic signals in V_{OI} and V_{O2}. V_{RQ} and V_{RIP} are the quadrature and in-phase reference voltages, respectively. Since the goal is to drive both rotational and vertical motion to zero, these voltages are set equal to zero. The transfer functions H_{CQ} and H_{CIP} are the compensation required to drive the signals to zero in a stable way. The control signals V_Q and V_{IP} are the quadrature and in-phase components at the baseband frequencies, respectively. Finally, F_{IP} and F_Q include all external forces (in-phase and quadrature) applied along the given SEO coordinate, i.e., cross-coupling from the other modes and Coriolis forces.

In order to design adequate compensators for this system, it is useful to linearize the modulation and demodulation portions of the feedback loop [8, 27]. Since it has been shown that the in-phase and quadrature components of the vertical (or rotational motion) are nearly independent, each sub-control loop will be analyzed separately.

First, the quadrature control loop of Figure 5.1 will be investigated [14, 36]. Let V_Q be a slowly varying signal at the non-dimensional baseband frequency $\tilde{\omega}$, which is much less than 1:

$$V_Q = V_{Q_0} \cos \tilde{\omega} \tau \tag{5.8}$$

This signal is modulated by x_pos and amplified by K_f to generate a control force

$$F_C = -\frac{2K_f V_{Q_0}}{\pi} \left(\cos(1 + \tilde{\omega})\tau + \cos(1 - \tilde{\omega})\tau \right) \tag{5.9}$$

The output of the SEO may then be written as

$$V_O = -\frac{2K_s K_f V_{Q_0}}{\pi} \left[M(+)\cos\left((1 + \tilde{\omega})\tau + \varphi(+)\right) + M(-)\cos\left((1 - \tilde{\omega})\tau + \varphi(-)\right) \right] \tag{5.10}$$

where,

$$x\_pos = \text{csqr } \tau = \frac{4}{\pi}\cos \tau + \frac{4}{3\pi}\cos 3\tau + \dots$$

$$x\_vel = \text{sqr } \tau = \frac{4}{\pi}\sin \tau + \frac{4}{3\pi}\sin 3\tau + \dots$$

$$M(+) = \left| G\left[j(1 + \tilde{\omega}) \right] \right|$$

$$\varphi(+) = \angle G\left[j(1 + \tilde{\omega}) \right]$$

$$M(-) = \left| G\left[j(1 - \tilde{\omega}) \right] \right|$$

$$\varphi(-) = \angle G\left[j(1 - \tilde{\omega}) \right]$$

After this signal has been demodulated by x_pos and the low-pass filter has removed the higher harmonic terms, V_{O1} can be expressed as

$$V_{O1} = -\frac{4K_sK_fV_{Q0}}{\pi^2}\left\{M(+)\cos\left(\tilde{\omega}\tau + \varphi(+)\right) + M(-)\cos\left(\tilde{\omega}\tau - \varphi(-)\right)\right\} \quad (5.11)$$

The negative phase in the second term of the right hand side represents the complex conjugate of $G(j(1-\tilde{\omega}))$, such that the transfer function from V_Q to V_{O1} may be written as

$$\frac{V_{O1}}{V_Q} = -\frac{4K_sK_f}{\pi^2}\left\{G_p(+) + G_p^*(-)\right\} \quad (5.12)$$

Similarly, x_vel demodulates the output signal V_O to yield the signal V_{O2}. After low-pass filtering, this signal becomes

$$V_{O2} = -\frac{4K_sK_fV_{Q0}}{\pi^2}\left\{-M(+)\sin\left(\tilde{\omega}\tau + \varphi(+)\right) + M(-)\sin\left(\tilde{\omega}\tau - \varphi(-)\right)\right\} \quad (5.13)$$

Along this demodulation path, the signal has been shifted by -90° or $1/j$. Therefore, in terms of the plant $G_p(s)$, the transfer function between V_{O2} and V_Q may be expressed as

$$\frac{V_{O2}}{V_Q} = -j\frac{4K_sK_f}{\pi^2}\left\{G_p(+) - G_p^*(-)\right\} \quad (5.14)$$

An identical approach may now be taken to examine the effects of the in-phase modulation/demodulation loop on the SEO plant. Define V_{IP} as the slowly varying value

$$V_{IP} = V_{IP0}\sin\tilde{\omega}\tau \quad (5.15)$$

This voltage, modulated by x_vel, is then applied to the plant through the forcing constant K_f, which yields an input force

$$F_{IN} = -\frac{2K_fV_{IP0}}{\pi}\left(\cos(1-\tilde{\omega})\tau - \cos(1+\tilde{\omega})\tau\right) \quad (5.16)$$

The output of the SEO may then be written as

$$V_O = -\frac{2K_sK_fV_{IP0}}{\pi}\left[M(-)\cos\left((1-\tilde{\omega})\tau + \varphi(-)\right) - M(+)\cos\left((1+\tilde{\omega})\tau + \varphi(+)\right)\right] \quad (5.17)$$

Once again, demodulation by x_pos yields V_{O1} after the low-pass filter

$$V_{O1} = \frac{4K_sK_fV_{IP0}}{\pi^2}\left[M(+)\cos\left(\tilde{\omega}\tau + \varphi(+)\right) - M(-)\cos\left(\tilde{\omega}\tau - \varphi(-)\right)\right] \quad (5.18)$$

which, when divided by Equation 5.15, yields the transfer function

$$\frac{V_{O1}}{V_{IP}} = j\frac{4K_sK_f}{\pi^2}\left[G_p(+) - G_p^*(-)\right] \qquad (5.19)$$

A similar exercise yields the transfer function between V_{O2} and V_{IP}

$$\frac{V_{O2}}{V_{IP}} = -\frac{4K_sK_f}{\pi^2}\left[G_p(+) + G_p^*(-)\right] \qquad (5.20)$$

The preceding analysis allows the non-linear modulation/demodulation loops to be approximated as linear transfer functions for small $\tilde{\omega}$ [14, 36].

Before redrawing Figure 5.1 with these linear approximations, it would be helpful to find the transfer function between the error forces and V_{O1} and V_{O2} [14, 36]. Figure 5.2 shows the block diagram path between the error signals and the desired voltage outputs.
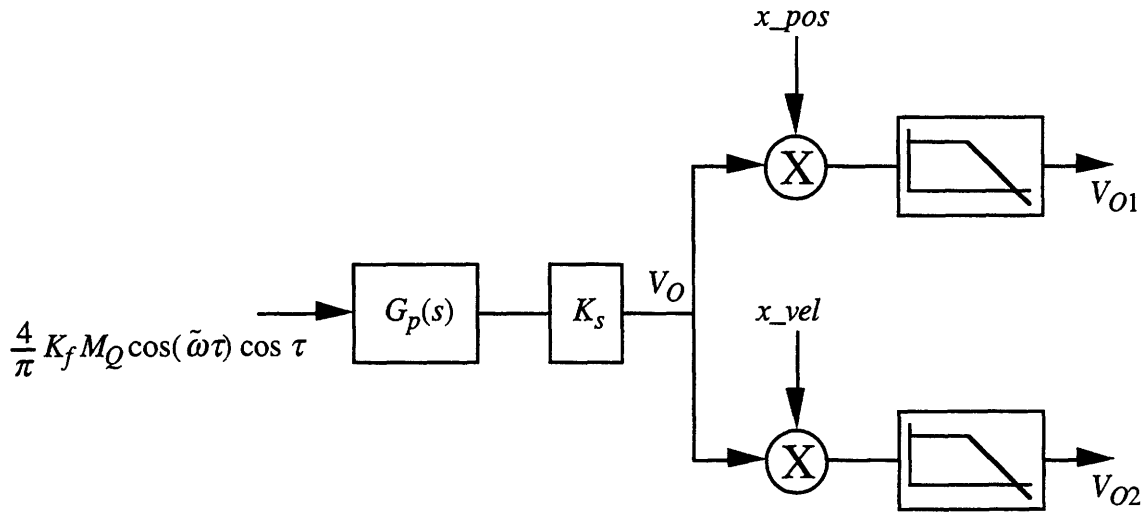
Figure 5.2. Block Diagram Between Error Signals and Demodulation Outputs

An input error force

$$F_{err} = \frac{4}{\pi}K_fM_Q\cos\tilde{\omega}\tau\cos\tau \qquad (5.21)$$

into the plant $G_p(s)$ may be rewritten as

$$F_{err} = \frac{2}{\pi}K_fM_Q\left(\cos(1+\tilde{\omega})\tau + \cos(1-\tilde{\omega})\tau\right) \qquad (5.22)$$

After the SEO plant, the parallel demodulations by x_pos and x_vel yield the transfer functions

$$\frac{V_{O1}}{M_Q} = \frac{4K_sK_f}{\pi^2}\left[G_p(+) + G_p^*(-)\right] \tag{5.23}$$

$$\frac{V_{O2}}{M_Q} = j\frac{4K_sK_f}{\pi^2}\left[G_p(+) - G_p^*(-)\right] \tag{5.24}$$

In addition, for an error force

$$F_{err} = \frac{4}{\pi}K_f M_{IP}\sin\tilde{\omega}\tau\sin\tau \tag{5.25}$$

the transfer functions are

$$\frac{V_{O1}}{M_{IP}} = -j\frac{4K_sK_f}{\pi^2}\left[G_p(+) - G_p^*(-)\right] \tag{5.26}$$

$$\frac{V_{O2}}{M_{IP}} = \frac{4K_sK_f}{\pi^2}\left[G_p(+) + G_p^*(-)\right] \tag{5.27}$$

This result is quite convenient. Since these transfer functions are identical to those derived above, the closed-loop system of Figure 5.1 may be redrawn as Figure 5.3 [8, 27, 36, 37].
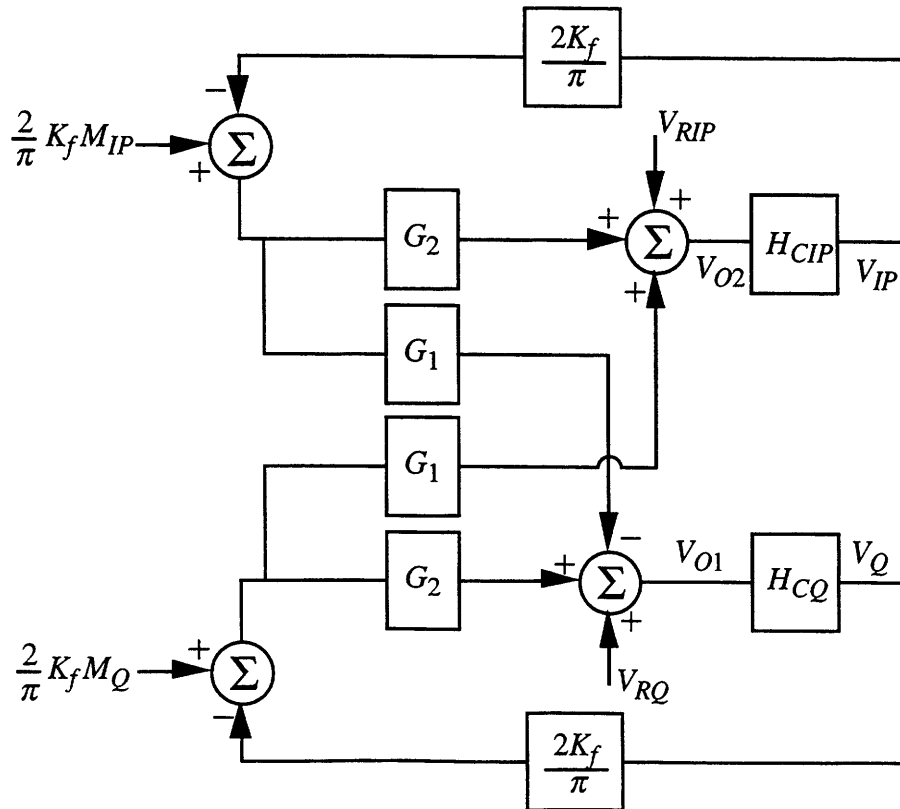
Figure 5.3. Simplified Block Diagram for Vertical and Rotational Control

In this figure, the transfer functions G_1 and G_2 may be expressed in terms of the baseband plant responses

$$G_1 = j\frac{2K_s}{\pi}\left[G_p(+) - G_p^*(-)\right]$$ (5.28)

$$G_2 = \frac{2K_s}{\pi}\left[G_p(+) + G_p^*(-)\right]$$ (5.29)

and,

$G_p(+)$ = evaluation of plant transfer function at $1+\tilde{\omega}$, and

$G_p^*(-)$ = evaluation of complex conjugate of plant transfer function at $1-\tilde{\omega}$.

This block diagram represents the baseband control for both off-drive SEO axes [14, 36].

5.1.2 Analysis of Baseband Transfer Functions

The two baseband transfer functions (G_1 and G_2) derived above are the key to designing adequate compensation for the SEO. Both of these transfer functions may be expanded using the actual plant dynamics. The analysis performed below will use the vertical axis dynamics [14, 36]; a similar derivation exists for the rotational axis.

It is assumed in this section that an adequate control system has been designed to minimize the vertical displacements of the proof mass. With this assumption, the baseband transfer functions will be analyzed and simplified as though the system is linear. After this reduction, compensation will be designed in order to drive the displacements to zero in the presence of sinusoidal disturbances. The reason for this assumption is to provide a basic shape to the control system so that analysis is possible. This is very similar to the "guess a solution and solve" approach learned in first-year calculus.

For a plant transfer function,

$$G_p = \frac{1}{\tilde{s}^2 + \dfrac{\tilde{\omega}_2}{Q_2}\tilde{s} + \tilde{\omega}_2^2}$$ (5.30)

the two transfer functions G_1 and G_2 may be expressed as

$$G_1 = \frac{4K_s}{\pi} \frac{2\tilde{\omega}_d \left(\tilde{s} + \frac{\tilde{\omega}_2}{2Q_2} \right)}{\left[\tilde{s}^2 + \frac{\tilde{\omega}_2}{Q_2}\tilde{s} + \left(\tilde{\omega}_2^2 - \tilde{\omega}_d^2 \right) \right]^2 + 4\tilde{\omega}_d^2 \left(\tilde{s} + \frac{\tilde{\omega}_2}{2Q_2} \right)^2} \qquad (5.31)$$

$$G_2 = \frac{4K_s}{\pi} \frac{\tilde{s}^2 + \frac{\tilde{\omega}_y}{Q_2}\tilde{s} + \left(\tilde{\omega}_2^2 - \tilde{\omega}_d^2 \right)}{\left[\tilde{s}^2 + \frac{\tilde{\omega}_2}{Q_2}\tilde{s} + \left(\tilde{\omega}_2^2 - \tilde{\omega}_d^2 \right) \right]^2 + 4\tilde{\omega}_d^2 \left(\tilde{s} + \frac{\tilde{\omega}_2}{2Q_2} \right)^2} \qquad (5.32)$$

where,

$\tilde{\omega}_d$ = drive axis resonant frequency

$\tilde{\omega}_2$ = vertical (or rotational) axis resonant frequency, and

Q_2 = vertical (or rotational) axis quality factor.

The poles of these transfer functions are simply those of $G_p(+)$ and $G_p^*(-)$, i.e.,

$$\lambda = -\frac{\tilde{\omega}_2}{Q_2} \pm j \left[\tilde{\omega}_2 \sqrt{1 - \frac{1}{4Q_2^2}} \pm \tilde{\omega}_d \right] \qquad (5.33)$$

For large Q_2, the poles become

$$\lambda_{1,2} = -\frac{\tilde{\omega}_2}{Q_2} \pm j \left[\tilde{\omega}_2 - \tilde{\omega}_d - \frac{\tilde{\omega}_2}{8Q_2^2} \right] \qquad (5.34)$$

$$\lambda_{3,4} = -\frac{\tilde{\omega}_2}{Q_2} \pm j \left[\tilde{\omega}_2 + \tilde{\omega}_d - \frac{\tilde{\omega}_2}{8Q_2^2} \right] \qquad (5.35)$$

For $\tilde{\omega}_2$ nearly equal to $\tilde{\omega}_d$, the second pair of eigenvalues ($\lambda_{3,4}$) is attenuated by the low-pass filter and may be neglected in further analyses. Using the large Q_2 assumption again, and by keeping the DC gains equal between the full- and reduced-order transfer functions, G_1 and G_2 may be reduced to

$$G_1 = \frac{4K_s}{\pi} \frac{2\tilde{\omega}_d}{\left(\tilde{\omega}_2 + \tilde{\omega}_d \right)^2} \frac{\left(\tilde{s} + \frac{\tilde{\omega}_2}{2Q_2} \right)}{\tilde{s}^2 + \frac{\tilde{\omega}_2}{Q_2}\tilde{s} + \left(\frac{\tilde{\omega}_2}{2Q_2} \right)^2 + \left(\tilde{\omega}_2 - \tilde{\omega}_d \right)^2} \qquad (5.36)$$

$$G_2 = \frac{4K_s}{\pi} \frac{1}{\left(\tilde{\omega}_2 + \tilde{\omega}_d \right)^2} \frac{\tilde{s}^2 + \frac{\tilde{\omega}_2}{Q_2}\tilde{s} + \left(\tilde{\omega}_2^2 - \tilde{\omega}_d^2 \right)}{\tilde{s}^2 + \frac{\tilde{\omega}_2}{Q_2}\tilde{s} + \left(\frac{\tilde{\omega}_2}{2Q_2} \right)^2 + \left(\tilde{\omega}_2 - \tilde{\omega}_d \right)^2} \qquad (5.37)$$

The ratio of G_2 to G_1 may be expressed as

$$\frac{G_2}{G_1} = \frac{s^2 + \dfrac{\tilde{\omega}_2}{Q_2}s + \left(\tilde{\omega}_2^2 - \tilde{\omega}_d^2\right)}{2\tilde{\omega}_d\left(s + \dfrac{\tilde{\omega}_2}{2Q_2}\right)}$$

(5.38)

For small $\tilde{s}$ ($\tilde{\omega} \ll 1$), this ratio may be approximated as

$$\frac{G_2}{G_1} \approx Q_2\frac{\tilde{\omega}_2^2 - \tilde{\omega}_d^2}{\tilde{\omega}_d\tilde{\omega}_2}$$

(5.39)

In typical oscillators, there is about a 9% separation between the drive and vertical resonant frequencies, and the quality factor of the vertical axis is about 30,000 when operating. Therefore, G_2 is much greater than G_1, and the two loops may be considered independent. For the above vertical dynamic parameters, the ratio of G_2 to G_1 is about equal to 5200. Since G_2 is the plant transfer function and G_1 is the coupling transfer function, this ratio is large enough to minimize the effects of coupling.

A concern may arise that if one phase-dependent (in-phase or quadrature) force is much greater than the other, then the coupling effect may be significant. A typical quadrature displacement may be on the order of 0.25 μm. If the in-phase amplitude was about 5 Å, then the G_1 coupled force would be one-tenth of the in-loop G_2 force. That is, if the in-phase force is 1/520 of the quadrature force, then the ratio of in-phase to quadrature effects in V_{Q2} would be 10. However, the resulting in-phase forces are at least 100 times greater, so that the cross-coupling effects of G_1 may be neglected. In the closed-loop systems, if both the in-phase and quadrature components are driven to zero, then the G_1 coupling is still not significant.

5.1.3 Development of Feedback Model for Vertical Control

By first determining the closed-loop transfer functions for each loop in Figure 5.3, then by writing the equations in matrix form, and finally, by inverting to isolate V_{IP} and V_Q, the following transfer functions may be derived [14, 36]:

$$\begin{bmatrix} V_{IP} \\ V_Q \end{bmatrix} =$$

$$4K_f^2 \frac{\begin{bmatrix} \dfrac{\pi}{2K_f} + G_2 H_{CQ} & -G_1 H_{CIP} \\ G_1 H_{CQ} & \dfrac{\pi}{2K_f} + G_2 H_{CIP} \end{bmatrix} \begin{bmatrix} H_{CIP}\left(G_2 M_{IP} + G_1 M_Q + \dfrac{\pi}{2K_f} V_{RIP} \right) \\ H_{CQ}\left(-G_1 M_{IP} + G_2 M_Q + \dfrac{\pi}{2K_f} V_{RQ} \right) \end{bmatrix}}{\left(\left(\pi + 2K_f G_2 H_{CQ} \right)\left(\pi + 2K_f G_2 H_{CIP} \right) + 4\left(K_f G_1 \right)^2 H_{CQ} H_{CIP} \right)} \tag{5.40}$$

This matrix expression may be multiplied to find transfer functions between the control voltages (V_{IP} and V_Q) and both the disturbances (M_{IP} and M_Q) and the reference voltages (V_{RIP} and V_{RQ}).

$$V_{IP} = \frac{\left(2\pi K_f G_2 H_{CIP} + 4 K_f^2 H_{CIP} H_{CQ}\left(G_1^2 + G_2^2 \right) \right) M_{IP} + 2\pi K_f G_1 H_{CIP} M_Q}{\left(\pi^2 + 2\pi K_f G_2\left(H_{CQ} + H_{CIP} \right) + 4 K_f^2 H_{CIP} H_{CQ}\left(G_1^2 + G_2^2 \right) \right)}$$

$$+ \frac{\left(\pi^2 + 2 K_f G_2 H_{CQ} \right) H_{CIP} V_{RIP} - 2 K_f G_1 H_{CIP} H_{CQ} V_{RQ}}{\left(\pi^2 + 2\pi K_f G_2\left(H_{CQ} + H_{CIP} \right) + 4 K_f^2 H_{CIP} H_{CQ}\left(G_1^2 + G_2^2 \right) \right)} \tag{5.41}$$

$$V_Q = \frac{-2\pi K_f G_1 H_{CQ} M_{IP} + (4 K_f^2 H_{CQ} H_{CIP}(G_1^2 + G_2^2) + 2\pi K_f G_2 H_{CQ}) M_Q}{\left(\pi^2 + 2\pi K_f G_2\left(H_{CQ} + H_{CIP} \right) + 4 K_f^2 H_{CIP} H_{CQ}\left(G_1^2 + G_2^2 \right) \right)}$$

$$+ \frac{2\pi K_f G_1 H_{CQ} H_{CIP} V_{RIP} + \left(\pi^2 + 2\pi K_f G_2 H_{CIP} \right) H_{CQ} V_{RQ}}{\left(\pi^2 + 2\pi K_f G_2\left(H_{CQ} + H_{CIP} \right) + 4 K_f^2 H_{CIP} H_{CQ}\left(G_1^2 + G_2^2 \right) \right)} \tag{5.42}$$

In this control system, both V_{RIP} and V_{RQ} are zero. If $G_2 \gg G_1$, as shown above, then Equations 5.41 and 5.42 simplify to

$$V_{IP} = \frac{2 K_f G_2 H_{CIP}}{\pi + 2 K_f G_2 H_{CIP}} M_{IP} + \frac{2\pi K_f G_1 H_{CIP}}{\left(\pi + 2 K_f G_2 H_{CQ} \right)\left(\pi + 2 K_f G_2 H_{CIP} \right)} M_Q$$

$$\approx \frac{2 K_f G_2 H_{CIP}}{\pi + 2 K_f G_2 H_{CIP}} M_{IP} \tag{5.43}$$

$$V_Q = \frac{2K_f G_2 H_{CQ}}{\left(\pi + 2K_f G_2 H_{CQ}\right)} M_Q - \frac{2\pi K_f G_1 H_{CQ}}{\left(\pi + 2K_f G_2 H_{CQ}\right)\left(\pi + 2K_f G_2 H_{CIP}\right)} M_{IP}$$

$$\approx \frac{2K_f G_2 H_{CQ}}{\left(\pi + 2K_f G_2 H_{CQ}\right)} M_Q \tag{5.44}$$

In both of these equations, as the baseband frequency $\tilde{\omega}$ goes to zero, the cross-coupling gain of the quadrature into the in-phase control voltage (and vice-versa) goes to zero, and the in-channel gain goes to one. As $\tilde{\omega}$ goes to infinity, both gains go to zero.

The open-loop transfer function for both loops is $2K_F H_{Ci} G_2/\pi$, where i represents either quadrature or in-phase. The appropriate compensator in this system is chosen as an integrator with recovery, i.e., a proportional plus integral controller with a low-pass element

$$H_C = K_C \frac{\left(s + \omega_z\right)}{s\left(s + \omega_p\right)} \tag{5.45}$$

where,

ω_z = 1 rad/sec, and

ω_p = 45 rad/sec.

The choice of these frequencies is somewhat arbitrary, and is driven mainly by the desired frequency response of the system. As long as the pole and zero are less than the resonant frequency of the second-order poles, then the final choice may be made based on the phase and magnitude responses. If the controller is non-dimensionalized, the transfer function becomes

$$\tilde{H}_C = \frac{K_C}{\omega_n} \frac{\left(\tilde{s} + \tilde{\omega}_z\right)}{\tilde{s}\left(\tilde{s} + \tilde{\omega}_p\right)} \tag{5.46}$$

The frequency response of the open-loop transfer function for this controller is shown in Figures 5.4a and 5.4b for an assumed controller gain, K_C, of 1. From this plot, it is clear that, in order to guarantee stability, the magnitudes at the -180° phase frequencies must be less than 0 dB. By choosing the proper K_C, the open-loop stability of the system can be guaranteed. The magnitude response crosses below .707 times its DC value twice; once at 286.5 Hz, and again at 1923 Hz. The bandwidth of the open-loop transfer function, defined from the error force input to the control force, is therefore 1923 Hz.
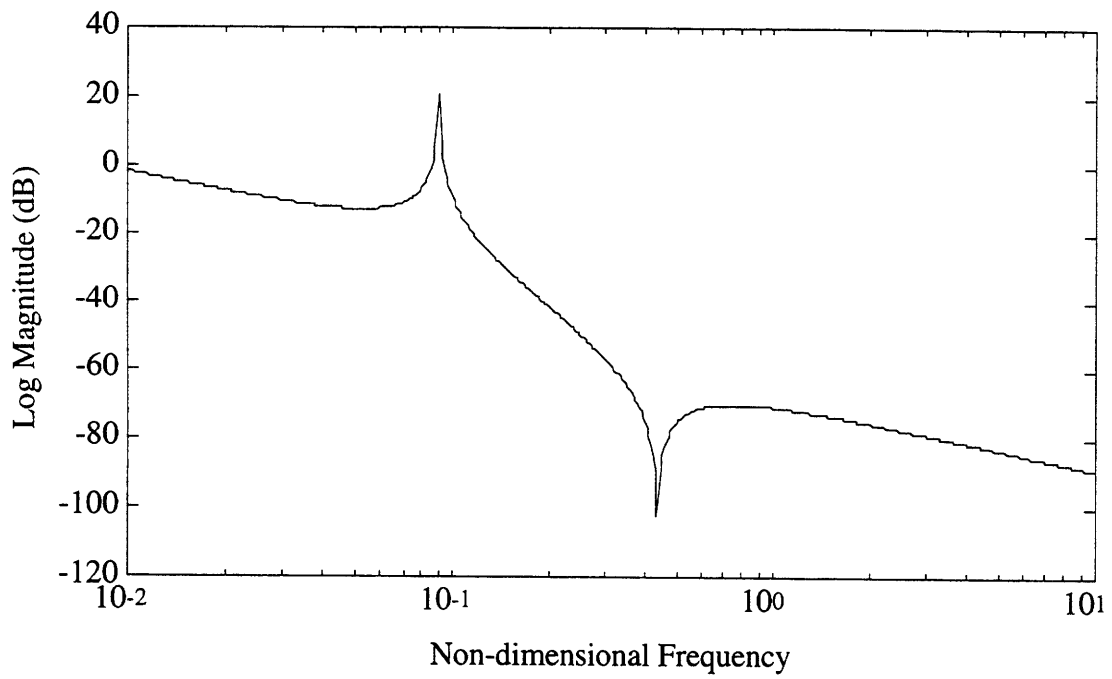
Figure 5.4a. Bode Magnitude of Open-Loop Transfer Function
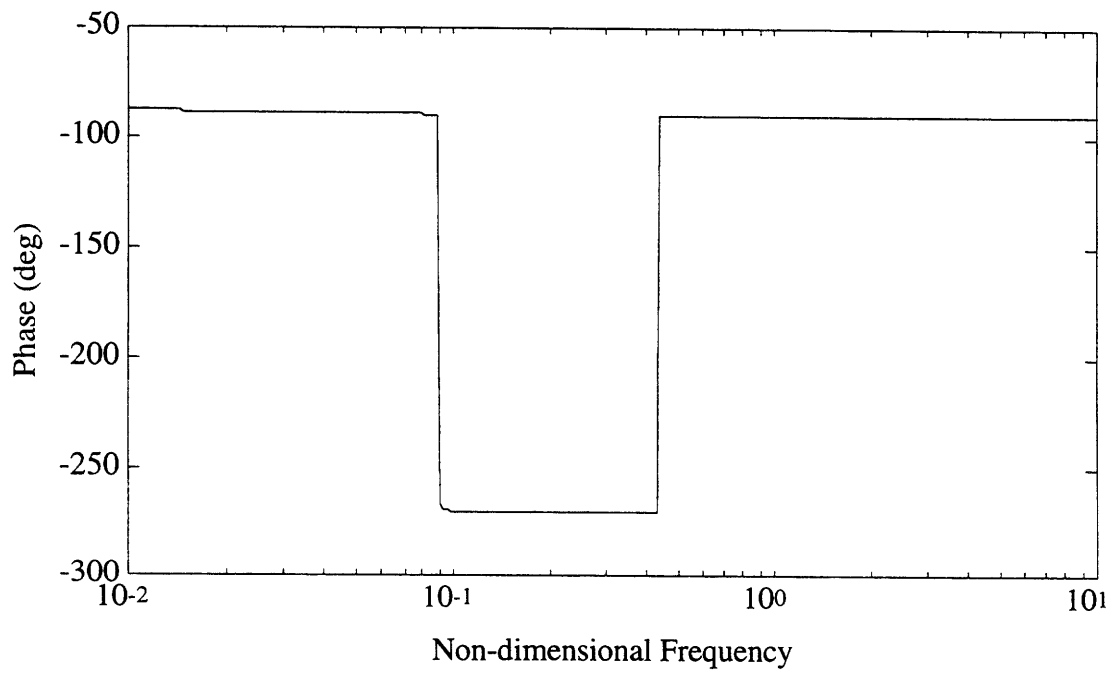
Figure 5.4b. Bode Phase of Open-Loop Transfer Function

174

The magnitude of the $-180°$ crossover point at the zero location, ω_z, is less than 0 dB by construction. The design choice is to pick K_C such that, at $\omega = \omega_2 - \omega_d$, the resonant peak is less than 0 dB[2]. At this peak, the value of the open-loop transfer function is

$$\|OL(\tilde{s})\| = \left\|\frac{2K_f}{\pi}\tilde{H}_C(\tilde{s})G_2(\tilde{s})\right\|_{\tilde{s}=(\tilde{\omega}_2-\tilde{\omega}_d)j}$$

$$\approx \frac{16K_fK_s}{\pi^2}\frac{Q_2\tilde{\omega}_d}{\omega_d\tilde{\omega}_2(\tilde{\omega}_2-\tilde{\omega}_d)(\tilde{\omega}_2+\tilde{\omega}_d)^2}K_C \qquad (5.47)$$

For stability, this gain must be less than 0 dB. Therefore, by chosing a proper K_C, the closed-loop control system will be stable. For typical values on the vertical axis, this leads to a maximum K_C of 600. For this value of K_C, the bandwidth of the closed-loop controller is 5771 Hz.

This PI controller may be implemented about an operational amplifier as shown in Figure 5.5.
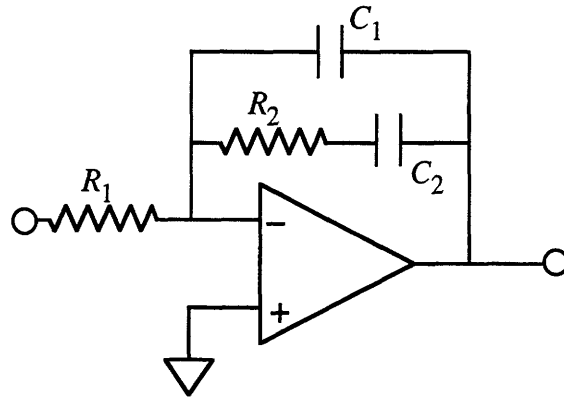
Figure 5.5. Amplitude Proportional Plus Integral Control Schematic

Here, the values R_1 and C_1 determine both the gain and contribute to the location of the pole. The impedence values R_2 and C_2 define the zero and aid in determining the location of the pole, as shown in Equation 5.48

$$H_C(s) = \frac{1}{R_1C_1}\frac{s+\dfrac{1}{R_2C_2}}{s\left(s+\dfrac{1}{R_2C_2}+\dfrac{1}{R_2C_1}\right)} \qquad (5.48)$$

$$= K_C\frac{s+\omega_z}{s(s+\omega_p)}$$

---

[2]Assumes a 9% separation between the lateral and vertical frequencies.

175

For the SEO, some reasonable choices for the impedences are $R_1 = 10$ kΩ, $C_1 = 0.022$ μF, $R_2 = 1$ MΩ, $C_2 = 1$ μF. These values may be used for both the quadrature and in-phase paths of the rotational and vertical control loops. In the actual construction of the control system, a potentiometer is used in place of R_1 to permit fine tuning of the compensator gain. With this choice of C_1, the maximum possible R_1 that guarantees stability is 75 kΩ. The value for R_1 was chosen to optimize the response of the closed-loop control system.

5.1.4 Simulation of Vertical Control System

The simulation introduced in Chapter 3 and expanded in Chapter 4 was modified again to include this vertical control system, using the dynamic model developed in Chapter 2. Later in this chapter, the 3 DOF dynamic model will be used for both vertical and rotational control system simulations. The nominal parameters for the vertical control simulations are listed in Table 5.1[3]. In this table, the value for Q_{xy} is very large because there is little cross-damping between the x and y coordinates[4]. The parameter β_x is the coupling of the drive force into the vertical axis. These two terms contribute to in-phase error forces; $\tilde{\omega}_{xy}$ generates undesirable quadrature motion.

Table 5.1. Non-dimensional Parameters for Vertical Control Simulations

Parameter	Value
$\tilde{\omega}_x$	1
$\tilde{k}_{x3}$	0.025
Q_x	150,000
$\tilde{\omega}_y$	1.09
Q_y	30,000
$\tilde{\omega}_{xy}^2$	0.003
Q_{xy}	5,000,000
β_x	0.5

The characteristics of the four closed-loop simulations are listed in Table 5.2. In the first run, the system was run with both in-phase and quadrature disturbances. In the second run, only disturbances in-phase with the proof mass horizontal velocity were

---

[3] A complete list of parameter values may be found in the MATLAB™ code of Appendix C.
[4] The damping varies as $1/Q_{xy}$.

permitted. For the third run, only disturbances in quadrature with the proof mass horizontal velocity were used. In the final run, at $\tau = 10^5$ non-dimensional seconds, the cross-coupling spring term was increased by 25%.

Table 5.2. Vertical Control Simulation Characteristics

Test Run	Characteristics
1	All parameters at nominal values
2	Quadrature disturbances set to zero
3	In-phase disturbances set to zero
4	At $\tau = 10^5$ sec, increase $\tilde{\omega}_{xy}^2$ by 25%

Plots of these simulations, including the in-phase and quadrature control voltages, are shown in Figures 5.6 through 5.25. Comparisons are made with open-loop responses, when applicable. A summary of all four simulations is presented in Table 5.3.

5.1.4.1 Vertical Control with In-Phase and Quadrature Disturbances

In the first simulation, the nominal parameters were used for all values. The results of this simulation are shown in Figures 5.6 through 5.11. In Figure 5.6, the open-loop, steady-state, non-dimensional amplitude of the vertical motion is about 0.0182, which is equal to 0.182 μm. With the control loop closed (Figure 5.7), the amplitude standard deviation has a non-dimensional value of 2.0323×10^{-4}, or 2 nm, which is about a factor of 90 reduction in amplitude. The standard deviation is 20 times the magnitude of the noise because the quadrature disturbances and control voltages[5] couple into the in-phase control loop, which generates an in-phase control force that is not balanced by an actual in-phase error force. There is also a steady-state displacement of the proof mass towards the sense plate, due the negative spring effect of the control plate. The non-dimensional offset is -2.7386×10^{-3}, or -27.4 nm. The open and closed-loop steady-state responses are compared in the phase-plane plot of Figure 5.8, which dramatically illustrates the reduction in the steady-state amplitude of the vertical motion.

---

[5]The control voltages can couple due to phase errors in the remodulation and low-pass filters.
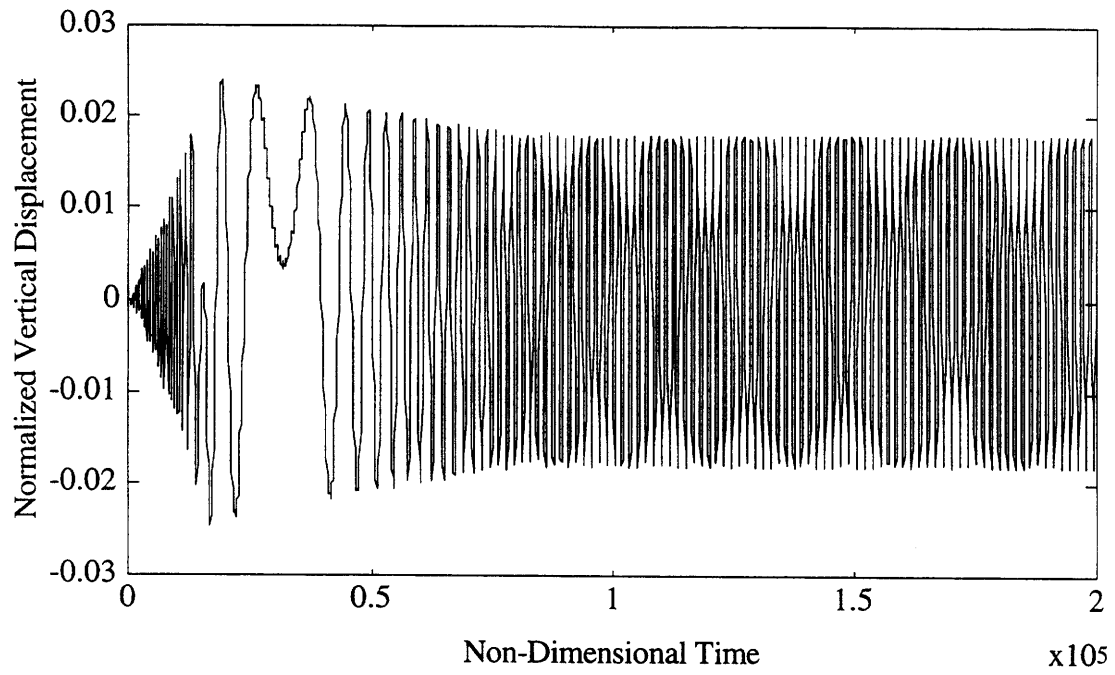
Figure 5.6. Open-Loop Response of Vertical Axis
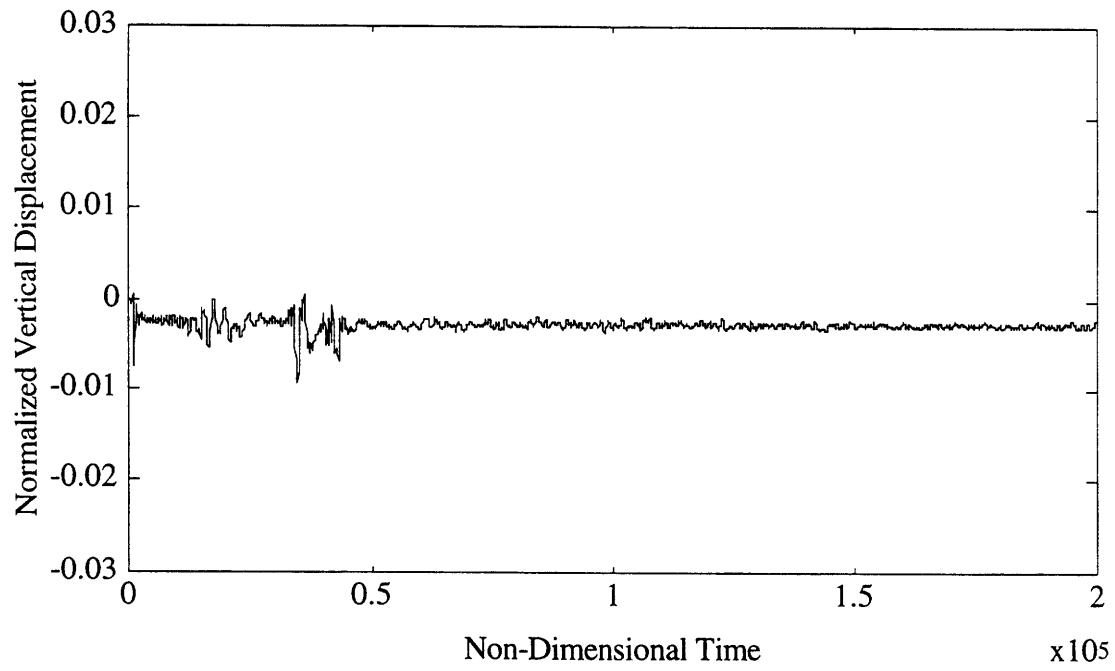
Figure 5.7. Closed-Loop Response of Vertical Axis
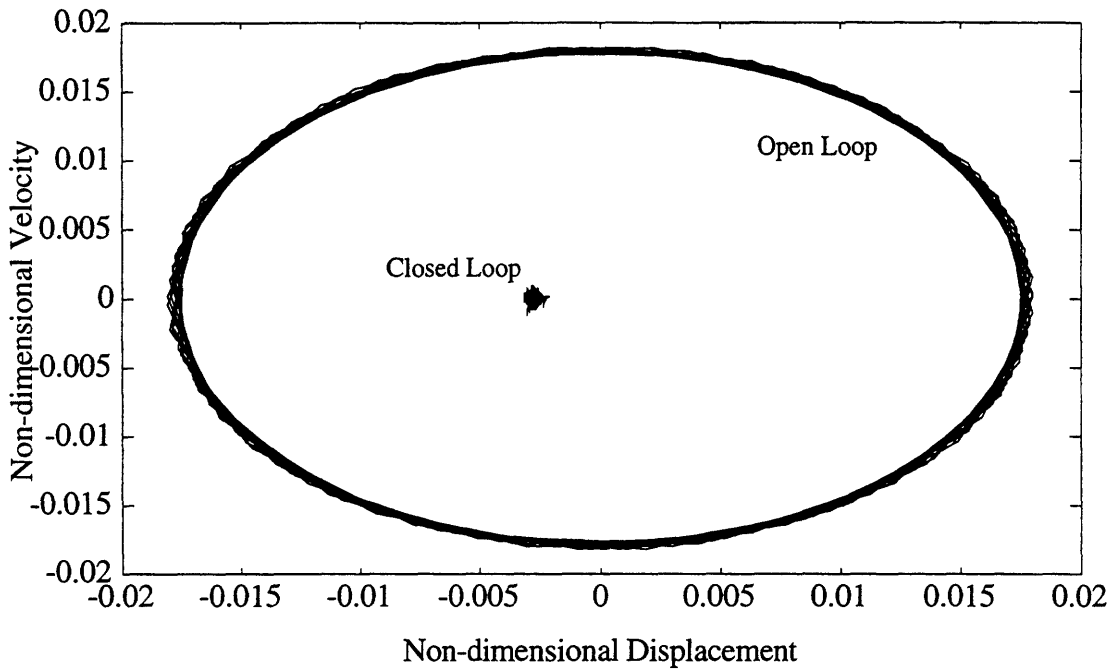
Figure 5.8. Phase Plane of Open and Closed-Loop Vertical Motion

The control voltages for both the in-phase and quadrature signals are shown in Figures 5.9 and 5.10. Here, since the quadrature is the main contributor to the vertical oscillations, its voltage has a large value of -4.1±0.0054 Volts. The in-phase control signal is smaller, at -0.0646±0.0064 Volts. The in-phase signal is slightly more noisy because of cross-coupling between the quadrature and in-phase signals, as discussed in the previous section. It was assumed above that the two control systems may be assumed to be independent, since the Q of the system was sufficiently high. However, there is still some cross-coupling and low-pass filter phase shift, and that causes a slight deterioration in the performance of the control system, especially along the in-phase loop. The horizontal motion of the system is not affected by the implementation of this control system, as shown in Figure 5.11.
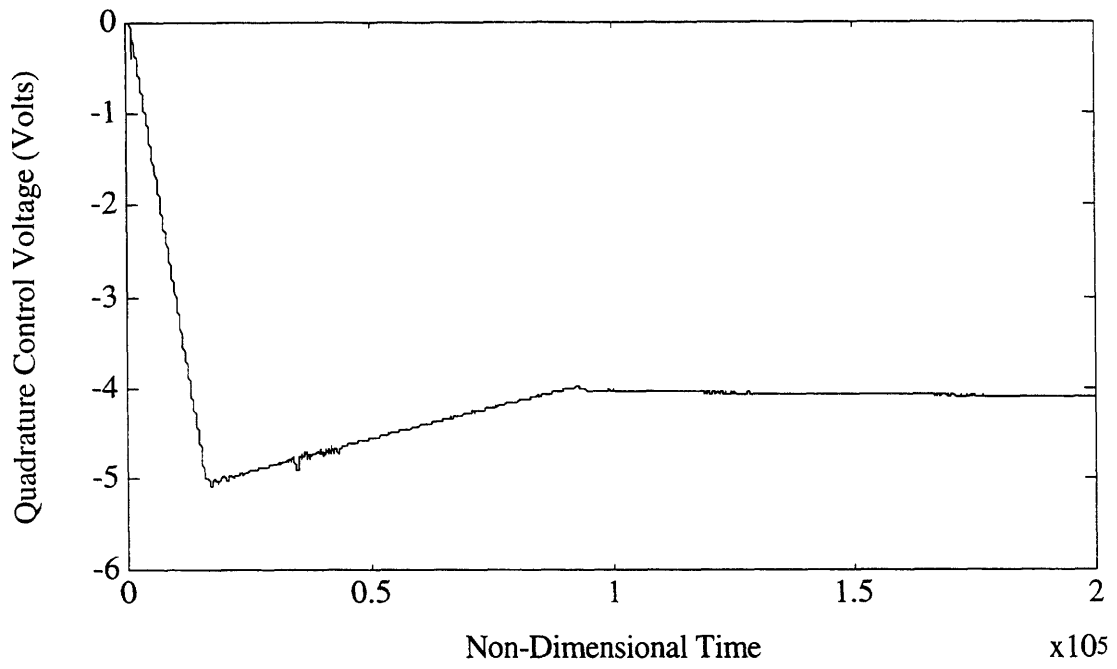
Figure 5.9. Vertical Quadrature Control Signal
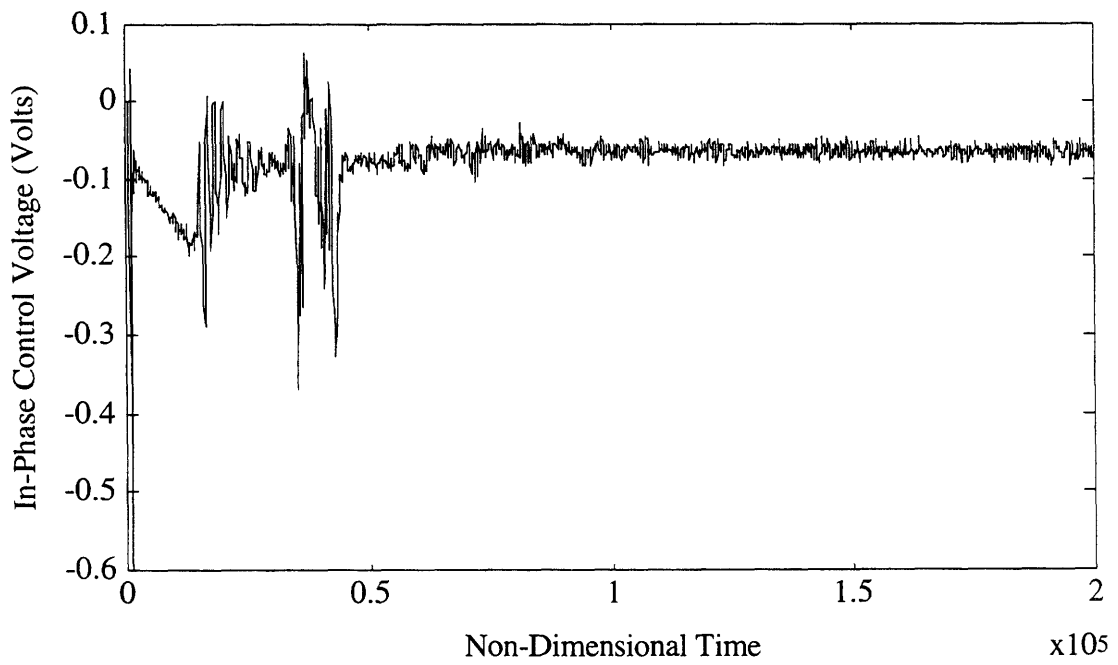
Figure 5.10. Vertical In-Phase Control Signal

180
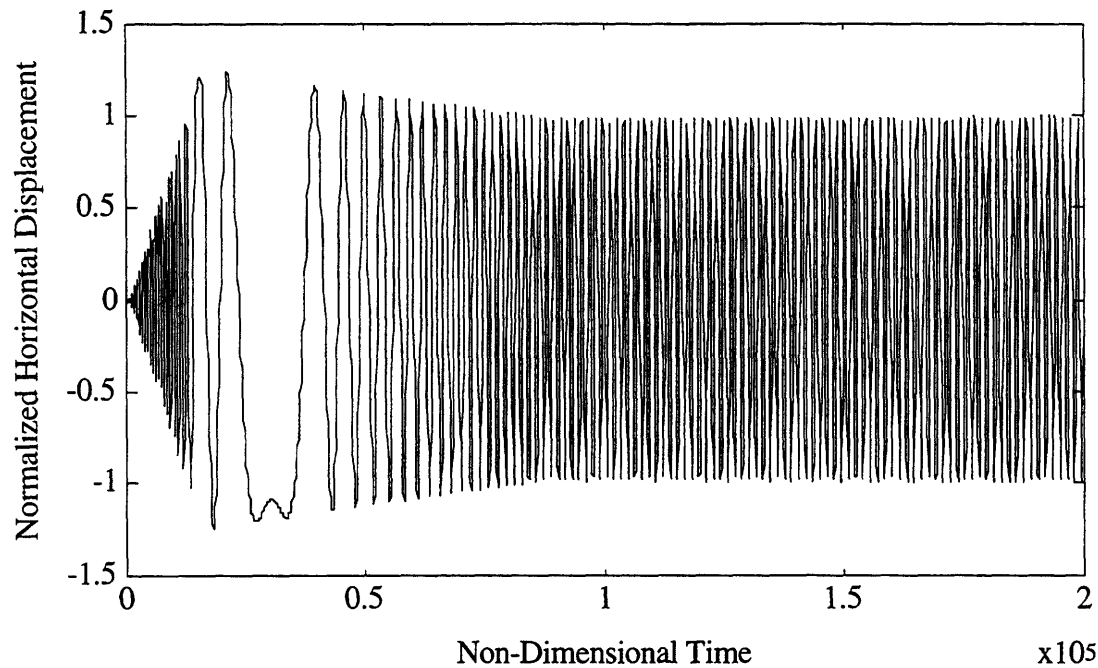
Figure 5.11. Horizontal Motion for Closed Vertical Loop

5.1.4.2 Vertical Control with Quadrature Disturbance Only

In the second simulation, only quadrature disturbances were introduced into the system. The results of this simulation are shown in Figures 5.12 through 5.15. The vertical displacement of Figure 5.12 has been reduced to a DC offset of -28.55 nm, with a standard deviation of 1.97 nm. This response is nearly identical to that of case 1, because the significant error source is the spring cross-coupling, which is present in both cases. The similarity between the two cases is also seen in the phase-plane plot of Figure 5.13.

As discussed earlier, there is some coupling between the in-phase and quadrature, which was assumed to be trivial. However, for no in-phase disturbances, the quadrature coupling can easily be observed in the in-phase channel, as shown in Figure 5.15. Although the in-phase disturbance is zero, a steady-state control voltage of -0.0377±0.0063 Volts is required to eliminate the "spill" from the quadrature channel disturbance and control voltage coupling and low-pass filter phase shift. This is half of the value required in the first case, which means that the quadrature coupling is about equal to the in-phase disturbances. The steady-state quadrature control voltage is -4.0785±0.0055 Volts, which is nearly identical to that of case 1.

181
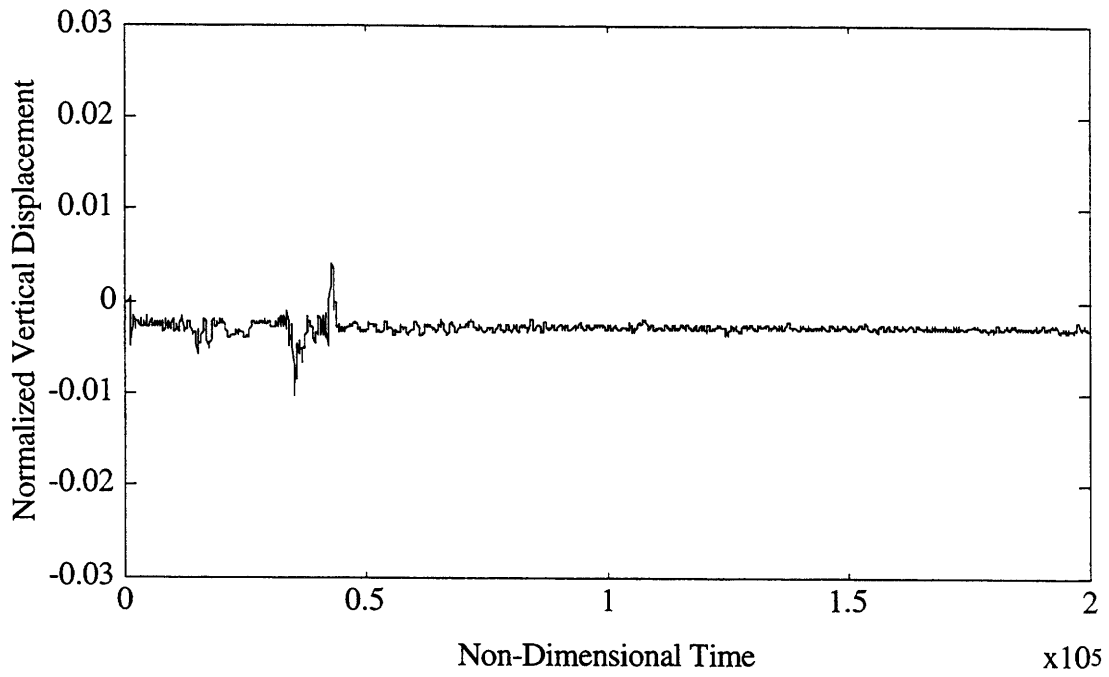
Figure 5.12. Vertical Motion with Quadrature Disturbance Only
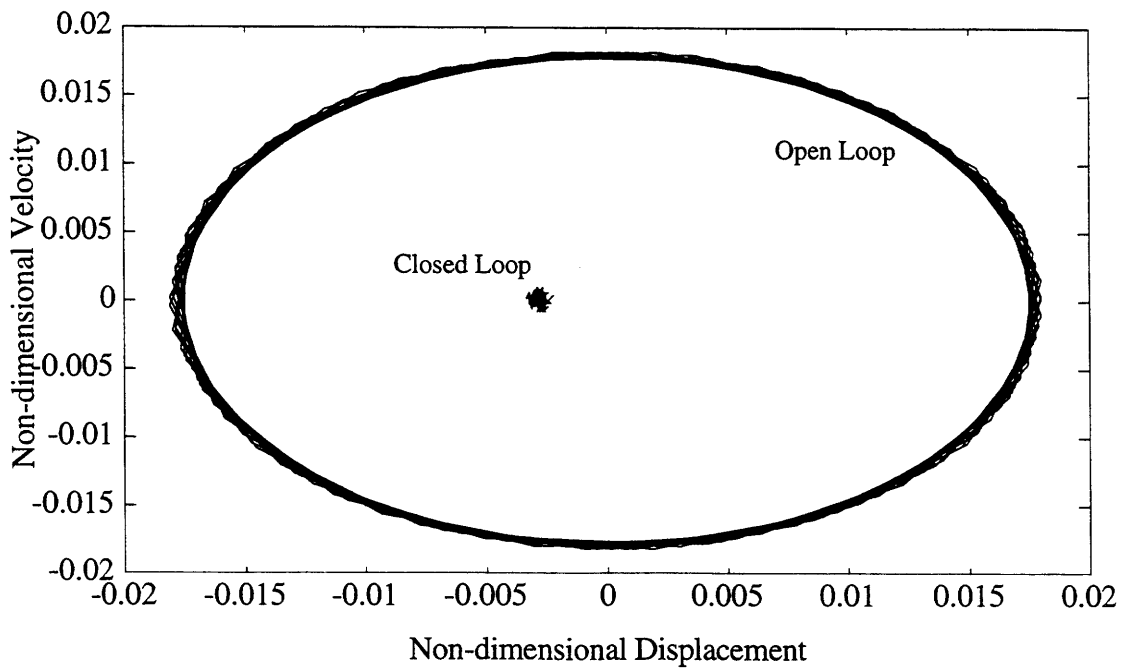
Figure 5.13. Phase Plane with Quadrature Disturbance Only
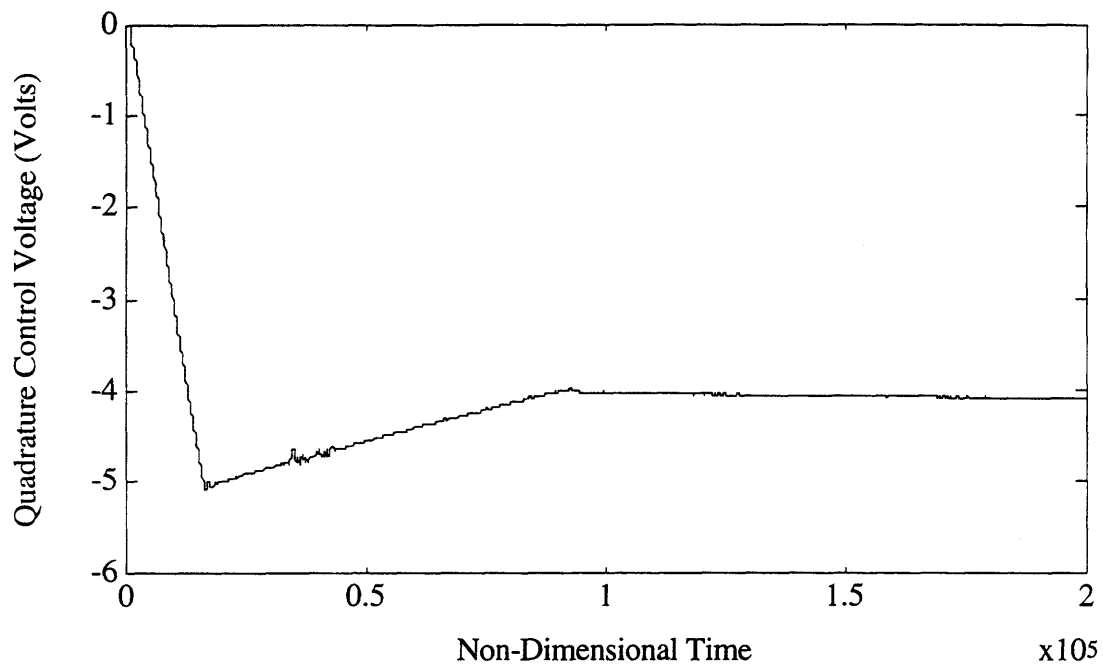
Figure 5.14. Quadrature Control Voltage for Quadrature Disturbance
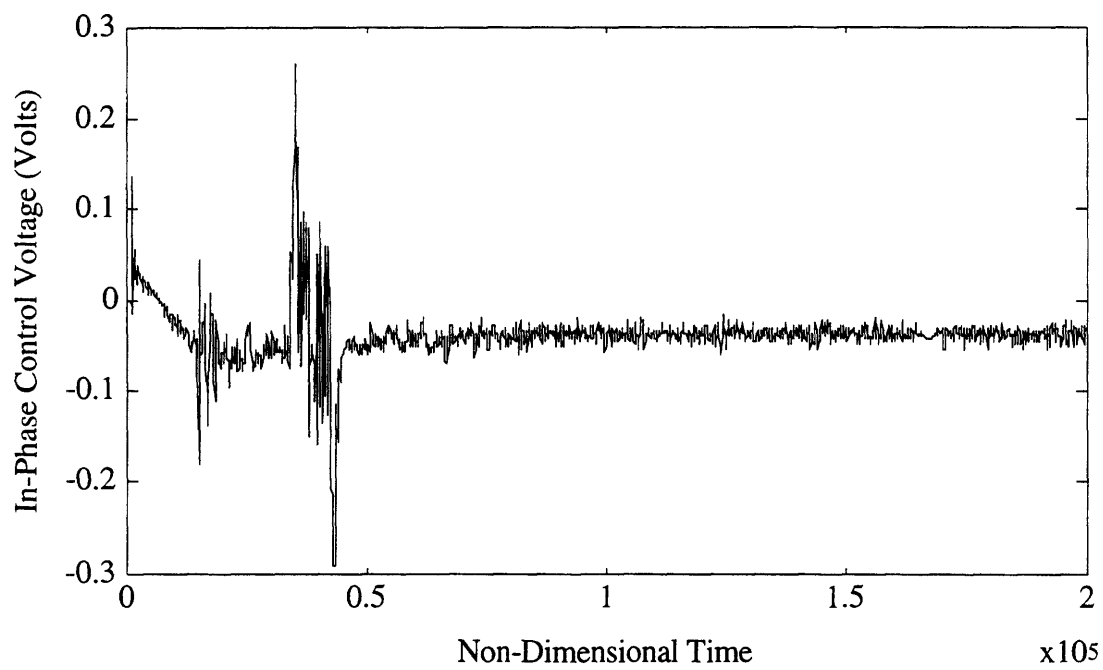
Figure 5.15. In-Phase Control Voltage for Quadrature Disturbance

5.1.4.3 Vertical Control with In-Phase Disturbances Only

The third simulation consists of in-phase disturbances only. These errors come from the damping and force cross-coupling between the horizontal and vertical axes, as well as from Coriolis forces induced by rotation of the device about the z-axis. In this case, the vertical motion of Figure 5.16 (and the phase-plane plot of Figure 5.17) is driven to a steady-state offset of -23.581 nm, with a standard deviation of 3.48 Å. This remarkable performance is due to the low magnitudes of the in-phase error forces and the lack of "spill" from the quadrature signal. The steady-state in-phase control signal is -0.0264±0.0002 Volts, and the quadrature control is 0.0012±0.0001 Volts. From these values, it is clear that the in-phase signal does not couple back into the quadrature channel in a significant amount, because of its small magnitude.

In Figure 5.19, the discontinuity corresponds to the behavior of the self-oscillator and amplitude regulator loops. Once the oscillator has locked onto the low-amplitude resonant frequency, the regulator increases the amplitude to a steady-state value of 1. During the amplitude growth, the magnitude of the in-phase and quadrature vertical error forces are changing, and the reference phase angles used to define these values are also varying due to the nonlinear spring. Once the steady-state amplitude and phase of the drive axis are established, both vertical control loops are able to determine the true phase of the disturbances, and proper control voltages are then applied.
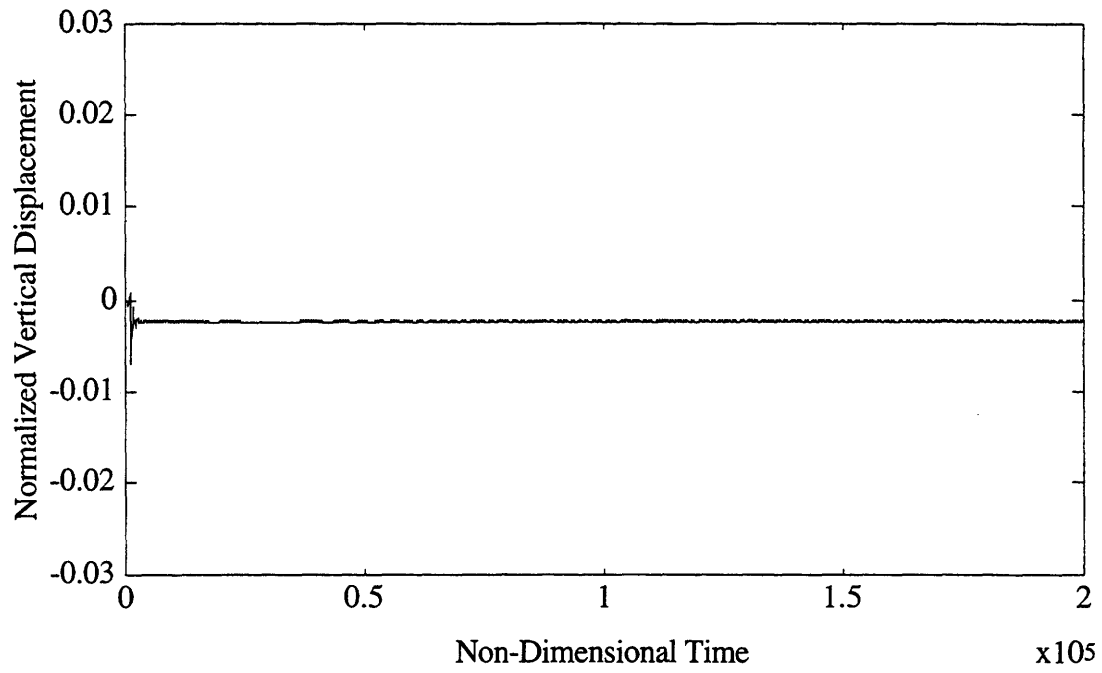
Figure 5.16. Vertical Motion with In-Phase Disturbance Only
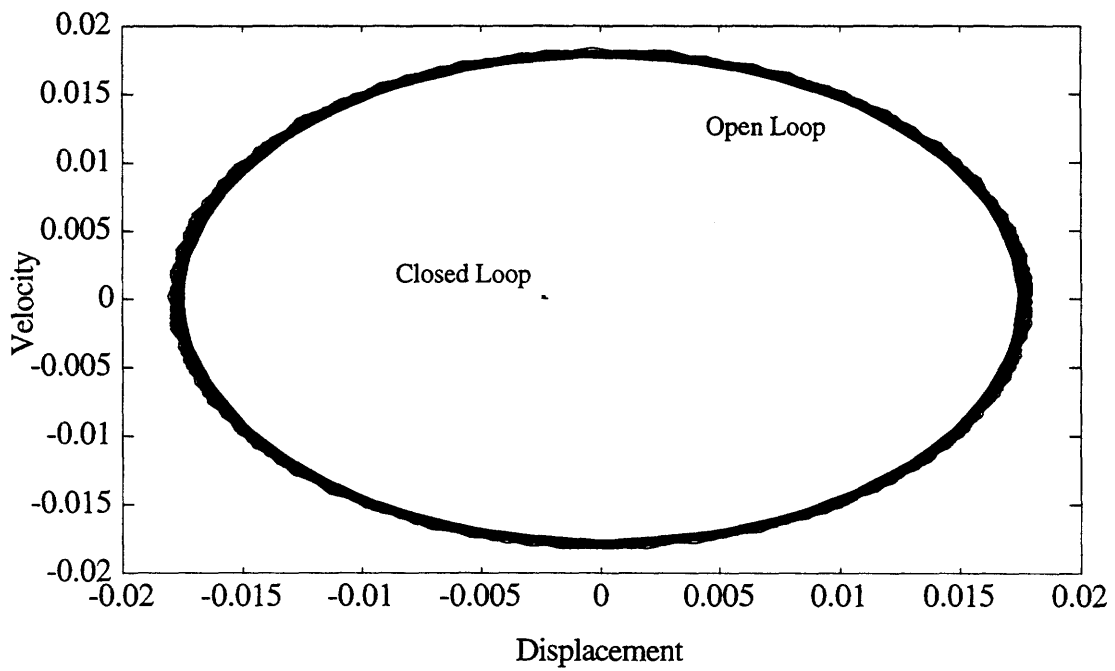
Figure 5.17. Phase Plane for In-Phase Disturbance Only
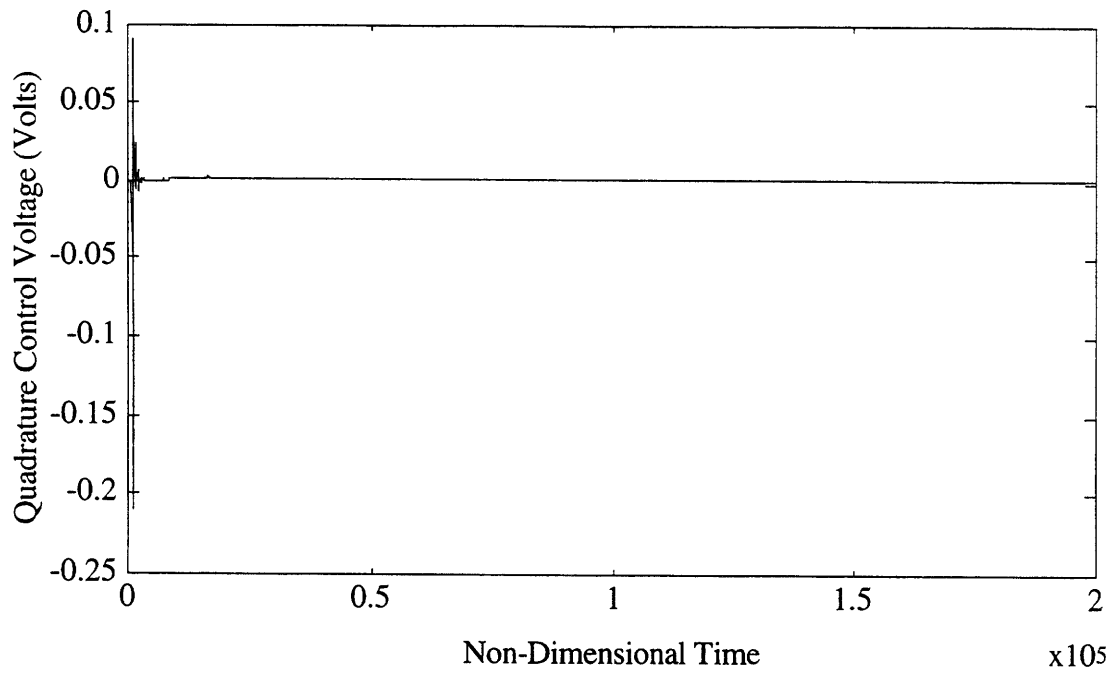
Figure 5.18. Quadrature Control Signal for In-Phase Voltage
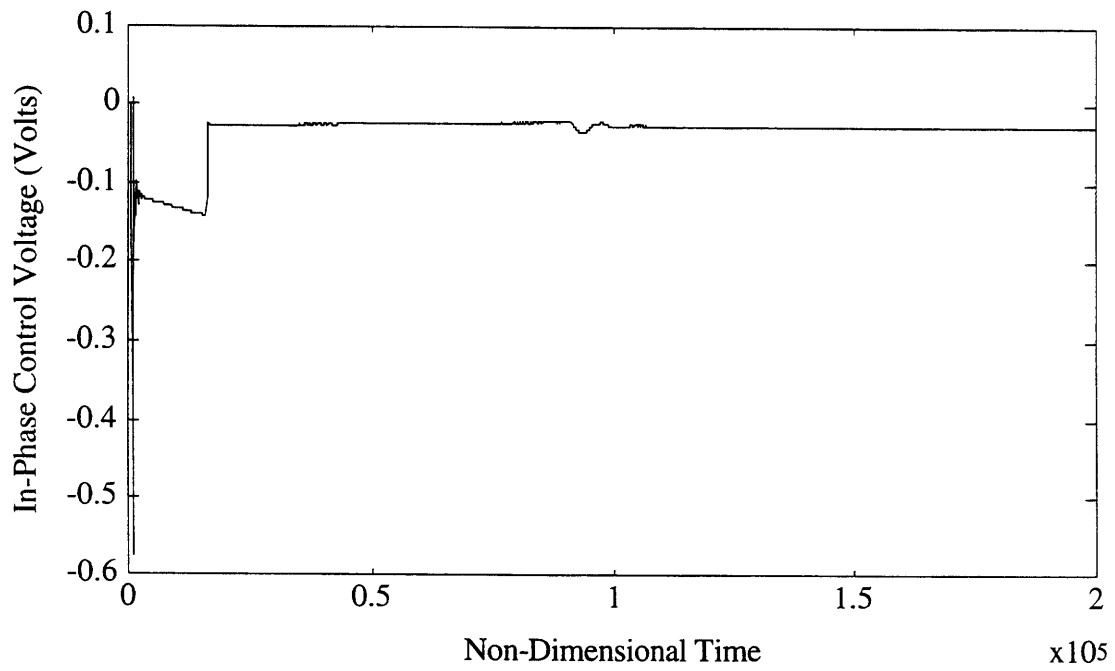
Figure 5.19. In-Phase Control Voltage for In-Phase Disturbance

5.1.4.4 Vertical Control with Variation in Quadrature Disturbance

Finally, the robustness of the vertical control system was examined by increasing the spring cross-coupling of the system by 25% at $\tau = 10^5$ non-dimensional seconds. The vertical motion of the corresponding open-loop situation is shown in Figure 5.20. Before increasing the spring cross-coupling, the open-loop magnitude is 0.182 μm. After the change in k_{xy}, the steady-state displacement amplitude increased to 0.22823 μm. The closed-loop response is shown in Figure 5.21. Before the increase, the vertical DC offset of the proof mass is -27.511 nm with a standard deviation of 3.1347 nm. After increasing k_{xy} and allowing the transients to decay, the DC displacement is -30.001 nm, with a standard deviation of 2.28 nm. Phase-plane responses of the vertical displacement and velocity before and after the change in k_{xy} are shown in Figures 5.22 and 5.23, respectively. In Figure 5.22, the open-loop vertical motion is still settling to a steady-state value, so the open-loop response is not as tight as that seen in Figure 5.23. By examining the closed-loop response before, during and after the change, it is clear that the control system is robust enough to keep y small while the system parameters are varied.

The reason for the improvement in the control is that the quadrature signal has been increased, and the resulting signal to noise ratio is larger. The impact of this increase may be seen in the quadrature and in-phase control signals, shown in Figures 5.24 and 5.25. At $\tau = 10^5$, the quadrature signal reacts instantaneously to the change in k_{xy}. The steady-state value of the quadrature is now -5.1273$\pm$ 0.00434 Volts, which is 25% greater than that for the constant k_{xy} case, which corresponds to case 1. The in-phase control signal is slightly affected by the change in the cross-coupling, with a steady-state value of -0.07392$\pm$0.0076 Volts. This simulation case confirms that the control system will respond proportionally to variations in the system parameters. In Chapter 6, a rate will be applied to the control system to demonstrate that the magnitudes of the in-phase and quadrature signals remains at zero while the in-phase control signal varies to account for the introduction of a time-varying force into the system.

187
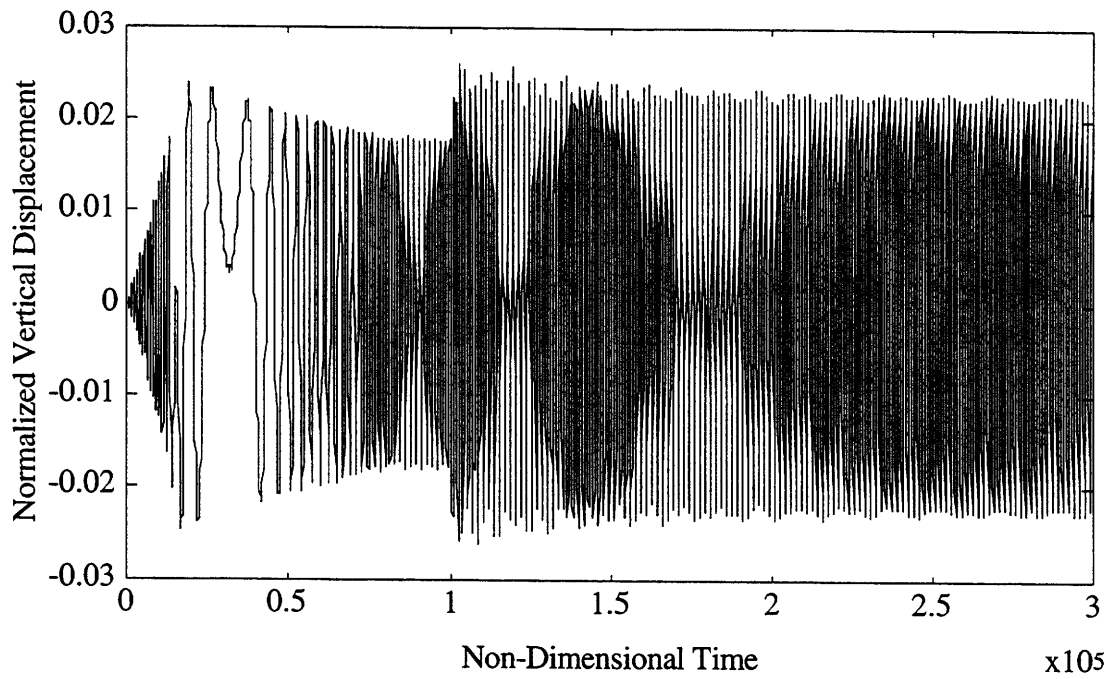
Figure 5.20. Vertical Open-Loop Response for Case 4
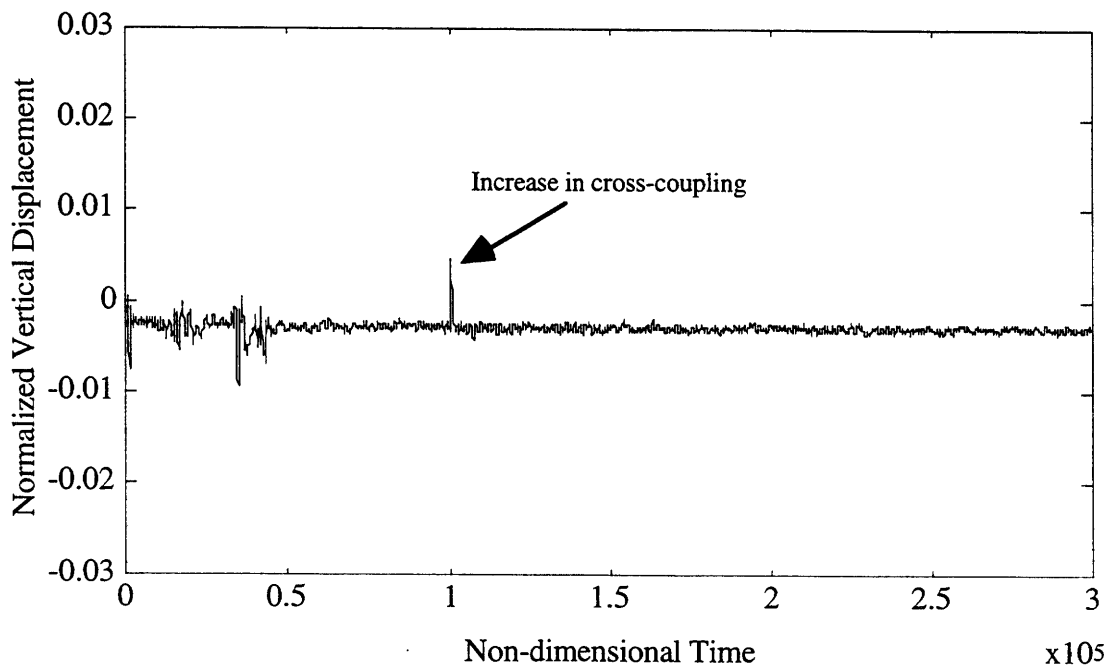
Figure 5.21. Closed-Loop Vertical Response for Case 4
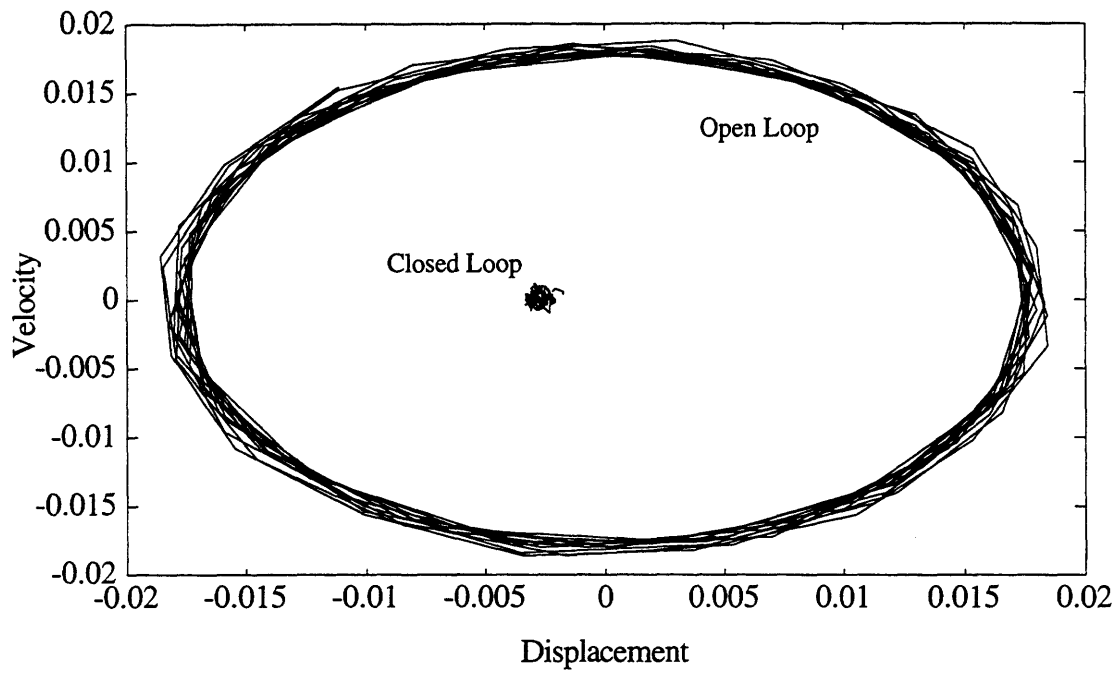
Figure 5.22. Phase-Plane Response before Increasing k_{xy}
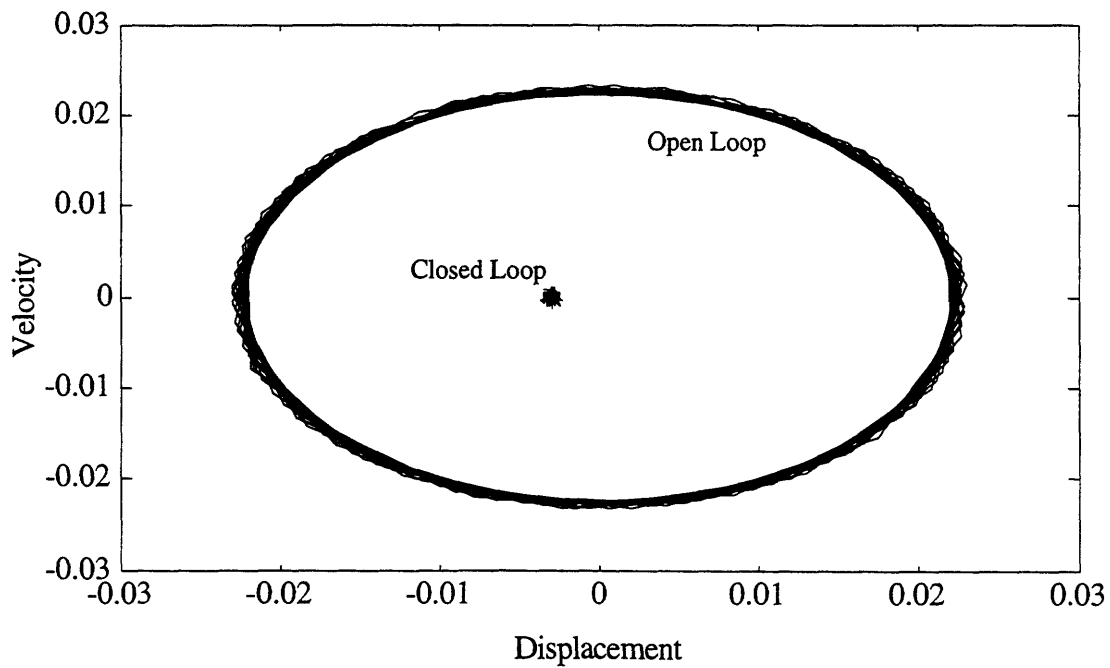
Figure 5.23. Phase-Plane Response after increasing k_{xy}

189
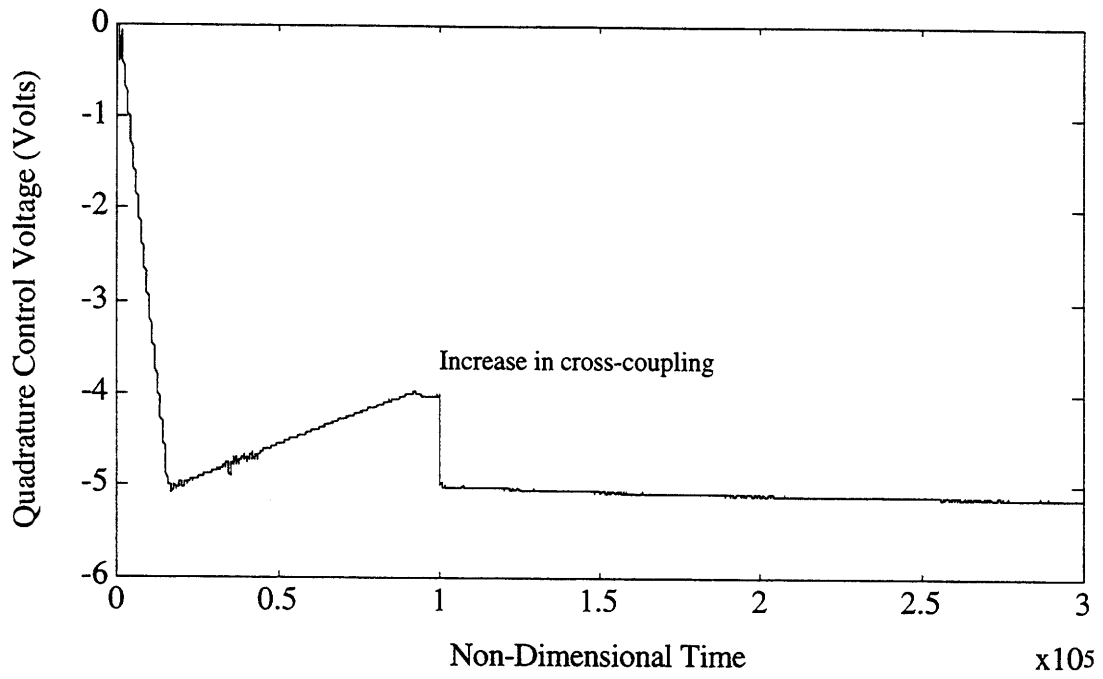
Figure 5.24. Quadrature Control Signal for Case 4
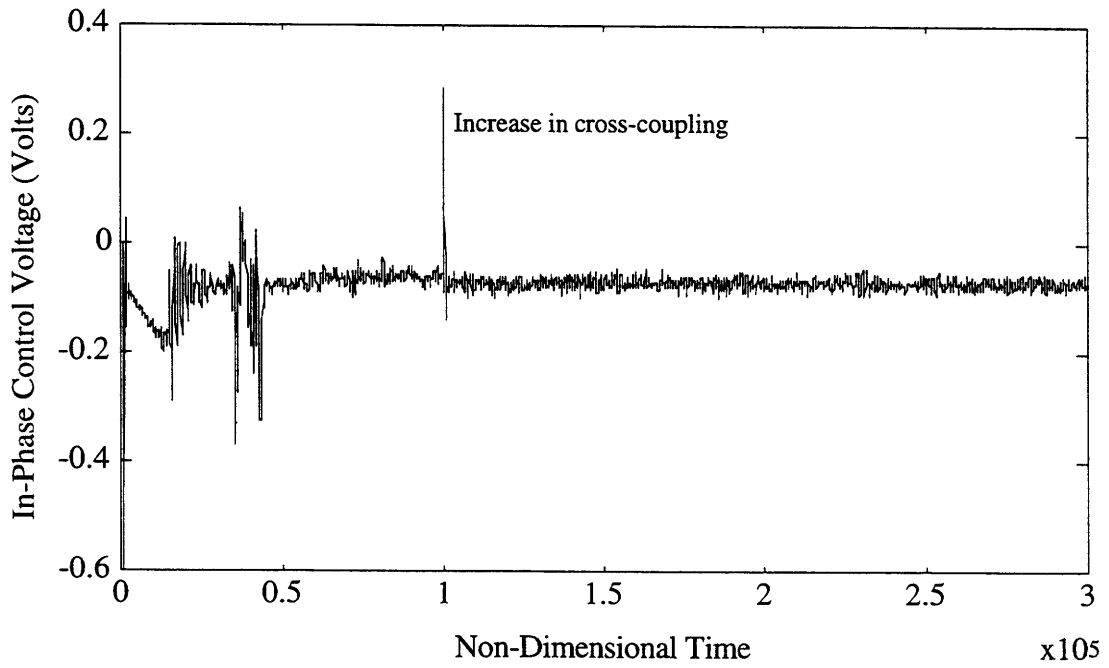
Figure 5.25. In-Phase Control Signal for Case 4

5.1.4.5 Summary of Vertical Control Simulations

In these simulations, it was demonstrated that undesired vertical motion may be reduced by a factor of 100. In cases 1 and 4, the closed-loop performance was compared to open-loop simulations of the same parameters. The results for all four cases are summarized in Table 5.3. Each case has its own column, except for the fourth case, which has a column for before and after the increase in the spring cross-coupling. The first row shows the amplitude of the oscillatory, open-loop, vertical-axis response for the given case. The closed-loop DC offset displacement is listed in the second row, and the standard deviation of the closed-loop response is presented in the third row. The reduction factor from the open-loop amplitude to the closed loop σ is given in the fourth row. Finally, the steady-state quadrature and in-phase control voltages, and their standard deviations are given in the fifth and sixth rows, respectively.

Table 5.3. Summary of Vertical Closed-Loop Simulations

	Case 1 Normal	Case 2 quad only	Case 3 in-phase only	Case 4 Before Δk_{xy}	Case 4 After Δk_{xy}
OL Amp. (μm)	0.182	–	–	0.182	0.228
CL DC Offset (nm)	-27.386	-28.551	-23.581	-27.511	-30.001
CL σ (nm)	2.0323	1.971	0.3480	3.135	2.287
Reduction Factor	88.57	–	–	58.06	99.81
Quad. Control (V) Quad. σ (V)	-4.100 0.0054	-4.079 0.0055	0.0012 0.0001	-4.100 0.0054	-5.127 0.0043
In-phase Control (V) In-phase σ (V)	-0.0646 0.0064	-0.0377 0.0063	-0.0264 0.0002	-0.0646 0.0064	-0.0739 0.0076

This table shows clearly that the steady-state offset of the vertical axis for these simulations was on the order of 20 nm, with a standard deviation of about 2 nm. As mentioned earlier, in case 4, when the cross-coupling is increased by 25%, the quadrature control voltage also increases by 25%, a confirmation that the control signals are directly proportional to the errors. Cases 2 and 3 demonstrated the independence of each loop; open-loop results were not necessary. This control loop is implemented in Chapter 6 on a micromechanical resonator with excellent results.

5.2 Rotational Motion Rebalance Loop Analysis

The development of a force rebalance loop for the rotational motion is very similar to that for the vertical motion developed in Section 5.1. However, there are two significant differences between the two systems. First, in controlling the rotational motion, there are control plates located under both sets of combs, as shown in Figure 5.26.
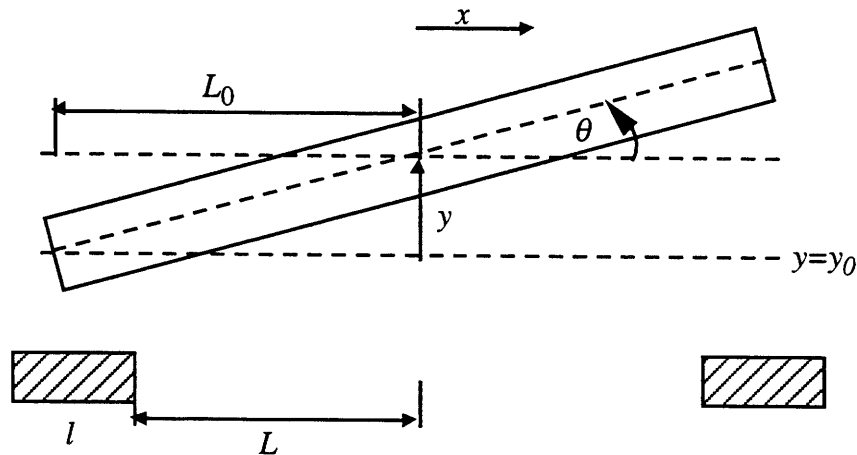
Figure 5.26. Torque Control Plate Geometry

where,

L_0 = half the length of the proof mass

l = width of a control plate, and

L = distance between center and inner edge of a control plate.

This metallization pattern allows a torque to be generated on either side of the proof mass by applying independent voltages to either the left or right control plate. For the SEO, this configuration will be exploited to overcome the second difference between the two systems, which is that, since the control plates are at the ends of the proof mass, the torquing coefficient is no longer a constant, but instead depends on x. Because the control plates are not completely under the proof mass, both the moment arm and the overlap area vary with the horizontal position of the proof mass, which, in turn, creates a position dependent torquing coefficient.

As in Section 5.1.3, the rotational control system may be designed as shown in Figure 5.27. The analysis of this loop may proceed directly, if, for now, it is assumed that it is possible to generate control signals that nullify the quadrature and in-phase torquing errors, i.e., that the control system eliminates rotational motion[6]. Later, it will be shown

---

[6]This is similar to the assumption made in Section 5.1.2.

that it is in fact possible to choose control signals to generate torques that reduce the unwanted in-phase and quadrature motions.
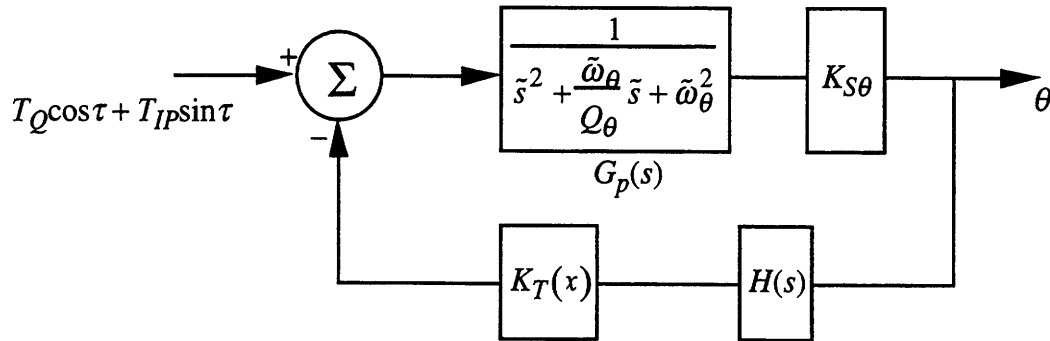
Figure 5.27. Block Diagram for Rotational Control

In this figure, both the in-phase and quadrature loops are modeled in one feedback path. In both the simulation and implementation of this system, there are two distinct paths, but the analysis is similar, so only one path is shown.

For a quadrature control voltage of

$$V_Q = V_{Q_0} \cos \tilde{\omega} \tau \tag{5.49}$$

a control torque of the form

$$T_{in} = -\frac{2 K_T V_{Q_0}}{\pi} \left(\cos(1 + \tilde{\omega}) \tau + \cos(1 - \tilde{\omega}) \tau \right) \tag{5.50}$$

may be generated, where K_T is the torquing constant. With this assumption, the block diagram of Figure 5.27 is nearly identical to that of Figure 5.1.

The only difference between the θ and y control loops now is that the remodulation that occurs after the AGC blocks H_C in Figure 5.1 is not straightforward for θ control. Instead, a more complex, non-linear scheme is required to generate the control signals V_Q and V_{IP}. If for now, it is assumed that this new, as yet undesigned, remodulation scheme produces signals similar to those for the vertical control system, then the closed-loop control systems are identical in structure, and the transfer functions may be derived in exactly the same way as Equations 5.43 and 5.44, with the large Q_θ assumption is used again. These equations are repeated here with changes in the subscript labels to emphasize that the degree of freedom now under consideration is θ:

$$V_{IP\theta} \approx \frac{2 K_T G_{2\theta} H_{CIP\theta}}{\pi + 2 K_T H_{CIP\theta} G_{2\theta}} M_{IP\theta} \tag{5.51}$$

$$V_{Q\theta} \approx \frac{2K_T H_{CQ\theta} G_{2\theta}}{\pi + 2K_T G_{2\theta} H_{CQ\theta}} M_{Q\theta} \qquad (5.52)$$

As before, G_1 and G_2 may be expressed as in Equations 5.36 and 5.37,

$$G_{1\theta} = \frac{4K_{S\theta}}{\pi} \frac{2\tilde{\omega}_d}{\left(\tilde{\omega}_\theta + \tilde{\omega}_d\right)^2} \frac{\left(\tilde{s} + \dfrac{\tilde{\omega}_\theta}{2Q_\theta}\right)}{\tilde{s}^2 + \dfrac{\tilde{\omega}_\theta}{Q_\theta}\tilde{s} + \left(\dfrac{\tilde{\omega}_\theta}{2Q_\theta}\right)^2 + \left(\tilde{\omega}_\theta - \tilde{\omega}_d\right)^2} \qquad (5.53)$$

$$G_{2\theta} = \frac{4K_{S\theta}}{\pi} \frac{1}{\left(\tilde{\omega}_\theta + \tilde{\omega}_d\right)^2} \frac{\tilde{s}^2 + \dfrac{\tilde{\omega}_\theta}{Q_\theta}\tilde{s} + \left(\tilde{\omega}_\theta^2 - \tilde{\omega}_d^2\right)}{\tilde{s}^2 + \dfrac{\tilde{\omega}_\theta}{Q_\theta}\tilde{s} + \left(\dfrac{\tilde{\omega}_\theta}{2Q_\theta}\right)^2 + \left(\tilde{\omega}_\theta - \tilde{\omega}_d\right)^2} \qquad (5.54)$$

where $K_{S\theta}$ is the rotational sensing constant. Once again, $G_{2\theta} \gg G_{1\theta}$ for $Q_\theta \gg 1$. Having derived the closed-loop transfer functions, the compensators H_C can now be designed, and a remodulation scheme is then developed to generate the required signals with the correct magnitude and phase.

5.2.1 Compensation Design for Rotational Motion

Since the information about the quadrature and in-phase errors is desired, it is sensible to use the same compensators designed for the vertical controller in order to integrate the error and guarantee stability of the closed loop. By choosing $H_{CIP\theta}$ and $H_{CQ\theta}$ identical to H_{CIP} and H_{CQ}, the only remaining task is to find a method of equating the partial block diagram of Figure 5.28 with that of Figure 5.29.

In Figure 5.28, the large unknown block emphasizes that, with a position-dependent torquing coefficient, it is not possible to modulate the control voltages by the corresponding clocks, as was done for the vertical control system. Here, the controller must compensate for the oscillating torquing coefficient so that the two sinusoidal control signals, of correct magnitude and phase, are generated. By exploiting the fact that the torque is generated by applying independent voltages on the left and right control plates, the design of this block may be determined by using different voltages on each plate. This will result in a control system that is equivalent to the linear control system shown in Figure 5.29. The configuration in this schematic is identical to that used in the vertical control system.

194
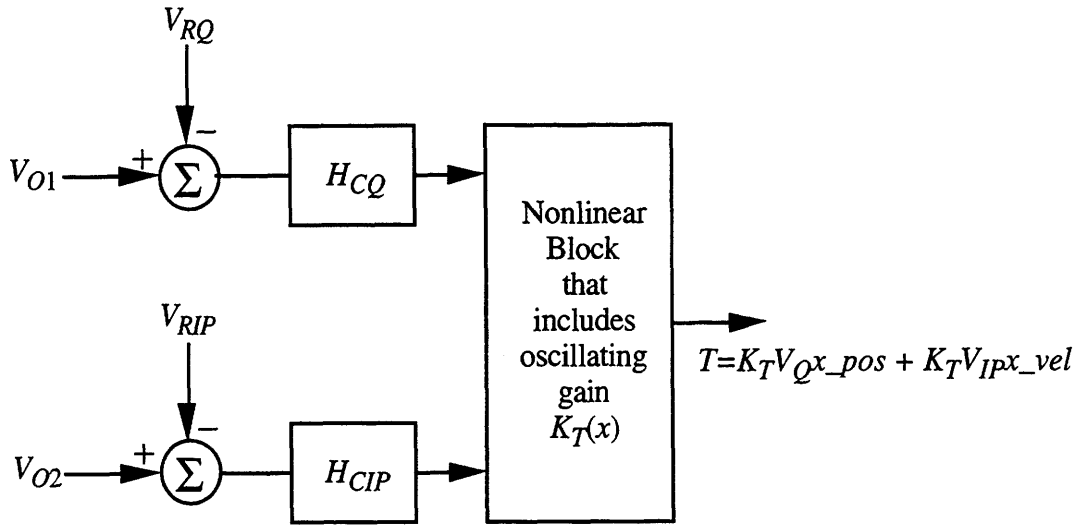
Figure 5.28. Nonlinear Block Diagram for Generation of Control Torques
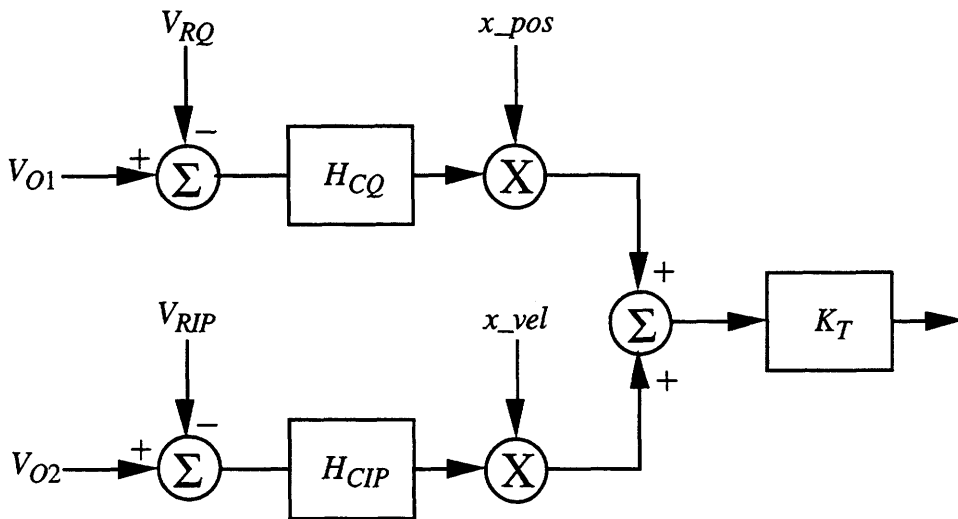
Figure 5.29. Linear Block Diagram for Generation of Control Torques

In order to linearize the block of Figure 5.28, the net torque generated by the left and right control plates may be expressed from Lagrange's energy method as

$$T_\theta = \frac{1}{2}\frac{\partial C_R(x)}{\partial \theta}V_R^2 + \frac{1}{2}\frac{\partial C_L(x)}{\partial \theta}V_L^2 \qquad (5.55)$$

i.e., the partial derivatives of the outer control plate capacitances generate a torque about the proof mass. The values used in deriving these capacitances are shown in Figure 5.30.
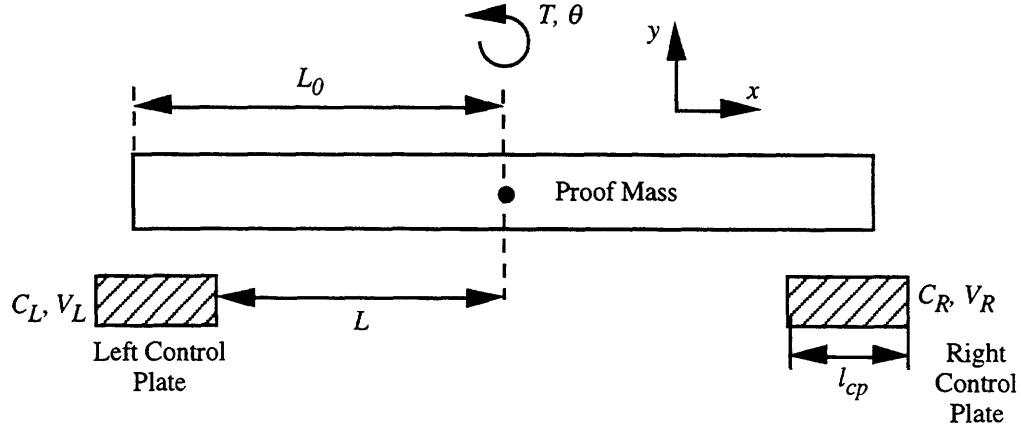
Figure 5.30. Schematic of Proof Mass and Torque Control Plates

The next step is to determine the partial derivatives of the control plate capacitances with respect to θ for a laterally oscillating proof mass. In this case, the capacitance depends on all three degrees of freedom of the center of mass. It can be shown that the capacitances for each control plate are

$$C_L = \frac{\varepsilon_0 w_{cp}}{\tan\theta} \ln\left[y_0 + y + (x' - x)\tan\theta\right]\Big|_{-(L_0)\cos\theta + x}^{-L}$$

$$= \frac{\varepsilon_0 w_{cp}}{\tan\theta} \ln\frac{y_0 + y - (L + x)\tan\theta}{y_0 + y - L_0\cos\theta\tan\theta} \qquad (5.56a)$$

$$C_R = \frac{\varepsilon_0 w_{cp}}{\tan\theta} \ln\left[y_0 + y + (x' - x)\tan\theta\right]\Big|_{L}^{L_0\cos\theta + x}$$

$$= \frac{\varepsilon_0 w_{cp}}{\tan\theta} \ln\frac{y_0 + y + L_0\cos\theta\tan\theta}{y_0 + y + (L - x)\tan\theta} \qquad (5.56b)$$

where,

w_{cp} = the width of the control plate into the page

L = the distance from the center to the inner edge of a torque control plate, and

L_0 = the distance from the center to the end of the proof mass.

These equations may be differentiated with respect to θ and then expanded to first order in θ and y by Taylor series to yield solutions that depend on x, y, and θ, as shown in Equations 5.57a and 5.57b. The sign change between the left and right capacitor derivatives makes sense because both plates exert attractive forces, and, since one plate is on either side of the center of mass, the torques will be in opposite directions. The coefficient for θ has both a constant term and a cubic term in x, while the y-coefficient is only quadratic in x.

196

$$\frac{\partial C_L}{\partial \theta} \approx -\frac{\varepsilon_0 w_{cp}}{y_0^2}\left\{\frac{1}{2}(x+L-L_0)(x+L_0+L)\left(1-2\frac{y}{y_0}\right)\right.$$
$$\left. +\left[L_0\left(y_0-\frac{2L_0^2}{3y_0}\right)+\frac{2(x+L)^3}{3y_0}\right]\theta\right\} \tag{5.57a}$$

$$\frac{\partial C_R}{\partial \theta} \approx \frac{\varepsilon_0 w_{cp}}{y_0^2}\left\{\frac{1}{2}(x-L-L_0)(x+L_0-L)\left(1-2\frac{y}{y_0}\right)\right.$$
$$\left. -\left[L_0\left(y_0-\frac{2L_0^2}{3y_0}\right)-\frac{2(x-L)^3}{3y_0}\right]\theta\right\} \tag{5.57b}$$

If it is assumed that the vertical and rotational motions of the proof mass are being controlled, i.e., the magnitudes of y and θ are nearly zero, then the partial derivative expansions of Equations 5.57a and 5.57b may be written as

$$\frac{\partial C_L}{\partial \theta} \approx -\frac{\varepsilon_0 w_{cp}}{2 y_0^2}\left\{(x+L-L_0)(x+L_0+L)\right\} \tag{5.58a}$$

$$\frac{\partial C_R}{\partial \theta} \approx \frac{\varepsilon_0 w_{cp}}{2 y_0^2}\left\{(x-L-L_0)(x+L_0-L)\right\} \tag{5.58b}$$

In these equations, the torquing coefficients depend only on the horizontal displacement of the proof mass. This fact is significant for linearizing the position depending torquing coefficient.

Next, the control voltages may be defined as

$$V_\theta \approx A\,\mathrm{sqr}\,\tau + B\,\mathrm{csqr}\,\tau + D \tag{5.59}$$

The torque of Equation 5.55 may now be rewritten as

$$T_\theta = \frac{1}{4}\frac{\varepsilon_0 w_{cp}}{y_0^2}\left[(x-L-L_0)(x+L_0-L)V_R^2 - (x+L_0+L)(x+L-L_0)V_L^2\right] \tag{5.60}$$

where the subscripts L and R indicate the left and right control plates, respectively. By substituting $x = A_x \sin \tau$ and Equation 5.59 for both V_L and V_R into Equation 5.60 and by then collecting like trigonometric terms, the DC offset, the quadrature, the in-phase, and the harmonic multiple torques may be determined. In order to be an effective control, it is desired to minimize the DC offset and set the in-phase and quadrature control torques[7] equal to the corresponding errors. The desired form of the torque is

---

[7] In these equations, the x motion is sin τ, such that the quadrature term is defined as sin τ, and the in-phase term is defined as cos τ. However, the results apply as well for $x = \cos \tau$.

197

$$T = -K_T\left(L_0^2 - L^2\right)V_{DC}V_{Q\theta}\sin\tau - K_T\left(L_0^2 - L^2\right)V_{DC}V_{IP\theta}\cos\tau \qquad (5.61)$$

The result from the substitution into Equation 5.60 is then set equal to Equation 5.61, and the first-order harmonic terms are set equal to each other. By choosing A_L and B_R equal to zero, and D_R and D_L equal to V_{DC}, the steady-state values for each control signal are reduced to

$$-\left(L_0^2 - L^2\right)V_{DC}V_{Q\theta} =$$

$$LA_xA_R^2 + \frac{4}{\pi}\left(L_0^2 - L^2 - \frac{2}{3}A_x^2\right)V_{DC}A_R + A_xLB_L^2 + 2A_xLV_{DC}^2 \qquad (5.62a)$$

$$-\left(L_0^2 - L^2\right)V_{DC}V_{IP\theta} = -\frac{4}{\pi}\left(L_0^2 - L^2 - \frac{A_x^2}{6}\right)V_{DC}B_L \qquad (5.62b)$$

Solving the in-phase torque for B_L using Equation 5.62b yields

$$B_L = -\frac{\pi\left(L_0^2 - L^2\right)}{4\left(L_0^2 - L^2 - \frac{1}{6}A_x^2\right)}V_{IP\theta} \qquad (5.63)$$

Inserting this solution into Equation 5.62a and solving for A_R gives the second voltage

$$A_R = -\frac{2\left(\Delta L^2 - \frac{2}{3}A_x^2\right)}{\pi A_x L}V_{DC}$$

$$\pm\sqrt{\left[\frac{4}{\pi^2 A_x^2 L^2}\left(\Delta L^2 - \frac{2}{3}A_x^2\right)^2 - 2\right]V_{DC}^2 - \left(\frac{\Delta L^2}{A_x L}V_{DC}V_{Q\theta} + \frac{\pi^2\left(\Delta L^2\right)^2}{16\left(\Delta L^2 - \frac{1}{6}A_x^2\right)^2}V_{IP\theta}^2\right)} \qquad (5.64)$$

where $\Delta L^2 = L_0^2 - L^2$, and V_{DC} must be chosen so that A_R is real for all possible values of $V_{Q\theta}$ and $V_{IP\theta}$. In order to permit A_R to be less than the saturation voltage of the op-amps, the summation term should be used. The choice of V_{DC} is determined by finding a V_{DC} such that the characteristic equation of A_R is positive for all $V_{Q\theta}$ and $V_{IP\theta}$. Minimum required values of V_{DC} are determined by letting $V_{Q\theta}$ and $V_{IP\theta}$ be their largest values of ±10 Volts. The additional constraint that emerges here is that L_0-L must be greater than 2.22 for V_{DC} to be a real number. For the SEO, $L_0 - L = 3.33$, such that the characteristic equation is positive. A constant 5 Volt signal for V_{DC} will guarantee that A_R is always real. The minimum DC value is 4.72 V, for typical resonator values. Unfortunately, the electronic implementation of the summations and square root is complicated, and will

198

drive up the cost of the control system, such that the decision to use rotational control must trade off the effects of the rotation versus the added complexity.

The rotational control voltages are distributed on the left and right plates so that

$$V_{\theta L} = B_L x\_vel + V_{DC}$$
$$V_{\theta R} = A_R x\_pos + V_{DC} \tag{5.66}$$

where A_R and B_L are defined in Equations 5.63 and 5.64. This choice of control voltages, when inserted into Equation 5.60, yields a net control torque of

$$T_\theta = T_{IP\theta} \cos \tau + T_{Q\theta} \sin \tau + C_2 \cos 2\tau + S_2 \sin 2\tau + DC \tag{5.67}$$

where,

$$DC = \frac{1}{2} K_T \left[\frac{\left(L_0^2 - L^2 - \frac{1}{2} A_x^2 \right)}{2} \left(A_R^2 - B_L^2 \right) + \frac{4}{\pi} A_x L V_{DC} A_R \right]$$

$$T_{IP\theta} = -\frac{1}{2} K_T \left(L_0^2 - L^2 \right) V_{DC} V_{IP\theta}$$

$$T_{Q\theta} = -\frac{1}{2} K_T \left(L_0^2 - L^2 \right) V_{DC} V_{Q\theta}$$

$$C_2 = K_T \left(\frac{A_x^2}{8} \left(A_R^2 - B_L^2 \right) - \frac{4 A_x L V_{DC}}{3\pi} A_R \right) \tag{5.68}$$

$$S_2 = -K_T \frac{4 A_x L V_{DC}}{3\pi} B_L$$

This control scheme will eliminate the rotational motion, but creates a DC rotation offset of the proof mass and also introduces torques at higher-order frequencies. The first harmonic forces are about 50 times greater than the second harmonic forces, so they do not affect the motion of the proof mass.

5.2.2 Improved Compensation Design for Rotational Motion

A better control system would generate neither DC nor second harmonic torques. Ideally, the square root term in A_R would also be eliminated to simplify the controller implementation. Because the proof mass oscillates, the moment arm will always be a function of x.. If the control torque plates are moved so that they are completely under the proof mass, not under the tines, then the torque coefficient will only be a first-order function of x. However, moving the control plates will reduce the sense plate area, decreasing the sensitivity of the system to vertical and rotational motion.

199

In this case, the control plate capacitances are

$$C_L = \frac{\varepsilon_0 w_{cp}}{\tan\theta}\ln\left[y_0 + y + (x' - x)\tan\theta\right]_{-L-l_{cp}}^{-L}$$

$$= \frac{\varepsilon_0 w_{cp}}{\tan\theta}\ln\frac{y_0 + y - (L + x)\tan\theta}{y_0 + y - \left(L + l_{cp} + x\right)\tan\theta} \tag{5.69a}$$

$$C_R = \frac{\varepsilon_0 w_{cp}}{\tan\theta}\ln\left[y_0 + y + (x' - x)\tan\theta\right]_{L}^{L+l_{cp}}$$

$$= \frac{\varepsilon_0 w_{cp}}{\tan\theta}\ln\frac{y_0 + y + \left(L + l_{cp} - x\right)\tan\theta}{y_0 + y + (L - x)\tan\theta} \tag{5.69b}$$

where l_{cp} is the width of the control plate, as shown in Figure 5.30. These capacitances are then differentiated with respect to θ and Taylor series expanded to first order in both y and θ to yield

$$\frac{\partial C_L}{\partial\theta} \approx \frac{\varepsilon_0 w_{cp} l_{cp}}{y_0^2}\left\{\left(x + L + \frac{l_{cp}}{2}\right)\left(1 - 2\frac{y}{y_0}\right) + \frac{1}{y_0}\left[2\left(x + L + \frac{l_{cp}}{2}\right)^2 + \frac{l_{cp}^2}{12}\right]\theta\right\} \tag{5.70a}$$

$$\frac{\partial C_R}{\partial\theta} \approx \frac{\varepsilon_0 w_{cp} l_{cp}}{y_0^2}\left\{\left(x - L - \frac{l_{cp}}{2}\right)\left(1 - 2\frac{y}{y_0}\right) + \frac{1}{y_0}\left[2\left(x - L - \frac{l_{cp}}{2}\right)^2 + \frac{l_{cp}^2}{12}\right]\theta\right\} \tag{5.70b}$$

Once again, these torques are exerted in opposite directions. The constant term in Equation 5.70b is negative for all x. As before, by substituting for x and collecting like terms, the actual torque may be equated with the ideal torque of Equation 5.61. Then, by letting $D_L = D_R = V_{DC}$, $A_L = 0$, and $B_R = 0$, solutions for B_L and A_R are found from

$$-\left(L_0^2 - L^2\right)V_{DC}V_{Q\theta} =$$

$$\left(L_0 - L\right)\left[A_x A_R^2 - \frac{4}{\pi}(L_0 + L)V_{DC}A_R + A_x B_L^2 + 2A_x V_{DC}^2\right] \tag{5.71a}$$

$$-\left(L_0^2 - L^2\right)V_{DC}V_{IP\theta} = \frac{4}{\pi}\left(L_0^2 - L^2\right)V_{DC}B_L \tag{5.71b}$$

In this case, the AC voltages A_R and B_L are

200

$$A_R = \frac{2}{\pi}(L_0 + L)V_{DC}$$

$$\pm \sqrt{2\left[\frac{2}{\pi^2 A_x^2}(L_0 + L)^2 - 1\right]V_{DC}^2 - (L_0 + L)\frac{V_{DC}}{A_x}V_{Q\theta} - \frac{\pi^2}{16}V_{IP\theta}^2} \qquad (5.72a)$$

$$B_L = -\frac{\pi}{4}V_{IP\theta} \qquad (5.72b)$$

Here, the DC voltage is again chosen to be 5 Volts, which guarantees that A_R will always be real. However, the square root term in A_R was not eliminated, and the compensation method still requires complex electronics.

This model also generates a DC torque and second harmonics. For this design, the terms of the net applied torque from Equation 5.67 are

$$DC = \frac{1}{2}K_T\left[\frac{(L_0^2 - L^2)}{2}(A_R^2 - B_L^2) + \frac{4}{\pi}A_x(L_0 - L)V_{DC}A_R\right]$$

$$T_{IP\theta} = -\frac{1}{2}K_T(L_0^2 - L^2)V_{DC}V_{IP\theta}$$

$$T_{Q\theta} = -\frac{1}{2}K_T(L_0^2 - L^2)V_{DC}V_{Q\theta}$$

$$C_2 = K_T\frac{4A_x(L_0 - L)V_{DC}}{3\pi}A_R \qquad (5.73)$$

$$S_2 = -K_T\frac{4A_x(L_0 - L)V_{DC}}{3\pi}B_L$$

The rebalance torques $T_{IP\theta}$ and $T_{Q\theta}$ are the same as those from Equation 5.68. The constant torque and second harmonics are less than those in the previous section. Therefore, by moving the control plates completely under the proof mass, the undesired torques are reduced. If the varying moment arm could be compensated for, then the DC and second harmonic torques would be equal to zero.

5.2.3 Simulation of Rotational Control System

For the rotational force rebalance system, the nominal x- and y-axis parameters from Table 4.3 of Chapter 4 were used. In the first simulation, the vertical axis was left open, and only the rotational control system was closed. In the second simulation, both the vertical and rotational force rebalance loops were closed, so that all three degrees of freedom were operating closed loop: the x-axis in a loop that sustained oscillations, and the y- and θ-axes in loops that eliminated all motion.

201

5.2.3.1 Open-Loop Simulation of Three DOF Oscillator

The horizontal, vertical, and rotational motions from the Chapter 4 simulations are shown in Figures 5.31 through 5.33 for open-loop y and θ operation. In these plots, the steady-state non-dimensional displacement of the x-axis is 1.0095; the y-axis, 0.0182; and the θ-axis, 79.5 μradians. Most of the motion in the vertical and rotational axes is due to coupling from the drive axis. The objective of the force rebalance loops is to drive the y and θ motions to zero and to obtain the magnitudes of the in-phase and quadrature signals for both degrees of freedom.
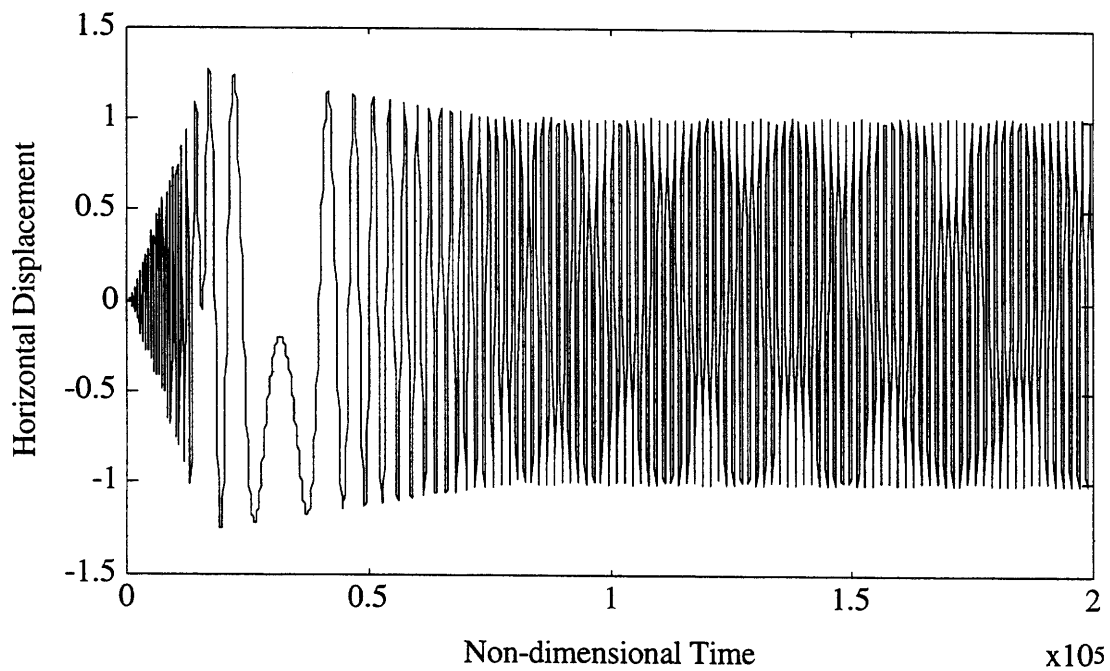
Figure 5.31. Horizontal Displacement of Open-Loop 3 DOF Simulation
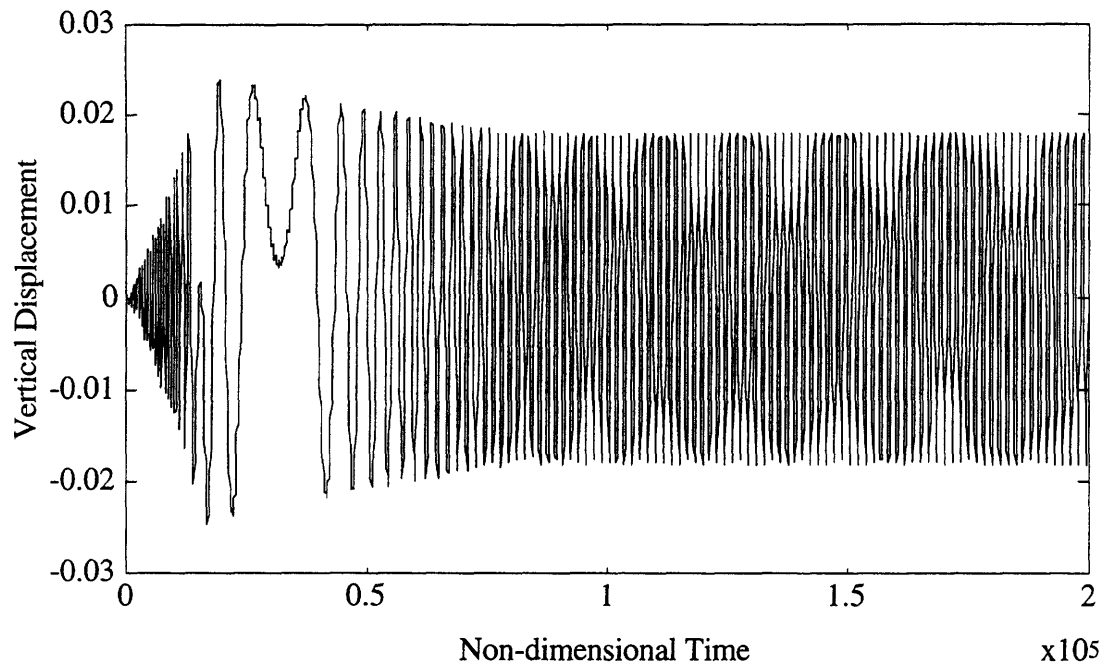
Figure 5.32. Vertical Displacement of Open-Loop 3 DOF Simulation
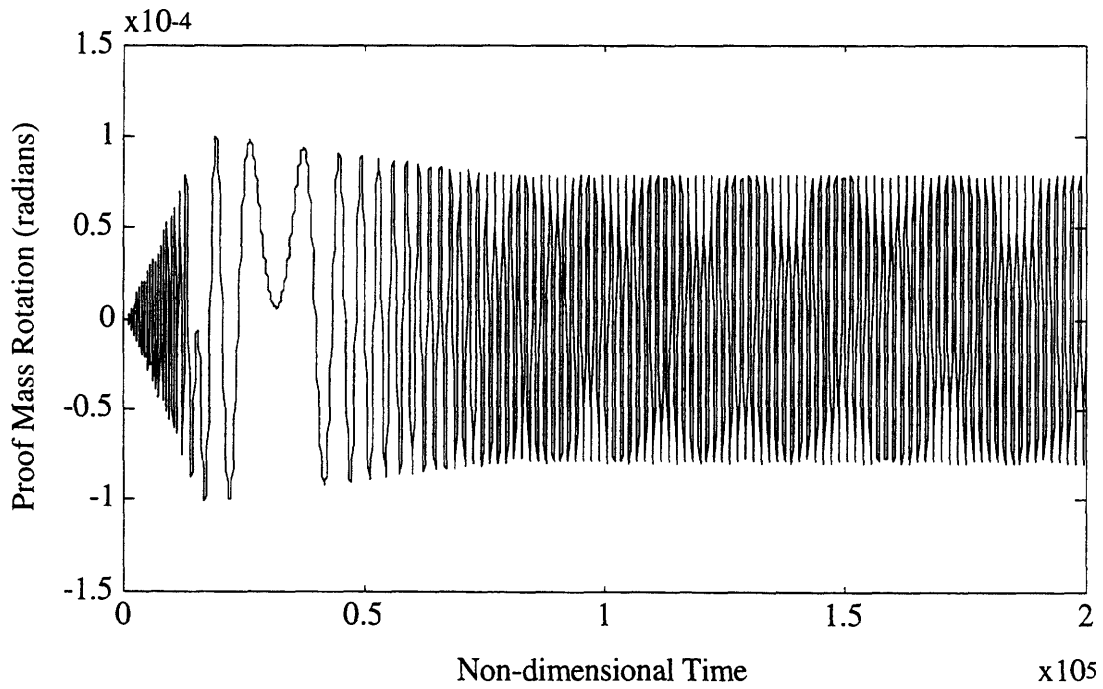
Figure 5.33. Rotational Displacement of Open-Loop 3 DOF Simulation

5.2.3.2 Closed Rotational Force Rebalance Loop Simulation

In the first simulation, the control loop for the θ degree of freedom was closed. As discussed above, the control voltages $V_{Q\theta}$ and $V_{IP\theta}$ have to be modified to generate the proper control torques by using the voltages A_R and B_L of Equations 5.63 and 5.64. These voltages were necessary because the torquing coefficient is no longer a constant, but instead depends on the horizontal position of the proof mass. In Figures 5.34 through 5.40, the rotation of the proof mass and the necessary control voltages are plotted.

The controlled response of the rotational axis is shown in Figure 5.34, and the phase-plane response is shown in Figure 5.35. The steady-state rotation angle of the proof mass is 36.35 μradians, with a standard deviation of 3.45 μradians, which is seen clearly in the phase-plane. With this control loop, the rotational motion has been reduced by a factor of 23. However, this is a factor of 47 above the noise floor determined in Chapter 4. This additional error comes from two sources. First, the coupling between the in-phase and quadrature channels, as in the vertical control, limits the performance of the control system. In addition, the second harmonic torques will generate small forces that are balanced by a control force. However, the reduction factor of 23 is substanial, since the magnitude of the rotation has been reduced from 0.080 mradians to 3.5 μradians.
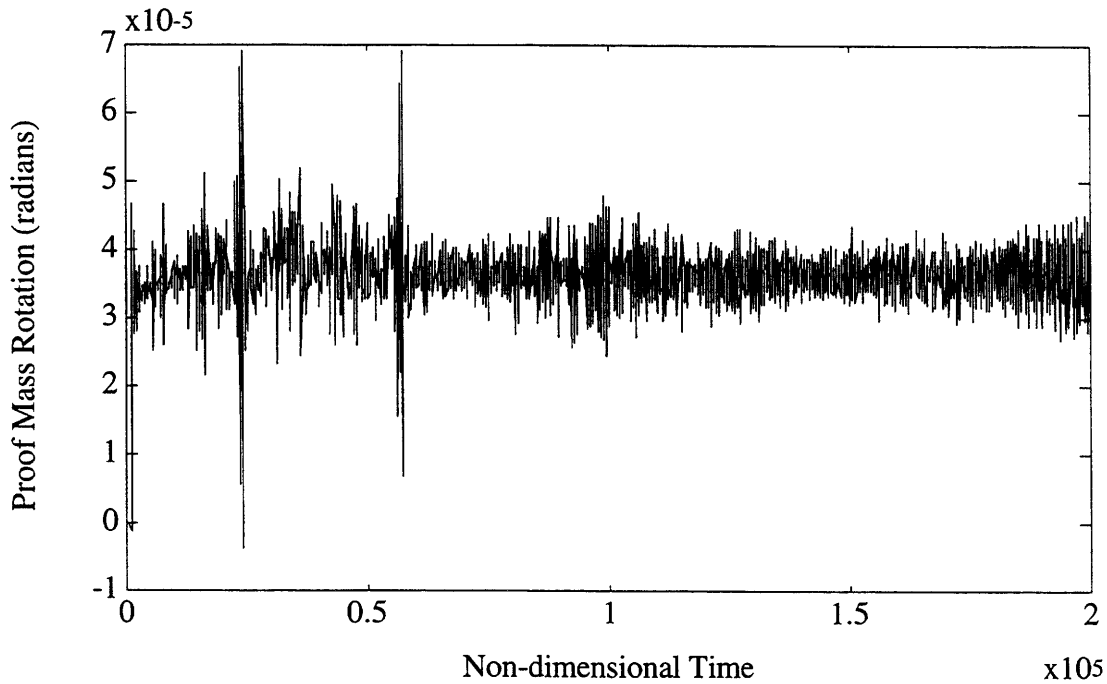
Figure 5.34. Rotational Displacement of θ Closed-Loop 3 DOF Simulation
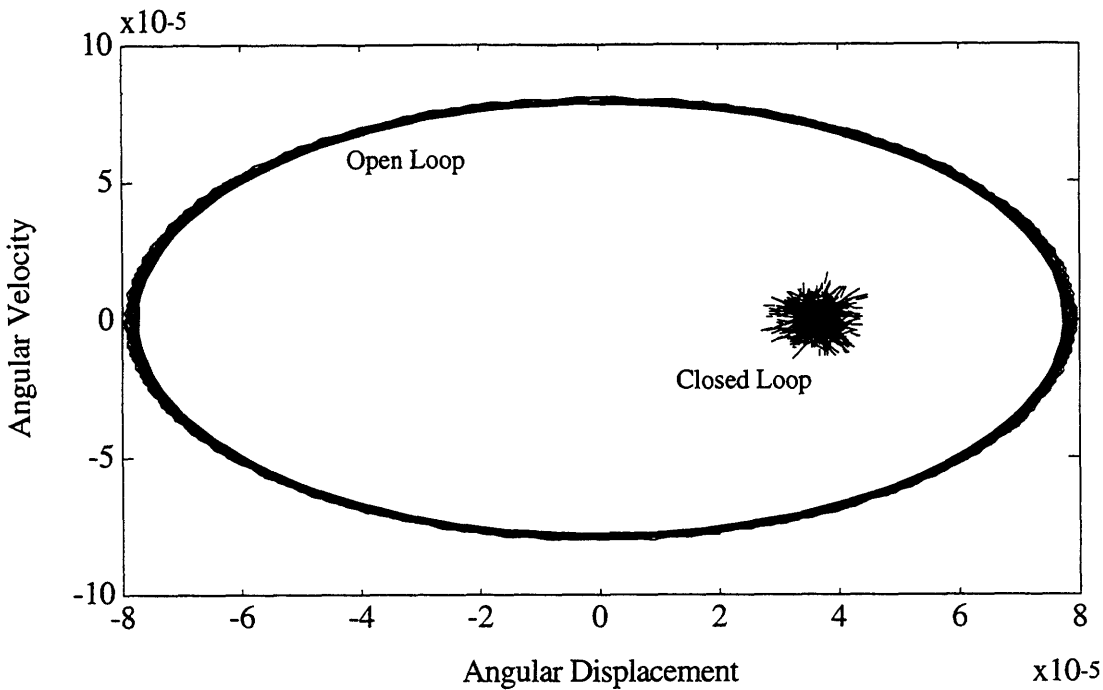
Figure 5.35. Phase-Plane of Open and Closed-Loop Rotational Response

The quadrature and in-phase control voltages are shown in Figures 5.36 and 5.37, respectively. The shapes of these responses are very similar to the vertical control voltages, as expected, since the control system compensator designs are very similar. The quadrature control voltage has a mean of -3.3513 Volts, with a standard deviation of 0.0053 Volts. For the in-phase channel, the control voltage is 0.3103±0.0242 Volts. The in-phase signal is noiser because of the coupling from the quadrature control loop, as discussed in Section 5.1.4.

The control voltages, A_R and B_L, are plotted in Figures 5.38 and 5.39, respectively. Because of the manipulations performed on these signals, especially A_R, the responses are similar to, but not exactly the same, as those for $V_{Q\theta}$ and $V_{IP\theta}$. As shown in Figure 5.38, the response of A_R is very similar to that of $V_{Q\theta}$, except for a minus sign. Here, the value starts at about -1.25 Volts, increases rapidly, and settles out to a steady-state value of 1.47±0.0057 Volts. Because of the small magnitude of $V_{IP\theta}$, A_R is nearly proportional to the square root of $V_{Q\theta}$. The response of B_L is directly proportional to -$V_{IP\theta}$, so it has much of the noise associated with $V_{IP\theta}$. The steady-state value of B_L is -0.2438±0.0190 Volts, which is -0.786 times the in-phase voltage; the expected scale factor. These two control voltages permit the sinusoidal rotational motion to be reduced by a factor of 23, a small enough level such that the rotation does not adversely affect the dynamics of the other two axes or the capacitances of the system.

205
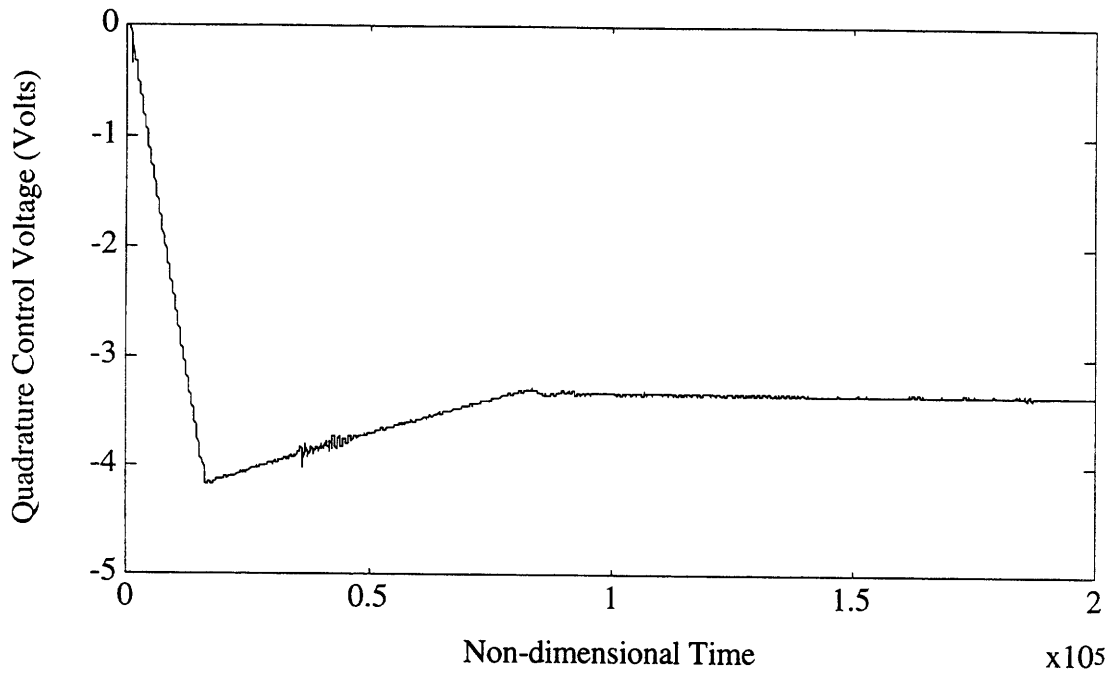
Figure 5.36. Quadrature Control Voltage of θ Closed-Loop 3 DOF Simulation
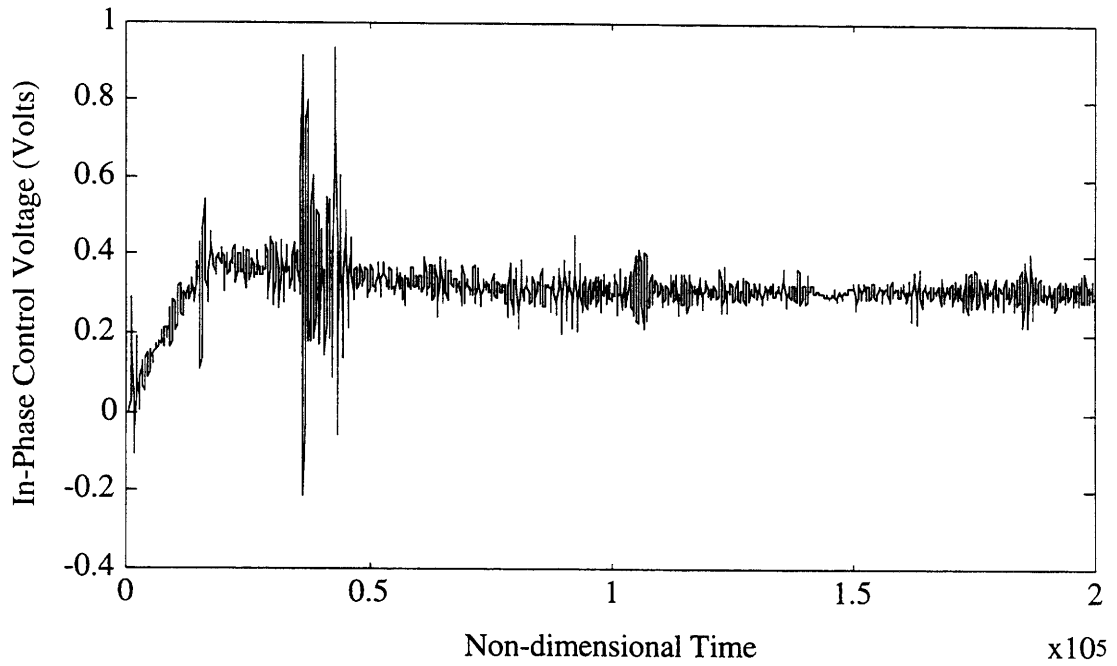
Figure 5.37. In-Phase Control Voltage of θ Closed-Loop 3 DOF Simulation
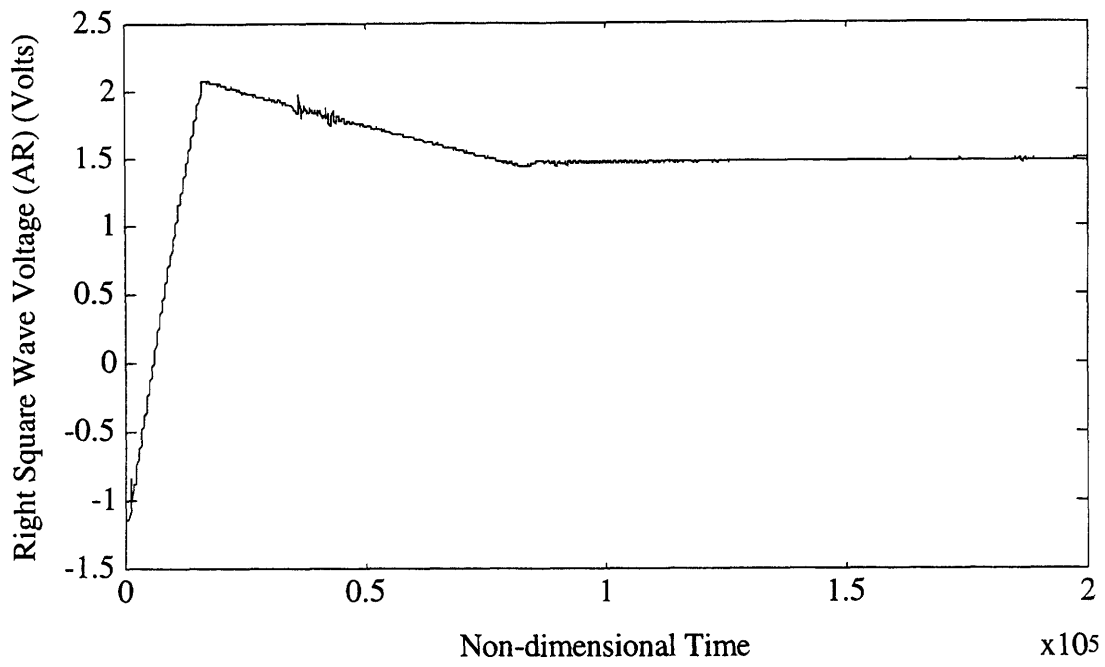
Figure 5.38. Right Square Wave Voltage, A_R, for θ Closed Loop
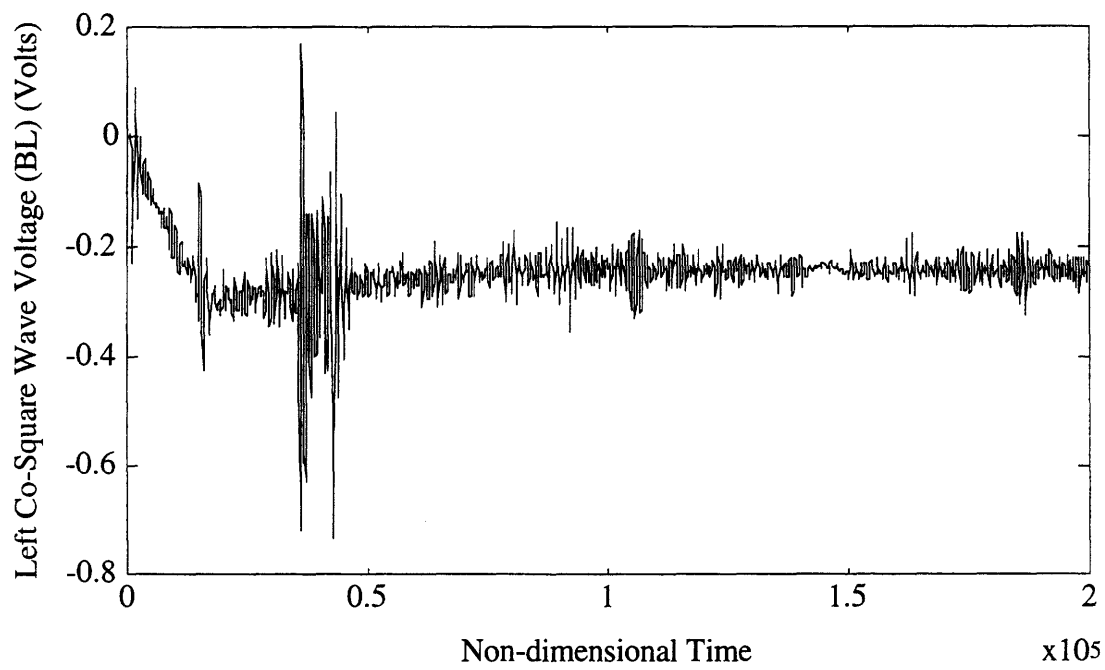
Figure 5.39. Left Co-Square Wave Voltage, B_L, for θ Closed Loop

In Figure 5.40, the torquing coefficient for the left control plate is shown for a small time period. The behavior of this term is, to first order, sinusoidal with the horizontal displacement, with a negligible contribution from the x^2 term in Equations 5.58a and 5.58b. The DC offset of the coefficient is 5.095×10^{-12} Volts^{-2}, with an oscillation amplitude of 1.473×10^{-12} Volts^{-2}. The right control plate torquing coefficient is 180° out of phase with the left one, with identical DC offsets and oscillation amplitudes. The two coefficients are in-phase at the second harmonic, a fact that is not observable in the plot.
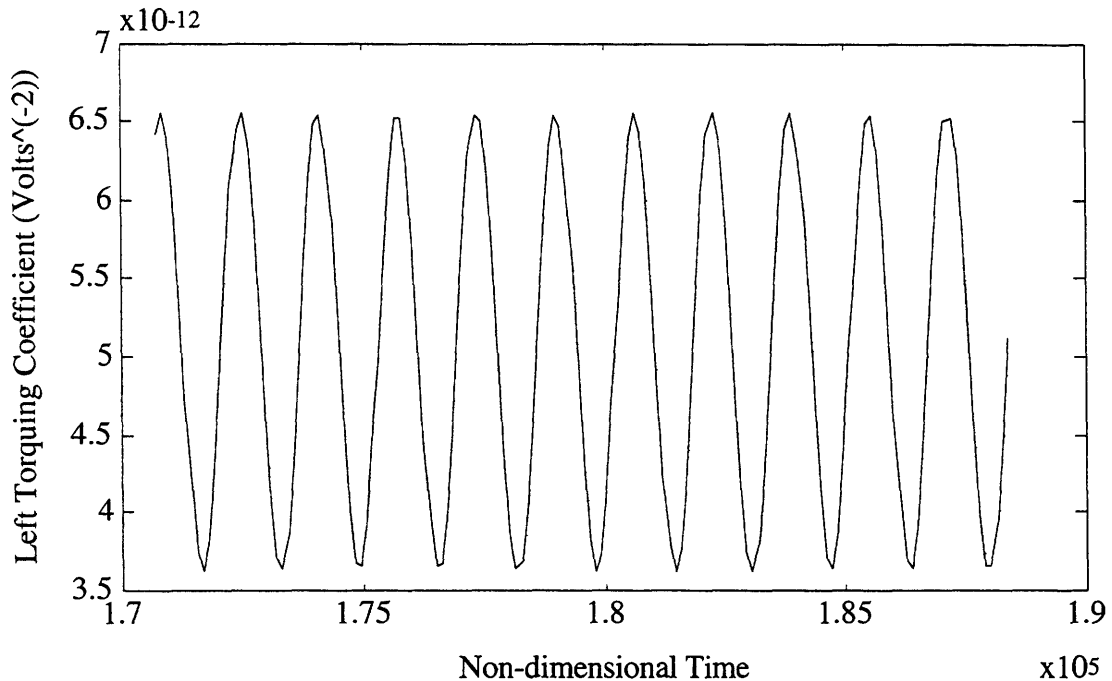
Figure 5.40. Torquing Coefficient of θ Closed-Loop 3 DOF Simulation

From this simulation, it is clear that the θ force rebalance loop is capable of reducing rotational motion. In the closed loop, the rotation standard deviation is sufficiently small that θ-coupling adverses affects neither the dynamics of x and y, nor the comb and parallel plate capacitor values. Therefore, the simulated θ force-rebalance loop may be considered successful; it provides the quadrature and in-phase information for the rotational dynamics and eliminates the undesired proof mass rotation.

5.2.3.3 Closed-Loop Control of All Three Degrees of Freedom

In the final simulation, both the vertical and rotational loops were closed, so that all three degrees of freedom were operating closed loop. The magnitudes of the vertical and rotational displacements are shown in Figures 5.41 and 5.42, respectively, and the phase-plane are plotted for both y and θ in Figures 5.43 and 5.44. The y-axis motion is reduced
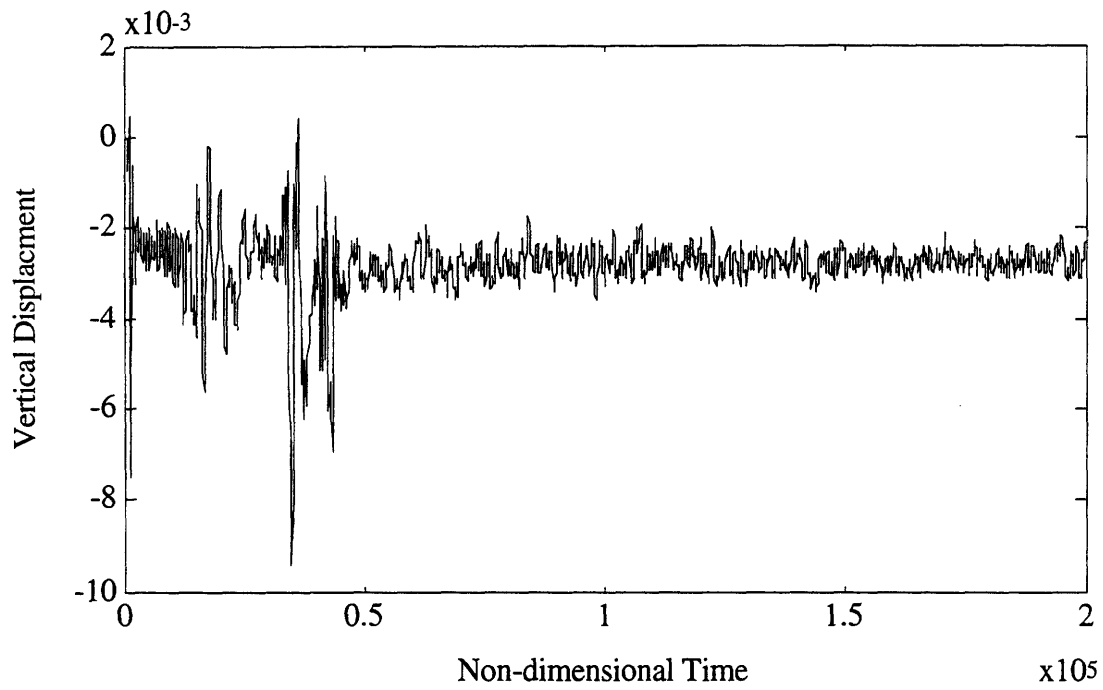
Figure 5.41. Proof Mass Vertical Displacement for Three-Closed-Loops Simulation
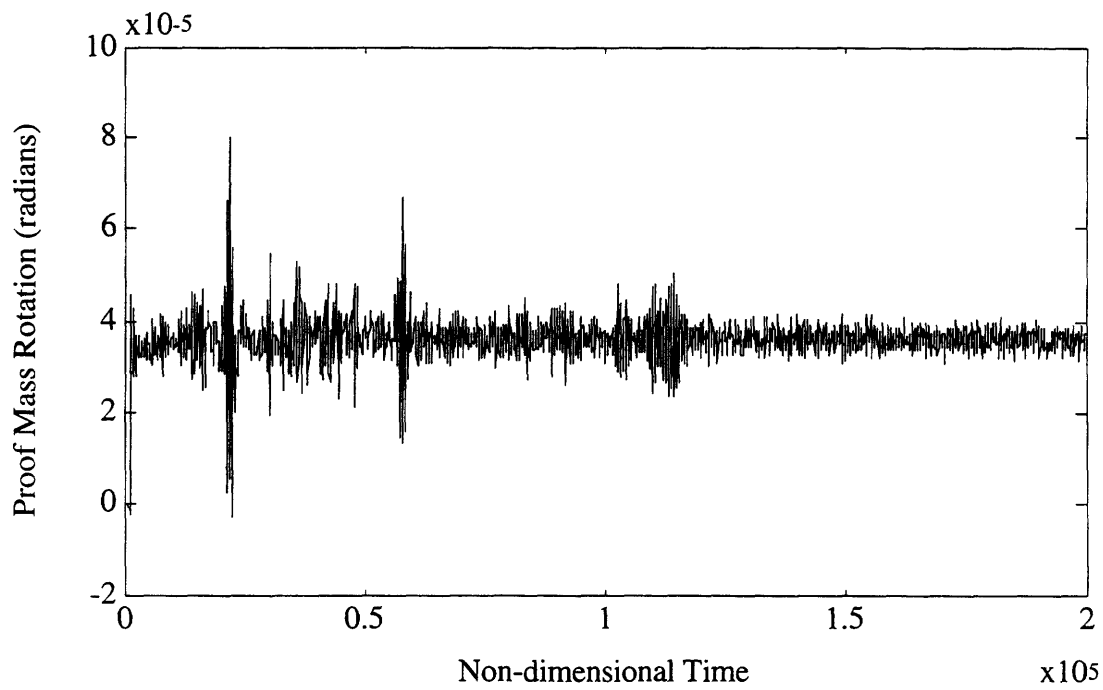
Figure 5.42. Proof Mass Rotation for Three-Closed-Loops Simulation
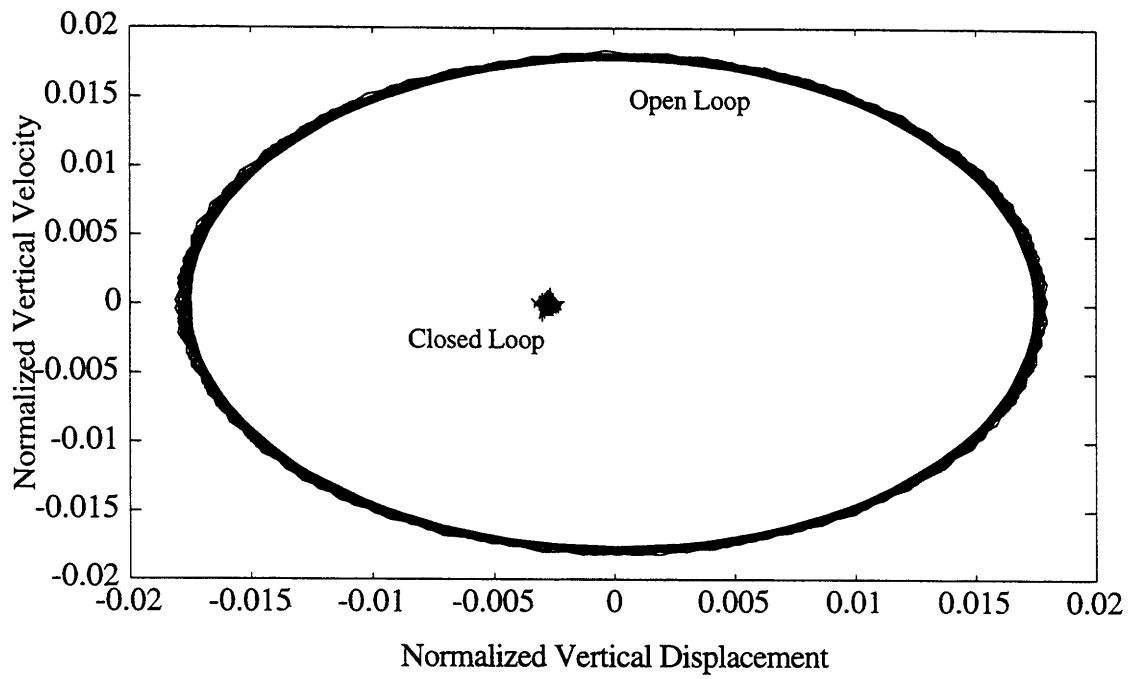
Figure 5.43. Phase-Plane of Vertical Response
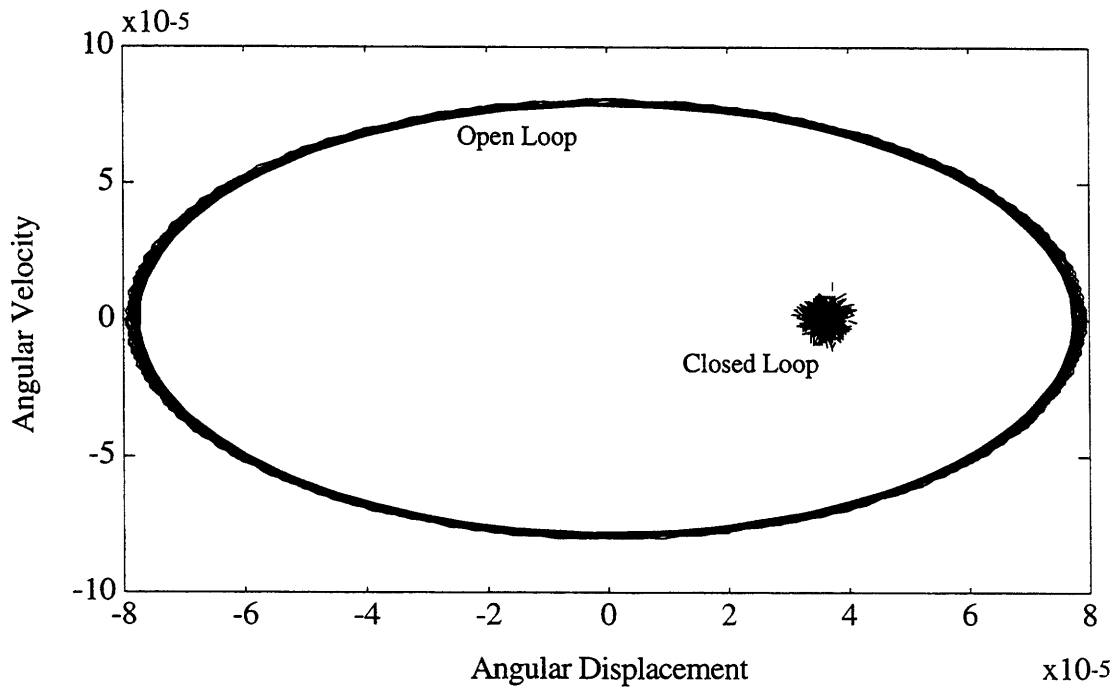
Figure 5.44. Phase-Plane for Proof Mass Rotation Response

to a DC offset of -27.6 nm with a standard deviation of 2.18 nm. The θ motion steady-state tilt is 36.2 μradians with a variation of 2.05 μradians. Because the vertical motion has also been reduced, the standard deviation of θ is less than in the previous simulation, since less control torque is necessary to counteract the vertical cross-coupling, and, as a result, the second harmonic errors are not as large. The responses of both y and θ are very similar to those of Sections 5.1.4.1 and 5.2.3.2, respectively.

The control voltages for the vertical axis are shown in Figure 5.45. The quadrature control voltage is -4.0722±0.0093 Volts; the in-phase control voltage is -0.0643±0.0068 Volts. The responses of the control signals are similar to those of Section 5.1.4; the addition of the θ-control does not adversely affect the performance of the vertical force rebalance loop.
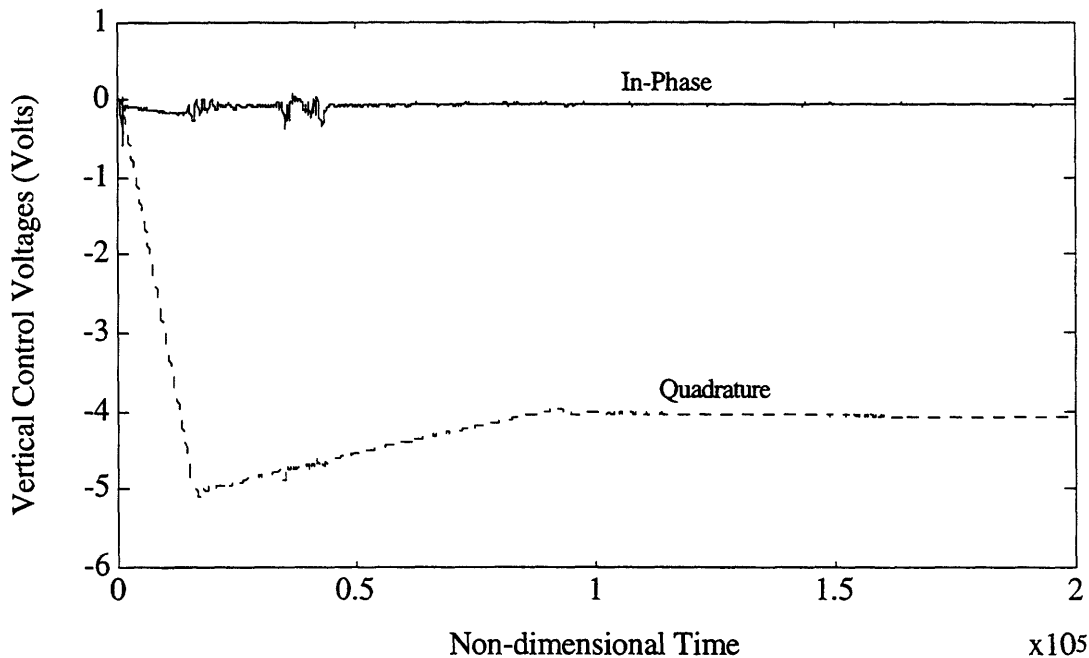
Figure 5.45. Vertical Control Voltages for 3 Controlled DOF

The corresponding quadrature and in-phase control voltages for rotation are shown in Figure 5.46. Here, both signals behave as expected; the introduction of the vertical control does not adversely affect the performance of the rotational force rebalance loop. The steady-state voltage for the quadrature is -3.3043±0.0061 Volts; the in-phase is 0.3056±0.0209 Volts. In Figure 5.47, the applied, nonlinear, control voltages, A_R and B_L, are shown. The steady-state value of A_R is 1.4334±0.0082 Volts; B_L is -0.2400±0.0163 Volts. The shapes of these two signals are similar to those in the previous section.

211
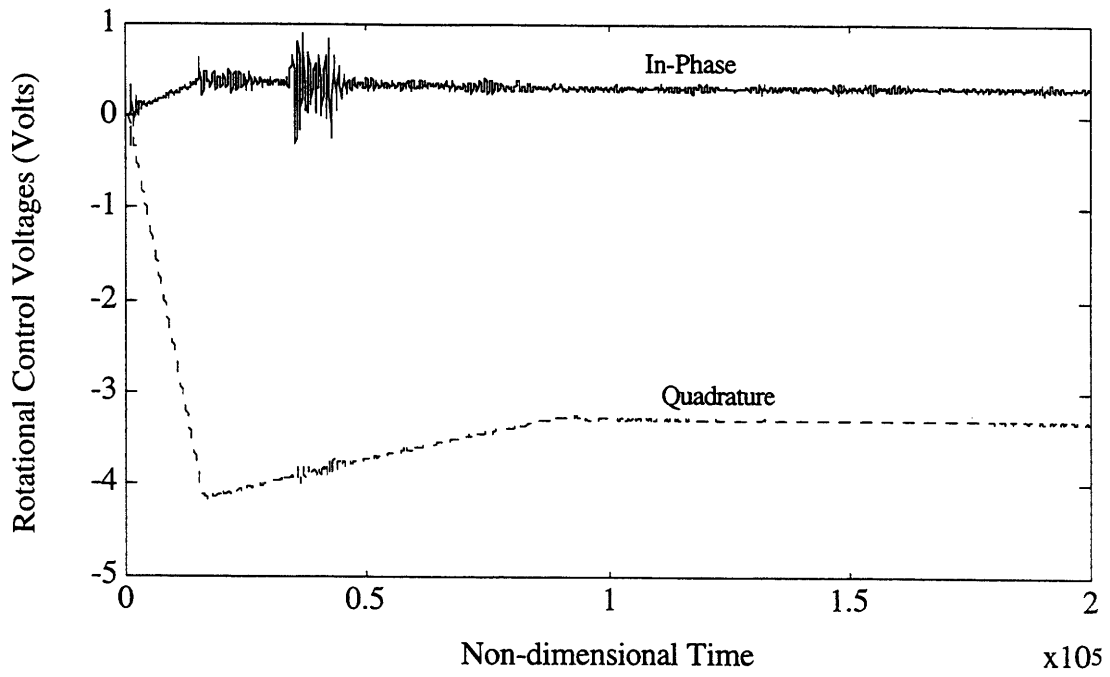
Figure 5.46. Rotational Control Voltages for 3 Controlled DOF
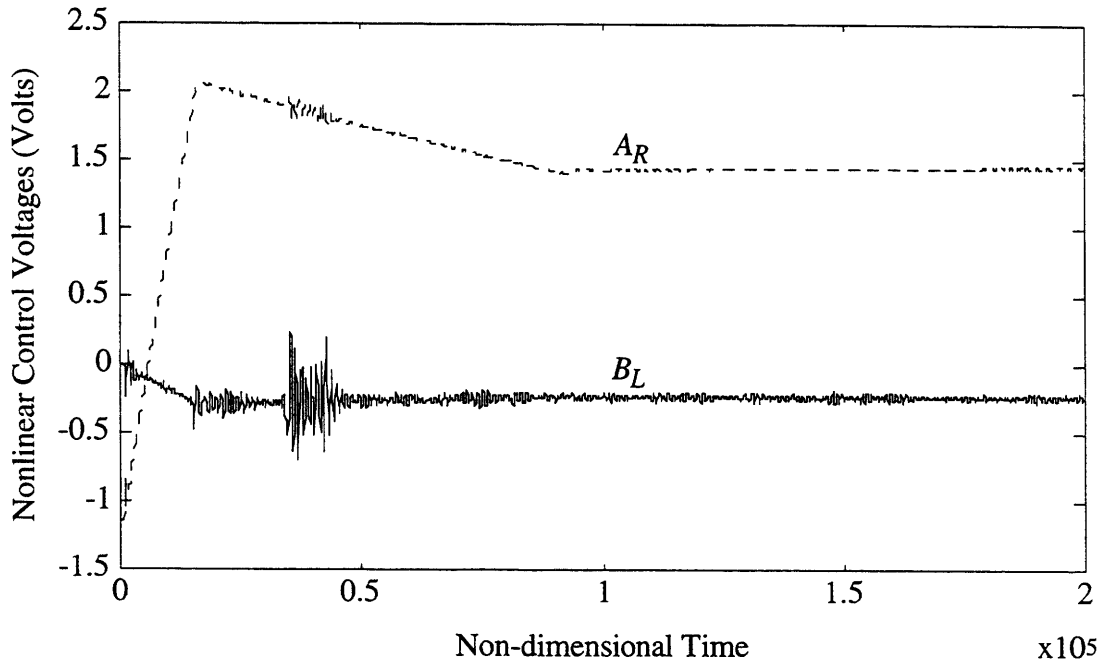
Figure 5.47. Applied Rotational Control Voltages for 3 Controlled DOF

212

Because $V_{IP\theta}$ is small, A_R is nearly proportional to $V_{Q\theta}$; however, a linearization of A_R as a function of the quadrature control voltage is not possible, because it cannot be safely assumed that the in-phase control voltage will always be small. Large $V_{IP\theta}$ will greatly affect the response of A_R. In this case, B_L is nearly identical to $V_{IP\theta}$, and A_R is proportional to $V_{Q\theta}$. From these results, it is clear that both vertical and rotational control may be run simultaneously.

5.3 Force Rebalance Loop Conclusions

A comparison of the closed vertical loop of Section 5.1.4.1, the closed rotational loop of Section 5.2.3.2, and the three closed loops of Section 5.2.3.3 are shown in Table 5.4. In this table, the open-loop (OL) magnitudes for both y and θ from Chapter 4 are given. For the closed-loop (CL) responses, the following values are given: the DC offsets and standard deviations for y and θ, the reduction factor (RF) for each DOF, the magnitudes and standard deviations of the in-phase and quadrature control voltages for each loop, and the nonlinear rotational control voltages and standard deviations.

Table 5.4. Summary of Force Rebalance for Vertical and Rotational Motion

	y-Control	θ-Control	y and θ Control
OL y	0.182 μm	0.182 μm	0.182 μm
OL θ	79.5 μrad	79.5 μrad	79.5 μrad
CL DC$_y$	-27.386 nm	–	-27.6 nm
CL σ_y	2.0323 nm	–	2.18 nm
CL DC$_\theta$	–	36.35 μrad	36.2 μrad
CL σ_θ	–	3.45 μrad	2.05 μrad
RF$_y$	88.57	–	83.49
RF$_\theta$	–	23.04	38.78
V_{Qy}	-4.100±0.0054 V	–	-4.0722±0.0093 V
V_{IPy}	-0.0646±0.0064 V	–	-0.0643±0.0068 V
$V_{Q\theta}$	–	-3.3513±0.0053 V	-3.3043±0.0061 V
$V_{IP\theta}$	–	0.3103±0.0242 V	0.3056±0.0209 V
A_R	–	1.47±0.0057 V	1.4334±0.0082 V
B_L	–	-0.2438±0.0190 V	-0.2400±0.0163 V

As can be seen in this table, there are minor reductions in both the vertical and rotational control signals when both modes are driven to zero. However, the signals are

essentially the same, verifying that the controls for both degrees of freedom operate independently, and that simultaneously closing both force rebalance loops will not adversely affect the system. In fact, closing the vertical loop improves the θ force rebalance loop performance, defined as the reduction factor, by 68%. Therefore, with the self-excitation control loop on the x-axis, this simulation demonstrates simultaneous control of three degrees of freedom for a micromechanical oscillator.

In this chapter, force rebalance loops were designed both to eliminate and to measure vertical and rotational motion. For each degree of freedom, both in-phase and quadrature components of the motion were determined through demodulation and used for rebalancing the proof mass. Linearization of the demodulator and remodulator permitted stability analysis to design a PI compensation scheme. The simulations verified the independent performance of both the y and θ control systems, and the simultaneous operation of both loops. In Chapter 6, the vertical force rebalance loop is implemented on a laterally oscillating proof mass.

Chapter 6

Measurements and Experiments
on Micromechanical Resonators

6.0 Introduction

Several experiments were designed, built, and implemented to confirm both the three degree of freedom state-space model developed in Chapter 4 and the control systems designed in Chapter 5. The first battery of tests characterized the static and dynamic parameters of the SEO and yielded estimates not only of the physical dimensions, but also of the spring, forcing, and sensing constants. With these parameters, more extensive experiments were conducted to determine the magnitude of both the on-axis parameters and the cross-coupling between the degrees of freedom. Once the SEO was completely characterized, the vertical control system of Chapter 5 was implemented successfully on a micromechanical resonator.

6.1 Static Parameter Characterization for the SEO

Before dynamic SEO testing, it was necessary to measure the physical characteristics of the system in order to determine its performance limits. The static parameters of the SEO include the capacitors, from the motor axis stator combs to the sense and control force plates; and the forcing and sensing constants of each degree of freedom. Some of the values, such as the mass and moment of inertia of the SEO, are best determined analytically, while others, such as the resonant frequencies, can be estimated through direct measurements.

6.1.1 Analytic Determination of the Mass and Moment of Inertia

The most straightforward way of determining both the mass and the moment of inertia of the proof mass is through analytic models based on the design of the device. The proof mass may be considered to have three elements: the plate, the holes in the proof mass, and the comb fingers. The effects of each of these components on both the

215

mass and moment of inertia may be examined separately and then incorporated into the final model. The plate and fingers will increase the mass and moment of inertia, while the holes will decrease both quantities.

6.1.1.1 Calculation of the Rotor Mass

The mass is simply the density of silicon times the volume of the entire proof mass. The volume of the proof mass may be calculated as the volume of a solid plate plus the total volume of the comb fingers and minus the total volume of the holes in the proof mass. For the SEO, the width, length, height, and the total number of each component are given in Table 6.1. The height was determined experimentally, as discussed as Section 6.1.2.1.

Table 6.1. Design Dimensions of SEO Proof Mass

	Width (μm)	Length (μm)	Height (μm)	Number	Volume (μm^3)
Plate	400	450	19	1	3.42x10^6
Holes	5	5	19	36x32	0.547x10^6
Fingers	5	50	19	28x2	0.266x10^6

For a silicon density of 2260 kg/m^3, the mass of the SEO proof mass is approximately 7.1x10^{-9} kg. This value will be used in Section 6.2.2 to determine the spring constants based on the resonant frequency measurements. The holes reduce the total mass to 84% of the value of a solid proof mass.

6.1.1.2 Calculation of the Rotor Moment of Inertia

Calculating the moment of inertia about the z-axis requires significantly more analysis of the layout of the proof mass than for the mass calculation. Not only the mass of each component, but also its horizontal distance from the center line of the rotor is needed. Once again, the rotor may be divided into three components, and the total moment of inertia may be determined by combining the effects of each. The moment of inertia is a volume integral, so the contribution of the holes may simply be subtracted from that of the entire proof mass. It can be shown that the moment of inertia of the holes is

$$I_{holes} = \frac{n_w \rho h m^2}{6} \sum_{k=1}^{n_l/2} \left(3(2k-1)n)^2 + m^2 \right) \tag{6.1}$$

216

where,

n_w = number of holes in one column of the proof mass = 32

n_l = number of holes in one row of the proof mass = 36

ρ = the density of silicon = 2260 kg/m^3

h = thickness of proof mass = 19 μm

m = length of side of square hole = 5 μm, and

n = distance between centers of two adjacent holes = 10 μm.

A similar analysis leads to a moment of inertia for the tines

$$I_{tines} = \frac{2n_{tines}\rho h l_t w_t}{3}\left(\frac{3}{4}l_0^2 + \frac{3}{2}l_0 l_t + l_t^2\right) \tag{6.2}$$

where,

n_{tines} = number of tines along one side of proof mass = 28

l_t = length of a tine = 50 μm

w_t = width of a tine = 5 μm, and

l_0 = length of proof mass without tines = 450 μm.

The moment of inertia of the entire proof mass may then be expressed as

$$I_{rotor} = \frac{\rho h w_0 l_0^3}{12} + I_{tines} - I_{holes} \tag{6.3}$$

Table 6.2 shows the contribution of each part to the total moment of inertia of the proof mass about the z-axis.

Table 6.2. Moment of Inertia for SEO Proof Mass

Quantity	Moment of Inertia
Plate	0.13043 g-μm^2
Holes	-0.04004 g-μm^2
Tines	0.03770 g-μm^2
Total	0.12809 g-μm^2

The largest contribution to the moment of inertia comes from the proof mass plate (without fingers or holes). For the SEO, the moment of inertia of the proof mass about the z-axis is 0.12809 g-μm^2. Using the mass calculated above, this yields a radius of gyration, R, of 134.316 μm. These values will be used later to determine spring constants from measured resonant frequencies.

6.1.2 Measurement of SEO Static Parameters

Micromechanical resonators have both static and dynamic parameters that can be measured experimentally. The static characteristics include the physical dimensions of the resonator and the values of the capacitors in the device. The nominal forcing and torquing constants for all three degrees of freedom may then be determined from the capacitor estimates. These measurements, made from straightforward techniques, provide a wealth of information on the resonator and its performance.

6.1.2.1 Physical Characterization of SEO

In order to determine the thickness and sense gap of the SEO, a WYCO® profilometer was used to measure the height of the proof mass above the substrate [5]. During fabrication, some rotors stick down to the substrate[1]. From these stuck devices, the gap between the proof mass and the sense plate and the thickness of the proof mass can be accurately estimated with a profilometer. For the SEO, the measured thickness of the proof mass was 18.98 µm, with a sense gap of 3 µm. These values are used throughout this chapter to determine various resonator characteristics.

6.1.2.2 Capacitor Measurements for SEO

The capacitors of interest are shown in Figure 6.1 (a repeat of Figure 2.33 from Chapter 2). By applying an AC signal to each capacitor of an SEO, an output voltage may be measured on the vertical axis preamplifier. This voltage is proportional to the ratio of the actual capacitance to the feedback capacitance, as shown in Equation 6.4

$$C_e = \frac{\left\|V_{out,y-\theta}\right\|}{\left\|V_{in}\right\|}C_{fb} \qquad (6.4)$$

where,

$\left\|V_{out,y-\theta}\right\|$ = RMS value of vertical axis preamplifier output voltage

$\left\|V_{in}\right\|$ = RMS value of input voltage

C_e = estimated value of capacitor under study, and

C_{fb} = feedback capacitance of preamplifier = 2 pF.

It is essential to choose the AC frequency near the resonant frequency since the electronics are designed to pass and filter signals based on a certain expected frequency range. If the SEO is at atmospheric pressure and the voltage applied is of sufficiently low amplitude so as to not excite the proof mass, then the unknown capacitances may be accurately measured. In this figure, the charge injected onto the proof mass may be

---

[1]Due to irregularities in fabrication and the snapdown effects discussed in Chapter 2.

218

measured at $V_{out,y-\theta}$, which yields both the vertical and rotational motion, and the charge injected on to the motor sense comb may be measured at $V_{out,x}$, which gives the horizontal motion of the proof mass.
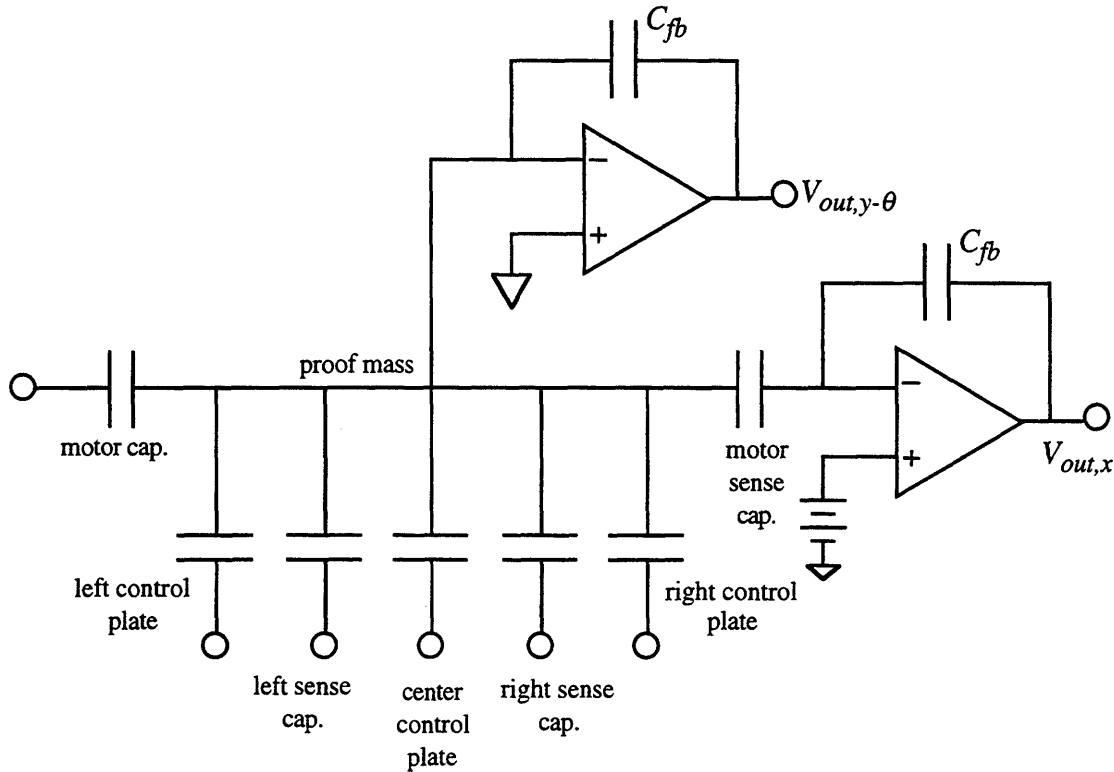
Figure 6.1. Capacitor Model for SEO

Based on the design parameters it is possible to estimate the capacitances, either analytically or by finite element analysis. The analytic approach is a straightforward application of parallel plate capacitor theory, as discussed in Chapter 2. However, this method does not include fringing, which limits its usefulness. Finite element analysis does consider the effects of the fringing fields, so its predictions are more useful. These predictions are not shown here because the actual vertical gap between the proof mass and substrate is 20% larger than that used in the finite element analysis of Chapters 2 and 4. However, the fringing coefficients determined in Chapter 2 are used in this chapter as reasonable approximations to the actual fringing coefficients of the capacitances. The measured capacitor values are presented in Table 6.3.

Table 6.3. Measured Capacitor Values for SEO

Capacitor	Measured (fF)
motor drive	103.7
motor sense	104.8
left sense plate	150.4
right sense plate	151.8
left control plate	65.72
right control plate	76.36
center control plate	87.4

The large discrepancy between the measured values of the left and right control plates is most likely due to misalignment between the combs and the control plates. If the proof mass is situated such that there is more rotor comb overlap on the right control plate than on the left control plate, then the right capacitance will be larger than the left capacitance. During fabrication, the silicon is aligned with and then anodically bonded to the glass. Misalignment during this process can create these imbalances. Both sense plates and the center control plate are not affected by this misalignment because they are completely under the proof mass.

6.1.3 Forcing and Sensing Constant Estimates from Capacitors

From these capacitor measurements, it is possible to determine the various constants used to generate and to measure the motions of the SEO. As shown in Chapters 2 and 4, these constants depend on both the physical dimensions and the capacitor sizes of the SEO. The relationships between these estimates are very useful for SEO characterization.

6.1.3.1 Horizontal Forcing and Sensing Constants

In Chapter 2, it was shown that the horizontal forcing and sensing schemes depend on the partial derivative of the stator capacitances with respect to x. Since the SEO was at rest when these measurements were made, it may be assumed that there is 25 μm of overlap between the tines. The values for the motor drive and motor sense capacitance may therefore be divided by 25 μm to yield a first-order estimate of the partial derivative with respect to x. This leads to estimates of the horizontal forcing and sensing constants[2]

---

[2]See Chapter 2 for a detailed analysis of horizontal forcing and sensing.

220

$$K_{F,x} = \frac{\partial C_m}{\partial x}$$

$$K_{S,x} = g_1 \frac{V_{ms}}{C_{fb}} \frac{\partial C_{ms}}{\partial x}$$

(6.5)

where,

g_1 = preamplifier gain = 10

V_{ms} = DC bias on motor sense comb = 5 V, and

C_{fb} = the feedback capacitor about the motor sense preamplifier = 2 pF.

For these values, $K_{F,x}$ is equal to 4.15 nN/V^2, and $K_{S,x}$ is equal to 105 mV/μm. These constants agree with other resonators of similar design. Assuming a fringing coefficient of 1.07 and a tine gap of 2 μm yields analytic estimates of $K_{F,x}$ = 4.69 nN/V^2 and $K_{S,x}$ = 117.25 mV/μm. These are very close to the measured values, and provide two conclusions: the tine gap is less than 2 μm, and the measured values are accurate. The maximum lateral comb force, assuming $V_{AC,max}$ equals 10 Volts and V_{DC} is 5 Volts, is 0.208 μN.

6.1.3.2 Vertical Forcing and Sensing Constants

The static values that may be determined for the vertical axis dynamics include the sense plate constants and the vertical force plate constant. Other parameters, such as the forcing and sensing due to the stator combs, cannot be extracted from these capacitor measurements. Finite element analysis is the best way to determine these values, as shown in Chapter 2. As discussed in Chapter 2, the vertical forcing and sensing constants are

$$K_{F,y} = \frac{C_{f_0}}{y_0}$$

$$K_{S,y} = 2g_s \frac{C_{s_0}}{y_0 C_{fb}} V_s$$

(6.6)

where C_{f0} and C_{s0} are the nominal vertical force and sense plate[3] capacitances, respectively; and g_s is the vertical axis gain, which is equal to 10 in these experiments. If the DC component of V_{out} is ignored (it is removed by a blocking capacitor), and if the sense gap measured by the profilometer is used for y_0, then the constant $K_{F,y}$ is equal to 29.133 nN/V^2; $K_{S,y}$ is equal to 2.506 V/μm. The maximum vertical control force, with the same voltage assumptions as above, is 1.457 μN.

---

[3]For one sense plate only.

6.1.3.3 Rotational Torquing and Sensing Constants

The rotational constants are the most difficult to estimate, because they depend not only on the capacitors, but also on the dimensions of the proof mass. Here, the ideal torquing and sensing models discussed in Chapter 4 will be used. The control plate torquing constant and the rotation sensing constant are

$$K_{T,\theta} = \frac{L_0 - w_{cp}}{2} \frac{C_{cp_0}}{y_0}$$

$$K_{S,\theta} = g_s \frac{C_{s_0}}{C_{fb}} \frac{V_s}{y_0} (L - w)$$

(6.7)

where,

C_{cp0} = the nominal torque plate capacitance

y_0 = gap between proof mass and substrate

L_0 = distance between the outer edges of the control torque plates

w_{cp} = width of control torque plate

L = distance between outer edges of sense plates, and

w = width of sense plate.

For the values shown in Table 4.2, the torquing constant $K_{T,\theta}$ is equal to 6.28 pN-m/V^2 and the sensing constant $K_{S,\theta}$ is equal to 661.2 V/radian. For 100 μradians, the output voltage is 66 mV, a small but measurable quantity. If both torque plates are used, the maximum possible control torque is 314 pN-m.

6.2 Dynamic Parameter Characterization for the SEO

While the static parameters describe the construction of the SEO, the dynamic parameters characterize its behavior. These values include the resonant frequency, quality factor, and spring non-linearities for each of the three modes, as well as the cross-coupling of the restoring, damping, and applied forces. In these experiments, external forces are applied to generate lateral, vertical, and rotational motions, and these motions are then measured on each axis.

On-axis dynamic parameters are determined by observing the motion on the same axis the force is applied on, e.g., drive axis parameters may be measured by applying a force along the drive axis and measuring the motion at the motor sense comb. The cross-axis parameters are determined by applying a force on one axis and observing the motions induced by it in the other two degrees of freedom.

6.2.1 Snapdown Voltage for Vertical Axis

The first dynamic measurement performed on the SEO was the snapdown test. In this test, a voltage is applied to both sense plates, and the potential is slowly increased until the proof mass snaps down and contacts the sense plate, creating a short circuit. The details of the snapdown voltage are discussed in Section 2.2.4.1, and the governing equation is

$$V_{snap} = \sqrt{\frac{8k_y y_0^2}{27 C_{y0}}} \qquad (6.8)$$

where,

k_y = spring constant of vertical axis, and

C_{y0} = sum of left and right sense plate capacitances.

This measurement may then be used to estimate the spring constant of the vertical axis. For the SEO, the snapdown voltage was measured at 38 Volts, which results in a vertical axis spring constant of 163.6413 N/m by using the sense gap and capacitance measured in Section 6.1. Using the mass calculated in Section 6.1.1 yields a vertical resonant frequency of 24.162 kHz.

6.2.2 Open-Loop Frequency Response Measurements

Frequency response techniques are very useful for determining the dynamic characteristics of an open-loop resonator. The basic method for this test is to combine a swept sinusoid voltage at increasing frequencies with a DC bias and then to apply this signal to an actuator on the SEO, which, in turn, generates a force that is at the same frequency as the swept sine signal. This force induces motion in the SEO proof mass which may be measured by any of the three motion detection capacitors on the SEO. That output signal is then compared with the AC voltage to determine the magnitude and phase of the SEO response along that axis with respect to the swept sine voltage.

By applying forces and measuring the motions both on- and off-axis, the spring, damping, and forcing terms may be calculated for all axes. Table 6.4 summarizes the degree of freedom along which the force is applied, and the degree of freedom whose motion is measured, and the parameters that may be measured from that test. For example, if a force is applied along the horizontal axis, and the motion is detected along the vertical axis, then the cross-coupling parameters between x and y may be determined. In some cases, one or more tests must be run in a given configuration to separate the force coupling from the mechanical coupling, since the force coupling will depend on the voltage squared and the mechanical coupling is directly proportional to the lateral motion.

Table 6.4. On- and Off-Axis Open-Loop Frequency Response Experiments

Forced DOF	Sensed DOF	Parameters Measured
Horizontal	Horizontal	k_x, k_{x3}, Q_x
Horizontal	Vertical	k_{xy}, Q_{xy}, β_x
Horizontal	Rotational	$k_{x\theta}, Q_{x\theta}, \gamma_x$
Vertical	Horizontal	k_{xy}, Q_{xy}, α_y
Vertical	Vertical	k_y, k_{y3}, Q_y
Vertical	Rotational	$k_{y\theta}, Q_{y\theta}, \gamma_y$
Rotational	Horizontal	$k_{x\theta}, Q_{x\theta}, \alpha_\theta$
Rotational	Vertical	$k_{y\theta}, Q_{y\theta}, \beta_\theta$
Rotational	Rotational	$k_\theta, k_{\theta3}, Q_\theta$

In these experiments, the coupling of horizontal motion and force into the vertical and rotation dynamics is the significant issue. The coupling of vertical and rotational motions into the drive axis will be very small with respect to the other horizontal axis forces, and, as a result, difficult to observe accurately in the lateral dynamics. Therefore, the cross-coupling terms should be measured by inducing motion along the drive axis and examining its effects on the other two degrees of freedom. Likewise, the coupling between the vertical and rotational modes is not a significant parameter. The remaining dynamic parameters to be measured are the on-axis spring terms and damping, as well as the coupling between the horizontal motion and the other two modes. The reduced model parameters that were measured are listed in Table 6.5. These values can be used to develop a three degree of freedom system that adequately models the behavior of the resonator.

Table 6.5. Reduced Model Parameter Measurements

Forced DOF	Sensed DOF	Parameters Measured
Horizontal	Horizontal	k_x, k_{x3}, Q_x
Horizontal	Vertical	k_{xy}, β_x
Horizontal	Rotational	$k_{x\theta}, \gamma_x$
Vertical	Vertical	k_y, k_{y3}, Q_y
Rotational	Rotational	$k_\theta, k_{\theta3}, Q_\theta$

For the frequency responses, the SEO is placed in an airtight package, and a hose is connected to pull a vacuum inside the container. Since the Q measurements, both on-axis and coupled, will simply be an estimate of the pressure at the SEO, the pressure gauge attached to the system will be used to verify that a sufficiently low pressure exists at the SEO. The three Q measurements are performed to determine the relationships of the damping between the three degrees of freedom. Typical pressures have been on the order of 11 mTorr, which is more than adequate for open-loop characterization of this device. If the SEO had been vacuum sealed, then the Q measurements would be more significant, since they would then be the only means of determining the pressure in the package.

6.2.2.1 Drive Axis Dynamic Parameters

The frequency response approach was used to measure the drive axis parameters. For a nonlinear hard spring, the expected shark fin response is shown in Section 2.1.3. The actual drive axis frequency response of the SEO is shown in Figure 6.2[4]. For this response, the magnitude of the swept sine voltage was 0.25 Volts, and the DC voltage was 5 Volts. In the magnitude response plot, the spring hardening is clearly seen as the SEO amplitude increases over a range of 12.525 Hz. This system was driven sufficiently hard that the nonlinear effects of the cubic spring dominate the behavior of the resonator. In Figure 6.3, the swept sine voltage was reduced to 100 mV to generate a smaller response. In this figure, the peak value has a larger dB value, but the displacement is less than the large amplitude response. Since the system is nonlinear, the displacement of the small amplitude response is less than the large amplitude response, but the ratio of the outputs to the inputs is greater for the small amplitude. These plots represent the ratio of the sensed output voltage to the applied input voltage, so the displacement amplitude must be computed explicitly to examine the behavior of the system.

The value of the cubic spring coefficient, k_3, may be determined using the information from both the large and small amplitude responses. From both Chapters 2 and 3, the dimensional, nonlinear resonant frequency at the peak amplitude is

$$\omega_{nl} = \omega_d \left(1 + \frac{3}{8} \tilde{k}_3 A^2 \right) \tag{6.9}$$

---

[4]In the frequency response plots, the values shown along the frequency, magnitude, and phase axes correspond to the maximum and minimum values along that axis. The vertical axis have five values. To find the tick mark increment, subtract the minimum from the maximum and divide by 4. The frequency axis has 11 tick marks. To find the tick mark increment, subtract the minimum from the maximum and divide by 10.
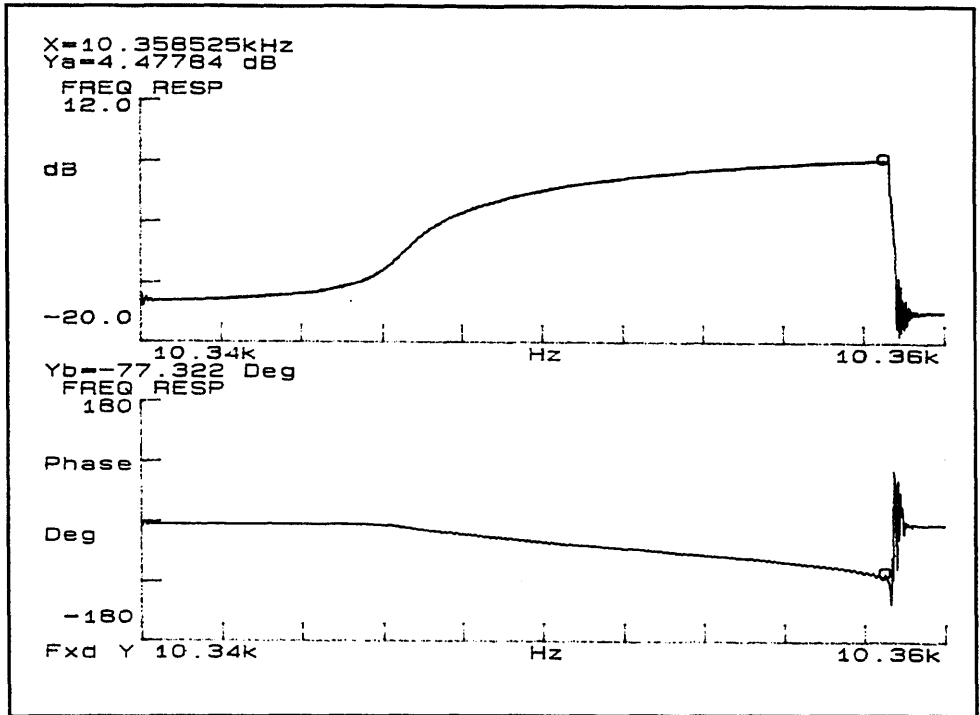
Figure 6.2. Large Amplitude Horizontal Axis Frequency Response
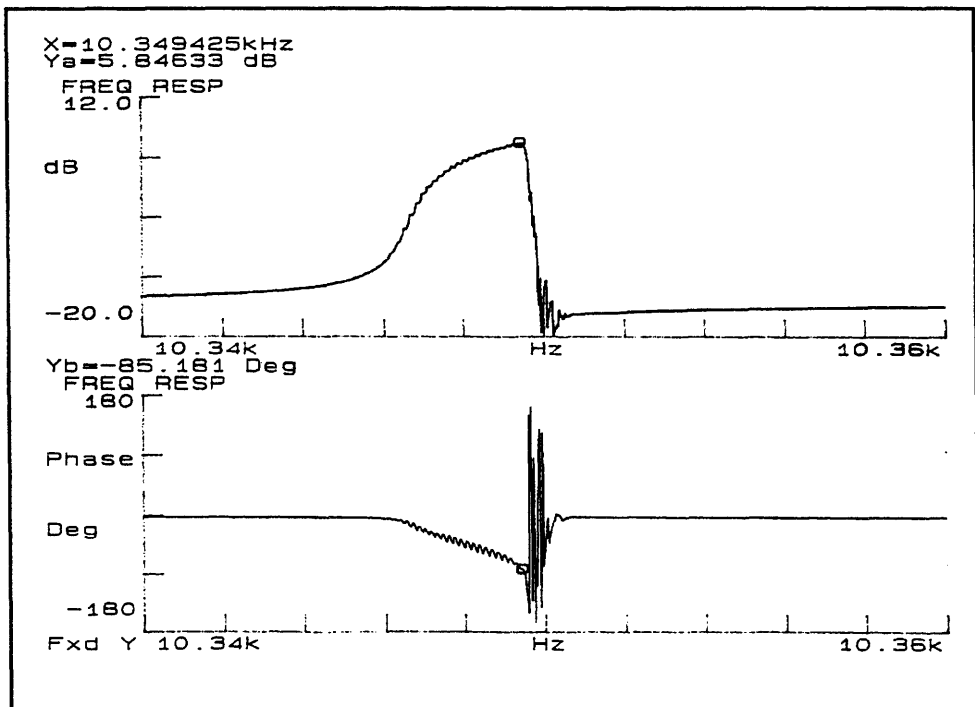
Figure 6.3. Small Amplitude Horizontal Axis Frequency Response

where,

A = the non-dimensional amplitude of the oscillation

ω_d = horizontal, linear resonant frequency

ω_{nl} = measured nonlinear resonant frequency, and

$\tilde{k}_3$ = non-dimensional cubic spring constant.

The peak magnitude of the oscillation of the large amplitude shark fin response occurred at a frequency of 10.35853 kHz, and was measured as 0.4186 Volts. Using the drive axis sensing constant from Equation 6.5, this value is equivalent to 3.987 µm, which is equal to a non-dimensional amplitude[5] of 0.3987. For the low amplitude response, the displacement is 1.8669 µm with a resonant frequency of 10.34943 kHz. In both of these responses, when the phase reaches -90°, the amplitude response jumps to a smaller value, as predicted by the analysis in Chapter 2.

The two peak amplitude measurements may be used for a least squares estimate of Equation 6.9. From this fit, the linear resonant frequency is 10.34687 kHz, which, given the mass from Section 6.1.1, yields a drive-axis linear spring constant of 30.008 N/m. The non-dimensional cubic spring constant is 0.0189, which, from Equation 2.11, gives a cubic spring constant of 5.672 nN/µm^3.

For the final drive axis open-loop test, an AC excitation of 5 mV was applied to generate linear oscillator behavior. From this response, both the linear resonant frequency and the quality factor of the system may be determined. For the horizontal axis, ω_x is 10.34664 kHz, and Q_x is 63,800. This frequency is within 0.03% of the frequency calculated by fitting the large and small amplitude responses to Equation 6.9.

6.2.2.2 Vertical Axis On-Axis Dynamic Parameters

To determine the linear and cubic springs, as well as the quality factor, of the vertical axis, open-loop frequency responses were performed by first applying the voltage to the vertical control force plate and then sensing the motion using the difference of the integrated charge outputs from the oppositely biased sense plates. Vertical responses are shown in Figures 6.4[6] and 6.5. In Figure 6.4, a 250 mV sine wave is swept both up (dashed line) and down (solid line) in frequency. The hysteresis of the soft cubic spring and the jump phenomenon is clearly seen, since the upsweep response peaks at a higher frequency than the downsweep response, as expected from Section 2.1.3.1. In Figure 6.5, the vertical axis response of the SEO to a 100 mV downswept sine excitation is plotted.

---

[5]Using a nominal displacement of 10 µm.

[6]For this section only, the sensing constant from Section 6.1.3.2 must be scaled by an additional factor of 20 because of an electronics modification.
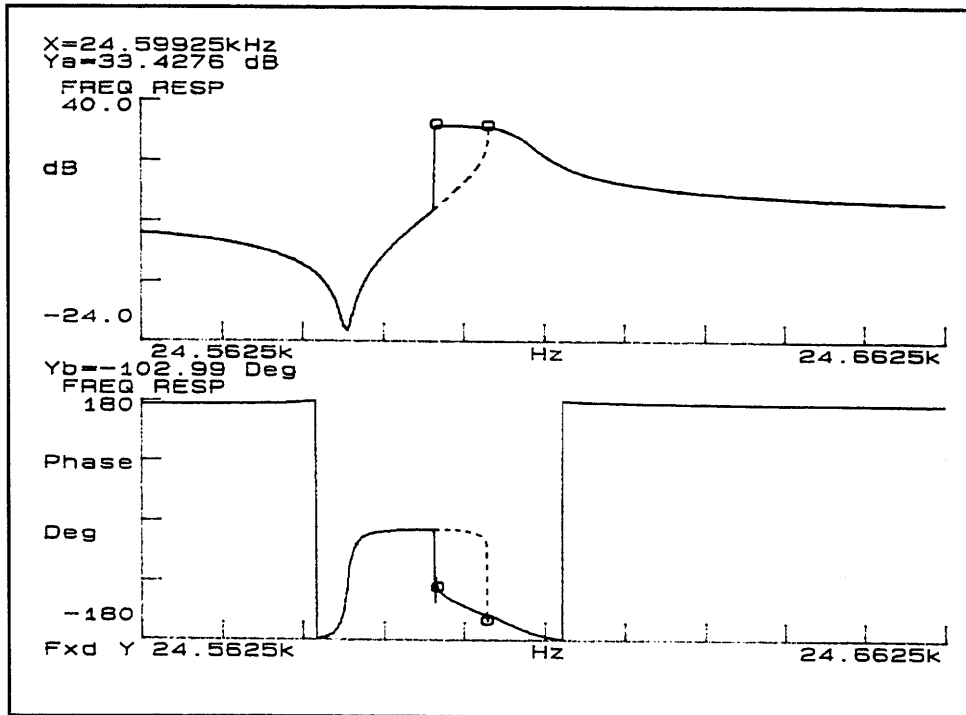
Figure 6.4. Large Amplitude Vertical Axis Frequency Response
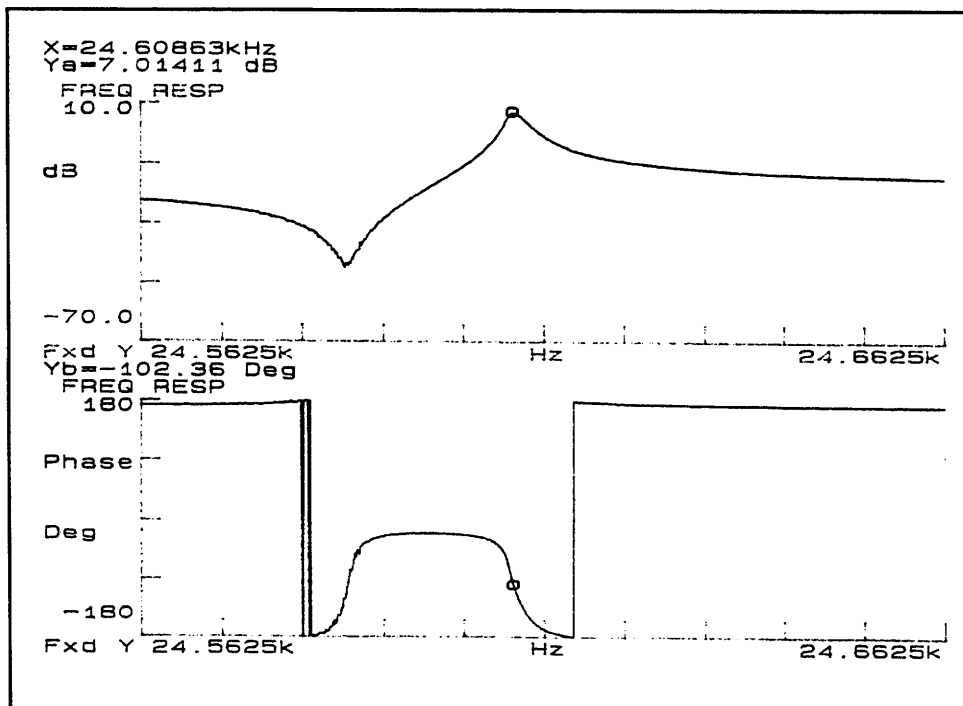
Figure 6.5. Small Amplitude Vertical Axis Frequency Response

228

From the two downsweep responses, the linear and cubic spring terms may be determined. In Figure 6.4, the peak is equivalent to a vertical displacement of 0.234 μm at 24.59925 kHz. The maximum displacement in Figure 6.5 occurs at 24.60863 kHz, and it is equal to 0.0895 μm. Solving Equation 6.9 by fitting these two measurements yields a vertical axis linear resonant frequency of 24.61024 kHz; the vertical spring constant is 169.77 N/m. The non-dimensional cubic spring constant is -2.173, which is equivalent to -0.652 μN/μm³. One conclusion that may be drawn here is that the snapdown experiment of Section 6.2.1 yielded an estimate of the vertical resonant frequency that was within 2% of the actual value; the snapdown test provides an accurate estimate of ω_y with much less effort. In addition, it has been shown here that the vertical axis does indeed have spring softening, as discussed in Chapter 2.

In the final test, a 5 mV swept sine amplitude was used again for a linear frequency response. Here, ω_y was measured at 24.608225 kHz, a difference of less than 0.1% from the value calculated from the least squares fit of the large and small amplitude responses. The quality factor was estimated at 13,450; about one-fifth the value of Q_x.

6.2.2.3 Vertical Axis Coupled Dynamic Parameters

To determine the cross-coupling between the x-axis and y-axis, two sets of frequency responses were collected. By applying a force at the horizontal drive combs and detecting the resulting vertical motion from the sense plates, both the spring cross-coupling, k_{xy}, and the force coupling, β_x, may be determined. In the first experiment, the region of interest was near the vertical resonant frequency. At ω_y, there is little to no x-axis motion, so that the dynamic coupling into the vertical axis comes from the force coupling term, β_x. Once this constant had been determined, the excitation was applied near ω_x in the second experiment to generate horizontal motion, which couples into the y-axis through k_{xy}.

Since these tests are run open loop, the force coupling is in-phase with the spring cross-coupling. In closed-loop operation, these two error forces are 90° out of phase. The resulting vertical motion may be expressed as

$$\|\tilde{y}\| = \frac{\left(\tilde{k}_{xy}\tilde{x} + \beta_x\tilde{F}_d\right)}{\left(\tilde{\omega}_y^2 - \tilde{\omega}^2\right)^2 + \left(\dfrac{\tilde{\omega}_y\tilde{\omega}}{Q_y}\right)^2}\left[\left(\tilde{\omega}_y^2 - \tilde{\omega}^2\right)\sin\tilde{\omega}\tau - \left(\dfrac{\tilde{\omega}_y\tilde{\omega}}{Q_y}\right)\cos\tilde{\omega}\tau\right] \qquad (6.10)$$

where,

$\tilde{\omega}$ = applied sinusoidal frequency

$\tilde{\omega}_y$ = vertical axis resonant frequency, and

$\tilde{F}_d$ = normalized x-axis force.

If the frequency is applied near the vertical resonance, then the cosine term will dominate; otherwise, the sine term will be the only observable term. Additionally, at the vertical resonant frequency, the lateral displacement is minimal, and may be neglected.

The frequency response plots are not shown here because they do not provide visual insight into the SEO behavior; the data are summarized for the parameter estimates. From the first set of frequency responses, for an applied AC voltage of 100 mV, the peak vertical displacement was 0.0227 μm; for 250 mV, 0.0553 μm. The applied forces were not large enough to generate nonlinear responses; both of the peaks occurred at a frequency of 24.6146 kHz. From these two measurements, the estimate of β_x is 0.1351. In the second set of frequency responses, the large (250 mV) and small (100 mV) vertical amplitudes are 0.0229 μm at 10.35853 kHz and 0.00926 μm at 10.34943 kHz, respectively. The horizontal peak displacements here are 3.987 μm and 1.8669 μm. The non-dimensional spring cross-coupling estimate is -0.00826, which is equivalent to -0.2479 N/m. The cross-damping term, Q_{xy}, was not determined, because it is small compared to these other forces.

6.2.2.4 Rotational Axis On-Axis Dynamic Parameters

The left and right torque control plates were used to generate rotational motion. The θ-axis downsweep frequency responses are plotted in Figures 6.6 and 6.7. As discussed in Chapter 4, the same DC voltage and equal and opposite AC voltages are applied to the control plates. This generates a torque with no DC component and no vertical force. In Figure 6.6, a 50 mV swept sine is applied to both torque plates, and, in Figure 6.7, a 25 mV swept sine is used. In both of these plots, the magnitude responses exhibit jump phenomenon at the nonlinear resonant peak when the phase reaches 90°. There is an additional 180° of phase shift in the electronics that moves the expected -90° phase to the observed +90°.

From these two measurements, the cubic spring softening constant and the rotational linear resonant frequency, ω_θ, may be calculated. In the first response, the rotational amplitude peak is 1.0 mrad (0.057°) at 18.20975 kHz. For the second response, the peak of 0.489 mrad (0.028°) occurs at 18.21825 kHz. Fitting these two measurements to Equation 6.9 yields a linear rotational resonant frequency of 18.2209 kHz; the corresponding rotational spring constant is 1.678 μN-m. The non-dimensional cubic
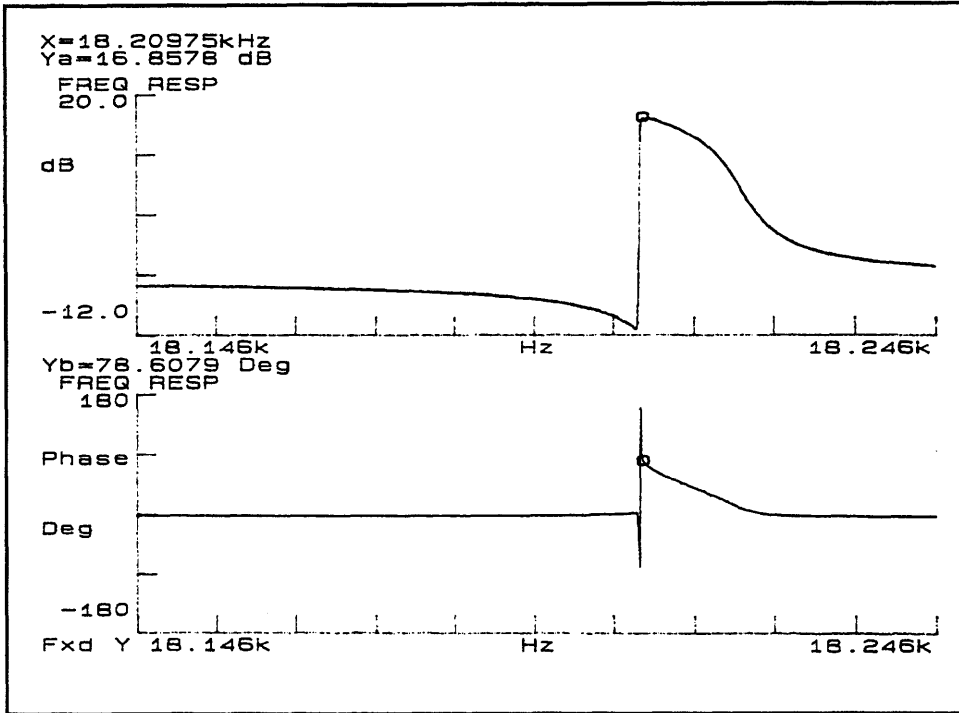
Figure 6.6. Large Amplitude Rotational Axis Frequency Response
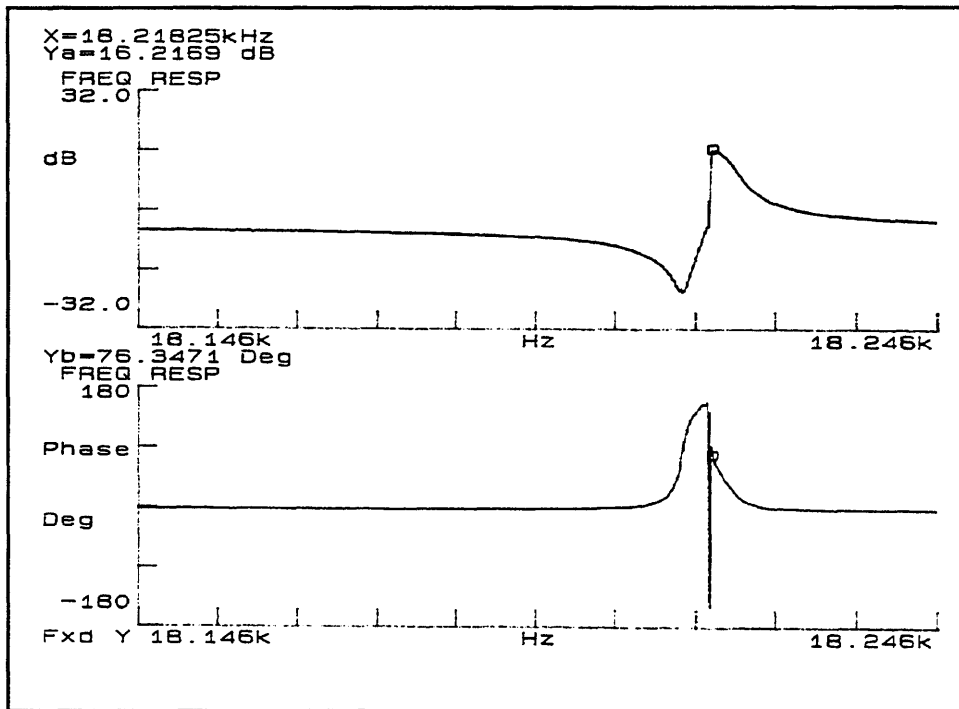
Figure 6.7. Small Amplitude Rotational Axis Frequency Response

231

spring constant is -1634.94, which is equivalent to -0.885 mN-m. As expected, the cubic spring for θ is soft.

A linear resonant response was generated by applying a 5 mV swept sine to the control plates. From this measurement, both ω_θ and Q_θ were determined. The linear resonant frequency was measured at 18.220348 kHz, an error of less than 0.005% from the calculated ω_θ. The rotational quality factor, Q_θ, was estimated at 16,000. This value is about one-fourth of the horizontal quality factor.

6.2.2.5 Rotational Axis Coupled Dynamic Parameters

To examine cross-coupling between horizontal and rotational motion, a voltage was applied to the motor comb to generate a vertical force that, because it is applied at the end of the proof mass, creates a torque. The motion was observed through the summation of the sense plate integrated charge outputs. Three frequency responses at ω_θ are shown in Figures 6.8 and 6.9. In the first plot, upsweep (dashed line) and downsweep (solid line) responses at 250 mV are shown on the same axes. Similar to the vertical axis, it is clear that the rotational axis has spring softening and exhibits jump phenomenon, since the upsweep peak of 634 μrad (0.0363°) at 18.249817 kHz occurs at a higher frequency than the downsweep peak of 913 μrad (0.0523°) at 18.246067 kHz. The hysteresis of the jump phenomenon is clearly seen in both the magnitude and phase of the response. In Figure 6.9, a 100 mV sine wave is swept down to generate a small amplitude response with a resonant peak of 367.47 μrad (0.021°) at 18.250567 kHz. Using Equation 6.10, modified for the rotational axis, the force coupling may be calculated from the two downsweep measurements. Here, γ_x is 0.0103, which includes the coupling of both the horizontal and vertical forces due to the comb finger interaction with the torque control plates. This result may then be used to determine the dynamic cross-coupling between x and θ by exciting rotational motion at the horizontal resonant frequency.

In these experiments, for a sine voltage of 175 mV, the peak rotational displacement of 171 μrad (0.00980°) occurs at 10.35515 kHz, and corresponds with an x-displacement of 3.789 μm. For an applied voltage of 250 mV, the peak is 186.139 μrad (0.0107°) at 10.361675 kHz with an x-displacement of 5.085 μm. With γ_x from above, the non-dimensional spring cross-coupling estimate is -0.00133, which is equivalent to -0.400 μN.

The magnitudes of the θ displacements due to cross-coupling at ω_x are sufficiently small (0.0107°) that rotational control is not required. Because these rotations will not adversely affect the oscillator performance, the increase in cost and complexity of this control system is not warranted. The deflection of the fingers at the end of the proof mass due to rotation on the order of 0.01° is about 50 nm.
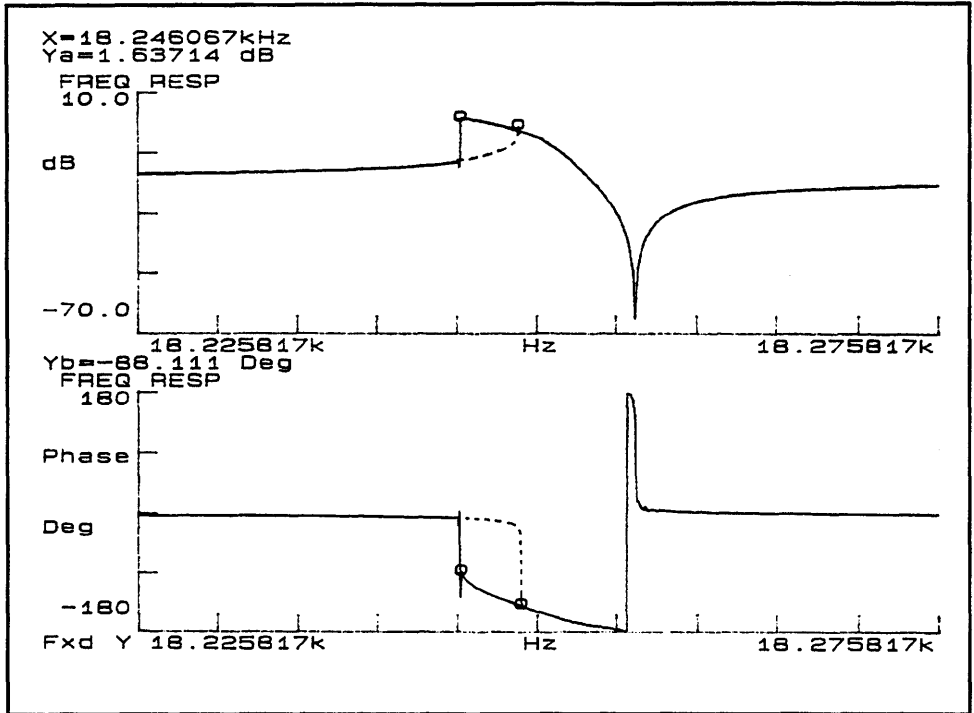
Figure 6.8. Large Amplitude Drive-Rotational Cross-Axis Frequency Response
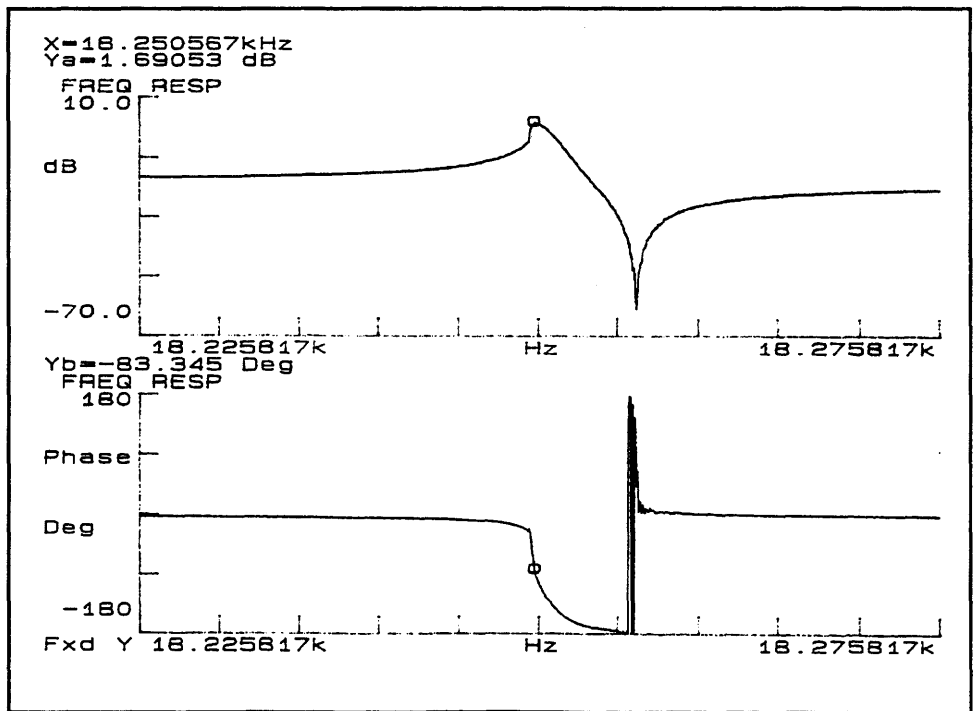
Figure 6.9. Small Amplitude Drive-Rotational Cross-Axis Frequency Response

233

6.2.3 Summary of SEO Dynamic Parameters

From the tests performed above, the parameters of the SEO are shown in Table 6.6. It is expected that these values are typical for the SEO family constructed in this process run. Preliminary tests on other SEOs, not presented here, confirmed that the mode order is the same and the resonant frequencies have similar values. From this table, a reduced-order, three degree of freedom model may be constructed. The couplings between y and θ have been neglected because their effects are negligible when compared with the coupling of the lateral motion into the vertical and rotational degrees of freedom.

Table 6.6. Summary of SEO Dynamic Parameters

Parameter	Value
k_x	30.008 N/m
k_{x3}	5.672 nN/μm^3
k_y	169.77 N/m
k_{y3}	-0.652 μN/μm^3
k_θ	1.678 μN/m/rad
$k_{\theta3}$	-0.885 mN-m/rad^3
k_{xy}	-0.2479 N/m
$k_{x\theta}$	-0.400 μN
Q_x	63,800
Q_y	13,450
Q_θ	16,000
β_x	0.1351
γ_x	0.0103

In the SEO design, the resonant frequency separations were much greater than assumed in Chapters 2 through 5. The vertical resonant frequency was 2.38 times the lateral resonant frequency, and the rotational resonant frequency was 1.76 times ω_x. The SEO was fabricated at a greater thickness than the design specification, and the proof mass support beams came out thinner than expected, due to manufacturing irregularities. These two changes would increase ω_y much more than ω_x; hence the large separation.

The significant conclusions from these open-loop experiments are that cubic spring behavior exists on all three degrees of freedom: spring hardening for the x-axis and spring softening for the y- and θ-axes. In addition, cross-coupling exists between the lateral motion and the other two degrees of freedom. The rotation due to lateral coupling

is negligible; a force rebalance loop is not necessary. The motion induced into the vertical axis is sufficiently large that a force rebalance loop should be designed for the vertical axis. The large Q assumptions used earlier to develop models and control systems are valid. The resonant mode order is horizontal, rotational, and vertical.

6.3 Closed-Loop Control of the Vertical Axis

Once the open-loop testing was completed, the vertical axis control system designed in Chapter 5 was constructed and implemented on a micromechanical tuning fork gyroscope. This device is very similar to the SEO with respect to the dynamics of the system and size of the proof mass, but is different in a very fundamental way. This gyroscope is a two proof mass design, which means that the sense plate under one proof mass must be grounded so that its motion is not observed. In this way, the only motion observed will be that of the controlled proof mass. The control system is a force rebalance loop, which means that, in addition to minimizing the vertical motion, the control signals are used to provide information on the magnitude and variation in both the quadrature and in-phase signals.

Potentiometers were used in both the in-phase and quadrature loops for the value of R_1 in Figure 5.5 to permit tuning of the gain of the compensator to optimize the performance of each control loop. The nominal values of R_1 are 3.3 kΩ on the in-phase loop and 6.7 kΩ for the quadrature loop. These resistances were determined from the simulations run in Chapter 5. The electronics were configured so that the vertical control loop could be opened and closed independently of the drive axis closed loop.

6.3.1 Physical Characterization of Closed-Loop Resonator

With this resonator, the critical static parameters, such as the forcing and sensing constants, had to be determined. The capacitor measurement techniques discussed in Section 6.1.2.2 were used to measure the motor drive, motor sense, vertical sense, and vertical force capacitors. These values, and the corresponding constants, are shown in Table 6.7. In these electronics, the gains for the horizontal and vertical sensing constants are very large. However, this does not adversely affect the performance of the closed loop. The maximum lateral and vertical forces are 0.108 μN and 0.2426 μN, respectively.

Table 6.7. Static Parameters for Closed-Loop Resonator

Parameter	Value
C_m	54.19 fF
C_{ms}	54.19 fF
C_{yf}	24.26 fF
C_{ys}	600 fF
$K_{F,x}$	2.1677 nN/V^2
$K_{S,x}$ (gain of 50)	0.2710 V/μm
$K_{F,y}$	4.852 nN/V^2
$K_{S,y}$ (gain of 1000)	700 V/μm

After completing the open-loop characterization of the device, the resonator was started with the vertical control loop open and the drive loop closed. Once the resonator was in steady-state lateral oscillations, its parameters were measured, and are shown in Table 6.8, where, as before, in-phase and quadrature vertical motions are defined with respect to the proof mass horizontal velocity.

Table 6.8. Laterally Oscillating Resonator Parameters with Open Vertical Axis

Parameter	Value
Drive Axis Frequency	23.595 kHz
Vertical Axis Frequency	25.35 kHz
Drive Amplitude	8 μm
Amplitude Control Voltage	1.059 V
In-phase Amplitude	-0.269 V
Quadrature Amplitude	6.969 V

The in-phase and quadrature voltages represent a vertical displacement amplitude of 9.963 nm, with 9.956 nm from the quadrature signal and 3.84 Å from the in-phase signal. With the open vertical loop, both of the control signals are saturated at the supply voltages of the op-amps. From the amplitude control voltage, the quality factor of the horizontal axis, Q_x, may be approximated as 78,340; a value similar to that of the open-loop experiments. Since this resonator was in a sealed container, this measurement verified that the package is still holding a vacuum.

236

6.3.2 Vertical Axis Closed-Loop Performance of Micromechanical Resonator

Once the horizontal motion reached closed-loop, steady-state operation, the vertical axis loop was then closed, and the vertical amplitude was reduced dramatically to less than an Angstrom. The pots were trimmed to optimize the performance of the control system. The results are shown in Table 6.9, where the open-loop, vertical axis amplitudes are compared with the closed-loop vertical axis amplitudes, and the control voltages are given.

Table 6.9. Comparison of Vertical Axis Open and Closed-Loop Operation

Quantity	Open Loop (Volts)	Closed Loop (Volts)
In-Phase Amplitude	-0.269	0.005
Quadrature Amplitude	6.969	0.04
In-Phase Control	N/A	-1.27
Quadrature Control	N/A	-7.5

From this table, it is clear that the vertical axis force rebalance loop is very effective. The vertical motion has been reduced by a factor of 173 to an amplitude of 0.57 Å. The in-phase motion is reduced by a factor of 54 to 0.0714 Å, and the quadrature motion is reduced by a factor of 174 to 0.5714 Å. The values for R_1 used in this case are 1.143 kΩ on the in-phase loop and 0.906 kΩ on the quadrature loop, compared to the Chapter 5 simulation values of 3.3 kΩ and 6.73 kΩ, respectively. In addition, the large value of the quadrature control signal suggests that quadrature over 8 Volts probably cannot be eliminated, but most certainly can be reduced by about 7 Volts. In such a situation, the resulting quadrature signal would be on the order of 1 Volt, instead of nearly 10 Volts. In this case, the quadrature loop does not close because of saturation of the control voltage. By tightening the manufacturing tolerances, the as-built quadrature may be reduced so that the control loop can close. Or, the force plate area can be enlarged to increase the maximum control force.

6.3.3 Force Rebalance Loop Response to Sinusoidal Disturbance

Once it was determined that the closed loop was indeed functional, the resonator was placed on a rate table to investigate the behavior of the control system to a sinusoidal disturbance. By applying a rate about the z-axis of the resonator, a Coriolis force is created, which will increase the in-phase component of the vertical motion. The rate

table was oscillated with a sine wave of 2 rad/sec amplitude at a frequency of 0.5 Hz. If the vertical force rebalance loop is operating correctly, then the in-phase control signal varies proportionally to the applied sinusoidal rate.

The open-loop vertical motion components were 0.1183 Volts for the in-phase, and 4.695 Volts for quadrature. When the vertical control loop was closed, the in-phase component was reduced to 0.0067 Volts, and the quadrature, 0.380 Volts. In this case, the quadrature loop saturated, and was only able to reduce the quadrature motion by a factor of 10. Feedthrough and other error sources most likely contributed to this degradation in performance from the previous section. Because the quadrature disturbance was larger than the maximum quadrature control force, the quadrature rebalance loop was able to counteract most, but not all of the quadrature disturbance. The control voltages were -2.63 Volts for the in-phase channel and -9.87 Volts for the quadrature channel. When the rate was applied to the table, the in-phase component of vertical motion remained at 6.7 mV, while the quadrature component moved slightly in response to the input rate, because the control loop was not closed about the quadrature component. The in-phase control signal, however, varied between +4 and -6 Volts to compensate for the sinusoidal disturbance. The scale factor between the applied rate and the in-phase control signal for this resonator is about 2.5 V/rad/sec.

6.4 Experimental Conclusions

In this chapter, the physical and dynamic parameters of the SEO are determined. It is shown that the rotation magnitudes are on the order of $0.01°$ for a lateral motion of 5 μm, and may therefore be neglected in most models; however, the rotor-sense plate capacitor model should still include the θ-effects for measuring both vertical and rotational motion. It was verified that both the vertical and rotational degrees of freedom have soft cubic spring constants. The reduced-order model ignores coupling between vertical and rotational motion, as well as the cross-damping terms of all degrees of freedom. The state-space model from Equation 4.5 may be used to derive the reduced-order state-space model by using the parameters listed in Table 6.5 and by setting all other terms equal to zero.

The force rebalance loop for vertical motion was successfully closed about both the in-phase and quadrature paths. The amplitude of the vertical motion was reduced by a factor of 200, from 10 nm to 0.57 Å. This performance is 350 times more precise than static vertical positioning of a non-oscillating proof mass [9, 10]. In addition, it was demonstrated that the control system is robust to sinusoidal disturbances, and that the components of vertical displacement can be held at zero while the control signal varies to

238

counteract the effects of the disturbance and give information on the disturbance forces. The saturation of the quadrature rebalance loop in this experiment should not be considered a failure. As the manufacturing processes improve, the as-built quadrature (initial quadrature of the device) will be reduced, and the quadrature force rebalance loop will work successfully. The fact that the quadrature loop was closed during the preliminary closed-loop tests demonstrates that both rebalance loops work. With less as-built quadrature, both the in-phase and quadrature force rebalance loops can be closed successfully.

Chapter 7

Conclusions and
Recommendations for Future Work

7.0 Introduction

In this thesis, a micromechanical single element oscillator was investigated. The behavior of a three degree of freedom dynamic and electrostatic model was studied in both open-loop and closed-loop configurations. Experiments were conducted to validate both the three degree of freedom model and the vertical and rotational force rebalance loops. In this chapter, the work performed in the thesis is summarized, and conclusions from this work are presented. The contributions to the development of micromechanical oscillators are listed, and suggestions for future work are made.

7.1 Thesis Summary

The existence and stability of a limit cycle at the lateral resonant frequency was demonstrated. A rotational degree of freedom was added to the dynamic model, and new capacitor models were derived to include proof mass rotation. The dynamic parameters of the SEO were measured for the three degree of freedom model. Force rebalance loops were designed for both the vertical and rotational degrees of freedom, and both performed successfully in simulation. The three degree of freedom dynamic parameters of the SEO were measured, and the vertical force rebalance loop was successfully implemented on a micromechanical gyroscope.

7.1.1 Sustained Lateral Oscillations of Proof Mass

Lateral oscillations are sustained with a self-excitation loop and an amplitude regulator. The self-excitation loop consists of the plant, an integrator, and a relay feedback element. The amplitude regulator loop contains the plant, an absolute value

241

function, a low-pass filter, and a PI controller. These two loops were analyzed to investigate the stability and behavior of the oscillator.

Both the existence and stability of the self-excitation loop limit cycle was proven using describing function analysis. The stability criterion was shown to be independent of pressure; the system is stable, as long as the restoring force of the horizontal motion is either a linear or hard spring. Therefore, the resonator may be operated closed loop at very low pressures without instabilities. Since this control system is analog, there is no concern of unstable limit cycles at low pressure; a phenomenon that has been observed in digital control systems [9, 10].

The amplitude regulator loop, which is a nonlinear control system, was linearized by assuming that the amplitude and phase are slowly varying with respect to the frequency of the oscillation. The amplitude behavior predicted by this simplified model closely matched that of the simulation, which is a more accurate representation of the oscillator. The simplified model demonstrated the three distinct regions of amplitude growth during oscillator self-excitation. During startup, this regulator varies between a first-order and second-order system to drive the oscillator to its steady-state amplitude in about 1 second.

7.1.2 Three Degree of Freedom Dynamic and Electrostatic Models

Once the behavior of the drive axis loop was modeled and analyzed, the rotational degree of freedom was added to the dynamics of the system. With finite element analysis, it was shown that, for rotations on the order of $0.01°$, the comb drive capacitor model may neglect the effects of rotation. A new parallel plate capacitor model was then developed to include the effects of proof mass rotation, and two sensing schemes were introduced to measure vertical and rotational motions simultaneously, both of which exist at the resonant frequency of the drive axis. By splitting the sense plate into two halves and applying equal and opposite potentials to each, both motions may be observed. In the open-loop frequency response experiments of Section 6.2, the charges injected onto each sense plate by the vertical and angular motions of the proof mass were integrated, and the resulting voltages were added and subtracted to yield both the rotational and vertical motions, respectively. This successfully demonstrated that the split sense plate design can be used to measure both rotation and vertical translation of the proof mass.

7.1.3 Vertical and Rotational Force Rebalance Loops

Finally, force rebalance loops were designed for both the vertical and angular motions. Through linearization of the nonlinear demodulators and remodulators in the control paths, a baseband model was developed and used to design PI compensators that

guaranteed stability. In addition, by closing the loop, the vertical axis bandwidth was increased from about 2000 Hz to 5770 Hz. These simple, low cost, and effective controllers met both goals of the force rebalance loop: to eliminate all of the motion and to provide information on the magnitudes of the in-phase and quadrature components of the forces. Simulations were performed to demonstrate the operation of the micromechanical oscillator when all three degrees of freedom were operated closed loop: the horizontal loop sustained limit cycle oscillations at the drive resonant frequency, and the vertical and rotational force rebalance loops eliminated almost all motion while providing information on the in-phase and quadrature magnitudes of both motions.

7.1.4 Measurements and Experimental Results for SEO

Parameter characterization tests were performed on the SEO to determine the forcing and sensing constants. Frequency response experiments were then performed to determine both the on-axis and cross-coupling constants. The on-axis, open-loop experiments showed that the mode order, in terms of increasing frequency, is horizontal, rotational, and vertical. The vertical axis Q is about one-fifth of the horizontal quality factor, and the rotational Q is about one-fourth Q_x. The x-y cross-coupling produced vertical displacements on the order of 22 nm for a 4 μm horizontal displacement. The x-θ cross-coupled rotations were on the order of 137 μradians, also for a 4 μm horizontal displacement. Since these angular displacements are on the order of 0.01°, the effects of rotation on the drive axis may be ignored; the rotational effects on the sense plate capacitance were retained.

The vertical force rebalance loop was implemented on a micromechanical gyroscope. Once the motor excitation loop and amplitude regulator reached steady-state, lateral, proof mass oscillations, the vertical force rebalance loop was closed. The performance of this control system was dramatic: the vertical motion was reduced from an amplitude of 10 nm to 0.57 Å, a factor of 173 improvement. The in-phase component was reduced from 3.84 Å to 0.07 Å, and the quadrature component was reduced from 9.956 nm to 0.57 Å.

A 2 rad/sec amplitude sinusoidal disturbance at 0.5 Hz was then applied about the z-axis of the oscillator to generate a Coriolis force. The in-phase control signal varied to compensate for this disturbance, while the in-phase component of the proof mass vertical displacement was unchanged. In this experiment, the quadrature loop saturated and did not close because the quadrature error force was greater than the maximum possible vertical control force. The force rebalance tests demonstrated that the force rebalance

loop minimizes the vertical motion while providing information on the disturbances through the control voltage levels.

7.2 Conclusions

This thesis investigated several areas of micromechanical resonators. The behaviors of the self-excitation and amplitude regulator loops for sustained lateral oscillations were examined in detail. A three degree of freedom model was used to determine advanced capacitor models and cross-coupling among the modes. Finally, force rebalance loops were designed and simulated for both vertical and rotational motions.

In Chapter 3, it was proven that the self-excitation loop sustains a unique limit cycle at the lateral resonant frequency and the desired amplitude. The limit cycle stability criterion was also derived. The limit cycle is stable for linear and hard springs; the criterion is pressure-independent. Transient responses of the limit cycle were shown to be stable, with a time constant of $2Q$. Also in Chapter 3, the amplitude regulator was modeled, and its behavior was broken into three regions: two areas of first-order behavior, and one of second-order behavior.

In Chapter 4, the three degree of freedom model was used to develop both a dynamic model and capacitor models as functions of x, y, and θ. With these models, two schemes for simultaneous detection of vertical and rotational motion were presented. In Chapter 6, the DC bias with two pre-amplifiers approach was used to measure successfully both y and θ. It was also shown in Chapter 4, that, for rotations on the order of $0.01°$, the comb drive capacitor model may be considered independent of θ.

Force rebalance loops were designed for both vertical and rotational motion in Chapter 5. Simulations confirmed that both rebalance loops reduce unwanted vertical and vertical motions and provide information on the in-phase and quadrature components of each motion. With the present control torque plate configuration, the torquing coefficients are functions of the lateral position of the proof mass; a redesign of the control plate shape is necessary to eliminate this dependence.

In Chapter 6, open-loop frequency responses on the SEO confirmed that cross-coupling exists between the lateral motion and both the vertical and rotational motions. In addition, the cubic spring behavior of all three degrees of freedom was verified. The vertical force rebalance loop was successfully implemented on the laterally oscillating proof mass of a micromechanical gyroscope. This accomplishment represents a significant advancement in the development of micromechanical resonators. Previous vertical control systems had been implemented on stationary proof masses, and often exhibited high-frequency limit cycles at low pressure due to the digital control system

244

design. The digital control system also limited control accuracy to 25 nm [9, 10]. In this thesis, the motion is controlled to 0.57 Å, a factor of 400 improvement over earlier attempts [9, 10], and the high-frequency limit cycles have been eliminated with analog control system design.

7.3 Contributions to Micromechanical Oscillators

In this thesis, several contributions have been made to the field of micromechanical oscillators. The analytic proof of the existence and stability of a unique limit cycle for a self-excitation loop demonstrated that the nature of the cubic spring determines stability. The simplified model of the amplitude regulator may be used to optimize the startup behavior of an oscillator. These contributions may be used to improve the self-excitation control system.

Adding rotation to the dynamic and capacitor models increased understanding of micromechanical resonators. The sensor and actuator capacitor models included lateral, vertical, and rotational motion. From these models, a method was presented to observe vertical and rotational motions simultaneously. Typical rotations were measured on the order of 0.01°. This is an important contribution because it is the first time that lateral, vertical, and rotational motions have been measured on a lateral micromechanical resonator. Cross-coupling between the degrees of freedom was also characterized, as was the cubic spring behavior of all three degrees of freedom.

Force rebalance loops have been designed for both vertical and rotational motion. Simulations validated the performance of these loops. The vertical force rebalance loop was implemented on a micromechanical gyroscope with great success. In the first test, both the in-phase and quadrature loops were closed, and the vertical motion of the laterally oscillating proof mass was reduced by a factor of 175. In the second test, the in-phase rebalance loop counteracted the Coriolis force from an applied rate, and the loop provided accurate information on the magnitude of the rate. These two tests are a significant contribution to the development of micromechanical resonators, because it is the first time that the vertical axis rebalance loop has been closed on a laterally oscillating device.

7.4 Recommendations for Future Work

While some important advances were made in this thesis, several topics remain to be addressed. First, the split sense plate design can be used on other micromechanical resonators to determine the magnitude of the angular displacement for other proof mass designs. For a two proof mass oscillator, this system would require four charge

integrators; clearly this is best done on a prototype basis, and conclusions may then be drawn for a family of resonators. Specifically, it would be interesting to examine how different anchoring designs affect the rotation of the proof mass.

For the force rebalance loop, the next step is to control independently both proof masses in a dual proof mass resonator, such as a tuning fork gyroscope. Accomplishing this task would require four control paths, one for the in-phase and quadrature components of each of the two proof masses. Since it is necessary to estimate the vertical motion of each proof mass independently, the net common mode and differential mode information could be determined from the in-phase and quadrature signals by summing and differencing these voltages. This approach would provide insight for improving the design of the resonator. In addition, since the vertical motion has a negative cubic spring term, the stability criterion for a soft cubic spring limit cycle should be examined in more detail to determine the value that makes the limit cycle unstable.

Another interesting area of investigation would be a metallization pattern for linear torquing coefficients, as mentioned in Chapter 5. As the proof mass oscillates, the moment arm for the torque control plate varies, resulting in a nonlinear torquing coefficient. Moving the control plate completely under the proof mass does not solve the problem. Perhaps changing the shape of the control plate as a function of x would allow the product of the area and the moment arm to yield a constant value, such that the rotational in-phase and quadrature control voltages can be fedback directly, without having to combine and manipulate the values, as was done in Section 5.2. By simplifying the rotational control system electronics, implementation of rotational force rebalance may prove to be cost effective.

Nonetheless, it is clear that closed-loop control of all three degrees of freedom is both possible and effective. By using a force rebalance approach, the bandwidth and sensitivity of the device to external disturbances are increased. The successful implementation of the vertical force rebalance loop and the observation of rotational motion are two significant contributions to the field of micromechanical resonators.

246

Appendix A

Square Wave Relationships and Trigonometric Identities

A.1 Square Wave Relationships

The hard limiter in the closed loop design generates square wave signals based on the sinusoidal inputs. Further manipulations of these waveforms produce some interesting results. Here, some basic relationships of square waves are given.

The function *sqr* is in-phase with a sine wave, and is defined as

$$\text{sqr } \alpha = \frac{4}{\pi}\sin\alpha + \frac{4}{3\pi}\sin 3\alpha + \frac{4}{5\pi}\sin 5\alpha + ... + \frac{4}{(2n+1)\pi}\sin(2n+1)\alpha \qquad (A.1)$$

The function *csqr* is in-phase with a cosine wave, and is defined as

$$\text{csqr } \alpha = \frac{4}{\pi}\cos\alpha + \frac{4}{3\pi}\cos 3\alpha + \frac{4}{5\pi}\cos 5\alpha + ... + \frac{4}{(2n+1)\pi}\cos(2n+1)\alpha \qquad (A.2)$$

From here, some basic identities are

$$\text{sqr}^2 \alpha = 1$$
$$\text{csqr}^2 \alpha = 1$$
$$\text{sqr } \alpha \text{ csqr } \alpha = \text{sqr } 2\alpha \qquad (A.3)$$
$$\text{sqr } \alpha \text{ sqr } 2\alpha = \text{csqr } \alpha$$
$$\text{csqr } \alpha \text{ sqr } 2\alpha = \text{sqr } \alpha$$

The function csqr 2α was not used in this thesis, so identities for this function are not included. It is sufficient to say that the csqr 2α function does not have straightforward relationships.

The significant identities here are that the square of either sqr α or csqr α is 1; this permitted forces to be generated at DC and the resonant frequency. The next harmonic

247

was at 3 times the resonant frequency, which is sufficiently attenuated by the high-Q resonator.

A.2 Trigonometric Identities

Some essential trigonometric relationships used in this thesis are provided to eliminate multiple trips to mathematical references. Chapters 2 and 3 have extensive trigonometric manipulations that make full use of the equations given here.

$$\sin(\alpha + \beta) = \sin\alpha\cos\beta + \cos\alpha\sin\beta$$

$$\cos(\alpha + \beta) = \cos\alpha\cos\beta - \sin\alpha\sin\beta$$

$$\sin 2\alpha = 2\sin\alpha\cos\alpha$$

$$\cos 2\alpha = \cos^2\alpha - \sin^2\alpha$$

$$\sin 3\alpha = 3\sin\alpha - 4\sin^3\alpha$$

$$\cos 3\alpha = 4\cos^3\alpha - 3\cos\alpha$$

$$2\sin\alpha\sin\beta = \cos(\alpha - \beta) - \cos(\alpha + \beta)$$

$$2\cos\alpha\cos\beta = \cos(\alpha - \beta) + \cos(\alpha + \beta)$$

$$2\sin\alpha\cos\beta = \sin(\alpha + \beta) + \sin(\alpha - \beta)$$

$$\sin\alpha + \sin\beta = 2\sin\left[\tfrac{1}{2}(\alpha + \beta)\right]\cos\left[\tfrac{1}{2}(\alpha - \beta)\right]$$

$$\sin\alpha - \sin\beta = 2\cos\left[\tfrac{1}{2}(\alpha + \beta)\right]\sin\left[\tfrac{1}{2}(\alpha - \beta)\right]$$

$$\cos\alpha + \cos\beta = 2\cos\left[\tfrac{1}{2}(\alpha + \beta)\right]\cos\left[\tfrac{1}{2}(\alpha - \beta)\right]$$

$$\cos\alpha - \cos\beta = -2\sin\left[\tfrac{1}{2}(\alpha + \beta)\right]\sin\left[\tfrac{1}{2}(\alpha - \beta)\right]$$

$$2\sin^2\alpha = 1 - \cos 2\alpha$$

$$2\cos^2\alpha = 1 + \cos 2\alpha$$

(A.4)

Appendix B

Finite Element Analysis of Electrostatic Fields and Forces

B.1 Determination of Force Given Electric Field Density

The Lorentz force on a charge q in an electric field $\mathbf{E}$ is [38]

$$\mathbf{f} = q\mathbf{E} \tag{B.1}$$

The force density may then be defined as the force exerted over an incremental volume of the total structure

$$\mathbf{F} = \rho_f \mathbf{E} \tag{B.2}$$

where ρ is the charge density (C/m^3). Using the constituent relation

$$\mathbf{D} = \varepsilon\mathbf{E} \tag{B.3}$$

in Gauss's law yields the force density

$$\mathbf{F} = (\nabla \cdot \varepsilon\mathbf{E})\mathbf{E} \tag{B.4}$$

In an electric field, $\nabla \times \mathbf{E} = 0$, which allows Equation B.4 to be rewritten as

$$\mathbf{F} = (\nabla \cdot \varepsilon\mathbf{E})\mathbf{E} + (\nabla \times \mathbf{E}) \times \varepsilon\mathbf{E} \tag{B.5}$$

From here, the vector identity

$$(\nabla \times \mathbf{A}) \times \mathbf{A} = (\mathbf{A} \cdot \nabla)\mathbf{A} - \frac{1}{2}\nabla(\mathbf{A} \cdot \mathbf{A}) \tag{B.6}$$

may be used to express Equation B.5 as

$$\mathbf{F} = (\nabla \cdot \varepsilon\mathbf{E})\mathbf{E} + \varepsilon(\mathbf{E} \cdot \nabla)\mathbf{E} - \tfrac{1}{2}\varepsilon\nabla(\mathbf{E} \cdot \mathbf{E})$$

With index notation, it is possible to rewrite the mth term of $\mathbf{F}$ as [38]

$$F_m = \frac{\partial}{\partial x_n}\left(\varepsilon E_m E_n - \tfrac{1}{2}\varepsilon \delta_{mn} E_k E_k\right)$$

$$= \frac{\partial T_{mn}}{\partial x_n} \tag{B.7}$$

where δ_{mn} is the Kronecker delta, and T_{mn} is a term of the Maxwell stress tensor. The Maxwell stress tensor is an ordered array of nine functions of space and time that may be written as

$$T_{mn}(\mathbf{r},t) = \begin{bmatrix} T_{11}(\mathbf{r},t) & T_{12}(\mathbf{r},t) & T_{13}(\mathbf{r},t) \\ T_{21}(\mathbf{r},t) & T_{22}(\mathbf{r},t) & T_{23}(\mathbf{r},t) \\ T_{31}(\mathbf{r},t) & T_{32}(\mathbf{r},t) & T_{33}(\mathbf{r},t) \end{bmatrix} \tag{B.8}$$

This tensor is symmetric, so that $T_{mn} = T_{nm}$. The units of T_{mn} are force per unit area, and may be used to define the traction, τ, which is a vector with components

$$\tau_m = T_{mn} n_n = T_{m1} n_1 + T_{m2} n_2 + T_{m3} n_3 \tag{B.9}$$

where n_n is the nth component of the outward-directed unit vector $\mathbf{n}$ which is normal to the surface of the volume V. From here, "the component T_{mn} of the stress tensor can be physically interpreted as the mth component of the traction applied to a surface with a normal vector in the n-direction" [38].

Having derived the Maxwell stress tensor, the force density is readily derived. In this case, the rotor tine, stator tines and control plate are assumed to be perfect conductors, which means that the electric field is perpendicular to the surface. This analysis has been performed for a volume. However, in two dimensional finite analysis, the third axis may be ignored, such that the stress tensor components are only

$$T_{11} = \frac{\varepsilon}{2} E_1^2 \tag{B.10}$$

$$T_{12} = 0 \tag{B.11}$$

$$T_{22} = \frac{\varepsilon}{2} E_2^2 \tag{B.12}$$

Since there is no tangential electric field on the surface, the cross tensor terms, such as T_{12}, are equal to zero. The total force exerted on the conductor may be expressed as

$$f_m = \int_V F_m dV = \int_V \frac{\partial T_{mn}}{\partial x_n} dV \tag{B.13}$$

If a vector $\mathbf{A}$ is defined to have the components

$$\mathbf{A} = \begin{bmatrix} A_1 \\ A_2 \\ A_3 \end{bmatrix} = \begin{bmatrix} T_{m1} \\ T_{m2} \\ T_{m3} \end{bmatrix} \qquad (B.14)$$

then Equation B.13 may be rewritten as

$$f_m = \int_V \frac{\partial A_n}{\partial x_n} dV = \int_V (\nabla \cdot \mathbf{A}) dV \qquad (B.15)$$

The divergence theorem may then be used to change the volume integral into a surface integral

$$f_m = \oint_S \mathbf{A} \cdot \mathbf{n}\, da = \oint_S A_n n_n\, da \qquad (B.16)$$

where n is the outward-directed unit vector normal to the surface S which encloses the volume V. If Equation B.14 is substituted into Equation B.16, then the mth component of the force becomes

$$f_m = \oint_S T_{mn} n_n\, da \qquad (B.17)$$

from this equation it is possible to determine the total electric force on a volume by knowing only the fields on the surface of the volume.

Appendix C

MATLAB and FORTRAN Code
for Oscillator Simulations

C.1 MATLAB Code For Parameter Definitions

For these simulations, a MATLAB file, seojk.m, was used to define the all of the parameters of a particular run. This m-file was executed in MATLAB, and the parameters were saved to an ASCII file that was read by the FORTRAN simulation code. In the attached code, the parameters are provided for the complete three degree of freedom, all loops closed, oscillator model. Simpler incarnations of the simulation would require fewer parameters.

C.2 FORTRAN Code For Oscillator Simulation

The FORTRAN code listed the first-order differential equations that defined the particular system under study, from the two degree of freedom lateral self-excitation loop to the three closed loop model. The integration was done with a fourth-order Runge-Kutta method. The FORTRAN file was named seojksim.for, and it called the ASCII file generated by MATLAB to define the parameters of the system. The code shown here includes the three degree of freedom, all loops closed, oscillator model. Both files were cleaned up to remove many comment lines, so the *seojk.dat* data matrix and some of the READ routines may refer to variables that are not defined. This was done to make the code easier for the reader to examine; both programs functioned during the simulation studies of this thesis.

```
%SEOJK.M
%ANALYZE SINGLE ELEMENT OSCILLATOR OPERATION FOR 3 DOF, 3 LOOPS CLOSED
%GENERATE THE INPUT FOR SEOJKSIM.FOR WHICH INCLUDES CROSS-COUPLING
%AND NON LINEAR TERMS
%INITIALLY CODED 1/29/95 by Marc S. Weinberg
%LATEST REVISION 7/9/97 by Jonathan Kossuth
%LATEST RUN 7/9/97
%clear,
format short e, format compact, diary tfgdf.dia, i=sqrt(-1);
% FIRST LETTER D INDICATES QUANTITY WITH DIMENSIONS
dwn = 2e4*2*pi              %RAD/S SMALL AMPLITUDE DRIVE RESONANT FREQUENCY
dm = 2.73e-9               %KG, MASS OF ONE PROOF MASS TFG 13
dx =1e-5                   %NOMINAL DRIVE MAGNITUDE (0 TO PEAK)
%INPUT SEO DRIVE AXIS PARAMETERS
q=1.5e5                    %X AXIS QUALITY FACTOR
xk3=0.025                  %CUBIC TERM
kx=43;                     %DIMENSIONAL SPRING CONSTANT
% READ IN VARIABLES ASSOCIATED WITH VERTICAL MOTION
q2 = q/5                   %VERTICAL AXIS QUALITY FACTOR
wn2=1+0.09                 %RESONANCE OF VERTICAL AXIS
xm2=1                      %ALLOWS FOR THETA MODES (IF ONLY X AND THETA)
xkxy= 0.003                %THE X-Y SPRING CROSS-COUPLING
bxy=.03/q                  %X-Y CROSS-DAMPING
Vs=5;                      %SENSE PLATE BIAS VOLTAGE
Cy0=1e-12;                 %NOMINAL SENSE CAPACITANCE
y0=2.5e-6;                 %NOMINAL SENSE GAP
yk2=3/2*Cy0*Vs^2*dx/kx/y0^3;      %QUADRATIC Y-AXIS SPRING TERM
yk3=-2*Cy0*Vs^2*dx^2/kx/y0^4;     %CUBIC Y-AXIS SPRING TERM
W=1/dwn;                   %INPUT RATE (RAD/SEC)

%ROTATIONAL MODE PARAMETERS
wt=1+0.25;                 %RESONANCE OF THETA AXIS
Qt=30000;                  %QUALITY FACTOR OF ROTATIONAL MOTION
kxt=.005;                  %X-THETA SPRING CROSS-COUPLING
kyt=0.001;                 %Y-THETA SPRING CROSS-COUPLING
bxt=0.0005;                %X-THETA CROSS-DAMPING
byt=0*0.005/q2;            %Y-THETA CROSS-DAMPING
Rt2=117;                   %NON-DIMENSIONAL RADIUS OF GYRATION SQUARED


% READ IN THE SECOND ORDER FILTER FOR PHASE AND MAGNITUDE (ALIASING)
wf=0.01                    %FREQUENCY OF FILTER
qf=2                       %QUALITY FACTOR OF FILTER

% READ IN VARIABLES ASSOCIATED WITH DRIVE FORCE
vsat=5                     %SATURATION VOLTAGE
vhiagcs=10                 %VERTICAL/ROTATIONAL AXIS HIGH SIDE AGC VOLTAGE
vhiagc=0                   %HIGH SIDE OF AGC BAND FOR DRIVE
vloagc=-10                 %LOW SIDE OF AGC FOR ALL CLOSED LOOPS
vc=vsat                    %COMB DRIVE AMPLITUDE

ktg=2.3e-9                 %FORCING CONSTANT FOR DRIVE AXIS
f1=0.5*ktg/(dm*dwn^2*dx)          %NON-DIMENSIONAL FORCING CONSTANT
f12=0.5                    %DIRECT COUPLING OF FORCE INTO VERTICAL MODE
sxy=0.7                    %COUPLING OF Y MOTION INTO SENSED X MOTION

%PREAMPLIFIER, MOTOR SENSE, AND GAIN
vdnom = pi/(4*vc*q*f1)     %NOMINAL DRIVE VOLTAGE
```

```
ksg=ktg                          %SENSING CONSTANT FOR DRIVE AXIS
vbs=5                            %BIAS VOLTAGE ON MOTOR SENSE COMB
cfb = 2e-12                      %F, FEEDBACK CAPACITOR
rfb=200e6                        %OHM, FEEDBACK CAPACITOR
cn=4e-12                         %NOISE CAPACITANCE
nf=1+cn/cfb                      %PREAMP V NOISE GAIN FACTOR
g1=10                           %DRIVE AXIS GAIN
gpre=ksg*dx*vbs/cfb              %PRE-AMP GAIN
wpre=1/(rfb*cfb*dwn)             %LOW-PASS FREQUENCY OF PRE-AMP

% LOW PASS FILTER AFTER PEAK DETECTOR
wp1=6000, wp1=wp1/dwn            %NON-DIMENSIONAL LOW-PASS FREQUENCY

%DRIVE AXIS AGC INTEGRAL COMPENSATOR
dgagc=50                         %V/V-s, DRIVE AXIS AGC GAIN
wp2=45, wp2=wp2/dwn              %NON-DIMENSIONAL LOW-PASS FREQUENCY IN AGC
wz=1,    wz=wz/dwn               %N-D ZERO LOCATION IN AGC PI COMPENSATION
gagc=dgagc*wp2/(dwn*wz)          %N-D AGC GAIN

%MISC. ELECTRONICS PARAMETERS
vhard=0.006                      %DEAD ZONE FOR HARD LIMITER
phiv=1e-16*dwn                   %WHITE NOISE PSD (SINGLE SIDED IN V^2/HZ)
dseed=1317                       %SEED FOR RANDOM NUMBER GENERATION

% INITIAL CONDITIONS OF START VARIABLES
xinit=[0.0, 0, zeros(1,60)]
dt=2*pi/80                       %DT=TIME STEP
t=0
tf=t+.4e5                        %FINAL TIME

%PRINT EVERY IPRIN'TH POINT
iprin=1500

%CALCULATE NUMBER OF LOOP INCREMENTS
n=ceil((tf-t)/dt)

%NYQUIST FREQUENCY OF STORED DATA
walcalc=1+0.375*xk3              %FREQUENCY FOR WHICH ALIASING IS CALCULATED
fny2=0.5/(dt*iprin)
fn2=0.5*walcalc/pi
nny=fix(fn2/fny2)
if rem(nny,2)==0, falias=fn2-nny*fny2, else falias=(nny+1)*fny2-fn2, end

%90 DEGREE PHASE SHIFTER, AS RESISTOR AND CAPACITOR VALUES
c51=680e-12                      %THE INTEGRATOR
rv8=1000                         %INPUT RESISTOR
r7=1000                          %THE BRIDGE ON THE PLUS INPUT
r5=1e4
ai1=[0]
bi1=[-1  r7/(r5+r7)]/(c51*rv8*dwn)
ci1=[1]
di1=[0 r7/(r5+r7)]
c6=1e-7
c7=1e-7
r9=1000
r19=430
numi2=-[c7*r9*dwn 1]/r19
deni2=[c6*c7*r9*dwn c6+c7 0]*dwn
```

```
[ai2,bi2,ci2,di2]=tf2ss(numi2,deni2)

%DERIVE THE CLOSED LOOP PHASE SHIFTER
[ai,bi,ci,di]=append(ai1,bi1,ci1,di1,ai2,bi2,ci2,di2);
xk=[0 0;0 1; 1 0]
xout=[1 0]
xin=[1 0 0]'

%CHANGE SIGNS AND MAGNITUDE OF LOOP
[ap,bp,cp,dp]=combine(ai,bi,ci,di,xin,xout,xk)
[zp,ppp,kp]=ss2zp(ap,bp,cp,dp,1)

%REFERENCE VOLTAGE FOR AGC LOOP
[mm,pp]=bode(ap,bp,cp,dp,1,walcalc)
vref=gpre*g1*(2/pi)*mm

%GAINS FOR CLOSED LOOP ANALYSIS
k=[0.1 0.5 1 2 4];
[num,den]=ss2tf(a,b,c(3,:),d(3,:),1);
roots(num);
xroot=rlocus(num,den,k);
outroot=[k; xroot']

%OPEN LOOP OF GAIN CONTROL LOOP
%GAIN OF ABSOLUTE VALUE IS 2/PI AND 0 TO 1 SWITCH REMOVES A FACTOR OF 2.
ag=[-0.5/q        0        0          0;
     gpre*g1   -wp1        0          0;
         0        1        0          0;
         0  gagc/pi   gagc/pi*wz   -wp2];
bg=[(4/pi)*f1*vc 0 0 0 ]';
cg=[0 0 0 1];
dg=[0];
[numg,deng]=ss2tf(ag,bg,cg,dg);
numgroots=roots(numg);
dengroots=roots(deng);

%GAINS FOR CLOSED LOOP ANALYSIS
kg=[0.1 0.5 1 2 4];
xrootg=rlocus(numg,deng,kg);
outrootg=[kg; xrootg'];
%PARAMETERS FOR THIRD ORDER PHASE LOCK LOOP
%CROSSOVER FREQUENCY (DIMENSIONLESS ANGULAR FREQ.)
wc=wf;
wcen=walcalc;               %CENTER FREQUENCY OF PHASE LOCKED LOOP

%COMPENSATOR ZERO-POLE SEPARATION
rtal=sqrt(6);

%LINEAR PORTION GAIN (ADDITIONAL GAIN FROM INPUT AMPLITUDE FIRST
%HARMONIC AND 0.5 FROM PHASE DETECTOR)
%AMPLIFIER SATURATION VOLTAGE
%AMPLITUDE OF INPUT SINUSOID
xamp=1
kc=2*wc*wc*rtal/xamp
apll=[0 0 0; 1 -wc*rtal 0; 0 1 0];
bpll=[kc*wc/rtal kc 0]';
cpll=[0 0 1];
dpll=[0];
```

```
xin=[1];
xk=xamp*[-1]/2;
xout=-xk;
[ac,bc,cc,dc]=combine(apll,bpll,cpll,dpll,xin,xout,xk)
eig(ac)
[nc,ddc]=ss2tf(ac,bc,cc,dc,1);
w=logspace(-4,-1);
[mc,pc]=bode(nc,ddc,w);
clg, subplot(211)
loglog(w,mc),ylabel('PLL OUT'), title('PHASE LOCKED LOOP'),grid
semilogx(w,pc), xlabel('ANGULAR FREQUENCY'),grid, ylabel('PHASE (DEG)')
%pause
zerospll=roots(nc)

%VERTICAL AXIS CLOSED LOOP PARAMETERS
Vs=5;                      %SENSE PLATE BIAS
e0=8.854e-12;              %DIELECTRIC CONSTANT
Ae=2.88e-7;                %EFFECTIVE AREA OF PROOF MASS
Ri=499e3;                  %IN-PHASE TIME CONSTANT RESISTOR
Ci=33e-12;                 %IN-PHASE TIME CONSTANT CAPACITOR
Rq=162e3;                  %QUADRATURE TIME CONSTANT RESISTOR
Cq=99e-12;                 %QUADRATURE TIME CONSTANT CAPACITOR
gs=110;                    %SENSE AXIS GAIN
gip=5;                     %IN-PHASE BIAS GAIN
gq=1.6;                    %QUADRATURE GAIN
wip=1/(Ri*Ci)/dwn;         %IN-PHASE LOWPASS FILTER FREQUENCY (RAD/SEC)
wq=1/(Rq*Cq)/dwn;          %QUADRATURE LOWPASS FILTER FREQUENCY (RAD/SEC)
Ae2=2*20*424*1e-12;        %AREA OF VERTICAL FORCE PLATE
Cyc=-e0*Ae2/(dm*dwn^2*dx*y0^2);    %VERTICAL FORCE CONTROL PLATE CAP.
Cys=Cy0/cfb;               %RATIO OF SENSE TO FEEDBACK CAPACITANCE
Kc=e0*400e-6/cfb;
l=225e-6/dx;               %N-D WIDTH OF ROTOR, WITHOUT COMB FINGERS
ls=510e-6/dx;              %N-D DISTANCE BETWEEN INSIDE OF TORQUE PLATES
wlp=2.5;                   %DIMENSIONLESS FREQUENCY FOR VERTICAL LOW-PASS
wbb=.01;                   %DIMENSIONLESS BASEBAND FREQUENCY


% ENTER PARAMETERS FOR MEMORY ELEMENTS OF HYSTERETIC RELAY
% LAST3 IS MEMORY FOR HARD LIMIT AFTER PHASE SHIFTER (IP SIGNAL)
% LAST4 IS THE SQUARE WAVE QUADRATURE SIGNAL

last3=0
last4=0;
ic = 0
nout=-1

%AGC GAINS FOR VERTICAL FORCE REBALANCE LOOP
gagcip=6*gagc;             %IN-PHASE AGC GAIN
gagcq=3*gagc;              %QUADRATURE AGC GAIN
gls=gl;                    %VERTIAL AXIS GAIN

lsp=200e-6;                %WIDTH OF ONE SENSE PLATE
Lsp=440e-6;                %LENGTH OF ONE SENSE PLATE
Wsp=440e-6;                %WIDTH OF PROOF MASS

%SENSING PARAMETERS FOR DUAL SENSE PLATE SCHEME
sk1=2*e0*Wsp*lsp/y0/cfb;
```

257

```
sk2=(3*Lsp^2-6*lsp*Lsp+4*lsp^2)/(12*y0^2);
sk3=e0*lsp*Wsp*(Lsp-lsp)/y0^2/cfb;

%NON-DIMENSIONAL PARTIAL DERIVATIVES OF COMB CAPACITORS
frpx=19.5e-12*57/(dm*dwn^2*dx);
fspx=(-6.5e-12)*57/(dm*dwn^2*dx);
frpy=44.5e-12*57/(dm*dwn^2*dx);
fspy=(-412e-12)*57/(dm*dwn^2*dx);
frsy=29.5e-12*57/(dm*dwn^2*dx);

tc=.5*44*e0*2/.25^2*dx

seojk= [q,xk2,xk3,0
         q2,wn2,xm2,xkxy
         yk2,yk3,W,bxy
         f1,f12,sxy,s1
         frpx,fspx,frpy,fspy
         frsy,Cyc,Cys,0
         wt,Qt,kxt,kyt
         bxt,byt,Rt2,0
         f2,km,0,0
         gpre,wpre,nf,g1
         sk1,sk2,sk3,0
         phiv,dseed,vref,delc
         wp1,wp2,wz,gagc
         vb,vsat,vhard,vw8
         nw8,vhiagc,vloagc,vhiagcs
         wf,qf,wcen,0
         apll,zeros(3,1)
         bpll,zeros(3,3)
         xinit(1:4)
         xinit(5:8)
         xinit(9:12)
         xinit(13:16)
         xinit(17:20)
         xinit(21:24)
         xinit(25:28)
         xinit(29:32)
         xinit(33:36)
         xinit(37:40)
         iprin,dt,t,tf
         last1,last2,last3,last4
         nout,ic,0,0
         gagcip,gagcq,g1s,tc
         Kc,y0/dx,1,ls
         wlp,wbb,wmd,gq
         ap,zeros(3,1)
         bp,zeros(3,3)
         cp,0];
save /sim/seojk.dat seojk /ascii /double;
note='/sim/seojk.dat saved'
diary off
%END OF INPUT
```

```
      implicit real*8(a-h,o-z)
C SEOJKSIM.FOR
C EXAMINATION OF SENSE AXIS CLOSED LOOP CONTROL
C INCLUDES ROTATIONAL DEGREE OF FREEDOM FOR ADVANCED MODELING
C INTEGRATE CLOSED LOOP SEO MOTOR AND AGC LOOPS
C BY FOURTH ORDER RUNGE KUTTA
C INCLUDES CROSS-COUPLING AND CUBIC STIFFNESS
C INCLUDES VERTICAL AXIS CHAIN, TORSIONAL MODE, SPLIT SENSE PLATE, ETC.
C FOR J. KOSSUTH PHD THESIS
C WRITTEN BY M. WEINBERG 1/27/95
C LATEST REVISION 8/6/97 by J. Kossuth
      common /model/ q,xk2,xk3,xk4,xk5,xbr,b2,yk,xkxy,xkxy2,bxy,
     1 f10,f12m,sxy,yk2,yk3,Wa,wt,qt,bt,tk,tkxt,tkyt,bxt,byt,f2,gk,
     2 frpx,fspx,frpy,fspy,frsy,Cyc,Cys,gagcip,gagcq,g1s,vhigcs,Rt2
      common /filter/ df1,df2,apll(3,3),bpll(3,1),wcen
      common /elect/ vb,vsat,vnoise,vnois2,vnoisSL,vnois3L,last1,last2,
     1 last3,last4,nout,ic,g,Dg,delc,wpre,gpre0,g1,gs,gagc,s1,wz,wp1,
     2 wp2,wmd,pm,vref,vhard,vw8,nw8,vhiagc,vloagc,vnoisSR,vnois3R,
     3 sKc,y0,s1,slt,wlp,wbb,sk1,sk2,sk3,lasty,tc,wip,wq,gip,gq
      common /shift/ ap(3,3), bp(3,1), cp(1,3)
      real*8 x(60), dx(60)
      real*4 gasdev

C C:\SIM\SEOJK2.DAT IS THE INPUT DATA
C C:\SIM\SEOOUT.DAT REPEATS THE INPUT DATA AND PRINTS OUTPUT
C \MLAB\BIN\RESTIME.DAT IS OUTPUT DATA THAT IS LOADED DIRECTLY INTO
C AND PLOTTED BY \MLAB\MW\PLOTTFG5.M (SIMILAR TO PLOTPIER.M)
C
C FILE 1 IS INPUT
C FILES 3 AND 4 ARE OUTPUT
      open(unit=1,file='c:\sim\seojk.dat',recl=80,status='old')
      open(unit=3,file='c:\sim\seoout.dat',status='unknown')
      open(unit=4,file='c:\mlab\bin\seorun.dat',status='unknown')

C READ IN CONSTANTS OF OSCILLATOR EQUATION
  220 read(1,10,end=210) q,xk2,xk3,xk4,xk5,xbr
   10 format(4d23.0)
      write(*,11) q,xk2,xk3,xk4,xk5,xbr
      write(3,11) q,xk2,xk3,xk4,xk5,xbr
   11 format(/1x,'q = ',1pd12.4,' xk2 = ',1pd12.4,' xk3 = ',1pd12.4,
     1' xk4 = ',1pd12.4/' xk5 = ',1pd12.4,' xbr = ',1pd12.4)

C READ IN VARIABLES ASSOCIATED WITH OUT OF PLANE MOTION
      read(1,10) q2,wn2,xm2,xkxy
      write(*,14) q2,wn2,xm2,xkxy
      write(3,14) q2,wn2,xm2,xkxy
   14 format(/' q2 = ',1pd12.4,' wn2 = ',1pd12.4,' xm2 = ',1pd12.4,
     1' xkxy = ',1pd12.4)
      read(1,10) yk2,yk3,Wa,bxy
      write(*,15) yk2,yk3,Wa
      write(3,15) yk2,yk3,Wa
   15 format(/' yk2 = ',1pd12.4,' yk3 = ',1pd12.4,' W = ',1pd12.4)

C READ IN VARIABLES ASSOCIATED WITH DRIVE FORCE
      read(1,10) f10,f12,sxy
      write(*,13) f10,f12,sxy
      write(3,13) f10,f12,sxy
   13 format(/' f10 = ',1pd12.4,' f12 = ',1pd12.4,' sxy = ',1pd12.4)
```

```
      read(1,10) frpx,fspx,frpy,fspy,frsy,Cyc,Cys

C SCALE PARAMETERS FOR SECOND MODE
C     wn2=1.5*wn2/1.2
      b2=wn2/q2
      yk=wn2*wn2
      xkxy2=xkxy/xm2
      f12m  = f12/xm2

C TORSIONAL MODE PARAMETERS
      read(1,10) wt,qt,tkxt,tkyt,bxt,byt,Rt2
      read(1,10) f2,gk
      write(*,31) wt,qt,tkxt,tkyt,bxt,byt,f2,gk
      write(3,31) wt,qt,tkxt,tkyt,bxt,byt,f2,gk
   31 format(/' wt = ',1pd12.4,' qt = ',1pd12.4,' kxt = ',1pd12.4,
     1' kyt = ',1pd12.4,' bxt = ',1pd12.4,' byt = ',1pd12.4,
     2' f2 = ',1pd12.4,' mk = ',1pd12.4)
      bt=wt/qt
      tk=wt*wt

      read(1,10) gpre0, wpre, xnf,g1
      write(*,25) gpre0, wpre, xnf,g1
      write(3,25) gpre0, wpre, xnf,g1
   25 format(/' gpre0 = ',1pd12.4,' wpre = ',1pd12.4, ' xnf = ',1pd12.4,
     1' g1 = ',1pd12.4)

C VERTICAL MOTION DETECTION GAINS
      read(1,10) sk1,sk2,sk3
      read(1,10) phiv,dseed,vref,delc
      write(*,26) phiv,dseed,vref,delc
      write(3,26) phiv,dseed,vref,delc

C AGC FILTER
   26 format(' phiv = ',1pd12.4, ' dseed = ',1pd12.4,' vref = ',1pd12.4/
     1' delc = ',1pd12.4)
      read(1,10) wp1,wp2,wz,gagc
      write(*,27) wp1,wp2,wz,gagc
      write(3,27) wp1,wp2,wz,gagc
   27 format(' wp1 = ',1pd12.4,' wp2 = ',1pd12.4,' wz = ',1pd12.4,
     1 ' gagc = ',1pd12.4)
      read(1,10) vb,vsat,vhard,vw8
      read(1,10) xnw8,vhiagc,vloagc,vhigcs
      write(*,28) vb,vsat,vhiagc,vloagc,vhard,vw8,xnw8
      write(3,28) vb,vsat,vhiagc,vloagc,vhard,vw8,xnw8
   28 format(/' vb = ',1pd12.4,' vsat = ',1pd12.4,' vhiagc = ', 1pd12.4,
     1 ' vloagc = ',1pd12.4/ ' vhard = ',1pd12.4,
     1 ' vw8 = ',1pd12.4,' xnw8 = ',1pd12.4)
      nw8=idint(xnw8/2.d0)

C READ IN THE SECOND ORDER FILTER FOR PHASE AND MAGNITUDE
C WCEN = VCO CENTER FREQUENCY (NON DIM ANGULAR FREQ.)
      read(1,10) wf,qf,wcen
      write(*,3) wf,qf,wcen
      write(3,3) wf,qf,wcen
    3 format(/1x,'wf = ',1pd12.4,' qf = ',1pd12.4,' wcen = ',1pd12.4)

C CALCULATE THE CONSTANTS FOR SECOND ORDER FILTER
      df2=wf*wf
```

```
      df1=wf/qf

C READ IN A MATRIX OF PHASE LOCK LOOP
      write(3,40)
      write(*,40)
   40 format(/1x,'APLL Matrix')
      do 41 i =1,3
      read(1,10) (apll(i,j), j=1,3)
   41 write(3,42) (apll(i,j), j=1,3)
   42 format(1x,1p6d15.6)

C READ IN B MATRIX OF PHASE LOCK LOOP
      write(3,43)
      write(*,43)
   43 format(/1x,'BPLL Matrix')
      read(1,44) bpll(1,1), bpll(2,1),bpll(3,1)
   44 format(d23.0/d23.0/d23.0)
      write(3,45) bpll(1,1), bpll(2,1),bpll(3,1)
   45 format(1x,1pd15.6)

C READ IN INITIAL CONDITIONS
      write (3,17)
      write(*,17)
   17 format(/1x,'INITIAL CONDITIONS')
      read(1,10) (x(i), i =1,39)
      write(*,12) (x(i), i =1,39)
      write(3,12) (x(i), i =1,39)
   12 format(1x,1p5d15.6)

C IPRIN = PRINT EVERY IPRIN'TH TIME STEP
C DT = TIME STEP
C T = INITIAL TIME (IMPORTANT BECAUSE OF REFERENCE COS IN DRIVE VOLTAGE)
C TF = FINAL TIME
C NUMBER OF STEP PRINTED = ((TF-T0)/DT+1)/IPRIN
      read(1,10) xprin,dt,t,tf
      iprin=idint(xprin)
      ns=idint(((tf-t)/dt+1)/iprin)
      write(*,18) iprin,ns,dt,t,tf
      write(3,18) iprin,ns,dt,t,tf
   18 format(/' iprin = ',i5,' ns = ',i6,/' dt = ',1pd12.5,' t = ',d15.6,
     1  ' tf = ',d15.6)
      iseed=idint(dseed)
      write(3,22) iseed
   22 format(' iseed = ',i10)

C ENTER PARAMETERS FOR MEMORY ELEMENTS
C LAST3 IS MEMORY FOR HARD LIMIT AFTER PHASE SHIFTER
c last4 is hard limiter for quadrature demodulation
      read(1,10) xlast3,xlast4
      last3=idint(xlast3)
      last4=idint(xlast4)
      write(*,46) last3,last4
      write(3,46) last3,last4
   46 format(/' last3 = ',i2,' last4 =',i2//)

C ENTER PARAMETERS FOR SENSE AXIS CHAIN
      read(1,10) gagcip,gagcq,g1s,tc
      read(1,10) sKc,y0,sl,slt,wip,wq,gip,gq
```

```
      write(*,52) sKc,y0,sl,slt,wip,wq,gip
      write(3,52) sKc,y0,sl,slt,wip,wq,gip
   52 format(/' sKc = ',1pd12.4,' y0 = ',1pd12.4,' l = ',1pd12.4,
     1' ls = ',1pd12.4,' wlp = ',1pd12.4,' wbb = ',1pd12.4,
     2' wmd = ',1pd12.4,' km = ',1pd12.4)

C ENTER THE PRECISION PHASE SHIFTER
C READ IN A MATRIX OF PRECISION PHASE SHIFTER
      write(3,47)
      write(*,47)
   47 format(/1x,'AP Matrix')
      do 48 i =1,3
      read(1,10) (ap(i,j), j=1,3)
   48 write(3,42) (ap(i,j), j=1,3)

C READ IN B MATRIX OF PRECISION PHASE SHIFTER
      write(3,49)
      write(*,49)
   49 format(/1x,'BP Matrix')
      read(1,44) bp(1,1), bp(2,1),bp(3,1)
      write(3,42) bp(1,1), bp(2,1),bp(3,1)

C READ IN C MATRIX OF PRECISION PHASE SHIFTER
      write(3,50)
      write(*,50)
   50 format(/1x,'CP Matrix')
      read(1,10) (cp(1,j), j=1,3)
      write(3,42) (cp(1,j), j=1,3)

C MULTIPLIERS FOR RMS NOISE GIVEN WHITE SINGLE SIDED SPECTRUM AND DT
C SCALE THE WHITE NOISE TO CORRECT STANDARD DEVIATION AND ACCOUNT FOR
C VOLTAGE NOISE GAIN
      fny=.5d0/dt
      rmsv=dsqrt(phiv*fny)*xnf
      rmsvS=dsqrt(phiv/10*fny)*xnf
      xnf2=(1.d0/xnf-1.d0)

C N = NUMBER OF STATES
      n=41

C IP = NUMBER OF VARIABLES IN VECTOR TO BE PRINTED
      ip=60

C INITIALIZE VARIABLES THAT CONTROL PRINTING IN SUB. OUTPUT
      jprin = 0
      icalc = 0
  200 if(t.gt.tf) go to 100
      call output(x,t,ip,jprin,icalc,iprin)

C DETERMINE NOISES FOR THE MOTION DETECTION PREAMPLIFIERS
      vnoise=rmsv*gasdev(iseed)
      vnois2=vnoise*xnf2
      vnoisSL=rmsvS*gasdev(iseed)
      vnois3L=vnoisSL*xnf2
      vnoisSR=rmsvS*gasdev(iseed)
      vnois3R=vnoisSR*xnf2
      call rungejk(t,dt,x,dx,n)
      t = t + dt
```

```
      go to 200
  100 tfinal = t
      write(3,33) tfinal
   33 format(' final time = ',1pd20.12)
      write(3,34) (x(i),i=1,21)
   34 format(4d20.12)
      write(3,46) last1,last2,last3,nout,ic
      go to 220
  210 stop
      end

      SUBROUTINE DIFFUN(N,T,X,DX)
      implicit real*8(a-h,o-z)
      common /model/ q,xk2,xk3,xk4,xk5,xbr,b2,yk,xkxy,xkxy2,bxy,
     1 f10,f12m,sxy,yk2,yk3,Wa,wt,qt,bt,tk,tkxt,tkyt,bxt,byt,f2,gk,
     2 frpx,fspx,frpy,fspy,frsy,Cyc,Cys,gagcip,gagcq,g1s,vhigcs,Rt2
      common /filter/ df1,df2,apll(3,3),bpll(3,1),wcen
      common /elect/ vb,vsat,vnoise,vnois2,vnoisSL,vnois3L,last1,last2,
     1 last3,last4,nout,ic,g,Dg,delc,wpre,gpre0,g1,gs,gagc,s1,wz,wp1,
     2 wp2,wmd,pm,vref,vhard,vw8,nw8,vhiagc,vloagc,vnoisSR,vnois3R,
     3 sKc,y0,s1,slt,wlp,wbb,sk1,sk2,sk3,lasty,tc,wip,wq,gip,gq
      common /shift/ ap(3,3), bp(3,1), cp(1,3)
      real*8 x(60), dx(60)
      data twopi/6.28318530717958647692d0/

C THE STATES ARE DEFINED
C
C X1 = DERIVATIVE OF GAP
C X2 = DIMENSIONLESS GAP
C X3 = DERIVATIVE OF VERTICAL (OUT OF PLANE) POSITION
C X4 = VERTICAL POSITION
C X5 = MOTOR SENSE PREAMPLIFIER OUTPUT
C X6 = 90 DEGREE PHASE SHIFTER (INTEGRATOR)
c X7 = FILTER ABSOLUTE VALUE OF PREAMP OUTPUT
C X8 = AGC INTEGRATOR OUTPUT
C X9 = AGC OUTPUT, THE MAGNITUDE OF THE CARRIER VOLTAGE
C X10 = FILTERED LATERAL MAGNITUDE SQUARED DERIVATIVE
C X11 = FILTERED SQUARED MAGNITUDE DIVIDED BY 2 (M^2/2)
C X12 = PHASE LOCK LOOP INTERNAL STATE FOR LATERAL AXIS
C X13 = PHASE LOCK LOOP TIME DERIVATIVE OF VCO PHASE
C X14 = PHASE LOCK LOOP VCO PHASE
C X15 = PRECISION SHIFTER FEEDBACK STATES
C X16 = PRECISION SHIFTER FEEDBACK STATES
C x17 = ROTATIONAL VELOCITY
C X18 = ROTATIONAL POSITION
C X19 = LEFT SENSE PLATE PREAMPLIFIER OUTPUT
C X20 = RIGHT SENSE PLATE PREAMPLIFIER OUTPUT
C X21 = LOW-PASS FILTER OF THETA IN-PHASE OUTPUT
C X22 = LOW-PASS FILTER OF THETA QUADRATURE OUTPUT
C X23 = SECOND LOW-PASS FILTER OF THETA IN-PHASE (NOT USED)
C X24 = SECOND LOW-PASS FILTER OF THETA QUADRATURE (NOT USED)
C X25 = LOW-PASS FILTER OF VERTICAL IN-PHASE OUTPUT
C X26 = LOW-PASS FILTER OF VERTICAL QUADRATURE OUTPUT
C X27 = OBSOLETE STATE (NOT USED)
C X28 = VERTICAL IN-PHASE AGC LOW-PASS FILTER TO DETERMINE ERROR
C X29 = VERTICAL IN-PHASE AGC INTEGRATOR OUTPUT
C X30 = VERTICAL IN-PHASE AGC OUTPUT, MAGNITUDE OF IN-PHASE ERROR
C X31 = VERTICAL QUADRATURE AGC LOW-PASS FILTER TO DETERMINE ERROR
```

```
C X32 = VERTICAL QUADRATURE AGC INTEGRATOR OUTPUT
C X33 = VERTICAL QUADRATURE AGC OUTPUT, MAGNITUDE OF IN-PHASE ERROR
C X34 = ROTATIONAL IN-PHASE AGC LOW-PASS FILTER TO DETERMINE ERROR
C X35 = ROTATIONAL IN-PHASE AGC INTEGRATOR OUTPUT
C X36 = ROTATIONAL IN-PHASE AGC OUTPUT, MAGNITUDE OF IN-PHASE ERROR
C X37 = ROTATIONAL QUADRATURE AGC LOW-PASS FILTER TO DETERMINE ERROR
C X38 = ROTATIONAL QUADRATURE AGC INTEGRATOR OUTPUT
C X39 = ROTATIONAL QUADRATURE AGC OUTPUT, MAGNITUDE OF IN-PHASE ERROR
C X40 = FILTERED VERTICAL MAGNITUDE SQUARED DERIVATIVE
C X41 = FILTERED SQUARED MAGNITUDE DIVIDED BY 2 (M^2/2)

C STORED VARIABLES OF INTEREST, NOT STATE VARIABLES
C X42 = LATERAL DRIVE VOLTAGE
C X43 = LATERAL DRIVE FORCE
C X44 = VERTICAL CONTROL FORCE
C X45 = VERTICAL QUADRATURE CONTROL VOLTAGE
C X46 = VERTICAL IN-PHASE CONTROL VOLTAGE
C X47 = LATERAL AGC VOLTAGE
C X48 = RIGHT SENSE PLATE OUTPUT VOLTAGE
C X49 = RIGHT TORQUE CONTROL PLATE VOLTAGE
C X50 = LEFT TORQUE CONTROL PLATE VOLTAGE
C X51 = OBSOLETE STATE
C X52 = LEFT SENSE PLATE OUTPUT VOLTAGE
C X53 = ROTATIONAL QUADRATURE CONTROL VOLTAGE
C X54 = ROTATIONAL IN-PHASE CONTROL VOLTAGE
C X55 = ROTATIONAL CONTROL TORQUE
C X56 = TOTAL RIGHT TORQUE CONTROL PLATE VOLTAGE (INCLUDES DC OFFSET)
C X57 = TOTAL LEFT TORQUE CONTROL PLATE VOLTAGE (INCLUDES DC OFFSET)


C LOW AMPLITUDE NATURAL FREQUENCY IS ONE
C
C F1 = AMPLITUDE OF DRIVE FORCE
C THE INPUTS ARE DEFINED
C Q = QUALITY FACTOR OF DRIVE
      f1=f10
      gpre=gpre0
C GENERATE THE MOTOR DRIVE FORCE
C VD = OUTPUT OF HARD LIMITER AND IS PLUS/MINUS ONE
C LAST3 IS THE OUTPUT OF HARD LIMITER WITH AMPLITUDE +/- ONE
C PHASE SHIFTER OUTPUT VOLTAGE
      vps=x(6)+cp(1,2)*x(15)+cp(1,3)*x(16)
      call limit(vps,last3,vhard)

C MOTOR AXIS PREAMPLIFIER OUTPUT
      vpre=g1*(vnoise+x(5)-vdrive*delc)
      call limit(dfloat(last3),last1,vw8)
      call limit(vpre,last4,vhard)

C HARD LIMIT AFTER 90 DEG. PHASE SHIFTER
C OUTPUT OF SATURATION AT AGC
      vagc = sat(x(9),vhiagc,vloagc)

C VERTICAL AXIS CONTROL VOLTAGE SIGNALS
      Vq=sat(x(33),vhigcs,-vhigcs)
      Vip=sat(x(30),vhigcs,-vhigcs)

C ROTATIONAL AXIS CONTROL VOLTAGE SIGNALS
```

264

```fortran
      Vqt=sat(x(39),vhigcs,-vhigcs)
      Vipt=sat(x(36),vhigcs,-vhigcs)

C CONSTRUCT CONTROL VOLTAGES FOR ALL THREE AXES
      Vdc=2*Vsat
      vcon=nout*(Vdc+Vq*last4+Vip*last3+0*x(27)
     1 -0*Vq*Vip/(Vdc)*last4*last3)
      BL=twopi/8/(3.3)/Vsat*Vipt
      AR=-2*(3.3)*2/twopi*Vsat+
     1 sqrt(2*(2*(3.3/(twopi/2))**2-1)*Vsat**2-Vqt-
     2 ((twopi/2)/(4*(3.3)*Vsat)*Vipt)**2)
      vctr=nout*(Vsat+AR*last4)
      vctl=nout*(Vsat+BL*last3)
      vdrive=(0.5d0*vagc+last3*vsat)
      forc2=0*.5*(frpx*x(27)**2+fspx*(vdrive-x(27))**2)
      force=f1*(vdrive**2)*(1.d0+xk5*x(2))
      forc2y=0*.5*(frpy*x(27)**2+fspy*(vdrive-x(27))**2+frsy*vdrive**2)
      if (t.lt.1e3) then
       forccy=0
       forcct=0
      else
       forccy=.5*Cyc/(x(4)/y0+1)**2*(vcon**2)
       forcct=(.0000102)*(Vipt*last3+Vqt*last4+
     1   (3.3/2*(AR**2-BL**2)+8/twopi*Vsat*AR))
      endif
      if (t.gt.0) then
       Wa=1/(20000*twopi)
      endif

C SUBROUTINE TO TURN ON/OFF CROSS-COUPLING FOR CHAPTER 5 SIMULATIONS
      xkxy0=xkxy
      tkxt0=tkxt
      tkyt0=tkyt
      if (t.gt.1e6) then
       xkxy0=1.25*xkxy
       tkxt0=1.25*tkxt
       tkyt0=1.25*tkyt
      endif

C INTEGRATE THE MECHANICAL TERMS
C THE DRIVE AXIS
      dx(1)=-x(1)/q-x(2)*(1+xk2*x(2)+xk3*x(2)**2)+force-xkxy0*x(4)
     1+0*forc2+2*Wa*x(3)-0*tkxt*x(18)-0*bxt*x(17)-0*bxy*x(3)
      dx(2)=x(1)
C THE COUPLED AXIS
      dx(3)=-b2*x(3)-x(4)*(yk+yk2*x(4)+yk3*x(4)**2)-bxy*x(1)
     1 -xkxy0*x(2)+0*forc2y+2*Wa*x(1)+0*forccy+f12m*force
     2 -0*tkyt0*x(18)-0*byt*x(17)
      dx(4)=x(3)
C THE MOTOR SENSE PREAMPLIFIER WITH COUPLING TO OUT-OF-PLANE
      dx(5)=(x(1)+sxy*x(3))*gpre+(vnois2-x(5)+vdrive*delc)*wpre
C THE 90 DEGREE PHASE SHIFTER
      dx(6)=bp(1,1)*vpre+ap(1,2)*x(15)+ap(1,3)*x(16)
c vhard = half width of rectangular dead zone
      dx(7) = (dabs(vps)-x(7))*wp1
      dx(8) = x(7)-vref
      dx(9) = gagc*(x(7)-vref+wz*x(8))-wp2*x(9)
C OBTAIN THE MAGNITUDE SQUARED OF MOTION BY SQUARING AND PASSING THROUGH
```

```
C SECOND ORDER FILTER
      dx(10)=-x(10)*df1-x(11)*df2+df2*x(2)*x(2)
      dx(11)=x(10)
C OBTAIN THE PHASE OF THE POSITION X(2) WITH RESPECT TO WCEN
C MODEL VCO
      phase=dmod((wcen*t+x(14)),twopi)
      vcoout=dcos(phase)
C MODEL PHASE DETECTOR
      pherr=x(2)*vcoout
C INTEGRATE TYPE 2, THIRD ORDER PHASE LOCK LOOP
      dx(12) = bpll(1,1)*pherr
      dx(13) = x(12)+apll(2,2)*x(13)+bpll(2,1)*pherr
      dx(14) = x(13)
      dx(15)=x(6)+ap(2,2)*x(15)+ap(2,3)*x(16)
      dx(16)=x(15)
C TORSIONAL MODE
      dx(17)=-bt*x(17)-tk*x(18)-tkxt0/Rt2*x(2)-tkyt0/Rt2*x(4)
     1 -bxt/Rt2*x(1)-byt/Rt2*x(3)-0*forcct
      dx(18)=x(17)
C LEFT AND RIGHT SENSE PLATE PREAMPLIFIER OUTPUT
      dx(19)=-Vsat*sk1/2*(-x(3)/y0+(47.4-20.95)/2/y0*x(17))
     1 +wpre*(vnois3L-x(19))
      dx(20)=Vsat*sk1/2*(-x(3)/y0-(47.4-20.95)/2/y0*x(17))
     1 +wpre*(vnois3R-x(20))
      VoutL=-g1s*(x(19)+vnoisSL)
      VoutR=-g1s*(x(20)+vnoisSR)
C BASEBAND DEMODULATION WITH DRIVE POSITION AND VELOCITY
      vthet=VoutL+VoutR
      vy=VoutR-VoutL
      Vti=last3*Vthet
      Vtq=last4*Vthet
      Vyi=last3*Vy
      Vyq=last4*Vy
C FINAL LOW PASS OF IN-PHASE AND QUADRATURE SIGNALS TO OBTAIN
C BASEBAND ROTATION AND SENSE AXIS MOTIONS
      dx(21)=wp1*(Vti-x(21))
      dx(22)=wp1*(Vtq-x(22))
      dx(23)=wp1*(x(21)-x(23))
      dx(24)=wp1*(x(22)-x(24))
      dx(25)=wp1*(Vyi-x(25))
      dx(26)=wp1*(Vyq-x(26))
      dx(27)=Vout-.001*x(27)
C IN-PHASE AGC FOR SENSE AXIS
      dx(28)=wp1*(x(25)-x(28))
      dx(29)=x(28)-0
      dx(30)=gagcip*(x(28)-0+wz*x(29))-wp2*x(30)
C QUAD AGC FOR SENSE AXIS
      dx(31)=wp1*(x(26)-x(31))
      dx(32)=x(31)-0
      dx(33)=gagcq*(x(31)-0+wz*x(32))-wp2*x(33)
C IN-PHASE AGC FOR TORSIONAL MODE
      dx(34)=wp1*(x(21)-x(34))
      dx(35)=x(34)-0
      dx(36)=65*gagcip*(x(34)-0+wz*x(35))-wp2*x(36)
C QUAD AGC FOR TORSIONAL MODE
      dx(37)=wp1*(x(22)-x(37))
      dx(38)=x(37)-0
      dx(39)=65*gagcq*(x(37)-0+wz*x(38))-wp2*x(39)
```

```
      dx(40)=-x(40)*df1-x(41)*df2+df2*x(4)*x(4)
      dx(41)=x(40)
C STORE VARIABLES OF INTEREST
      X(42)=vdrive
      X(43)=force
      X(44)=forccy
      X(45)=Vq
      X(46)=Vip
      X(47)=vagc
      X(48)=VoutR
      X(49)=last3
      X(50)=last4
      X(51)=dQs
      X(52)=VoutL
      X(53)=Vqt
      X(54)=Vipt
      X(55)=forcct
      X(56)=AR
      X(57)=BL
      RETURN
      END

C DEFINE FUNCTIONS USED THROUGHOUT SIMULATIONS
C SATURATION OF OP-AMP OUTPUTS
      FUNCTION SAT(XIN,VSATHI,VSATLO)
      implicit real*8(a-h,o-z)
C MODEL AMPLIFIER SATURATION WITH LINEAR AND CORNERS
      sat=xin
      if(xin.ge.vsathi) sat=vsathi
      if(xin.le.vsatlo) sat=vsatlo
      return
      end
      SUBROUTINE LIMIT(XIN,LAST,DEL)
      implicit real*8(a-h,o-z)
C HARD LIMITER WITH HYSTERESIS
C AFTER INITIAL START UP LAST IS -1 OR +1
C LAST NOT EQUAL TO  0 PERMITTED AT START UP UNTIL THRESHOLD REACHED
C SWITCHING THRESHOLD AT +/- DEL
      if(abs(last).ne.1) go to 10
      if(last.eq.-1) go to 20
C LAST OUTPUT WAS ON UPPER LIMIT
      if(xin.le.-del) last=-1
      return
C LAST OUTPUT WAS ON LOWER LIMIT
   20 if(xin.ge.del) last =1
      return
C LAST = 0, A POSSIBLE INITIAL STATE
   10 last=0
      if (xin.ge.del) last=1
      if (xin.le.-del) last=-1
      return
      end

C GENERATE RANDOM NOISE ON PRE-AMP OUTPUTS
      FUNCTION GASDEV(IDUM)
      data iset /0/
      if (iset.eq.0) then
    1    v1=2.*ran1(idum)-1
```

```
                 v2=2.*ran1(idum)-1
                 r=v1*v1+v2*v2
                 if(r.ge.1) go to 1
                 fac=sqrt(-2*log(r)/r)
                 gset=v1*fac
                 gasdev=v2*fac
                 iset=1
              else
                 gasdev=gset
                 iset=0
              endif
              return
              end
           FUNCTION RAN1(IDUM)
           DIMENSION R(97)
           PARAMETER (M1=259200,IA1=7141,IC1=54773,RM1=3.8580247E-6)
           PARAMETER (M2=134456,IA2=8121,IC2=28411,RM2=7.4373773E-6)
           PARAMETER (M3=243000,IA3=4561,IC3=51349)
           DATA IFF /0/
           IF (IDUM.LT.0.OR.IFF.EQ.0) THEN
              IFF=1
              IX1=MOD(IC1-IDUM,M1)
              IX1=MOD(IA1*IX1+IC1,M1)
              IX2=MOD(IX1,M2)
              IX1=MOD(IA1*IX1+IC1,M1)
              IX3=MOD(IX1,M3)
              DO 11 J=1,97
                 IX1=MOD(IA1*IX1+IC1,M1)
                 IX2=MOD(IA2*IX2+IC2,M2)
                 R(J)=(FLOAT(IX1)+FLOAT(IX2)*RM2)*RM1
11            CONTINUE
              IDUM=1
           ENDIF
           IX1=MOD(IA1*IX1+IC1,M1)
           IX2=MOD(IA2*IX2+IC2,M2)
           IX3=MOD(IA3*IX3+IC3,M3)
           J=1+(97*IX3)/M3
           IF(J.GT.97.OR.J.LT.1)PAUSE
           RAN1=R(J)
           R(J)=(FLOAT(IX1)+FLOAT(IX2)*RM2)*RM1
           RETURN
           END
```

References

[1]   Adams, Scott G., Fred Bertsch, and Noel C. MacDonald. "Independent Tuning of the Linear and Nonlinear Stiffness Coefficients of a Micromechanical Device." *Proceedings, IEEE MEMS Workshop*, 1996. 32-37.

[2]   Bernstein, Jonathan and Marc Weinberg. "A Micromachined Comb-Drive Tuning Fork Gyroscope." *21st Joint Services Data Exchange for Guidance, Navigation and Control.* Oct. 1992. 302-312.

[3]   Bernstein, Jonathan, S. Cho, A.T. King, A. Kourepenis, P. Maciel, and M. Weinberg. "A Micromachined Comb-Drive Tuning Fork Rate Gyroscope." *Proceedings, IEEE MEMS Workshop*, 1993. 143-148.

[4]   Blom, F.R., S. Bouwstra, M. Elwenspoek, and J.H.J. Fluitman. "Dependence of the quality factor of micromachined silicon beam resonators on pressure and geometry." *Journal of Vacuum Science Technology B.* Vol. 10(1). Jan/Feb 1992. pp. 19-26.

[5]   Borenstein, J., P. Greiff, J.B. Sohn, and M.S. Weinberg. "Characterization of Membrane Curvature in Micromachined Silicon Accelerometers and Gyroscopes Using Optical Interferometry." *SPIE Proceedings of Micromachining and Microfabrication Process Technology II.* October 1996. Vol. 2879. pp 116-125.

[6]   Cho, Young-Ho, Albert Pisano, and Roger Howe. "Viscous Damping Model for Laterally Oscillating Microstructures." *Journal of Microelectromechanical Systems.* Vol. 3, No. 2. June 1994. pp. 81-87.

[7]   Cho, Young-Ho, Byung Man Kwak, Albert P. Pisano and Roger T. Howe. "Slide Film Damping in Laterally Driven Microstructures." *Sensors and Actuators A.* Vol. 40. 1994. pp. 31-39.

[8]   Elwell, John and Capt. Tim Poth. "Micromechanical Inertial Guidance System." CSDL-P-2994.

[9]   Fedder, Gary K. and Roger T. Howe. "Multimode Digital Control of a Suspended Polysilicon Microstructure." *Journal of Microelectromechanical Systems.* Vol. 5, No. 4. December 1996. pp. 283-297.

[10]   Fedder, Gary K. *Simulation of Microelectromechanical Systems.* Ph.D. Thesis, Department of Electrical Engineering and Computer Sciences, University of California, Berkeley. Berkeley, CA. September 1994.

[11]   Feynman, Richard. "Infinitesimal Machinery." *Journal of Microelectromechanical Systems.* Vol. 2, No. 1. March 1993. pp. 4-14.

[12]   Feynman, Richard. "There's Plenty of Room at the Bottom." *Journal of Microelectromechanical Systems.* Vol. 1, No. 1. March 1992. pp. 60-66.

[13]   Gelb, Arthur and Wallace E. Vander Velde. *Multiple-Input Describing Functions and Nonlinear System Design*. McGraw-Hill, Inc.: New York, 1968.

[14]   Grieff, Paul, B. Boxenhorn, T. King, and L. Niles. "Silicon Monolithic Micromechanical Gyroscope. *Transducers '91, Digest of Technical Papers.* 1991 International Conference on Solid State Sensors and Actuators. June 1991. pp. 966-969.

[15]   Johnson, William A. and Larry K. Warne. "Electrophysics of Micromechanical Comb Actuators." *Journal of Microelectromechanical Systems.* Vol. 4, No. 1. March 1995. pp. 49-59.

[16]   Kourepenis, A., J. Borenstein, J. Connelly, P. Ward, and M. Weinberg. "Performance of Small, Low-Cost Rate Sensors for Military and Commercial Applications." 1996 Joint Service Data Exchange, Orlando, FL. November 1996.

[17]   Krylov, N. and N. Bogoliubov. *Introduction to Non-linear Mechanics.* Princeton University Press: Princeton, NJ, 1947.

[18]   Ku, Y.H. *Analysis and Control of Nonlinear Systems: Nonlinear Vibrations and Oscillations in Physical Systems* The Ronald Press Company: New York, 1958.

[19]   Maudal, I. "Stability Analysis of a Bi-Stable Multiloop System." *Preprints of Technical Papers: Fourth Joint Automatic Control Conference*, Minneapolis, Minnesota, June 1963, pp. 665-674.

[20]   Minorsky, Nicolai. *Theory of Nonlinear Control Systems.* McGraw-Hill, Inc.: New York, 1969.

[21]   Murdock, James A. *Perturbations: Theory and Methods.* John Wiley and Sons: New York, 1991.

[22]   Nayfeh, Ali H. and Dean T. Mook. *Nonlinear Oscillations.* John Wiley & Sons: New York, 1979.

[23]   Newell, William E. "Miniaturization of Tuning Forks." *Science.* Vol. 161 27 Sept. 1968. pp. 1320-1326.

[24]   Nguyen, Clark T.-C. and Roger Howe. "Quality Factor Control for Micromechanical Resonators." *Technical Digest of Int. Electron Devices Meeting.* San Francisco, CA. Dec. 1992. pp. 505-508.

[25]   Pisano, Albert. "Resonant-structure Micromotors: Historical Perspective and Analysis." *Sensors and Actuators.* Vol. 20. 1989. pp 83-89.

[26]   Pisano, Albert. "Resonant-Structure Micromotors." *IEEE Proceedings of Micro Electro Mechanical Systems Workshop.* Salt Lake City, UT, Feb 1989. pp. 44-48.

[27]   Poth, Capt. Tim and John Elwell. "Progress on Micromechanical Inertial Guidance System." *21st Joint Services Data Exchange for Guidance, Navigation and Control.* Oct. 1992. 253-261.

[28]   Starr, James B. "Squeeze-film Damping in Solid-State Accelerometers." *Technical Digest, IEEE Solid-state Sensor and Actuator Workshop*, June 1990, 44-47.

[29] Tang, William C., Martin G. Lim, and Roger T. Howe. "Electrostatic Comb Drive Levitation and Control Method." *Journal of Microelectromechanical Systems.* Vol. 1 No. 4. Dec. 1992. pp 170-178.

[30] Tang, William C., Martin G. Lim, and Roger T. Howe. "Electrostatically Balanced Comb Drive for Controlled Levitation." *Technical Digest, IEEE Solid-state and Actuator Workshop.* 1990. pp 23-27.

[31] Tang, William C., T.H. Nguyen, and R.T. Howe. "Laterally Driven Polysilicon Resonant Microstructures." *IEEE Proceedings of Micro Electro Mechanical Systems.* Salt Lake City, UT, Feb 1989. pp. 53-59.

[32] Tang, William C., Tu-Cuong H. Nguyen, and Roger T. Howe. "Laterally Driven Polysilicon Resonant Microstructures." *Sensors and Actuators.* Vol. 20. 1989. pp 25-32.

[33] Tang, William C., Tu-Cuong H. Nguyen, Michael W. Judy, and Roger T. Howe. "Electrostatic-comb Drive of Lateral Polysilicon Resonators." *Sensors and Actuators.* Vol. A21-23. 1990. pp 328-331.

[34] Vander Velde, W. Personal Facsimile.

[35] Voronov, A.A. "An Approximate Determination of the Self-Oscillation Startup Process in Certain Nonlinear Automatic Control Systems." *Automation and Remote Control.* Vol. 18 No. 7. July 1957. pp. 683-694.

[36] Weinberg, M. Personal Communication.

[37] Weinberg, M., J. Bernstein, S. Cho, A.T. King, A. Kourepenis, and P. Ward. "Initial Results on Micromachined Comb Drive Gyroscope with EDM2 Electronics." 1994 Joint Service Data Exchange, Scottsdale, AZ. October 1994.

[38] Woodson, Herbert H. and James R. Melcher. *Electromechanical Dynamics Part II: Fields, Forces, and Motions.* John Wiley & Sons: New York, 1968.

[39] Zhang, Xia and William Tang. "Viscous Air Damping in Laterally Driven Microresonators." *Proceedings of IEEE Micro Electro Mechanical Systems Workshop.* Oiso, Japan. January 1994. pp. 199-204.